Defense Threat Reduction Agency
8725 John J. Kingman Road, MS 6201
Fort Belvoir, VA 22060-6201

DTRA-TR-00-17

TECHNICAL REPORT

Plasma Radiation Source Development Program

Approved for public release; distribution is unlimited.

March 2006

DARE Tracking
73740

DSWA01-97-C-0058

Henry Sze, et al.

Prepared by:
Maxwell Physics International
Company
9244 Balboa Avenue
San Diego, CA 92123

DESTRUCTION NOTICE

FOR CLASSIFIED documents, follow the procedures in DoD 5550.22-M, National Industrial Security Program Operating Manual, Chapter 5, Section 7 (NISPOM) or DoD 5200.1-R, Information Security Program Regulation, Chapter 1X.

FOR UNCLASSIFIED limited documents, destroyed by any method that will prevent disclosure of contents or reconstruction of the document.

Retention of this document by DoD contractors is authorized in accordance with DoD 5220.22M, Industrial Security manual.

PLEASE NOTIFY THE DEFENSE THREAT REDUCTION AGENCY, ATTN: IMMI, 8725 JOHN J. KINGMAN ROAD, MS-6201, FT. BELVOIR, VA 22060-6201. IF YOUR ADDRESS IS INCORRECT, IF YOU WISH IT DELETED FROM THE DISTRIBUTION LIST, OR IF THE ADDRESSEE IS NO LONGER EMPLOYED BY YOUR ORGANIZATION.

DISTRIBUTION LIST UPDATE

This mailer is provided to enable DTRA to maintain current distribution lists for reports. (We would appreciate you providing the requested information.)

- ❑ Add the individual listed to your distribution list.
- ❑ Delete the cited organization/individual.
- ❑ Change of address.

Note:
Please return the mailing label from the document so that any additions, changes, corrections or deletions can be made easily. For distribution cancellation or more information call DTRA/BDLMI (703) 767-4725.

NAME: _____

ORGANIZATION: _____

OLD ADDRESS	NEW ADDRESS
_____	_____
_____	_____
_____	_____

TELEPHONE NUMBER: ( ) _____

DTRA PUBLICATION NUMBER/TITLE	CHANGES/DELETIONS/ADDITONS, etc. *(Attach Sheet if more Space is Required)*
_____	_____
_____	_____
_____	_____

DTRA or other GOVERNMENT CONTRACT NUMBER: _____

CERTIFICATION of NEED-TO-KNOW BY GOVERNMENT SPONSOR (if other than DTRA):

SPONSORING ORGANIZATION: _____

CONTRACTING OFFICER or REPRESENTATIVE: _____

SIGNATURE: _____

DEFENSE THREAT REDUCTION AGENCY
ATTN: BDLMI
8725 John J Kingman Road, MS 6201
Fort Belvoir, VA 22060-6201

DEFENSE THREAT REDUCTION AGENCY
ATTN: BDLMI
8725 John J Kingman Road, MS 6201
Fort Belvoir, VA 22060-6201

REPORT DOCUMENTATION PAGE

Form Approved
OMB No. 0704-0188

Public reporting for this collection of information is estimated to average 1 hour per response, including the time for reviewing instructions, searching existing data sources, gathering and maintaining the data needed, and completing and reviewing the collection of information. Send comments regarding this burden estimate or any other aspect of this collection of information, including suggestions for reducing this burden to Washington Headquarters Services, Directorate for Information Operations and Reports, 1215 Jefferson Davis Highway, Suite 1204, Arlington, VA 22022-4302, and to the Office of Management and Budget, Paperwork Reduction Project (0704-0188), Washington, DC 20503.

1. AGENCY USE ONLY *(Leave Blank)*	2. REPORT DATE	3. REPORT TYPE AND DATE COVERED
	March 2006	Technical 970312-000311

4. TITLE AND SUBTITLE
Plasma Radiation Source Development Program

5. FUNDING NUMBERS
C - DSWA01-97-C-0058
PE - 62715H
PR - AB
TA - GE
WU - DH54442

6. AUTHOR(S)
Henry Sze, Phil Coleman, Bruce Failor, Jerry Levine, John Riordan, Yuanxu Song, and Eduardo Waisman

7. PERFORMING ORGANIZATION NAME(S) AND ADDRESS(ES)
Maxwell Physics International Company
P.O. Box 5010
San Leandro, CA 94577-0599

8. PERFORMING ORGANIZATION REPORT NUMBER
PITR-6584

9. SPONSORING/MONITORING AGENCY NAMES(S) AND ADDRESS(ES)
Defense Threat Reduction Agency
8725 John J. Kingman Road, MS-6201
Ft. Belvoir, VA 22060-6201
TDANS/Bell

10 SPONSORING/MONITORING AGENCY REPORT NUMBER
DTRA-TR-00-17

11. SUPPLEMENTARY NOTES
This work was sponsored by the Defense Threat Reduction Agency under RDT&E RMC code B 4662 D AB GE 54442 3E10 25904D.

12a. DISTRIBUTUION AVAILABILITY STATEMENT
Approved for public release; distribution is unlimited

12b. DISTRIBUTION CODE

ABSTRACT (Maximum 200 words)
This report summarizes the results of a 3 year effort to develop long implosion time (>150 ns) z-pinch loads for use on the planned Decade Quad (DQ) pulsed power generator. Well diagnosed experiments demonstrated high quality, 200 ns implosions using argon gas puff loads. We show that solid fill and double shell mass distributions perform better than thin shells. The dual plenum, double shell load has unique diagnostic features that enhance our understanding of z-pinch implosion dynamics. Long pulse tests with aluminum wire arrays as well as the argon gas puffs show a decrease in K-shell yield as implosion time increases.

13. SUBJECT TERMS
Z-pinch
pulsed-power
CCDs
x-ray diagnostics
x-ray spectroscopy
ultraviolet preionization
Rayleigh-Taylor instability
supersonic nozzle design & testing

15. PAGE COUNT
188

16. PRICE CODE

17. SECURITY CLASSIFICATION OF REPORT	18. SECURITY CLASSIFICATION OF THIS PAGE	19. SECURITY CLASSIFICATION OF ABSTRACT	20. LIMITATION OF ABTSTRACT
UNCLASSIFIED	UNCLASSIFIED	UNCLASSIFIED	SAR

NSN 7540-01-280-5500

Standard Form 298 (Rev 2-89)
Prescribed by ANSI Sta. 239-18
298-102

EXECUTIVE SUMMARY

This is the final technical report for Defense Threat Reduction Agency Contract No. DSWA01-97-C-0058, the Decade Quad Plasma Radiation Source Development Program, covering the period 12 March 1997 through 11 March 2000. During the three years of this program, the Maxwell Physics International (MPI) team has achieved significant progress in developing plasma radiation sources (PRS) for the longer current risetime typical of the direct-drive Decade Quad (DQ). In particular, we have successfully developed an argon gas puff PRS that produces a high quality pinch with a ~ 200-ns implosion time. Conservative scaling of this result to the expected operating current of DQ implies that we know how to build a load that will meet the program objective of a 40-kJ K-shell x-ray yield on DQ. This and other achievements are summarized below.

We have shown that large-diameter, solid-fill gas puffs can achieve adequate heating and stability for long-implosion z-pinches with good K-shell yield. To produce high x-ray yields, the imploding z-pinch must reach comparable temperature and density in the final plasma as seen with a conventional ≤ 100-ns implosion. This requires that a long implosion time z-pinch must start from larger initial radius and still achieve high compression, as described in Section 1. The hydromagnetic Rayleigh-Taylor instability will disrupt the implosion of large-diameter, hollow shells, limiting the temperature and density of the radiating mass. The data presented here and in other experiments show that the instability is effectively mitigated for large loads by the continuous mass accretion during the "snowplow" of a filled-in initial density profile.

A solid-fill argon gas puff with 7-cm diameter has been developed for high x-ray yields with ~ 200-ns implosions. Section 2 describes experiments with this nozzle. On Double-EAGLE in the long-pulse mode, we demonstrated ≥ 13 kJ K-shell x-ray yield with a 4.0-MA peak current and a 190-ns implosion time. These experiments also confirmed that the long-implosion yield has an I^4 current scaling up to 4 MA as observed for short-implosion PRS. In addition, we have performed extensive optimization and measurements of not only the solid-fill PRS, but also the conventional shell PRS with both long and short-implosion times.

Long-implosion argon PRS experiments were also performed on DM2 and Saturn. The DM2 experiments had implosion times near 300 ns and peak currents near 2.3 MA. The three nozzles (5-cm-diameter thin shell, 5-cm-diameter thick shell, and 7-cm-diameter solid-fill) used in the first DM2 campaign all gave peak K-shell yields near 1.3 kJ, but the thin shell showed more variability in yield and significantly lower pinch quality. In the second campaign, the use of an improved pre-ionizer and nozzle exit wires increased the yield to 1.8 kJ for the 7-cm solid-fill load. A brief, unoptimized, high-current test series on Saturn achieved 18-kJ yield with 6.5-MA peak current and 170-ns implosion time.

In the final year of this project we also developed a double-shell ("shell-on-shell") gas puff for use with a long implosion time driver. The double-shell load performed as well as (or better than) the 7-cm uniform fill load in experiments on Double-EAGLE and Saturn. The double

shell's dual plenum feature permits some very useful diagnostics that shed light on critical details of the implosion process. See Section 3 for details.

We have demonstrated efficient x-ray emission from large-diameter wire array loads. Such loads will be required for the mixed-element, high-fidelity PRS goal. Section 4 describes long-implosion tests of aluminum wire arrays with 4-cm diameter on DM2, Double-EAGLE, and Saturn. The respective K-shell yields were 4, > 18 and > 60 kJ. A wire number scan in the Double-EAGLE long-pulse mode confirmed the pulse-sharpening effects that have previously been observed for short implosion times. However, K-shell yield does not seem to be affected by wire number. We also tested molybdenum wire arrays with 2.5-cm diameter in the Double-EAGLE short-pulse mode (4.5 MA, 100 ns). The L-shell yield (with a mean photon energy of 2.6 keV) was < 3 kJ, significantly lower than the > 20 kJ argon K-shell yield at similar current.

Section 5 summarizes our experiences with long-implosion time loads and compares their performance with that of "short" implosion time loads. We identify empirical trends and discuss some of the physics behind the trends and the prospects for PRS loads on the Decade Quad.

The argon K-shell x-ray yields observed in both short- and long-implosion PRS can be correlated using simple, "zero-dimensional" (0D) models. The analysis of Section 6 shows that the theoretical yields are in reasonable agreement with the Double-EAGLE results for effective compression ratios of 15 to 17. The analysis also highlights the dependence of yield upon final density, giving different optimized yields when final radius or compression ratio is held fixed.

Detailed measurements of local conditions in the final pinched plasma were performed to understand the similarities and differences between long- and short-implosion PRS. Section 7 presents analyses of spectra using a chlorine dopant to obtain temperature and density measurements for the Double-EAGLE argon experiments. The electron temperature increases with the initial gas puff radius, while the electron density decreases. Axially-resolved spectra show more intense emission from regions that are initially filled in, and that higher density leads to better thermalization of the ion energy. Average plasma conditions inferred from chlorine are consistent with the measured argon yields.

Two new x-ray imaging and a (revived) optical diagnostic were used to study the initiation and implosion of both gas puff and wire array PRS, as described in Section 8. First we show how optical framing camera images can help us understand the initiation and implosion phases of the z-pinches. In some cases with a "shell" PRS, a two-dimensional mode can be seen with an axial wavelength of 4 mm growing on the periphery. Second we used an axially-resolved x-ray detector array to measure and minimize the "zipper" (non-simultaneous assembly on axis) in the gas puff implosion. The zipper broadens the argon x-ray pulse by about 5 ns, but has no deleterious effect on yield. One-dimensional calculations using measured density profiles (per Section 9) show good agreement with implosion times measured with the zipper array. No systematic zipper was observed with wire arrays but we did see statistically significant yield variations along the pinch axis. Third, we show that CCDs (charge coupled devices) can give very high quality data for both x-ray pinhole images and spectra. The wide dynamic range, linearity and ease of use of CCDs compared to conventional film make the CCDs very attractive as PRS diagnostics.

Initial conditions for the long-implosion argon PRS have been characterized in detail using interferometers at the Naval Research Laboratory and at Alameda Applied Sciences Corporation. Section 9 presents radial profiles of initial gas density at several axial locations for a variety of nozzles, nominal "shells" to solid fills. We also describe the development of the double shell gas puff in this section.

Section 10 covers the development of circular flashboard pre-ionizers. These pre-ionizers provide > 1% ionization at the periphery of the gas flow with excellent azimuthal uniformity.

PREFACE

A large number of scientists, engineers and technicians contributed to the success of the project. At the SATURN facility of Sandia, we had excellent support from C. Coverdale, C. Deeney, D. Jobe, J. McGurn, B. Peyton, and the SATURN crew. At the Naval Research Laboratory, B. Weber and B. Moosman provided high quality interferometry data on gas flows; we also thank D. Mosher for valuable technical discussions. J. Apruzese, Y. Chong, J. Davis, F. Cochran, J. Thornhill, and A. Velikovich offered both detailed data analysis/interpretation and guidance for test design. A. Fisher gave us excellent advice for the development and testing of the double-shell nozzle. M. Krishnan and N. Qi at AASC contributed gas flow data from their interferometer. E. Yadlowsky of HyTech supported the DM2 tests with innovative diagnostics. At DM2 and Double-EAGLE, the Maxwell support personnel were essential to our good results. Finally, we greatly appreciate the technical, programmatic and financial assistance from the DTRA program monitors, Dr. R. Schneider and his successor, Dr. D. Bell.

CONVERSION TABLE

Conversion Table

Conversion factors for U.S. Customary to metric (SI) units of measurement.

MULTIPLY → TO GET	by	← TO GET DIVIDE
angstrom	1.000 000 X E -10	meters (m)
atmosphere (normal)	1.013 25 X E +2	kilo pascal (kPa)
bar	1.000 000 X E +2	kilo pascal (kPa)
barn	1.000 000 X E -28	meter^2 (m^2)
British thermal unit (thermochemical)	1.054 350 X E +3	joule (J)
calorie (thermochemical)	4.184 000 X E -2	joule (J)
cal (thermochemical/cm^2)	4.184 000 X E -2	mega joule/m^2 (MJ/m^2)
curie	3.700 000 X E +1	* giga becquerel (GBq)
degree (angle)	1.745 329 X E -2	radian (rad)
degree Fahrenheit	$t_k = (t\ °f + 459.67)/1.8$	degree kelvin (K)
electron volt	1.602 19 X E -19	joule (J)
erg	1.000 000 X E -7	joule (J)
erg/second	1.000 000 X E -7	watt (W)
foot	3.048 000 X E -1	meter (m)
foot-pound-force	1.355 818	joule (J)
gallon (U.S. liquid)	3.785 412 X E -3	meter^3 (m^3)
inch	2.540 000 X E -2	meter (m)
jerk	1.000 000 X E +9	joule (J)
joule/kilogram (J/kg) radiation dose absorbed	1.000 000	** Gray (Gy)
kilotons	4.183	terajoules
kip (1000 lbf)	4.448 222 X E +3	newton (N)
kip/inch^2 (ksi)	6.894 757 X E +3	kilo pascal (kPa)
ktap	1.000 000 X E +2	newton-second/m^2 (N-s/m^2)
micron	1.000 000 X E -6	meter (m)
mil	2.540 000 X E -5	meter (m)
mile (international)	1.609 344 X E +3	meter (m)
ounce	2.834 952 X E -2	kilogram (kg)
pound-force (lbs avoirdupois)	4.448 222	newton (N)
pound-force inch	1.129 848 X E -1	newton-meter (N•m)
pound-force/inch	1.751 2688 X E +2	newton/meter (N/m)
pound-force/foot^2	4.788 026 X E -2	kilo pascal (kPa)
pound-force/inch^2 (psi)	6.894 757	kilo pascal (kPa)
pound-mass (lbm avoirdupois)	4.535 924 X E -1	kilogram (kg)
pound-mass-foot^2 (moment of inertia)	4.214 011 X E -2	kilogram-meter^2 (kg•m^2)
pound-mass/foot^3	1.601 846 X E +1	kilogram/meter^3 (kg/m^3)
rad (radiation dose absorbed)	1.000 000 X E -2	** Gray (Gy)
roentgen	2.579 760 X E 4	coulomb/kilogram (C/kg)
shake	1.000 000 X E -8	second (s)
slug	1.459 390 X E +1	kilogram (kg)
torr (mm Hg, 0°C)	1.333 22 X E -1	kilo pascal (kPa)

*The becquerel (Bq) is the SI unit of radioactivity; 1 Bq = 1 event/s.

**The Gray (GY) is the SI unit of absorbed radiation.

TABLE OF CONTENTS

TABLE OF CONTENTS (Continued)

TABLE OF CONTENTS (Continued)

FIGURES

FIGURES (Continued)

FIGURES (Continued)

FIGURES (Continued)

FIGURES (Continued)

FIGURES (Continued)

FIGURES (Continued)

FIGURES (Continued)

TABLES

SECTION 1

INTRODUCTION: BASIC SCALING CONSIDERATIONS FOR LONG-IMPLOSION TIME Z-PINCHES

Efficient generation of "cold" x-rays (1-5 keV) has been achieved in many laboratories using z-pinch plasma radiation sources (PRS) driven by short (≤ 100 ns) pulses of multi-megampere currents (Reference 1, 2, 3). In a typical PRS z-pinch, an annular "shell" gas puff or cylindrical array of wires is accelerated radially inward by the JxB interaction of the pinch current and its self-generated magnetic field. The imploding mass ultimately stagnates on the pinch axis, creating a hot, dense plasma that converts the kinetic energy of the implosion to radiation. Experiment and theory have shown that the x-ray yield increases as the imploded mass increases. For low masses, the yield varies as the product of electron and ion densities, i.e., as the square of the mass. Simple dynamic arguments (see below) show that for fixed initial radius of the mass and a fixed implosion time, the imploded mass varies as the square of the peak current. Hence, for a fixed implosion velocity (roughly load radius divided by implosion time), the yield should scale as the fourth power of the peak current, I^4. This is termed the "inefficient" regime. As the radiated yield becomes comparable to the available kinetic energy, energy conservation limits the yield. Then we expect the yield to increase as the mass or as I^2; this is called the "efficient" regime (References 4, 5). For K-shell emission, the current at which this transition occurs increases with at least the cube of the atomic number of the radiating plasma.

Until recently, PRSs have operated with implosion times of 100 ns or less, requiring megavolt pulsed-power generators to drive the required current into the inductive PRS load. Higher-current x-ray simulators envisioned to produce higher x-ray yields at higher photon energies must then operate at higher voltages. Unfortunately, the higher voltage operation requires additional volume and inductance, thereby limiting the electrical power that can be coupled through the dielectric-vacuum interface from the pulsed power generator to the load. During the past decade, much effort has been devoted to the development of inductive-store, plasma-opening-switch (IS/POS) systems that can perform power multiplication in vacuum. The development of a high-current, fast-opening switch has proven to be a technological challenge with only limited success to date.

A "long" implosion time (> 150 ns) PRS provides an alternative approach that can mitigate the pulse-power risk in the IS/POS approach. The longer implosion time allows the current to ramp up more slowly, thereby reducing the voltage and power requirements on the generator. In effect, the PRS provides additional pulse compression in vacuum as the electromagnetic energy from the generator is converted into kinetic energy in the imploding z-pinch. The key risk in this approach is whether the radiation efficiency of the short (≤ 100-ns) implosion can be maintained at significantly longer implosion times.

The objective of the present program was to develop long-implosion PRSs that can be scaled to the Decade Quad (DQ) generator, which is expected to deliver over 8 MA peak current with a 300-ns risetime. Two cold x-ray sources are under development: an argon PRS with a mean photon energy near 3 keV and a high-fidelity, mixed-element PRS to simulate a 1-keV blackbody spectrum. The argon PRS has a K-shell x-ray yield goal of 40-kJ on DQ; we believe that this goal can be achieved by extrapolating the technology described in this report. The high-fidelity PRS has simultaneous yield goals of 45 kJ at > 1 keV, 25 kJ at > 3 keV, and 10 kJ at > 4.5 keV on DQ. Although these three yields have been achieved individually with ≈ 60-ns implosions at DQ current levels on Saturn (Reference 6), the best mixed-element results to date are about a factor of 10 below the DQ goals (Reference 7).

To achieve efficient K-shell x-ray emission from a PRS, it is necessary to heat the plasma to a temperature of at least 30% of the He-α line energy, or $T_e > 1$ keV for argon. This requires that the kinetic energy of an imploding atom exceed a minimum energy E_{min} equal to the sum of the outer shell ionization energies plus the electron and ion thermal energies ($E_{min} = 40$ keV for argon). This requirement is usually expressed by the condition $\eta > 1$, where η is the kinetic energy per atom divided by E_{min} (Reference 8). Since the implosion velocity scales as the initial radius divided by implosion time, the initial radius must increase in proportion to the implosion time to maintain the same final velocity and η.

In the "efficient" (I^2 scaling) regime (Reference 5) the radiated energy becomes a large fraction of the available implosion energy. Hence the K-shell emission scales linearly with mass/length, so that mass/length as well as temperature must be maintained for a long-implosion PRS. To investigate the scaling with implosion time, consider the dimensionless equation of motion of a thin shell accelerated by a linearly rising current:

$$x\frac{d^2x}{d\tau^2} = \frac{-\mu_0}{4\pi m}\left[\frac{I_{pk}\, t_{imp}}{r_0}\right]^2 \tau^2$$

where x is the shell radius normalized to its initial value r_0, τ is time normalized to the implosion time t_{imp}, m is the mass/length, and I_{pk} is the peak current. Analysis of this equation leads to the general relation

$$m = k\,(I_{pk}\, t_{imp} / r_0)^2$$

where the constant k depends on the shape of the radial mass distribution of the imploding mass (a shell or solid fill, etc.) and on the shape of the current's rise to its peak value. For example, with mass in μg/cm, current in megamps (MA), time in nanoseconds (ns) and radius in centimeters (cm), a linear current ramp driving an ideal shell has a value for k of 0.0012. For other mass distributions, use the mean radius as defined below for r_0.

Assuming the short and long implosions have the same ratio of initial radius to implosion time, then the mass/length scales as the peak current squared independent of implosion time. Thus both long- and short-implosion PRS with the same peak currents should produce the same x-ray

yield, provided they can achieve the same compression ratio (ratio of initial to final radii) required to maintain η.

In the non-efficient (I^4 scaling) regime, the PRS plasma must also achieve high density to radiate a significant x-ray yield because the x-ray power is proportional to the product of electron and ion densities (n_e and n_i). Assuming that the radiating volume and pulsewidth respectively scale as r_f^2 and r_f, where r_f is the final compressed radius of the pinch, the yield then scales as mass-squared (Reference 5):

$$Y \propto n_e n_i r_f^3 \propto m^2 / r_f .$$

But we see that the yield also scales inversely with r_f, so the long-implosion PRS must pinch to the same final radius to maintain the x-ray yield. Since the long implosion starts at a larger initial radius, it requires a higher compression ratio to achieve the same final radius and density achieved in the short-implosion PRS.

Imploding z-pinches are susceptible to the hydromagnetic Rayleigh-Taylor (RT) instability, which can limit the density and temperature achieved in a PRS. Two-dimensional magneto-hydrodynamic simulations predict large-scale "bubble and spike" structures that disrupt the implosion of thin shells, especially for large initial diameters (References 9, 10). Nevertheless, other theoretical studies have shown that the RT instability is mitigated for filled-in density profiles, where the continuous mass accretion provides "snowplow stabilization" (Reference 11, 12).

We have experimentally examined long-implosion PRS using large-diameter gas puffs with both shell and solid-fill density profiles. For a filled gas puff, the implosion energy includes not only kinetic energy but also shock heating associated with the snowplow; thus η is generalized to a quantity η^* defined as the total JxB work per atom divided by E_{min}. We define a mass-weighted-mean initial radius in terms of the radial density profile $\rho(r)$ as

$$r_m^2 \equiv \frac{\int_0^\infty r^2 \rho(r)\, r dr}{\int_0^\infty \rho(r)\, r dr}$$

Thus, the initial outer radius of a uniform fill distribution (constant density) must be 41% larger than that of a thin shell to have the same mean radius. If the compression ratio is defined as the ratio of the mean initial radius to the final pinch radius, then shell and uniform-fill loads with equal compression ratios will reach the same final density and η^* (based on a snowplow calculation).

On the basis of these concepts, we come to the following expectations. Assume that a given pulsed power generator like Double-EAGLE can reach the same peak current independent of current risetime. Assume that compression ratio (mean initial radius to final pinch radius) is fixed. Then at a fixed implosion time, ideal shell and corresponding uniform fill mass distributions will give similar yields if instabilities are not serious. As implosion time is increased and thus initial radius is increased, the final radius will also increase and yield will decrease roughly inversely with implosion time.

With the objective of understanding how to build a gas puff load that can deliver 40 kJ of argon K-shell radiation on DQ, this project has conducted experiments to test the expectations noted above. Our results are presented in this final report and summarized below.

In brief, we find that a nominal "shell" load always performs worse than the corresponding uniform fill load. This result confirms results seen in earlier experiments on ACE 4 and Saturn (Reference 13). The implication is that (1) instabilities do seriously disrupt the shell implosions and (2) snowplow stabilization is effective for the uniform fill loads.

A second key observation from our tests is that there is a yield penalty as implosion time increases. The exact dependence is not well established, but to zeroth order the yield varies inversely with implosion time. The implication is that the compression ratio of the pinch is roughly fixed. Although simple models exist to explain this result, the models cannot explain key pinch parameters, such as K-shell pulse width, that do not seem to be well-correlated with implosion time. In particular, long implosion times do not always imply wide pulse width, which should scale with the final pinch radius.

In spite of these complications, our results (Section 2) show that we know enough to design a gas flow that should reach the 40 kJ objective on DQ. A solid-fill gas puff with 7-cm diameter did perform well in long-pulse experiments on Double-EAGLE, producing more than 13 kJ of K-shell yield at a peak current of 4.0 MA and 190-ns implosion time. A more complex load, a double shell (Section 3), achieved comparable results and offers very useful diagnostic advantages. Unoptimized tests with a 10-cm uniform fill load on Double-EAGLE (and earlier on ACE 4) show that such large radius uniform fill loads do work well and are not seriously disrupted by instabilities.

We have also made significant progress with large-diameter wire array loads (Section 4) required for the long-implosion, high-fidelity PRS. Experiments using 4-cm-diameter arrays of aluminum wires on DM2 (2.5 MA, 300 ns) and Saturn (7.5 MA, 165 ns) have achieved over 80% of the K-shell yields typical of < 100-ns implosions at similar currents. We project that DQ should exceed the 45 kJ goal for x-rays at > 1 keV. However, the 10-kJ yield goal at > 4.5 keV remains a major challenge for mixed-element PRS with either short or long implosion time.

SECTION 2

DEVELOPMENT OF UNIFORM-FILL GAS LOADS FOR LONG-IMPLOSION TIME Z-PINCHES

2.1 INTRODUCTION.

We started our research effort from the tradition of using nominal shell loads in 100 ns implosions. The Double-EAGLE 2.5-cm diameter argon gas puff was the basis for that tradition. Our challenge was to demonstrate good quality 200-ns implosions that were not hopelessly disrupted by instabilities. We began with a comparison of two loads appropriate for 200 ns implosion times: a 5-cm "shell" and the corresponding 7-cm (40% larger) uniform fill. In tests first on DM2 and then on Double-EAGLE, we showed that the uniform fill could work well and that it was always superior (by > 40% in yield and > 100% in power) to the shell load. Table 2-1 compares yield and peak K-power data from those experiments as well as comparable data from ACE 4.

Table 2-1. Comparison of shell and uniform-fill long-pulse argon results on 3 machines.

Machine	Current	Implosion Time	7-cm Uniform Fill		5-cm Shell	
	MA	ns	K-Power TW	K-Yield kJ	K-Power TW	K-Yield kJ
DM2	2.3	300	0.08	1.7	0.04	1.2
ACE 4	2.9	200	0.7	3.7	0.2	1.9
Double-EAGLE	3.6	180	0.8	10.6	0.3	6.8

In Section 5 we review these data empirically to see that they scale with current as expected and to demonstrate how they correlate with short implosion time data. In Section 6 we will show that the uniform fill results are consistent with "0-D" predictions (Reference 14) for well-behaved implosions with realistic compression ratios.

In this section we also discuss a limited number of tests with a 10-cm diameter uniform fill nozzle; those results were encouraging, showing that such large loads are not seriously disrupted

by instabilities. Hence all of our data imply that a large radius, uniform fill load is a practical approach to achieving the desired 40 kJ on DQ.

We now describe in detail our test results for uniform fill loads. Most of our effort used Double-EAGLE and those results are presented in Section 2.2. Our initial long implosion time results, taken on DM2, appear in Section 2.3. A very limited test series with the 7-cm uniform fill nozzle on SATURN is described in Section 2.4. A more recent development, the double shell nozzle, is discussed in Section 3.

2.2 DOUBLE-EAGLE ARGON PRS EXPERIMENTS.

During this project we performed several test series to optimize the K-shell x-ray yield from an argon gas-puff with a long implosion time. The key objective of those experiments was to understand significant physics differences between long- and short-implosion PRS by holding other key variables (current, mass, coupled energy) constant. Double-EAGLE was selected as the test bed because of its demonstrated capability to deliver high current (up to 4 MA) into a PRS with a risetime adjustable from 100 to 300 ns. Using a 7-cm solid-fill gas puff, we achieved a > 13 kJ x-ray yield and a < 16 ns pulsewidth (FWHM) with a 190-ns implosion time and 4.0-MA peak current. Spectral diagnostics indicate that the density in the radiating core decreased by a factor > 2 for the longer implosion time (compared to 100-ns implosions), while the temperature showed no significant change (see Section 7 for details). High-current experiments also confirmed that the long-implosion yield scaled as I^4 for currents up to at least 4.0-MA. Although mass accretion from the snowplow appears to mitigate the hydromagnetic Rayleigh-Taylor instability, there remain two-dimensional effects that may limit the density, x-ray yield, and x-ray power in long-implosion PRS.

2.2.1 Double-EAGLE Long-pulse Mode.

For a given pulse-power generator, the x-ray output from a PRS is typically optimized when the implosion time is nearly equal to the risetime of the current pulse into a non-imploding inductive load. The conventional argon PRS on Double-EAGLE, for example, gives maximum x-ray yield at a 100-ns implosion time that is equal to the risetime of the short-circuit current. Thus, to investigate an optimized 200-ns implosion PRS, it was necessary to have a test bed with a 200-ns current risetime. Fortunately, the design of the Double-EAGLE pulse-forming line (PFL) provides sufficient flexibility to extend the current risetime to 200 ns with no decrease in peak current. This 200-ns long-pulse operating mode is achieved by completely closing the water switch gaps downstream from the PFL and by reducing the water switch gaps upstream of the PFL from 13 cm to 4 cm.

The Double-EAGLE generator delivers the same > 3.5 MA peak current to an imploding gas puff PRS in both its short- and long-pulse modes. The current is measured with Rogowski coils at the upper and lower insulator stacks, in the upper and lower magnetically insulated transmission lines (MITLs) just upstream from the post-hole convolute, and at the PRS load downstream from the convolute (See Figure 2-1). The upper and lower currents are summed and compared to the total load current in Figure 2-2. Notice that current waveforms are in excellent agreement,

indicating full current coupling through the MITLs and convolute, even in the long-pulse mode. Furthermore, the current dip caused by the back electromotive force (I * dL/dt) of the imploding pinch is clearly visible on all waveforms, indicating that the load is well-coupled to the generator through the entire implosion.

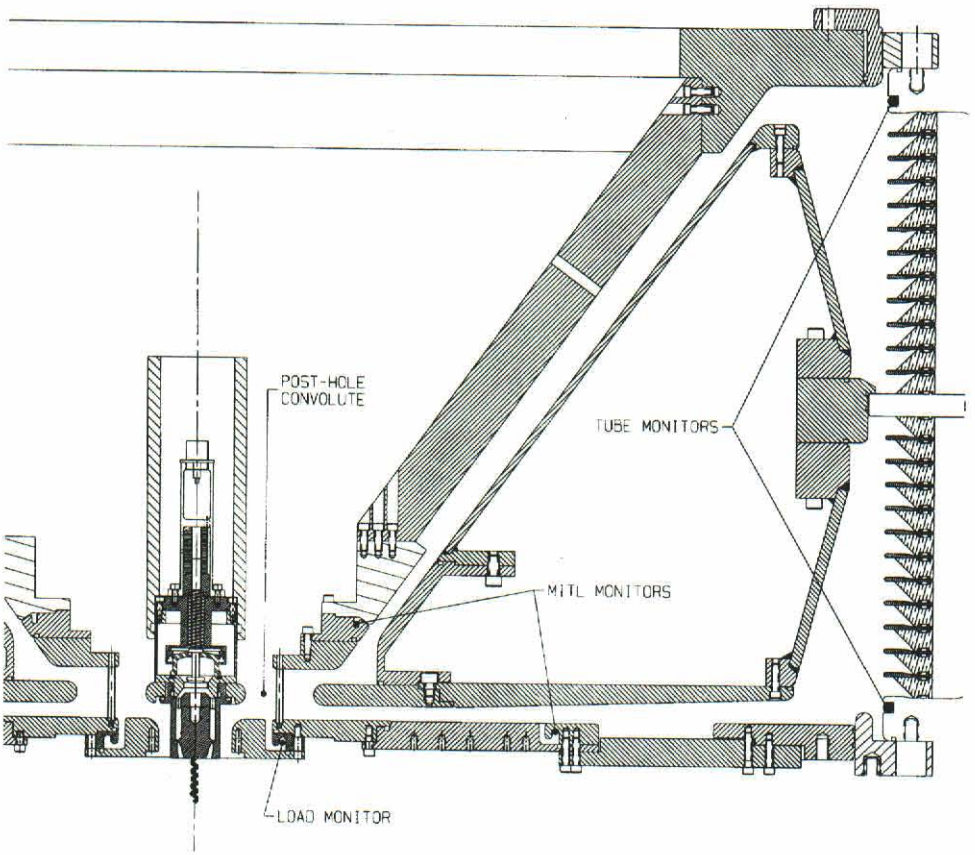

Figure 2-1. Location of Double-EAGLE current monitors.

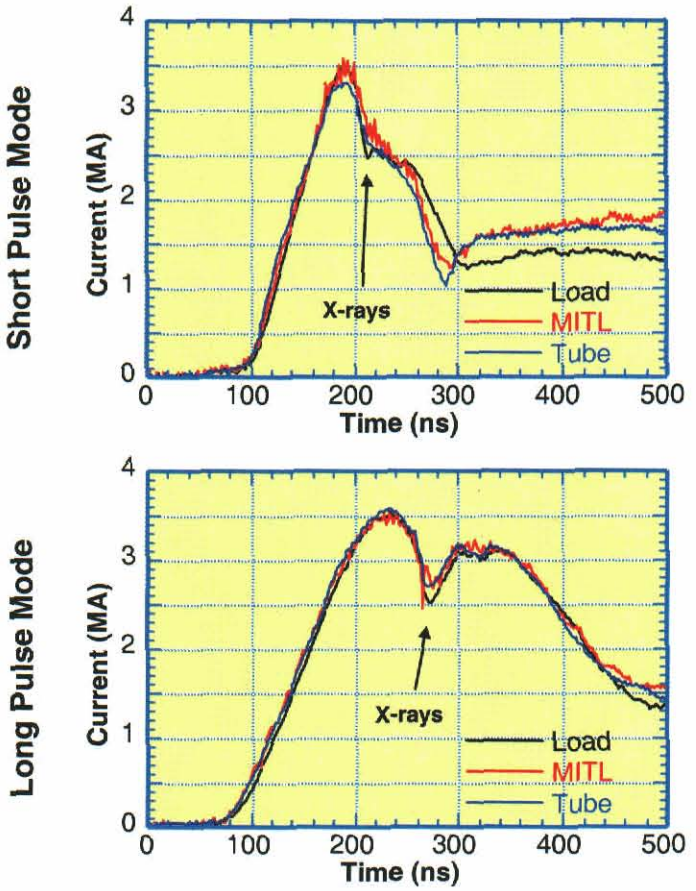

Figure 2-2. Current monitors show excellent power coupling through the convolute to the load in both short- and long-pulse modes.

Operation at even longer current pulses is possible on Double-EAGLE, but was not pursued extensively for these experiments. However, we did perform several shots in which both water-switches (upstream and downstream from the PFL) were completely closed. These shots demonstrated a 300-ns current risetime, but the peak current decreased slightly to ~ 3 MA. Additional pulse-line variations utilizing the triggered gas switches can provide a 300-ns mode with higher current.

For the long-implosion PRS, we wanted to produce a z-pinch plasma with the same implosion velocity as that of the standard Double-EAGLE argon PRS, which uses a 2.5-cm-diameter shell with a 100-ns implosion time. Thus, we chose a 5-cm-mean-diameter to give the required final velocity for the 200-ns implosion. However, it is important to note that achieving the same final density would require reaching the same final radius, which is a factor of 2 higher compression ratio than achieved with the 2.5-cm, 100-ns implosion. In comparing short- and long-implosion PRS, we also wanted to investigate a solid-fill gas puff that had demonstrated improved x-ray output in previous experiments (Reference 13). Thus, we selected a 7-cm initial outer diameter for the solid fill nozzle to provide an effective diameter similar to that of the 5-cm shell.

Three different gas puffs were produced by the supersonic nozzles shown in Figure 2-3. A fast-opening puff valve located behind each nozzle provided a pressure pulse at the nozzle that rose to a plateau in ~ 400 μs. The short-implosion-time nozzle (2.5-cm diameter shell) profile was based upon an ideal, steady state calculation, while the profiles of the larger, long-implosion nozzles were calculated using a viscous, transient gas-dynamic code (Reference 15). The solid-fill nozzle is actually annular, but its wide annulus and narrow center stub provide a gas density profile that is essentially filled in. The central stub was found to be necessary to protect the puff valve and to shorten the nozzle length to fit within space constraints. The solid-fill nozzle had a 90%-open mesh attached to its exit plane to define a current path back to the outer wall. All three gas puff loads had the same 3.8-cm pinch length, which was defined by an array of wires attached to 12-current return posts; the wire pattern consisted of 6 chord pairs wound between the six opposing pairs of return posts.

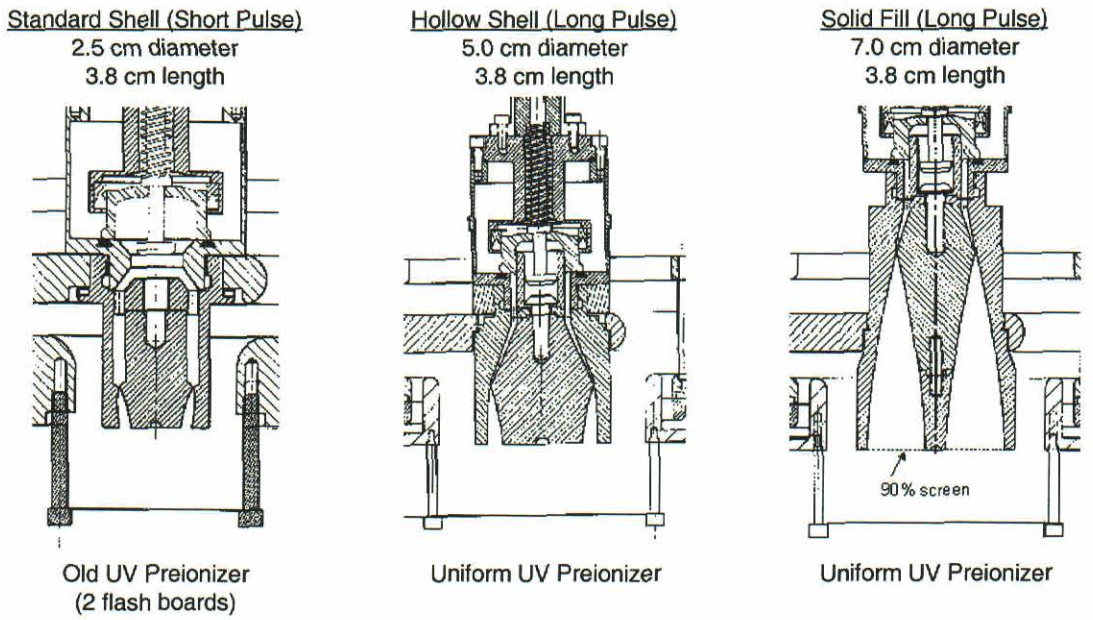

Figure 2-3. Hollow-shell and solid-fill gas puffs load configurations.

The initial gas density profiles produced by these nozzles evolve downstream from the nozzle exit. Because PRS z-pinches typically operate on the rising portion of the transient gas puff, the density will always be higher near the nozzle (cathode) than at the anode end. In addition, radial expansion causes a broadening of the radial profile as one moves downstream. Initial density measurements (Reference 16, 17) for plenum pressures and flow times similar to those used on Double-EAGLE are shown in Figure 2-4 for the 5-cm shell and the 7-cm solid fill. The shell profiles are indeed hollow near the nozzle, but become partially filled-in at the midpoint, and nearly solid-fill at the anode end; the mass/length decreases by 39% from cathode to anode (i.e., z=2 mm to z=4 cm). The solid-fill profiles show much less change from cathode to anode and the mass/length decreases by only 16% over the same distance. Section 9 describes the initial density measurements in more detail.

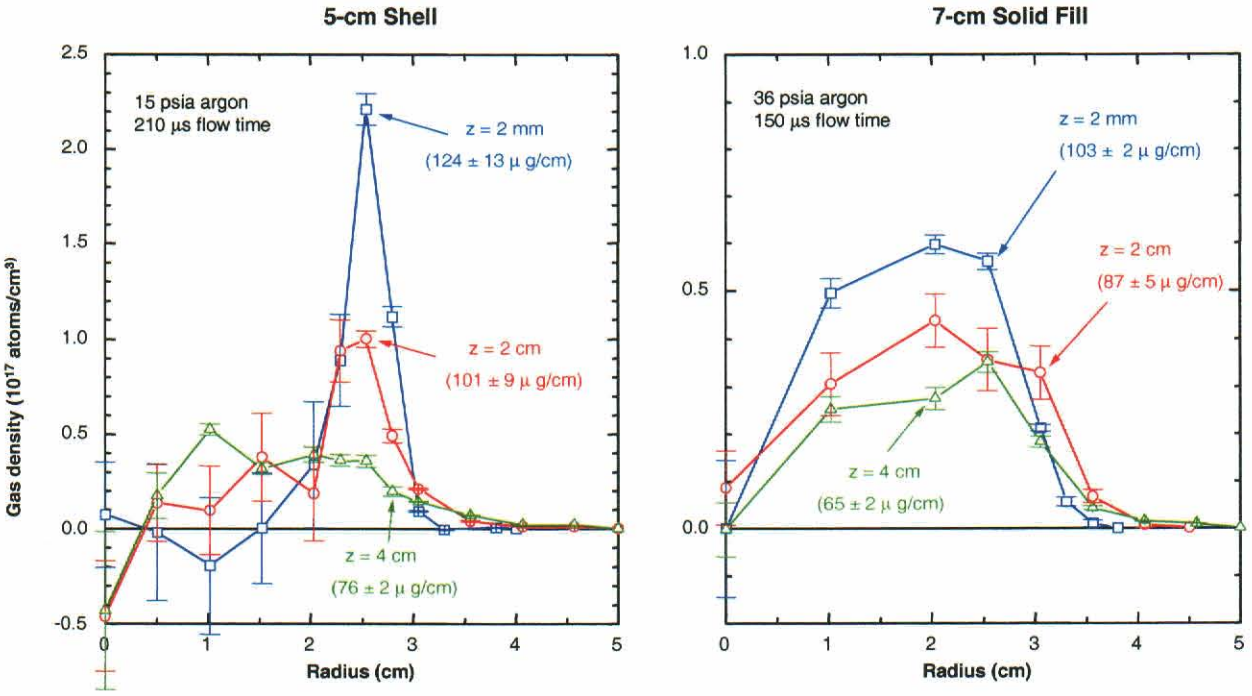

Figure 2-4. Initial density profiles for shell and solid-fill gas puffs.

Ultraviolet pre-ionization was used on virtually all of the Double-EAGLE experiments, because it was found to be beneficial in earlier experiments on DM2 (Section 2-3). The long-pulse experiments used a robust, circular flashboard that provided > 1% ionization at the periphery with excellent azimuthal uniformity (Section 10). The short pulse experiments used the standard Double-EAGLE pre-ionizer consisting of an opposing pair of flat flashboards with much less intensity and uniformity.

2.2.2 Optimization of Shell and Solid-Fill Loads.

The first set of long-implosion experiments on Double-EAGLE optimized the x-ray performance of the 7-cm solid-fill and 5-cm shell gas puffs. As part of this optimization process, we varied the implosion time to maximize the x-ray yield. For a given generator and nozzle, the implosion time is determined by the mass per unit length, which was varied primarily by adjusting the puff valve plenum pressure. In addition, we also varied the "flow time," defined as the elapsed time between the onset of gas flow from the nozzle and the onset of current in the load.

Because the mass/length and radial density profiles vary with distance from the nozzle, the pinch will occur at different times along the length of the pinch, leading to the so called "zipper effect" (Section 8.2). Figure 2-5a shows the axially-resolved x-ray emission from a pinch that starts near the anode end and then propagates to the cathode with a zipper time of 20 ns. The time-integrated intensity profile at the right of the figure shows poor axial uniformity, with the cathode end radiating more strongly than the anode end. By adjusting the flow time, we can tradeoff the axial decrease in mass with the radial expansion of the gas. Figure 2-5b shows a near-optimum

pinch with a zipper time of only 5 ns and much improved axial uniformity. At the largest flow times used, the zipper proceeded in the opposite direction, i.e., from cathode to anode.

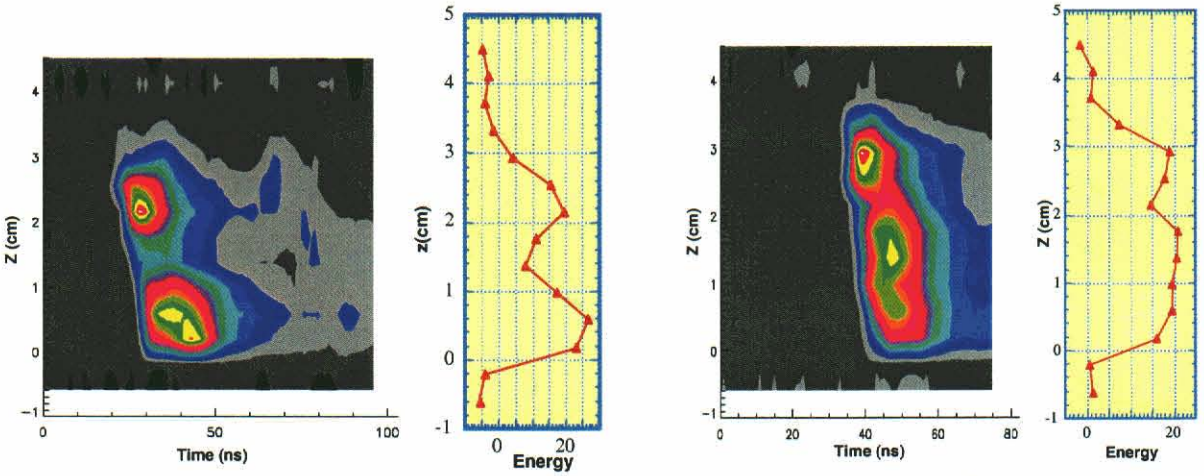

(a) strong zipper (b) minimal zipper

Figure 2-5. Axially-resolved x-ray emission from pinches.

At the standard 60-kV Marx charge voltage the Double-EAGLE generator delivered ~ 3.5 MA to both long-implosion loads, as shown in Figure 2-6. Implosion times were typically near 200 ns; here the implosion time is defined as the differences between the baseline intercepts of linear fits to the leading edge of the x-ray power and load current waveforms.

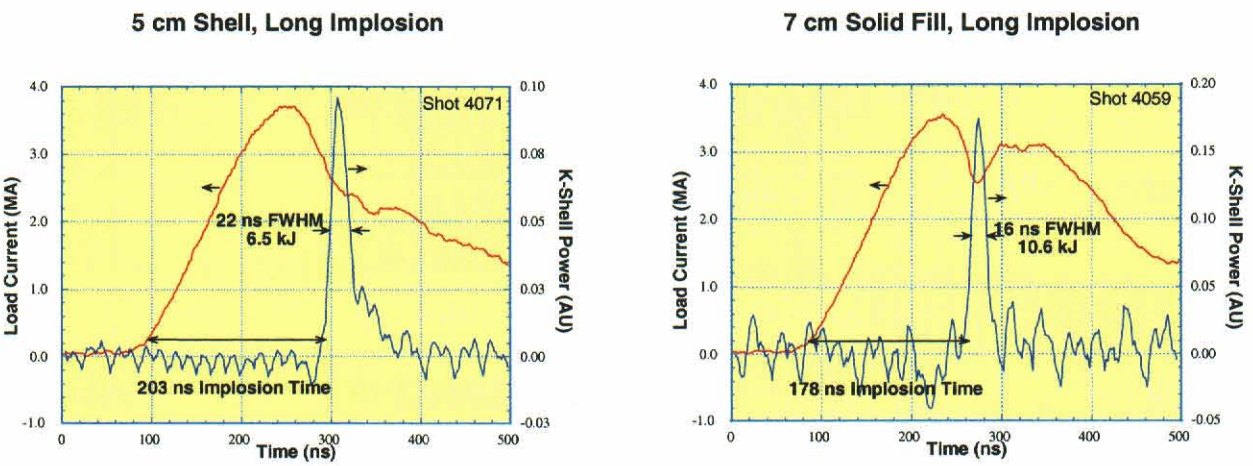

Figure 2-6. Current and x-ray power waveforms for shell and solid-fill PRSs.

The solid-fill gas puff produced argon K-shell x-ray yields that were ~ 50% higher than those of the shell gas puff. The primary yield diagnostic for all of our experiments consisted of a set of three tantalum foil calorimeters (7.3-μm thick) all filtered by 17-μm Kapton, 4-μm Kimfol, and 1.8-μm aluminum; a filter transmission of 55% was calculated from a typical measured spectrum. Figure 2-7 shows the measured x-ray yields plotted against peak load current and implosion time,

respectively. A maximum x-ray yield of 10.6 kJ was obtained with the solid-fill PRS, compared to 6.8 kJ with the shell. These yields were maximized for peak currents of 3.50 MA and 3.65 MA, respectively, for the solid-fill and shell. The optimum implosion time of 178 ns for the solid-fill PRS was somewhat less than the 198 ns that optimized the x-ray yield for the shell.

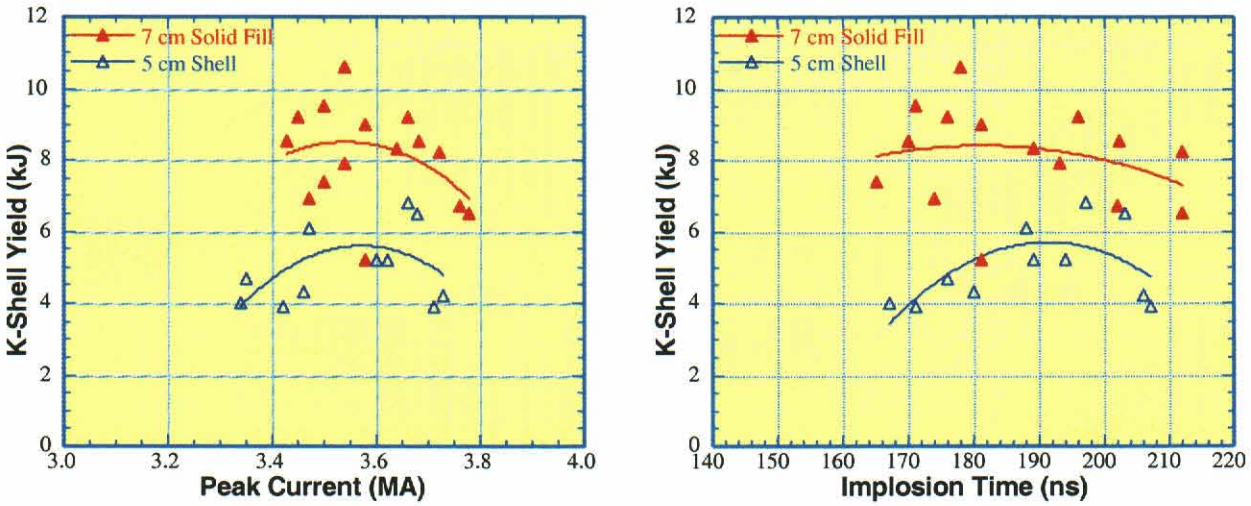

Figure 2-7. K-shell x-ray yield as a function of peak current and implosion time.

The solid-fill PRS produced an x-ray pulse that was typically 30% narrower than that of the shell load. The primary x-ray pulse shape diagnostic consisted of a set of three x-ray diodes (XRDs); each XRD had an aluminum photocathode and a filter stack designed to give a flat response over the K-shell spectrum. The highest-yield solid-fill shot had a pulsewidth of 16 ns FWHM, while most shots had a pulsewidth ranging from 10 to 20 ns. For near-optimum shots, the zipper effect accounts for one-third of the pulsewidth, while the remaining two-thirds (about 10 ns) is the intrinsic width that could be achieved if zippering were completely eliminated. For the shell load, the pulsewidth was 22 ns for the highest yield shot, with most pulsewidths falling in the 15 to 25 ns range. The combination of higher x-ray yield and narrower x-ray pulse for the solid-fill PRS produced an x-ray power that was typically ~ 100% higher than that of the shell.

Time integrated x-ray images (Figure 2-8) show significant differences between solid-fill and shell PRSs. The optimum solid-fill PRS gave fairly uniform x-ray emission from nearly the entire length of the pinch. The optimized shell PRS, however, gave stronger emission near the anode (where the shell is filled in) and only weak emission near the cathode or nozzle (where the shell is hollow). This may be a result of instability in the hollow shell. The absorption features at the anode end (and also in the center) of the images are artifacts of the anode wires, which partially obscure the diagnostic lines of sight tilted at 66 degrees to the pinch axis. Each image is color-scaled for intensity independently; comparisons should not be made between images based on color.

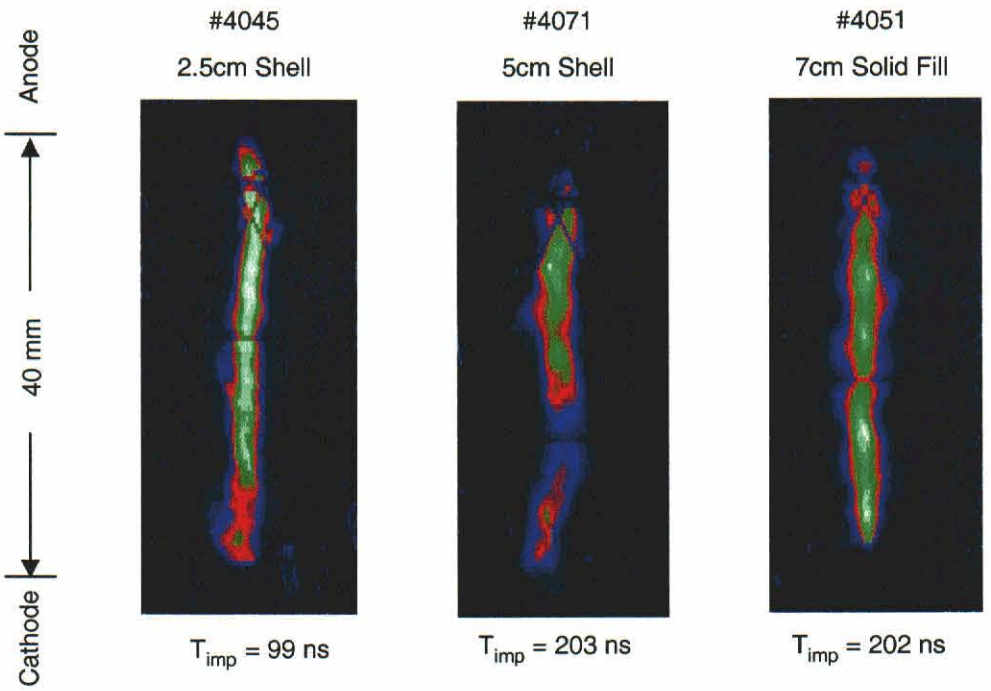

Figure 2-8. Time-integrated K-shell x-ray images of short- and long-implosion PRSs.

Thus, the solid-fill PRS is clearly superior to the 5-cm shell PRS because it produces 50% higher x-ray yield and 100% higher x-ray power. In the solid fill PRS, the initial conditions vary gradually enough from cathode to anode that one can optimize emission along the entire pinch length by simultaneously adjusting plenum pressure and flow time. The shell PRS, on the other hand, is difficult to optimize along its entire length because the initial conditions change markedly from cathode to anode.

2.2.3 Comparison of Short- and Long Implosion PRS.

It is instructive to compare the x-ray performance and plasma conditions of the optimized 7-cm solid-fill PRS for long implosions to those of the 2.5-cm shell load, which is used as the standard short-implosion argon PRS on Double-EAGLE (Reference 2). The latter PRS was operated near its nominal optimum for a series of 10 shots immediately prior to the long-implosion tests, providing a well-characterized database for comparison with the long-implosion PRS. The generator and source were quite stable, with only 3% and 7% standard deviations for the peak current and x-ray yield, respectively. Figure 2-9 presents typical load current and x-ray power waveforms for the short- and long-implosion PRS. Note that the load currents have similar peaks and shapes, with the exception of a factor of ~ 2 in risetime. Both x-ray power waveforms show a single, clean pulse, but the pulsewidth is a factor of ~ 2 larger for the long-implosion PRS.

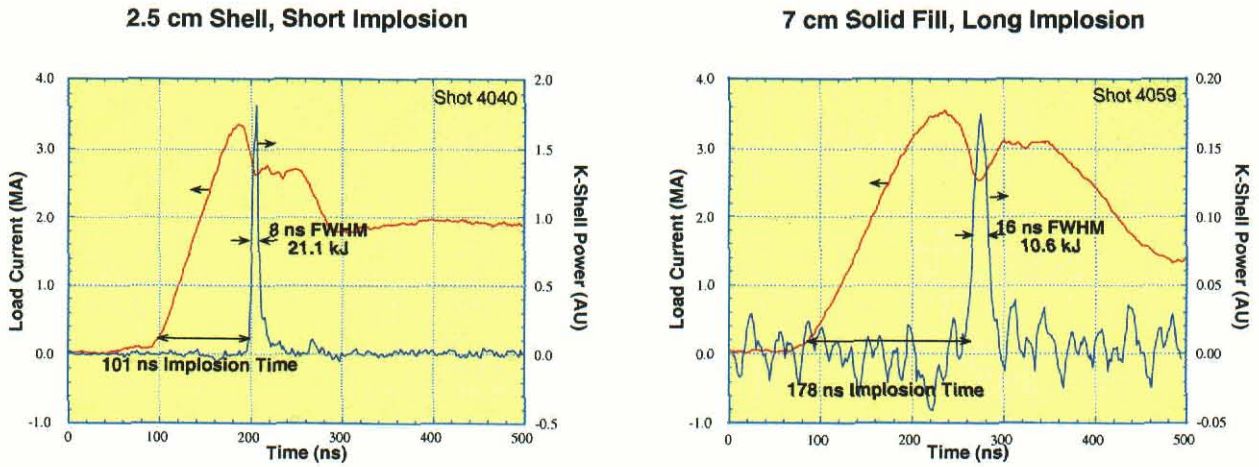

Figure 2-9. Current and x-ray power waveforms for short- and long-implosion PRSs.

Table 2-2 presents a comparison of key performance parameters for the short- and long-implosion PRS. Mean and standard deviation values are presented for the short-implosions, but only single shot optimum data are available for the long implosion PRS. There are a number of key differences, many of which appear related to the factor of ~ 2 difference in implosion time. First of all, the long-implosion PRS yield of 10.6 kJ is a factor of ~ 2 lower than the 21.2-kJ yield obtained with the short-implosion PRS. Secondly, the x-ray pulsewidth of 16 ns for the long-implosion PRS is a factor of ~ 2 wider than the 7-ns FWHM obtained in the short-implosion PRS. Finally, these factors combine to produce a factor of ~ 4 decrease in x-ray power from the short-implosion PRS (3.2 TW) to the long implosion PRS (0.84 TW). (Note however that a wide radiation pulse is not intrinsic to long implosion time as demonstrated in experiments on ACE 4.)

Table 2-2. Comparison of PRS performance with short- and long-implosion PRSs.

Generator Mode	60 kV, 100 ns	60 kV, 200 ns
Gas puff	2.5-cm shell	7-cm solid-fill
Implosion time (ns)	100 ± 3	178
Peak current (MA)	3.39 ± 0.11	3.54
K-shell x-ray yield (kJ)	21.2 ± 1.5	10.6
X-ray pulsewidth (ns FWHM)	7 ± 1	16
X-ray power (TW)	3.25 ± 0.55	0.84
Total radiated yield (kJ)	140 ± 11	127

Additional x-ray measurements were performed to diagnose the plasma conditions that underlie the PRS x-ray performance. K-shell x-ray images, for example, provide critical information on the size of the x-ray radiating core, which in turn provides the brightness data required to

determine plasma temperature and density. From the time-integrated images of Figure 2-8, we have determined the radiating diameter (best-fit gaussian FWHM) as a function of position along the pinch axis. The results displayed in Figure 2-10 show that the long-implosion PRS is consistently wider than the short-implosion PRS; the only exception is the region near the cathode (nozzle), where the hollow shell pinches poorly. Taking an intensity-weighted axial average of the data in Figure 2-10, we find that the 2.1-mm average radiating diameter of the long-implosion PRS is about 30% larger than the 1.6-mm average diameter for the short-implosion PRS.

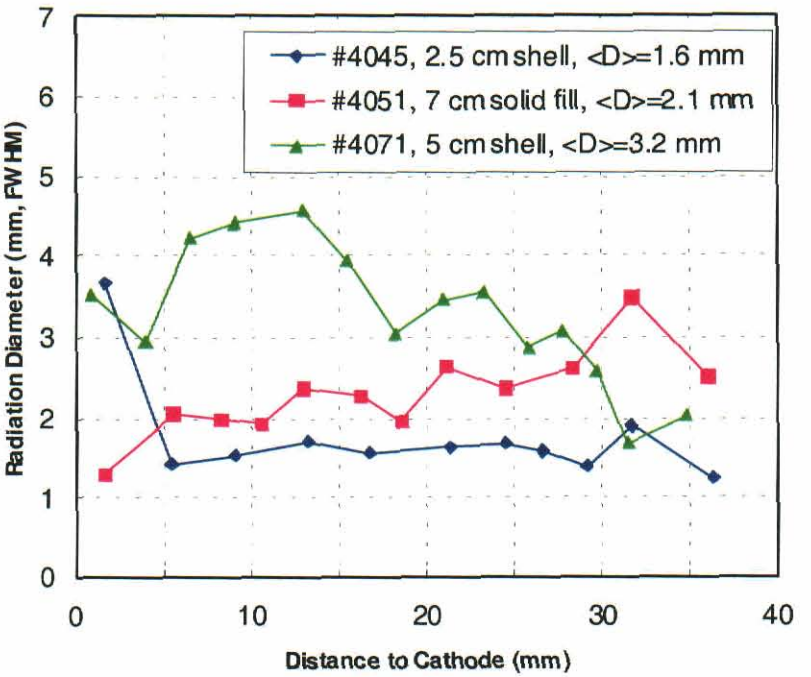

Figure 2-10. K-shell radiating diameters for long- and short-implosion PRSs.

K-shell spectra were measured using time-integrated and time-resolved spectrometers that are described in detail in Section 7. Figure 2-11 compares the time- and spatially-integrated spectra for the short- and long-implosion PRS. The He-α resonance and inter-combination (IC) lines near 3.1 keV dominate both spectra, but the Ly-α line has a higher relative intensity for the short-implosion PRS. Faint chlorine K-lines from a 2% CCl_2F_2 dopant can also be seen near 2.8 keV. Figure 2-12 shows axially-resolved data for the argon He line emission (α + IC) and the ratio of the Ly-α to helium lines. These data confirm that the long-implosion, solid-fill PRS radiates uniformly over most of the nominal pinch length. The short-implosion, shell PRS radiates more intensely near the anode (where it is filled in) and weakly near the cathode (where it is hollow).

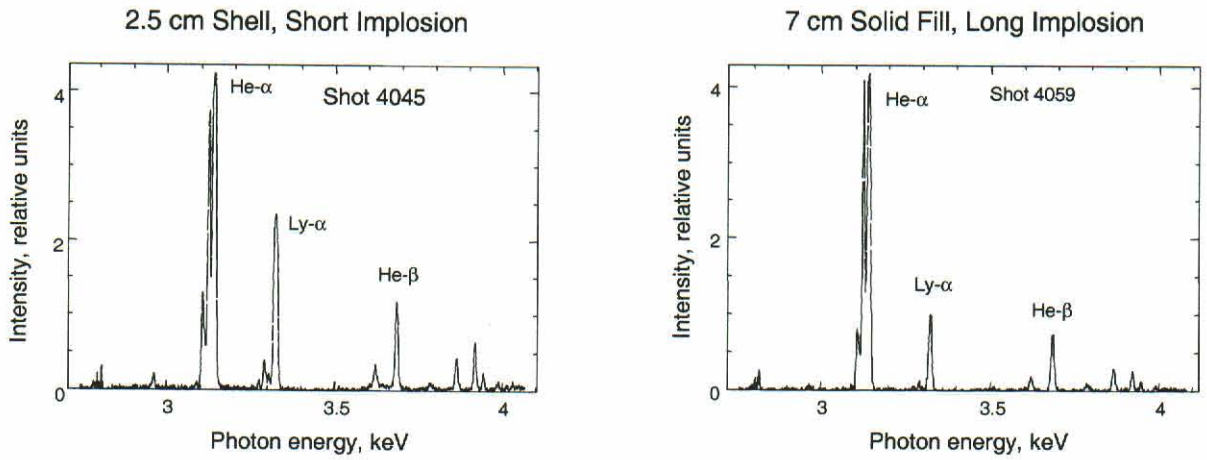

Figure 2-11. Time-integrated argon K-shell spectra for short- and long-implosion PRSs.

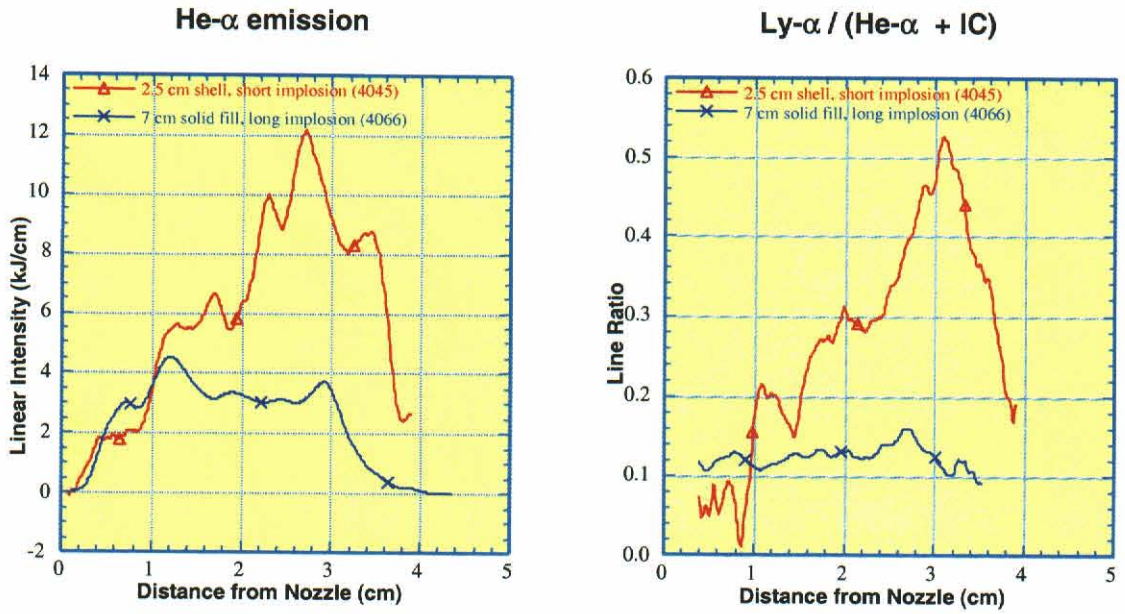

Figure 2-12. Spatially resolved spectrograph confirms better axial uniformity with solid-fill gas puff.

Plasma density and temperature in the K-shell radiating core were determined from time-integrated, axially-resolved K-shell spectra of both argon and chlorine. In the case of argon, the temperature was determined primarily from the Ly-α/(He-α+IC) line ratio, while the density was determined primarily from the K-shell brightness (Reference 18). For the chlorine case, the electron temperature was determined from the He-α/jkl satellite line ratio, the ion temperature was determined from the IC line width, and the density was determined from the He-α/IC ratio (Section 7). In all cases, we obtained axially-resolved profiles of temperature and density, which were then averaged to give the results displayed in Table 2-3.

Table 2-3. Comparison of plasma conditions for short- and long-implosion PRSs.

Generator Mode Gas Puff	60 kV, 100 ns 2.5-cm Shell	60 kV, 200 ns 7-cm Fill
Ar electron density, $10^{20}cm^{-3}$	5.1	2.1
Cl electron density, $10^{20}cm^{-3}$	13	5.1
Ar electron temperature, keV	1.9	1.45
Cl electron temperature, keV	1.2	1.1
Cl ion temperature, keV	16	22
K-shell radiating diameter, mm FWHM	1.6	2.1
K-shell radiating mass, μg/cm	43	30

The core temperature measurements generally show little difference between long and short implosions. This result validates our load design approach of scaling initial radius with implosion time to maintain temperature and η^*. Nevertheless, the electron temperature estimates from argon are consistently higher than from chlorine. Because the argon He-α line is optically thick, we believe that absorption in the cooler halo (which is neglected in the model) causes an overestimate of core electron temperature using argon data; this effect will be more pronounced for the higher-density, short-implosion PRS.

The core density measurements show a ~ 60% decrease in electron density between short- and long-implosion PRS, and a ~ 30% decrease in radiating mass. The chlorine data give consistently higher density than argon and also a greater difference between long- and short-implosions. We believe that opacity in the argon halo outside the core gives an underestimate of density, while the chlorine density diagnostic has low sensitivity and high error. Nevertheless, the true density in the long-implosion PRS appears to be lower by a factor > 2 than that of the short-implosion PRS. This result confirms our expectations that larger initial diameters require higher compression ratios to maintain the desired final densities in longer-implosion PRS.

2.2.4 Higher-current Scaling Experiments.

Additional experiments were performed with the 7-cm solid-fill PRS to determine the scaling of the K-shell yield with current. To achieve higher current on Double-EAGLE, the Marx charge voltage was increased from 60 to 65 kV, resulting in peak currents of ≈ 4 MA. The plenum pressure and flow time were then varied over a limited number of shots to optimize the x-ray yield as discussed in Section 2.2.2. A maximum yield of 15.3 kJ with 16-ns FWHM was obtained at a peak current of 4.0 MA and an implosion time of 188 ns. The time-integrated K-shell image shows good axial uniformity and an average radiating diameter of 2.7 mm. Plasma

density and temperature and other key PRS parameters are summarized in Table 2-4 for comparison with the short- and long-implosion PRS at ~ 3.5-MA peak current.

Table 2-4. Comparison of typical PRS parameters.

Generator Mode Gas Puff	60 kV, 100 ns 2.5-cm Shell	60 kV, 200 ns 7-cm Fill	65 kV, 200 ns 7-cm Fill
Implosion time, ns	100	180	190
Peak current, MA	3.4	3.5	4.0
Total radiated yield, kJ	140	115	182
K-shell yield, kJ	21.5	10.6	15.3
K-shell pulsewidth, ns FWHM	7	16	16
Ar electron density, 10^{20} cm^{-3}	5.1	2.1	1.8
Cl electron density, $10^{20}cm^{-3}$	13	5.1	8.4
Ar electron temperature, keV	1.9	1.45	1.35
Cl electron temperature, keV	1.2	1.1	1.0
Cl ion temperature, keV	16	22	20
K-shell radiating length, mm FWHM	16	24	20
K-shell radiating diameter, mm FWHM	1.6	2.1	2.7
K-shell radiating mass, μg/cm	43	30	43

To determine the scaling of the long-implosion x-ray yield with current, we have performed least-squares power-law fits to all data obtained using the 7-cm solid fill PRS. The data shown in Figure 2-13 includes the nominal and high-current results from Double-EAGLE, as well as earlier, low-current results from DM2 (see Section 2.3). Each data set is fit with a separate parabola, and then a power-law is fit to the peaks of the three parabolas; the best power-law fit gave an $I^{4.0}$ scaling. (It is actually remarkable that the DM2 data fit on this curve since DM2 used a 300 ns implosion time! Per the discussion in Section 1, I^4 scaling holds only if implosion velocity, roughly radius over implosion time, is held fixed. This same "over-performance" at low current but long implosion time appears in the GIT-12 data shown in Section 5.) Figure 2-13 also shows an I^2 fit through the 60-kV Double-EAGLE data; it misses the high- and low-current data by a wide mark. Thus, the K-shell yields at present current levels show the same I^4 scaling that has been observed in previous short-implosion argon PRS tests (Reference 2) up to currents of 4-MA. See Section 5 for more discussion of this topic.

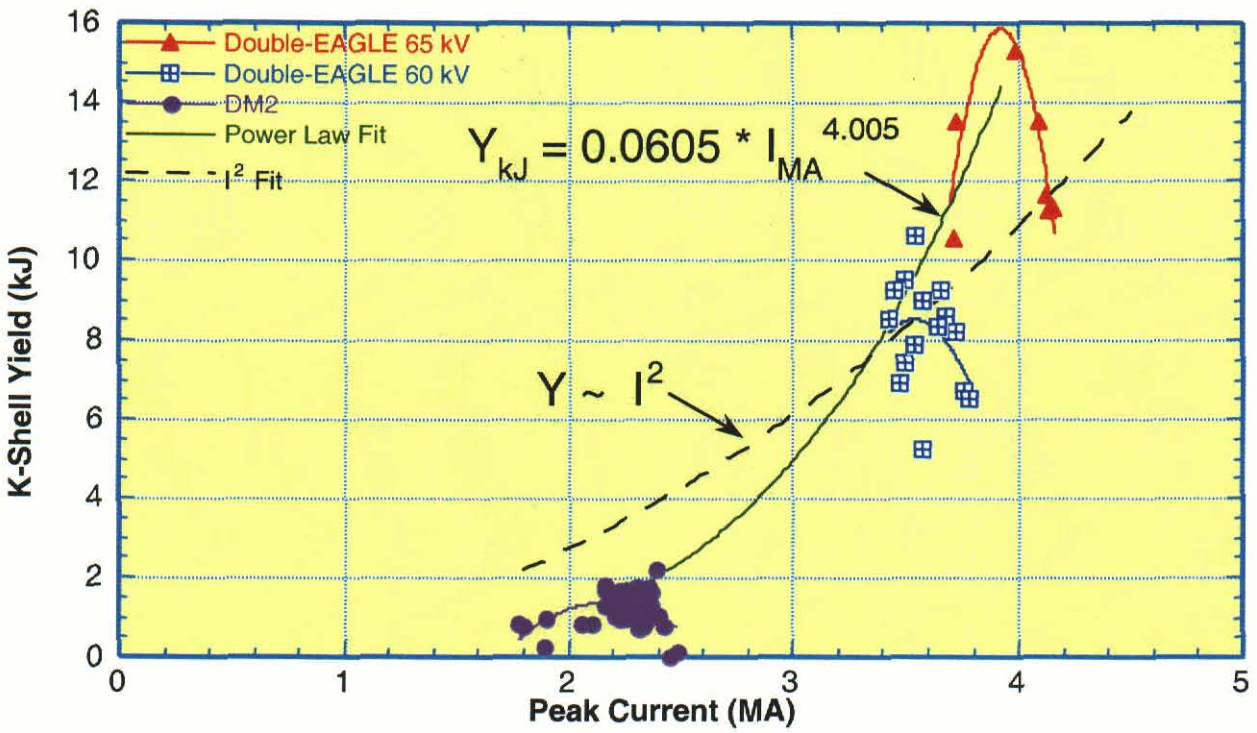

Figure 2-13. I^4 Scaling of Ar yields on Double-EAGLE and DM2.

Energy conservation arguments require that the I^4 yield scaling decrease to no faster than I^2 at arbitrarily high currents. Previous experiments and theory suggest that the transition between I^4 and I^2 scaling occurs near a "breakpoint" K-shell efficiency of ~ 30% (References 4, 5). Taking the total radiated yield (Table 2-4) as a measure of the total energy coupled to the pinch, we find that the short- and long-implosion PRS at 3.5-MA peak current have K-shell efficiencies of 15% and 8%, respectively. If a 30% breakpoint efficiency is not intrinsically a function of implosion time, then we calculate that the breakpoint currents will be ~ 4.9 MA and ~ 6.8 MA, respectively, for the short- and long-implosion PRS. Under this assumption, the yields for long- and short-implosion PRS would approach each other for currents above 7 MA, where the efficiency approaches 30% regardless of implosion time. We note that the limited amount of data for argon implosions at > 6 MA on SATURN imply breakpoint currents well below our estimates given above. Section 5 gives an empirical summary of all of these data (including long pulse aluminum data). Section 6 presents a more detailed discussion of scaling issues using a zero-dimensional model.

2.2.5 10-cm Solid Fill Experiments on Double-EAGLE.

To take full advantage of the maximum current that will be available on DQ, the PRS load will need to have an implosion time close to 300 ns. To maintain the implosion velocity, this will require an even larger load: 10-cm diameter or more. We performed a limited number of tests with a 10-cm nozzle to see if there were any serious stability issues for implosions with so large a gas flow. Our initial 10-cm tests were performed on DM2 at only 1 MA; see Section 2.3.

To test the 10-cm nozzle at higher current, Double-EAGLE was operated in the 200 ns mode and, for a few shots the pulse was further extended to 250 ns. With a peak current of over 4 MA and an implosion time of 247 ns, 7.3 kJ of K-shell radiation were produced with a 20 ns FWHM radiation pulse. Note that the current drive for this configuration of Double-EAGLE, Figure 2-14, is not at all like the expected linear ramp for DQ.

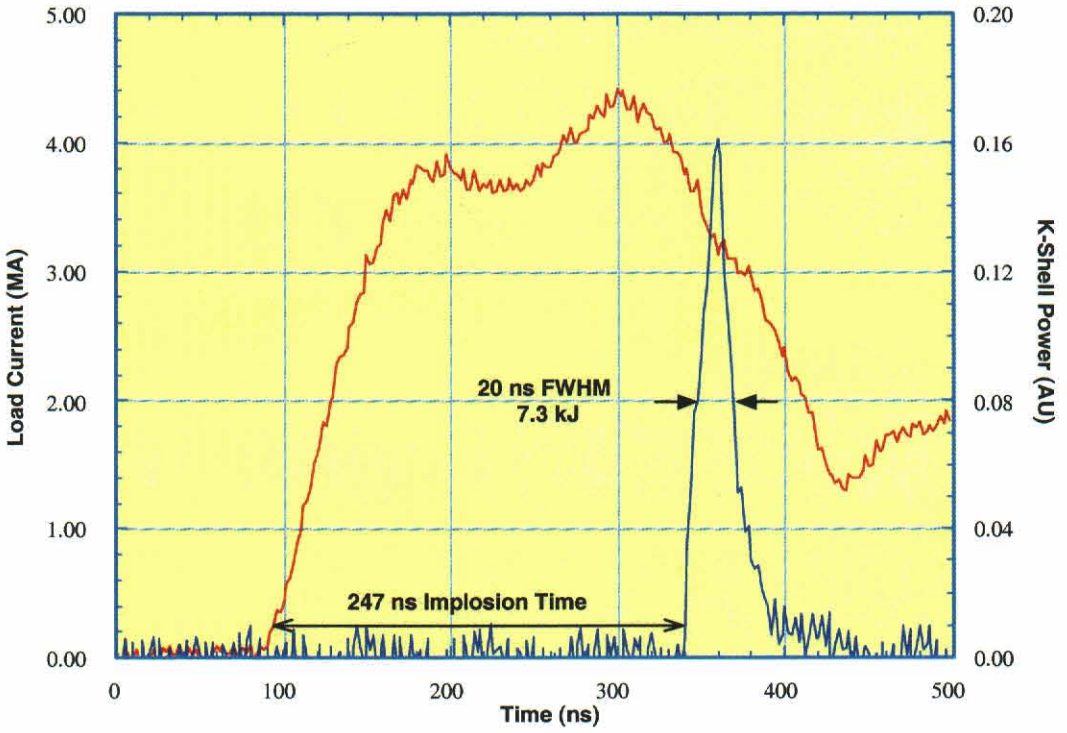

Figure 2-14. Current and K-shell power for 10-cm solid fill (#4459) on Double-EAGLE.

There were some initial azimuthal asymmetries that were suppressed as the shot progressed so that the pinch was circular at implosion. Compare the optical framing images, Figure 2-15, viewing the pinch axially, with the comparable view of the 7-cm load, Figure 2-16. The initial images for the 10-cm load are slightly elliptical. Because the magnetic field lines resist "bending", such azimuthal asymmetries are not expected to grow and become unstable.

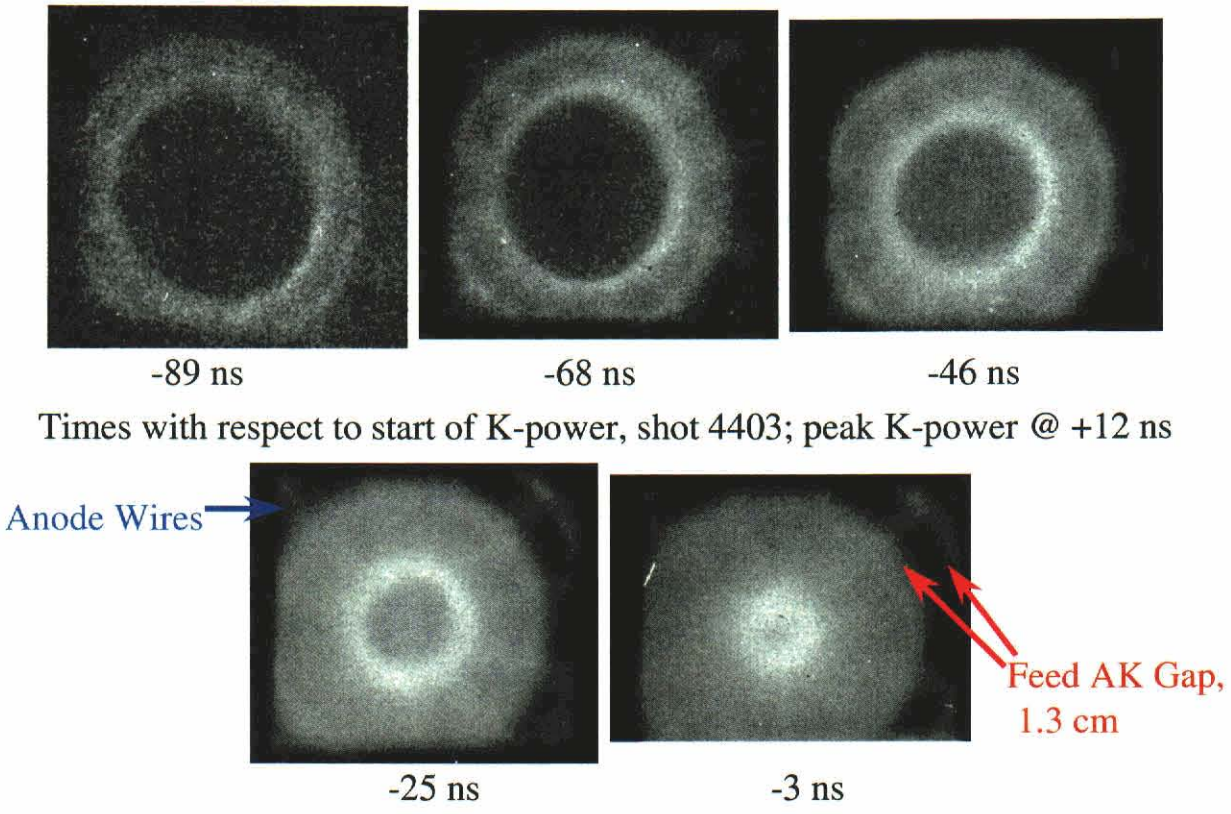

Figure 2-15. Optical framing images for the 10-cm solid-fill on Double-EAGLE.

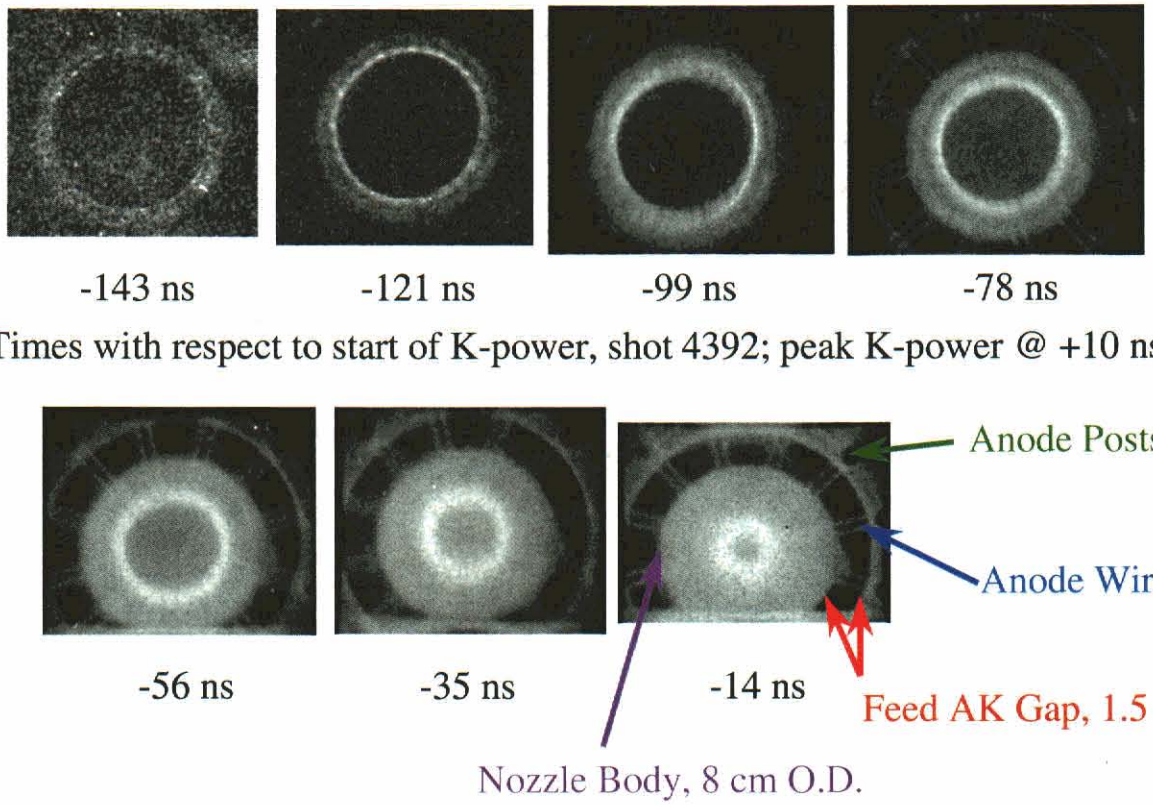

Figure 2-16. Optical framing images for the 7-cm solid-fill on Double-EAGLE.

2.3 LONG IMPLOSION ARGON PRS EXPERIMENTS ON DM2.

There were two PRS test campaigns on DM2 in this program. The first explored 4-cm long Argon pinches produced by three different nozzles: a 5-cm diameter thin shell, a 5-cm diameter thick shell and a 7-cm diameter solid fill. The second campaign incorporated several modifications into the hardware and focused on solid-fill argon puffs, mostly revisiting the 7-cm diameter nozzle with a few shots testing a 10-cm diameter nozzle. To examine higher η operation, a few shots were taken with Ne at the end of the run.

2.3.1 DM2 First Test Campaign.

All three nozzles, shown below in Figure 2-17, produced similar argon K-shell yields, peaking at > 1 kJ with an approximate 300 ns implosion time at a peak current of 2.3 MA. Compared to the shells, the solid-fill nozzle gave slightly higher yield but much higher power, due to its narrower pulse width. The solid fill nozzle also appeared to produce more stable and symmetric implosions than the shell nozzles.

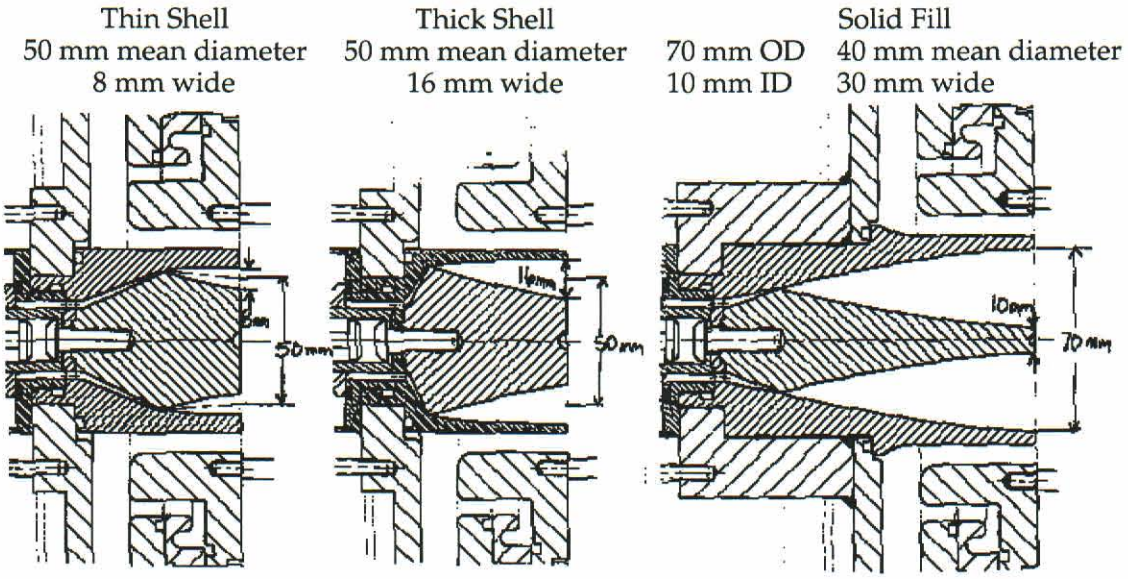

Figure 2-17. Three nozzles used for DM2 argon implosions.

To investigate pinches with varying implosion times, the plenum pressure was varied. The results, shown in Figure 2-18, demonstrate reasonable control of the implosion. (The lines in the figure are simple linear fits, drawn as a visual aid. The expectation that implosion time should vary as load mass to the 0.25 power would apply if DM2 was electrically "stiff." However, the impedance of DM2 is not high compared to the load impedance.) The 5-cm thin shell nozzle has significant scatter; the other nozzles behave more predictably. As seen in Figure 2-19, the load current was independent of the nozzle type and depended only weakly on the implosion time, reaching 2.3 MA for implosion times of 300 ns and longer.

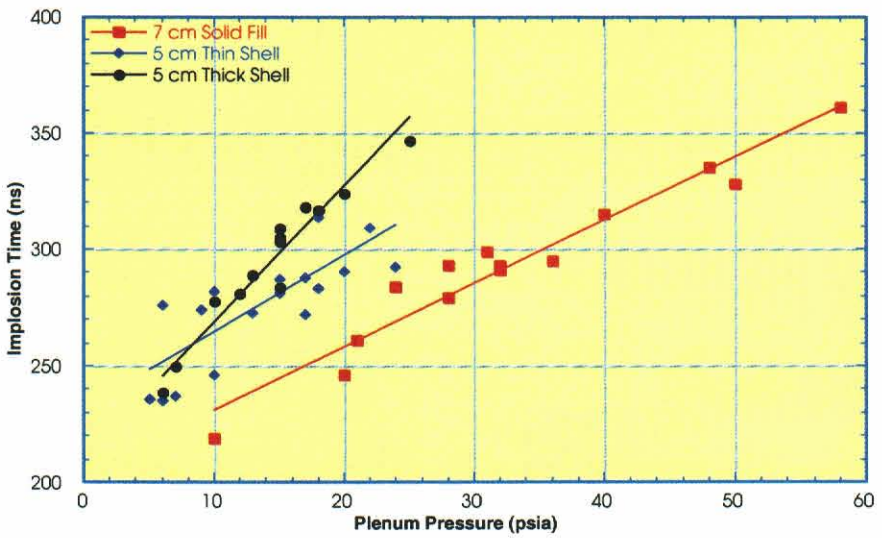

Figure 2-18. Implosion time on DM2 as a function of plenum pressure for the three nozzles.

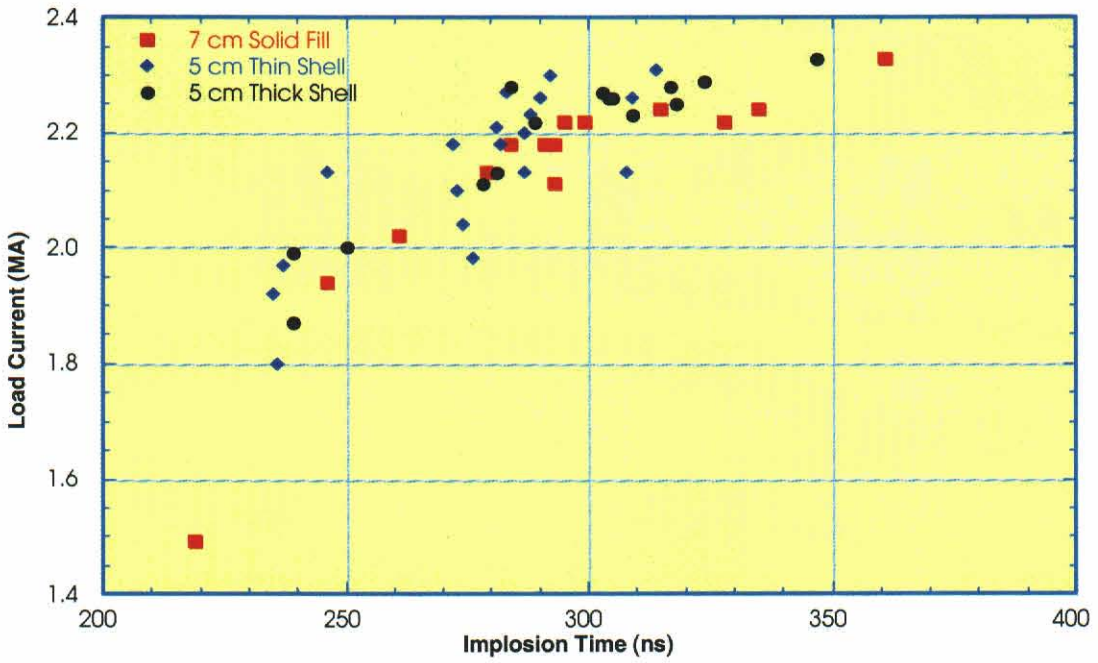

Figure 2-19. Load current on DM2 as a function of implosion time for the three nozzles.

The K-shell yields, averaging 1.3 kJ for the best shots, are also similar for the three nozzles, with the 5-cm thin shell nozzle showing the greatest variability.

2.3.2 Second DM2 Campaign.

To improve the power flow from the radial feed to the coaxial feed section of the nozzle, we opened both radial and coaxial gaps from 15 to 20 mm and from 10 to 15 mm, respectively. The pre-ionization scheme was upgraded by replacing the two flashboards with a complete loop (see Section 10 for a complete description). We also strung wires across the uniform fill nozzle's exit to provide an equipotential and a low inductance current path for the electrons when the pinch detached from the outer edge of the nozzle.

The 7-cm nozzle, wire anode, and pre-ionizer ring are shown in Figure 2-20. The nozzle wires, a set of 12 single-wire radial spokes, aligned with the anode wires, are not present in this picture.

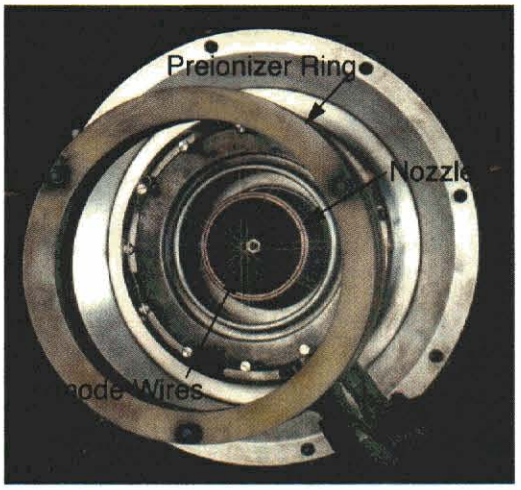

Figure 2-20. The 7-cm nozzle, wire anode, and pre-ionization ring.

We also modified the puff valve to include a breakdown pin to decrease the timing jitter of firing the DM2 Marx with respect to the gas flow from the nozzle. The breakdown pin is a metal pin, biased to 1500 V, and situated in the outlet of the puff valve. When the valve opens and gas begins to flow, the pin breaks down to the surrounding wall. This generates a pulse that is used to trigger the firing of the DM2 Marx. The mechanical jitter of the valve (35 μs under these test conditions) was reduced to only 6 μs by using the breakdown pin. Had the timing been based strictly on the firing of the puff valve, the 35 μs jitter would have translated to an approximately $\pm$ 12% variation in the gas fill in the pinch at the time of DM2 firing. With these changes, the 7-cm diameter uniform fill's yield slightly increased to 1.7 kJ but we still saw $\pm$ 10% variations in implosion time at fixed plenum pressure.

Several new diagnostics were added for this test series: a PCD/bolometer array, an XUV time-gated pinhole camera (sensitive to photons at ~ 200 eV), a visible light framing camera with a 480 nm filter (Ar II line), a high-resolution, radially resolved spectrograph, a second load current Rogowski coil to detect current loss at the radial-to-coaxial transition (Figure 2-21), and B-dot monitors on both of the pre-ionizer capacitor banks.

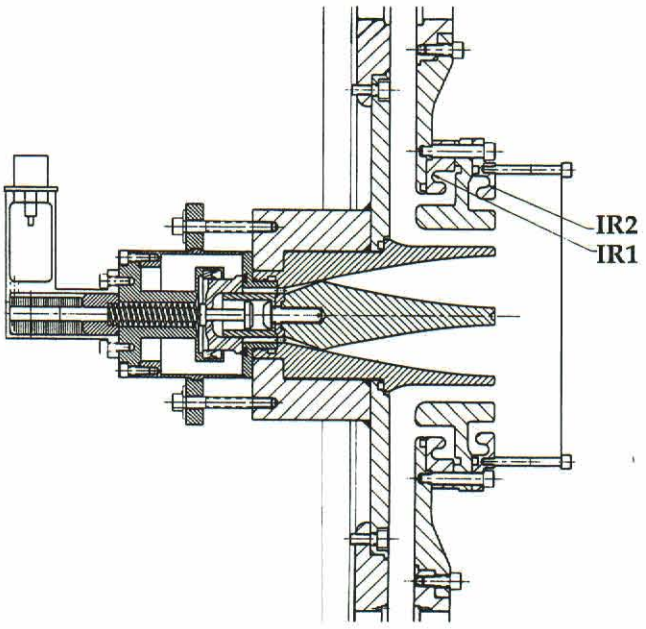

Figure 2-21. A second load current Rogowski coil was added in the 2nd DM2 campaign.

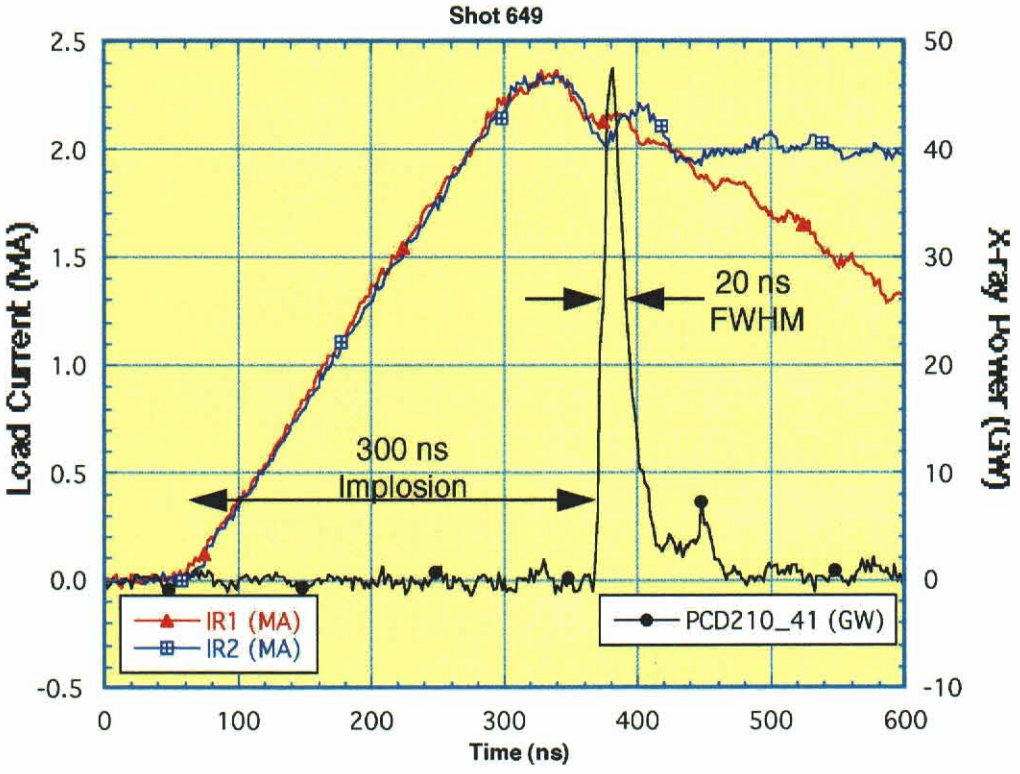

Figure 2-22. Current and x-ray signal for a 300 ns implosion on DM2.

Figure 2-22 shows an example of the DM2 current waveform and the K-shell power. Figure 2-23 presents the K-shell x-ray yields from a series of similar shots, with varying mass loads, with and without nozzle wires and with and without pre-ionization. Recognizing the spread in the results, but looking at the envelope of the data points, we see that neither the nozzle wires nor pre-ionization is absolutely necessary for obtaining peak performance, but that each of them is useful, in a statistical sense, for making a good shot more probable.

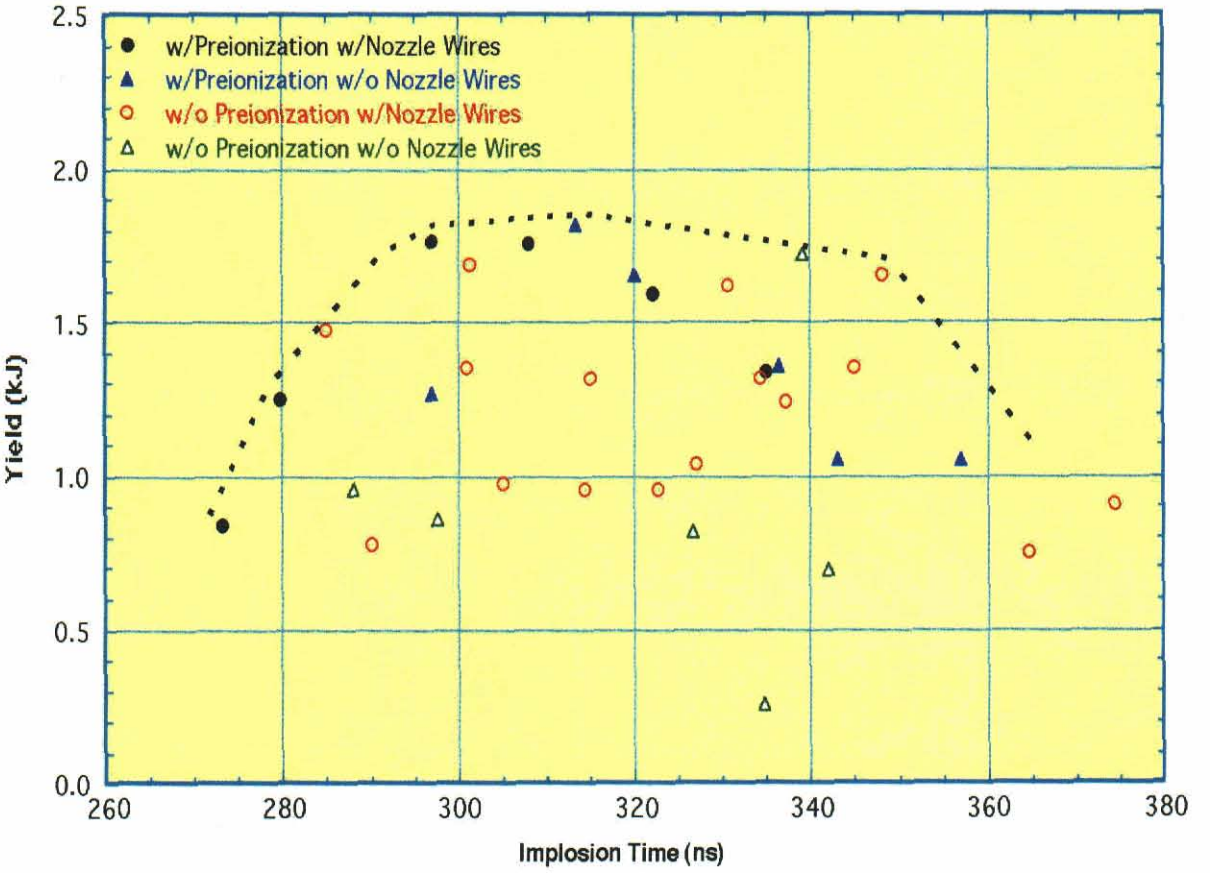

Figure 2-23. Argon K-shell yield vs. implosion time for a series of DM2 experiments; the dashed curve indicates the envelope of best results.

The zipper array (see Section 8.2), a set of 14 pin diodes that each view a small axial slice of the pinch, coupled with the PCDs, provide a good picture of the pinch. As an example, in Figure 2-24 we see that there are two spots that radiate strongly. They turn on nearly simultaneously, i.e., there is little zippering. The FWHM of the total radiation, as seen by the PCD, is representative of the temporal evolution at each point. The shot shown in Figure 2-25, on the other hand, shows one very intense, short lived spot in the middle of the pinch, with subsequent zippering toward the cathode. The temporal behavior of the spot is distinctly different than the region near the cathode and the region near the anode does not emit at all.

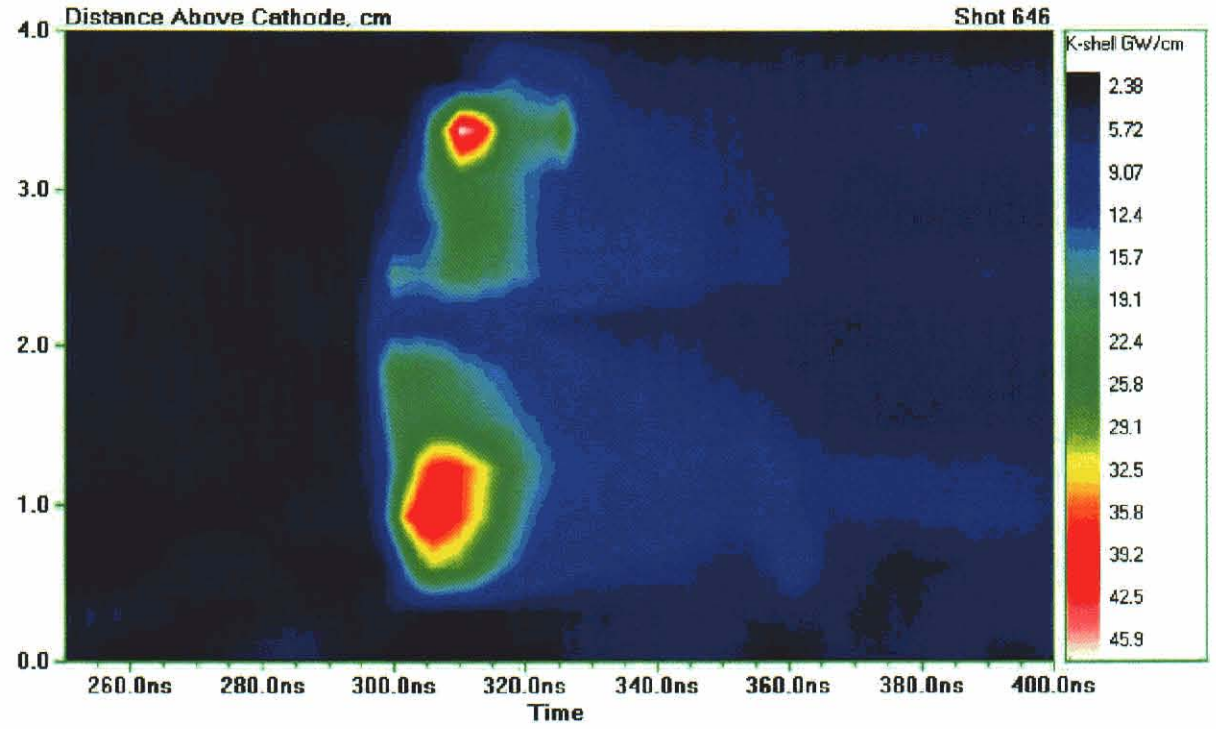

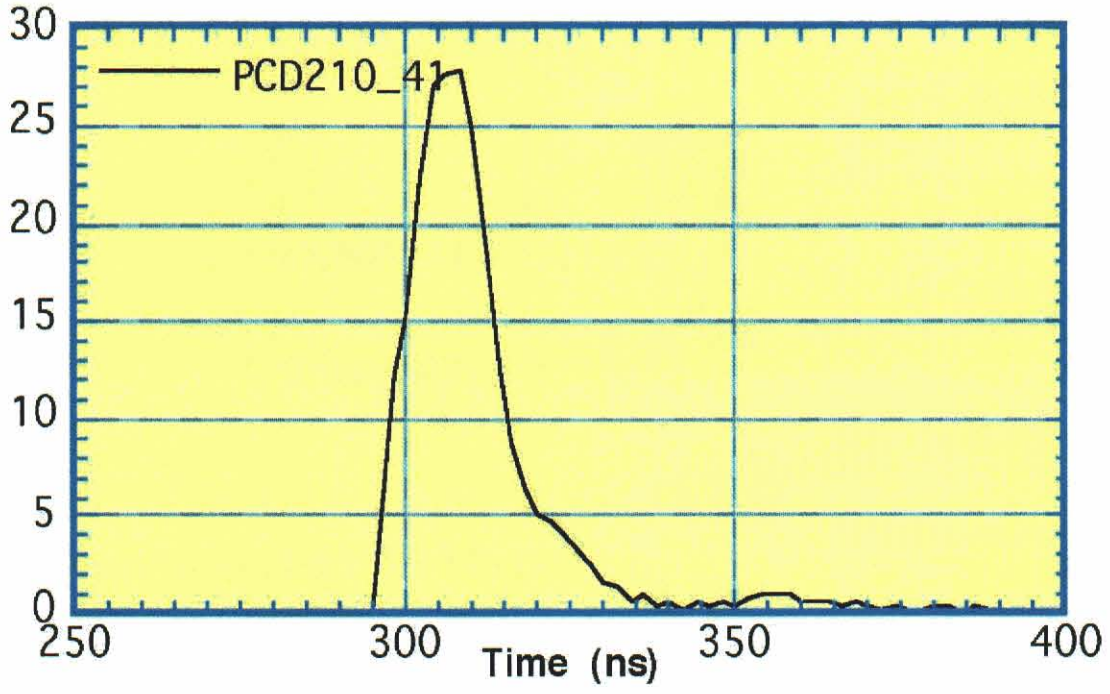

Figure 2-24. Zipper array contour plot and PCD signal for a shot with minimal zippering.

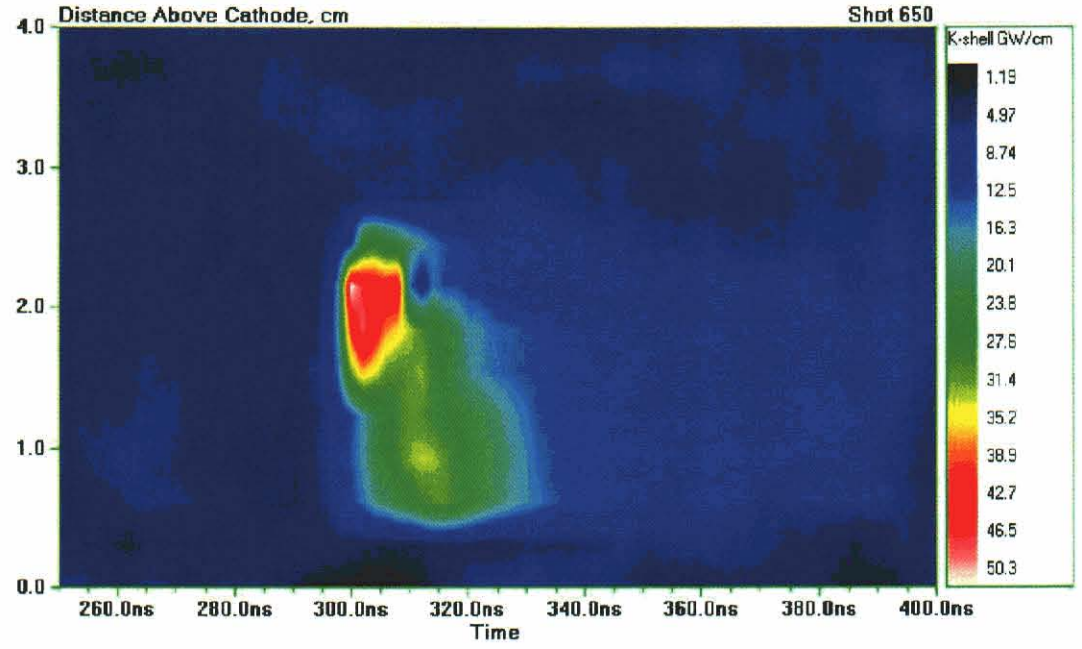

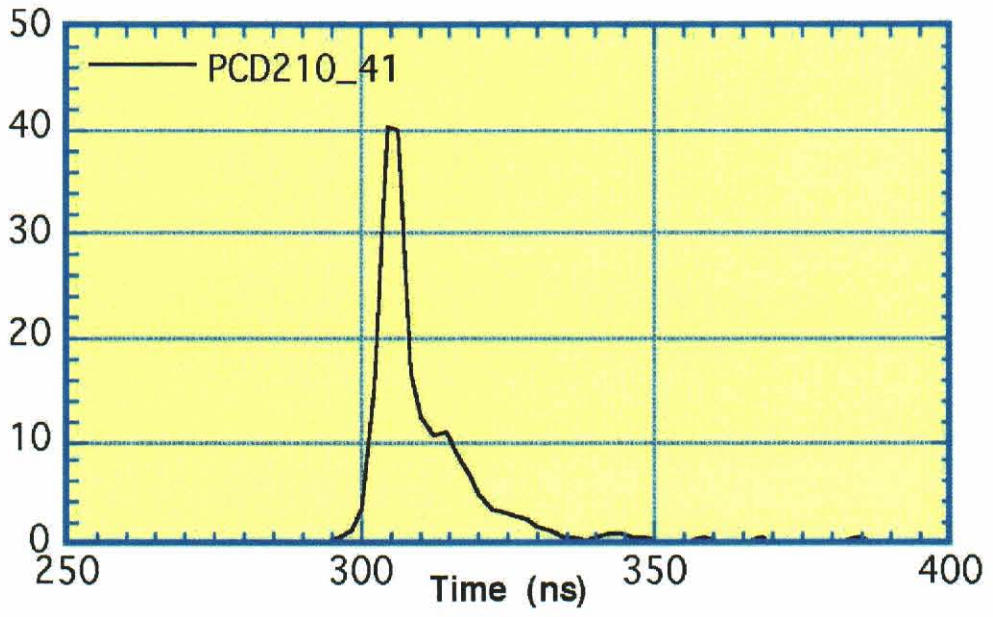

Figure 2-25. Zipper array contour plot and PCD signal for a shot with a single hot spot which then zippers toward the cathode.

As discussed above, the anticipated limitation to achieving a good pinch was the Rayleigh-Taylor instability. To determine the uniformity of the final pinch, we used a time-resolved pinhole camera sensitive to x-ray energy > 3 keV. A series of four images, each separated by 10 ns, is shown in Figure 2-26. As seen in the first frame, the pinch assembles well with no macroscopic disruptions, but breaks up in a non-uniform way, suggesting sausage or kink MHD instabilities.

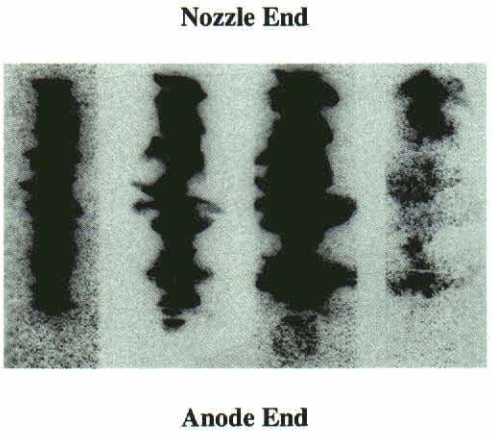

Figure 2-26. Four K-shell images (10-ns interframe time) of DM2 pinch.

The initiation phase of the pinch was also monitored with time-resolved cameras in both the visible and the XUV (~ 200 eV). As seen in Figure 2-27, axial filaments, consistent with the twelve-fold symmetry of the wire meshes at the anode and the nozzle, are often observed. They are more prominent on those shots with nozzle wires. Section 8.1.2 provides additional discussion of the filaments.

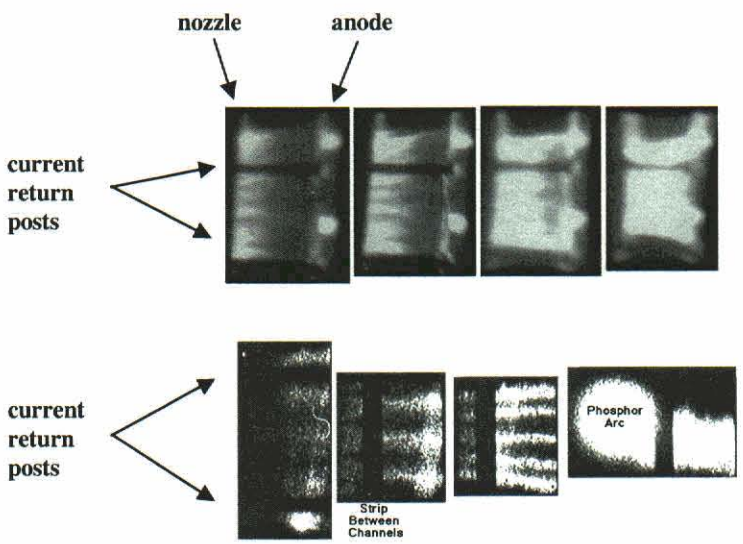

Figure 2-27. Four optical (21-ns interframe time) and XUV (40-ns interframe time) images of the initial phase of the pinch on DM2.

Spectroscopic analysis of the discharges, using a 2% CCl_2F_2 dopant in the argon to provide optically thin Cl lines, indicate an electron temperature and density of 0.84 keV and 4.0 x 10^{20} cm^{-3}, respectively, and an ion energy of 6.9 keV. The value of η^* was 1.1, which is marginal for good x-ray production.

In an attempt to achieve higher η^* and higher electron temperature, we replaced the 7-cm nozzle with a 10-cm nozzle of similar design. The load mass was reduced to provide the same 300 ns implosion time. This means that the initial density was reduced by approximately a factor of 3 from the 7-cm nozzle case (from $1.0 \times 10^{17} cm^{-3}$ to $0.3 \times 10^{17} cm^{-3}$). Yield results are shown in Figure 2-28. While this did result in a higher electron temperature and ion energy (0.95 keV and 16.6 keV, respectively), the pinch was unstable and axially non-uniform. The peak yield was 1.2 kJ with a peak current of 1.0 MA. We believe that the Rayleigh-Taylor instability was exacerbated by inhomogeneous initiation in the lower initial gas density.

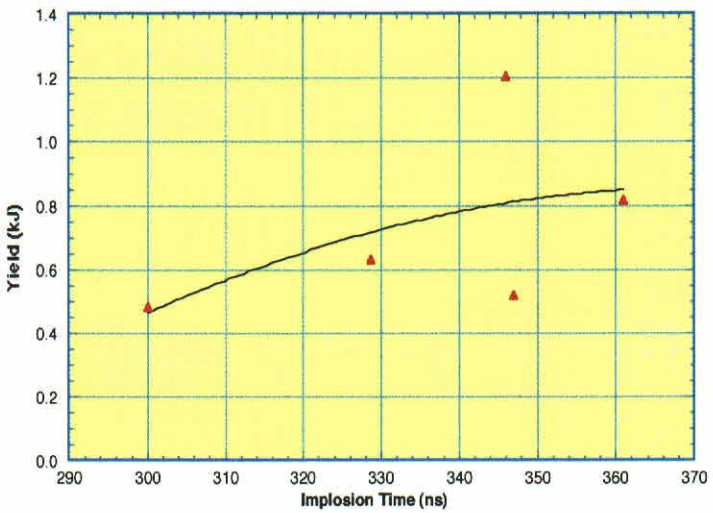

Figure 2-28. Argon K-shell yield results for the 10-cm nozzle on DM2.

To achieve higher η^* with the 7-cm nozzle, we performed a few experiments using a neon gas puff, which has a much lower E_{min} than argon. The x-ray yield peaked at 13 kJ.

2.4 SATURN TESTS OF THE 7-CM UNIFORM-FILL.

For these tests, SATURN was configured for long-pulse operation by shorting out the water switches. We took a very limited series of argon shots with the 7-cm nozzle at peak currents of 5.0 to 6.5 MA and implosion times of 160 - 200 ns, as shown in Figure 2-29. Best performance was 18 kJ of K-shell radiation using a 3.2-cm pinch length. The yields are summarized in Figure 2-30. (We discuss SATURN additional long-pulse shots with a double-shell argon load in Section 3.3 and with aluminum arrays in Section 4.)

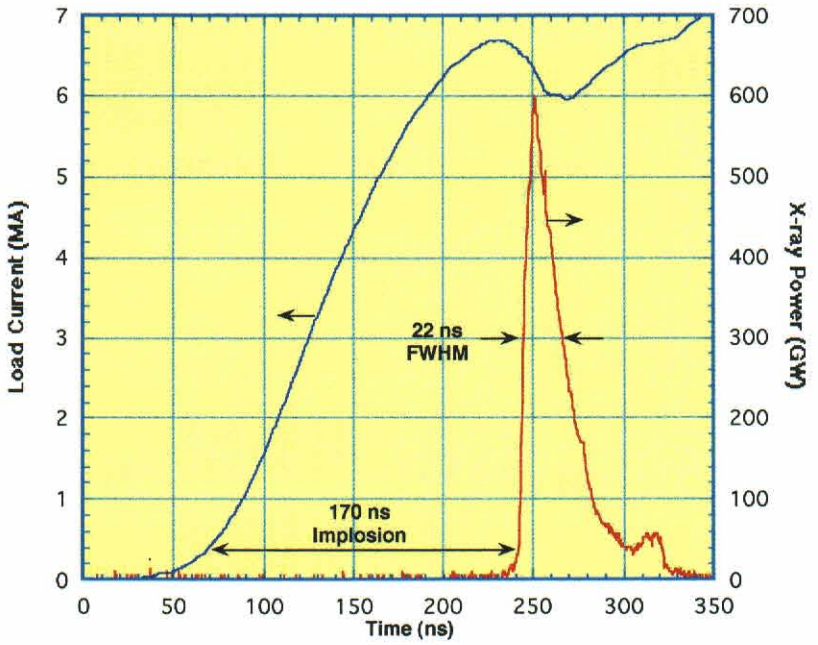

Figure 2-29. Current and PCD signal for an argon pinch on long-pulse SATURN.

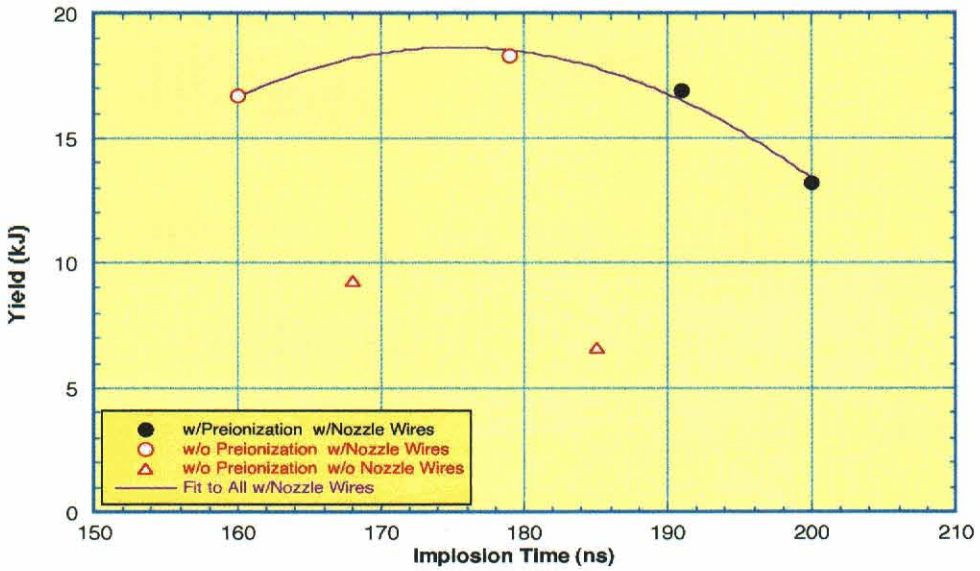

Figure 2-30. Yield vs. implosion time for the 7-cm argon gas puff shots on SATURN.

The importance of the nozzle wires is evident; they produced approximately a doubling of the K-shell yield. The pre-ionization was extremely non-uniform (a single flashboard), and its use of pre-ionization had no effect on the yield. It must be noted that pre-ionization in general seems to be of marginal utility with higher power drives.

K-shell images, as shown in Figure 2-31, demonstrate that, as on DM2 and Double-EAGLE, the pinch assembled, without macroscopic disruptions due to Rayleigh-Taylor instabilities.

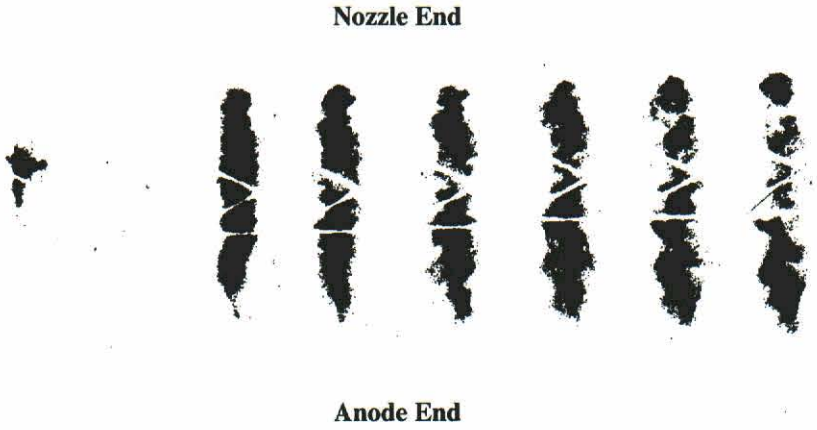

Figure 2-31. Eight K-shell images (3 ns interframe time) of SATURN pinch; the second frame is blank due to a dead strip in the camera.

Using the optically thin Cl lines from the dopant, the measured electron temperature and density were 1.16 keV and 8.8 x $10^{20}cm^{-3}$, respectively, and the ion energy was 12.1 keV. η^* was 1.5.

We had to make several design and operational compromises in order field the experiment on SATURN. In retrospect, it is likely that those compromises led to less than optimal results. Rather than using the MPI puff valve, we used a modified version of an existing SNL valve that included a breakdown pin with which the SNL staff had experience and confidence. This resulted in a longer path for the gas flow from the plenum region to the nozzle throat, changing the filling characteristics of the nozzle. The valve was also not in good electrical contact with the cathode plate, causing arcing. Since there were no current diagnostics along the nozzle, comparable to IR1 on DM2, it is not possible to determine what fraction of the "load current" was actually delivered to the pinch. Furthermore, the gas system at SATURN could not handle the higher plenum pressure needed for the higher current (required implosion mass is proportional to current squared) at the 150 μs flow time that we normally use. We were therefore forced to operate at a flow time of 450 μs. (The SNL gas puff system was unavailable prior to the test series for density profile measurements to establish initial conditions.) Finally, the improved circular pre-ionizer meant for use on Double-EAGLE was not yet ready for use at SATURN.

SECTION 3

DOUBLE GAS PUFF EXPERIMENTS ON DOUBLE-EAGLE AND SATURN

3.1 INTRODUCTION.

Recent z-pinch experiments have reported improved x-ray output with nested wire arrays (Reference 19) and double shell gas puffs (Reference 20). The standard rationale behind these double implosion configurations is that the interaction of the imploding outer shell with the inner shell suppresses Rayleigh-Taylor plasma instabilities developed during the longer implosion time of the outer shell (Reference 11 and 21-23). The level of suppression depends on the thicknesses and mass densities of both shells.

Based on such considerations, we designed and built a new double shell nozzle driven by a dual plenum valve. We cover design details in Section 9.4. Here we discuss the z-pinch results achieved on Double-EAGLE and SATURN.

3.2 DOUBLE-EAGLE EXPERIMENTS WITH THE DOUBLE SHELL.

Our initial double shell experiments performed on Double-EAGLE were configured for a 200 ns short-circuit rise-time with a peak current of 4 MA. A photograph of the shell-on-shell gas nozzle is shown in Figure 3-1a. A single valve controls the flow to both shells but each shell has its own plenum. Pinch length was 3.8 cm. We used the cylindrical UV source (Section 10) to pre-ionize the gas to ensure proper initiation of current flow.

Figure 3-1. Photograph of the shell-on-shell gas nozzle. The inner and outer radii of the outer nozzle exit are 3 and 4 cm; the inner nozzle exit radii are 1 and 2 cm.

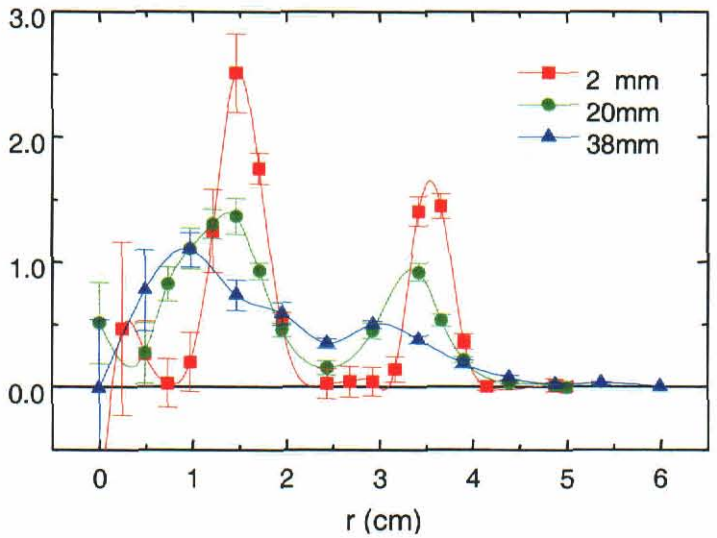

Figure 3-2. Argon radial density profiles of the shell-on-shell nozzle at 500 μs flow time. Measurements were taken at z = 2, 20, and 38 mm from the nozzle.

As described in Section 9, the gas and pre-ionization distributions for the nozzle were measured at the Naval Research Laboratory (NRL) using a high-sensitivity laser interferometer (Reference 24). The gas density profile is shown in Figure 3-1b. As expected, near the nozzle (2 mm), the flow consists of two distinct shells. Near the anode plane (38 mm), the divergences in each shell make the net density distribution more nearly uniform with radius.

The primary objective of our experiment was to search for the optimal total mass. We tested inner to outer mass ratios from 0.6 to 1.2 although most of our tests used a ratio of about 1.0. The optimum ratio will be determined in future experiments.

3.2.1 Summary of Double-EAGLE Double Shell Results.

Figure 3-2 is a sample of the current drive and K-shell power of a typical shell-on-shell implosion. Table 3-1 shows that the double shell results are on a par with the performance of a solid fill gas load. (Previous experiments [References 13 and 25; see also Section 2] have shown that the solid fill performs significantly better than a thin shell for large radius, long implosion time loads.) Using the measured gas profile and measured current, we find that the observed and calculated implosion times are in good agreement, Figure 3-3.

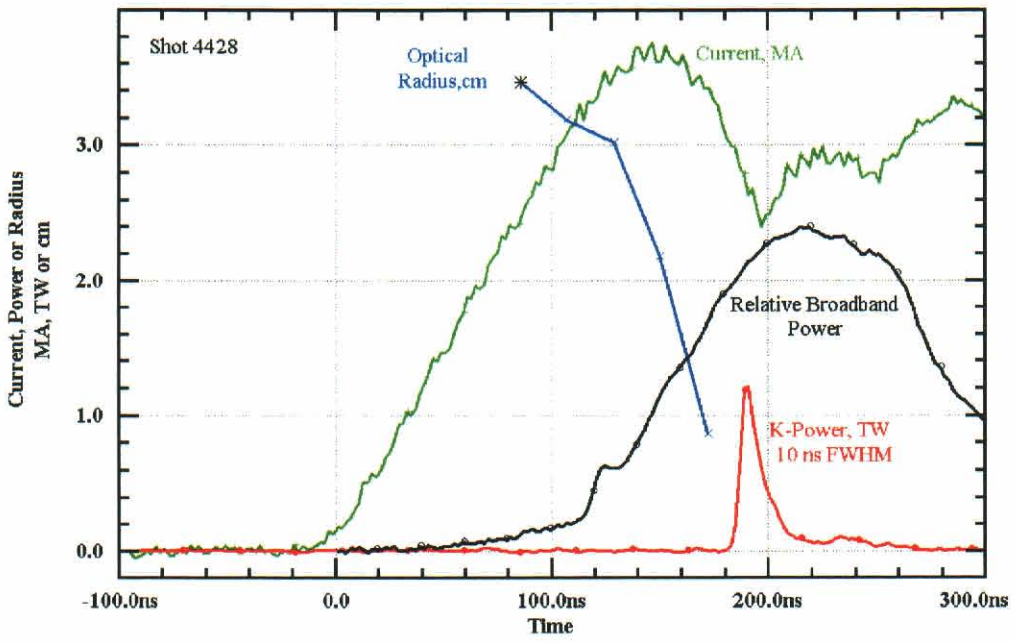

Figure 3-3. An overlay of the measured current, optical image radius, and x-ray powers pulse for Shot #4428, a typical double shell implosion. The "broadband" relative power is from a bare XRD; the step at 120 ns is characteristic of the double shell – it is not seen with uniform fill loads.

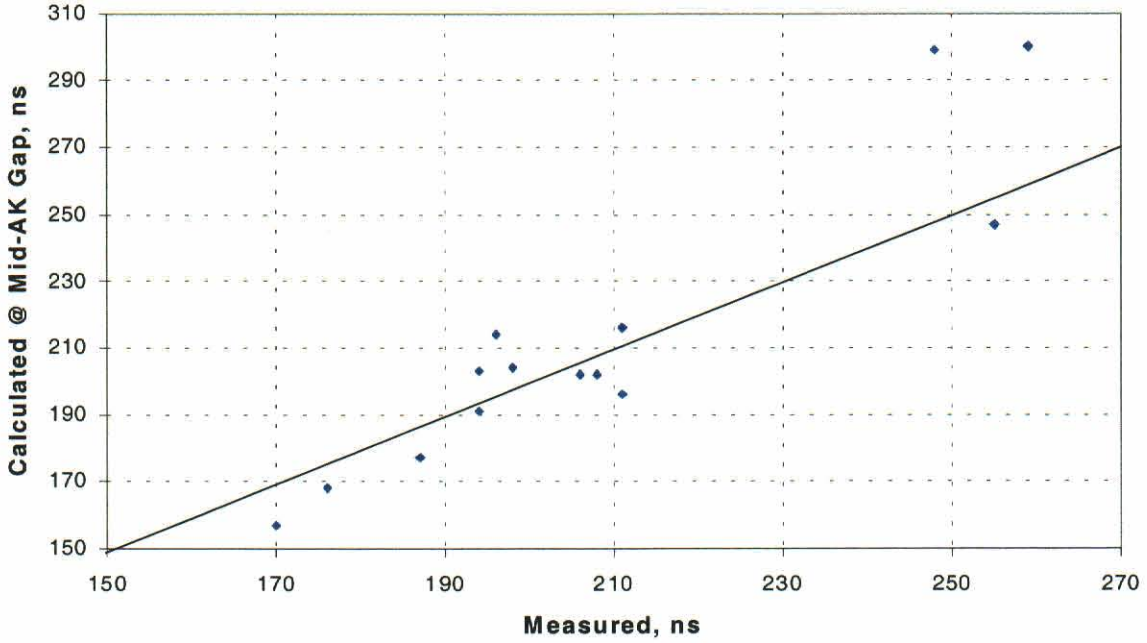

Figure 3-4. Calculated vs. observed implosion time for the double-shell on Double-EAGLE.

Table 3-1. Key results for double shell argon Z-pinches on Double-EAGLE.

Test# and Load Type	Pressures Pin/Pout (psia)	Inner/Outer Masses (μg/cm)	Current Peak (MA)	Timp (ns)	K-shell FWHM (ns)	K-shell Yield (kJ)
Shell-on-Shell						
4413	7.1*/8.9*	63/108	3.81	196	17	11.2
4415	11.5*/9.2*	102/112	3.81	211	14	10.4
4417	12*/8*	106/97	3.89	208	14	8.9
4418	10.2*/8.2	90/100	3.88	206	15	10.3
4419	9.6/7.7*	85/94	3.99	211	7	8.1
4421	8.9/7.1*	79/86	3.78	194	10	9.9
4428	6.1*/4.9	54/59	3.70	187	10	12.0
4429	5.0/4.0*	44/49	3.59	176	15	9.1
4430	4.0/3.2*	35/39	3.56	170	19	5.2
7 cm Solid Fill						
4432	40*	125	3.93	196	10	10.9
4433	46*	144	3.89	201	11	10.0
4434	58*	181	4.00	206	11	10.5
Estimated						
+-Uncertainties:		5%	0.2 MA	5 ns	1 ns	1 kJ

* Chlorine tracer

Optical images, each 4 ns in exposure with 21 ns between frames, covering the final 100 ns of the implosion, are shown in Figure 3-4. The first 3 images clearly show that the outer shell lights up well and implodes with good azimuthal symmetry. At t = -39 ns from the peak K-shell power, the fourth image, the outer edge of the inner shell is just beginning to light up. This suggests that there is no current flowing on the inner shell until the outer shell collides with it. At t = -17 ns, the pinch is approaching the axis. (The features inside of a 4-cm diameter around the axis, seen in the third and fourth frames, are scattered light off the surface of the central stub of the nozzle.)

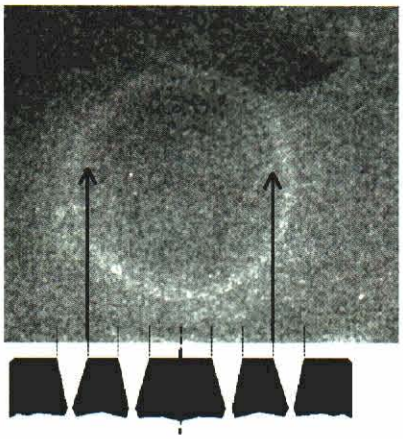

(a) -103 ns - Initiation and acceleration of the outer shell; the arrows mark the 6-cm ID of the outer shell

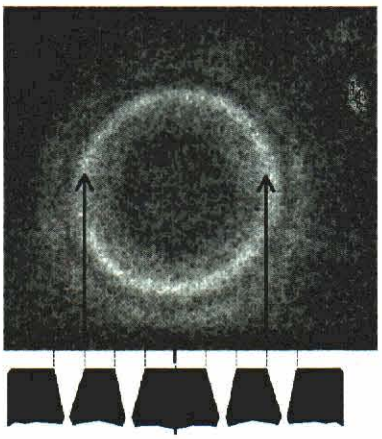

(b) -82 ns - Initiation and acceleration of the outer shell; the arrows mark the 6-cm ID of the outer shell

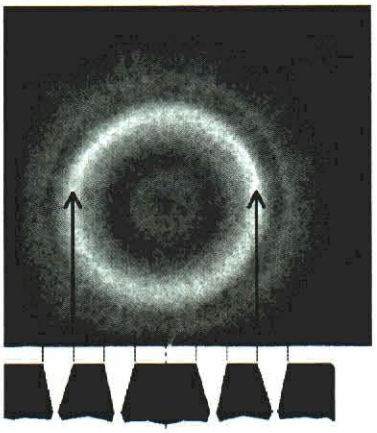

(c) -60 ns - Initiation and acceleration of the outer shell; the arrows mark the 6-cm ID of the outer shell

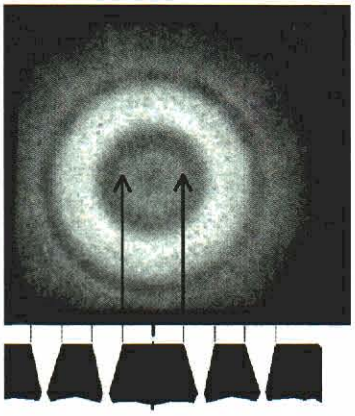

(d) -39 ns - Collision of the outer shell with the inner shell; outer edge of inner shell is just beginning to light up at this time. Sketches of the nozzle under the pictures are shown to illustrate the position of the plasma shells. The arrows mark the 2-cm ID of the inner shell.

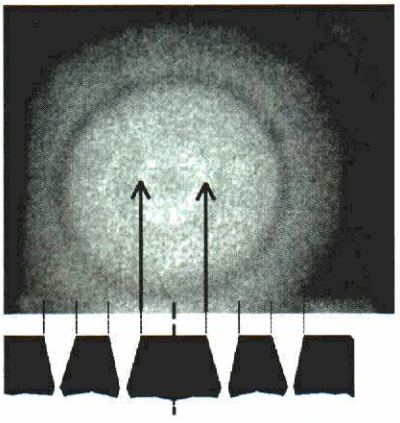

(e) -17 ns - Final implosion of the combined shells. Sketches of the nozzle under the pictures are shown to illustrate the position of the plasma shells. The arrows mark the 2-cm ID of the inner shell.

Figure 3-5. Optical pictures of the double shell implosions in the radial direction. Times are relative to peak K-shell power.

The predictable behavior of these pinches is clear in the correlation between the optical image radius, as seen in Figure 3-4 and the predicted position of the snowplow using a simple 1-D code: see Figure 3-5. Likewise, the zippering of the pinches is qualitatively well (Figure 3-6) to fairly (Figure 3-7) reproduced by the snowplow calculations. (Even the quantitative agreement, typically 10 ns out of a ~ 200 ns implosion, is remarkable given the coarse grid of the gas flow data and the one-dimensionality of the snowplow calculations.) These results imply that we

know where the initial mass and current are, and that there are no significant mass losses during the implosion.

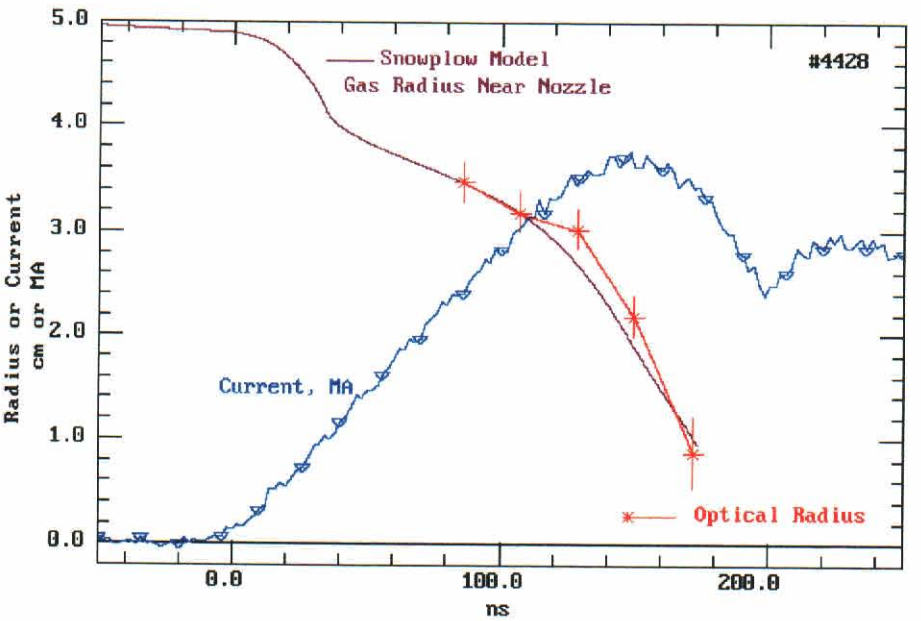

Figure 3-6. Observed and predicted radii of the double-shell implosion front.

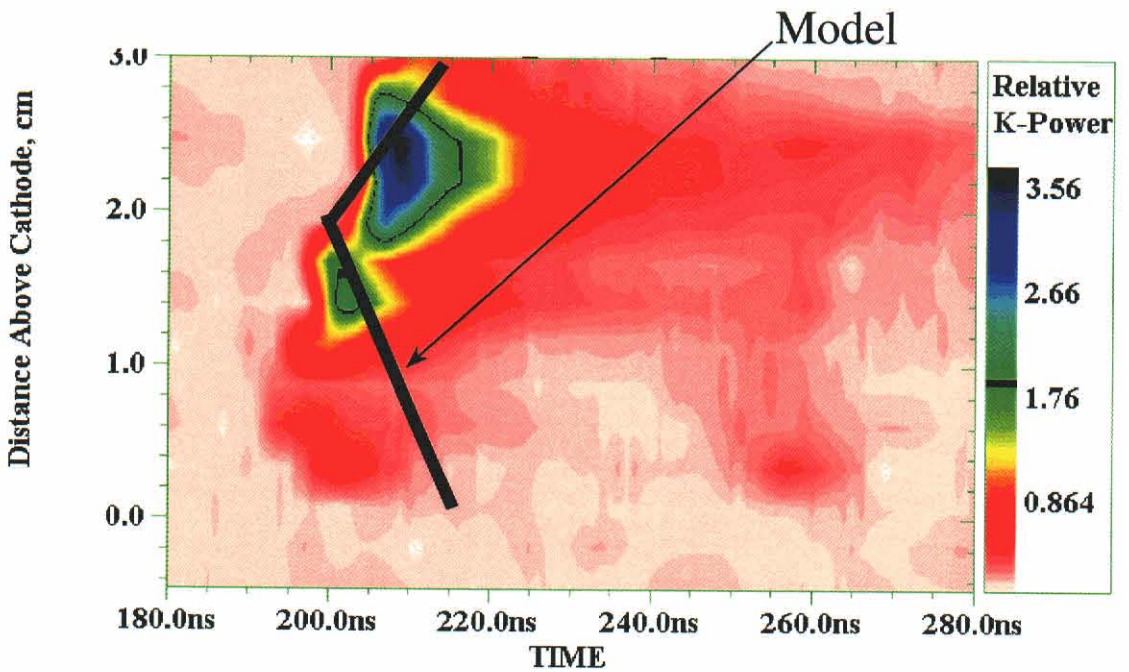

Figure 3-7. Observed and predicted zippering for shot 4411 (gas flow time pf 400 μs.)

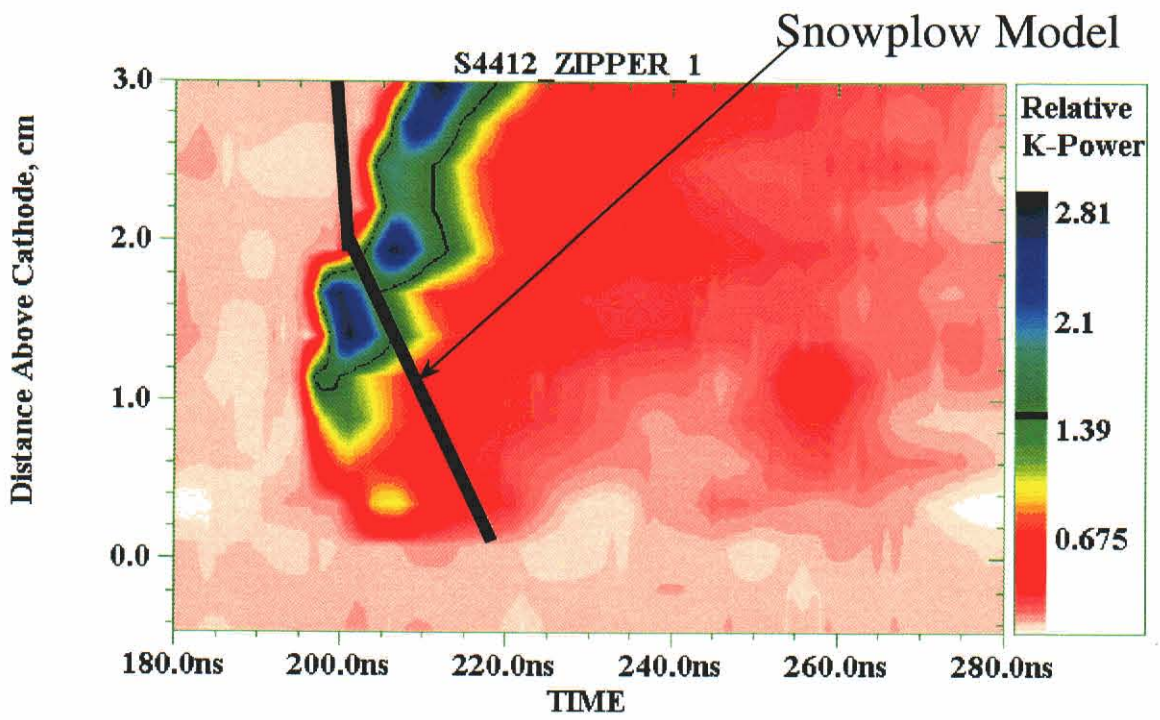

Figure 3-8. Observed and predicted zippering for shot 4412 (gas flow time of 500 μs.)

Time resolved x-ray pinhole pictures are shown in Figure 3-8. The pictures, confirmed with similar data from a 1-D diode array (Figures 3-6 and 3-7) and an x-ray streak camera, show that the imploding plasma began radiating in the K-shell first at 1 to 2 cm from the cathode (Figure 3-8a). Then over the next 5 ns it extended towards the cathode and more strongly towards the anode (Figure 3-8b). Integrated over time, the pinch was uniform in intensity to within a factor of 2.5 along its length. The FWHM of the radiating diameter was uniform along its length at about 0.2 cm.

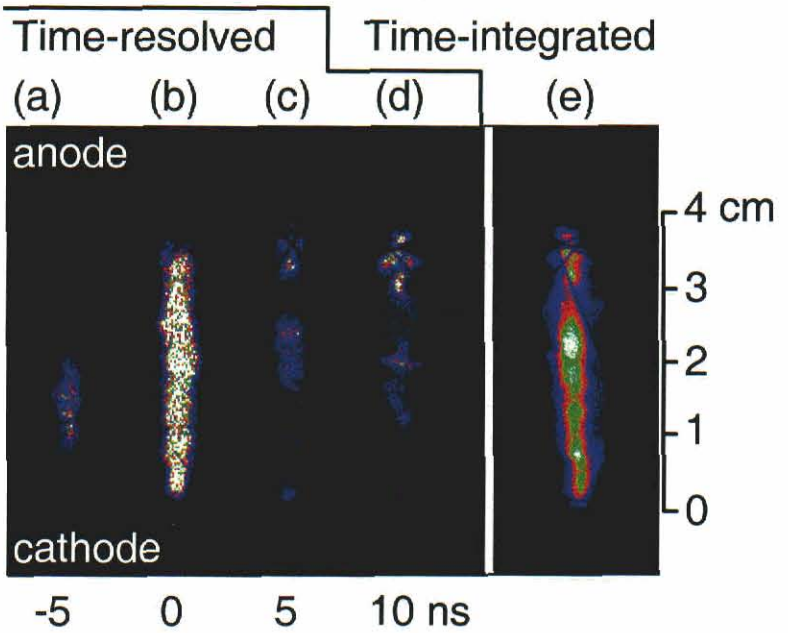

Figure 3-9. Time resolved K-shell x-ray pinhole pictures of the double shell on Double-EAGLE. (a) The first part of the pinch to light up was at 1-2 cm from the cathode (b) 5-10 ns later, the pinch extended weakly towards cathode and strongly towards the anode. (c-d) The pinch became unstable at later times and began to disintegrate. (e) Time-integrated picture of the pinch. Times are relative to peak K-shell power.

K-shell spectra are shown in Figure 3-9. The Ar He-α resonance and intercombination (IC) lines near 3.1 keV dominated the spectrum with less intense Ly-α at 3.3 keV. Plasma temperature in the K-shell radiating core was then determined from the Ly-α /(He-α +IC) line ratio while the density was determined from the K-shell brightness (Reference 18). Typical values for the plasma conditions are listed in Table 3-2. The average electron temperature was about 1.4 keV, but there was a significant variation of temperature along the length of the pinch with the anode end being hottest.

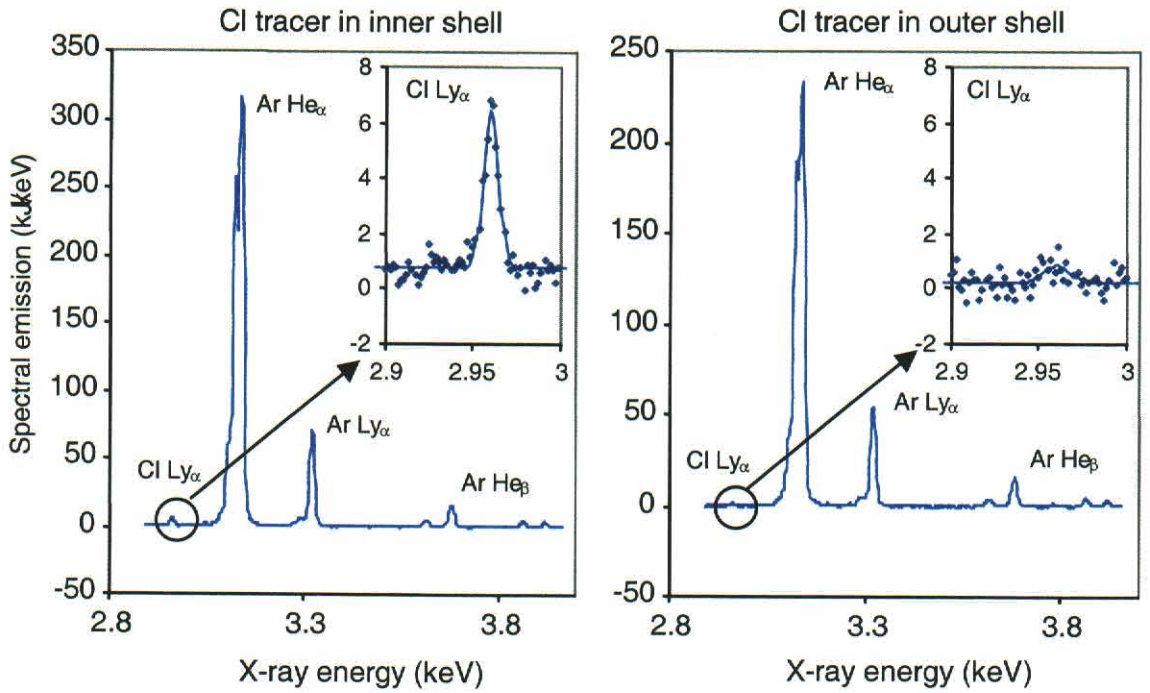

Figure 3-10. Argon K-shell spectra measured using time-integrated and spatially-resolved spectrometers. (a - Shot 4428) With chlorine present in the inner shell, the chlorine Ly-α line was observed easily. (b - Shot 4429) With the chlorine tracer in the outer shell, only a small amount of chlorine Ly-α was observed.

Table 3-2. Comparison of plasma conditions for selected double-shell tests.

Test # and Tracer Location	**K-shell Yield (kJ)**	**K-shell Ave. Dia. (mm)**	**Electron Temp. (keV)**	**Argon Ion Density (#/cm^{-3})**	**K-shell Radiating Mass Fraction**	**Intensity Cl Ly-alpha w.r.t.Argon He-β**
Shell-on-Shell						
4413, Cl both	11.2	2.7	1.42	1.2E+19	0.25	16.5%
4428, Cl inner	12.0	3.1	1.48	1.1E+19	0.49	13%
4421, Cl outer	9.9	1.9	1.45	2.2E+19	0.26	2.8%
4429, Cl outer	9.1	3.8	1.52	0.65E+19	0.52	1.8%
7-cm Solid Fill						
4432	10.9	2.5	1.45	1.4E+19	0.47	11.2%
Estimated						
+-Uncertainties:	1 kJ	0.2 mm	0.04 keV	20%	0.15	1%

Since each shell has an independent gas plenum, one unique feature of our experiment was the opportunity to trace the origin of the K-shell radiation. For some shots, we used a 98% argon and 2% freon 12 (CCl_2F_2) gas mixture in the outer shell and 100% pure argon in the inner shell. For other shots, we interchanged the gases in the two shells. Spectrographic data of these test shots are also shown in Figure 3-9. With the chlorine tracer present in the inner shell only, the chlorine Ly-α line was observed easily (Figure 3-9a, shot # 4428). For the shots with chlorine in the outer shell, only a very small amount of chlorine Ly-α like emission was observed (Figure 3-9b, Shot #4429). As Table 3-2 shows, the chlorine Ly-α lines were about 6 times stronger when the chlorine was in the inner shell than when the chlorine was present only in the outer shell. Lower energy chlorine He-α lines were 3-4 times stronger when the chlorine was present only in the inner, rather than in the outer shell. Although the tracer data presented are spatially-averaged, there is no pronounced difference in the raw spatially-resolved data along the entire pinch.

3.2.2 Discussion of Double Shell Dynamics.

It has been previously demonstrated (References 26 and 27) for wire array implosions that the center of a z-pinch is at the highest temperature. Based on MHD models, we expect this result to also apply to gas puffs. Hence the chlorine data imply that the hottest part of the pinch, i.e., the on-axis mass, is supplied predominantly by the inner shell. Although some mixing of the two shells due to the RT instability must undoubtedly take place, our measurements indicate that it there is no significant penetration of the outer shell mass into the core of the inner shell mass that produces most of the observed K-shell output.

An explanation for the low level of mixing is that the outer part of the inner shell is very effective at smoothing out the bubbles and spikes of the incident outer plasma shell, thus mixing only occurs near the boundary between the shells.

3.2.3 Load Length Experiments with the Double Shell.

For the SATURN tests of the double shell, we had to use a pinch length of 2 cm (see Section 3-3 below) compared to 3.8 cm on Double-EAGLE. To see if we could expect better performance on SATURN with a longer pinch, we made a limited study of the effects of pinch length.

Based on modeling considerations, yield per unit pinch length should primarily depend on the current driving the pinch. Since the electrical driver (e.g., Double-EAGLE or SATURN) has a fixed inductance of order 10's of nanohenries, a reduced load length means proportionately reduced load inductance and higher load current. Yield varies as at least the square of current and as the length, thus one expects that there should be an optimum length. For short loads where the load inductance is small compared to the generator impedance, yield should increase as length increases. For long loads where the load inductance dominates, yield should decrease inversely with length to the power (x-1) where x is 4 in the "inefficient" I^4 regime and x is 2 in the "efficient" I^2 regime. The optimum length corresponds (roughly) to

$$\text{(Generator Inductance)} / \text{(Load Inductance)} \sim x\text{-}1$$

Hence on Double-EAGLE (~ 20 nH), we might expect that for the double shell (return cage radius of 6.8 cm, outer shell radius of 3.5 cm), the "best" load length is ~ 5 cm. This oversimplified treatment, which ignores the dramatic change in load inductance during the pinch, implies that SATURN should benefit from equally long pinches if power flow problems do not dominate.

A competing effect is that not all parts of the pinch radiate equally well. In particular, the most shell-like gas flow near the nozzle emits less than the more filled-in regions of the gas flow (e.g., the zipper data in Figures 3-6 and 3-7).

On this basis, we conducted a limited series of 15 shots using pinch lengths of 2.0, 3.9, and 5.8 cm. The yield versus implosion time plot, Figure 3-10, indeed implies that the optimum length is probably between 3.9 and 5.8 cm for Double-EAGLE. Our simple analysis above argues that longer pinches should also be favored on SATURN where argon is "efficient." (The limits of this analysis are shown in Figure 3-11 where we see that our assumption that yield scales as length and I^4 is only roughly correct. The poorer performance of the shell-like gas flow near the nozzle exit probably explains the lower output of the 2-cm long pinches.)

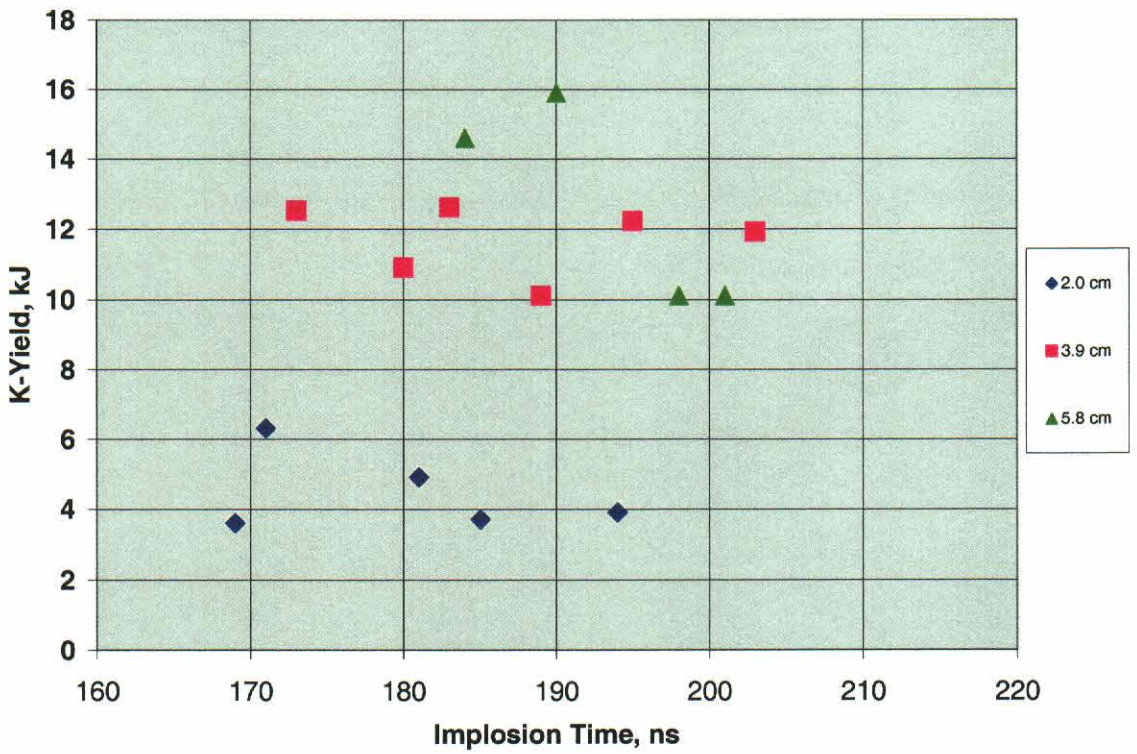

Figure 3-11. Yield vs. implosion time for the double-shell length scans on Double-EAGLE.

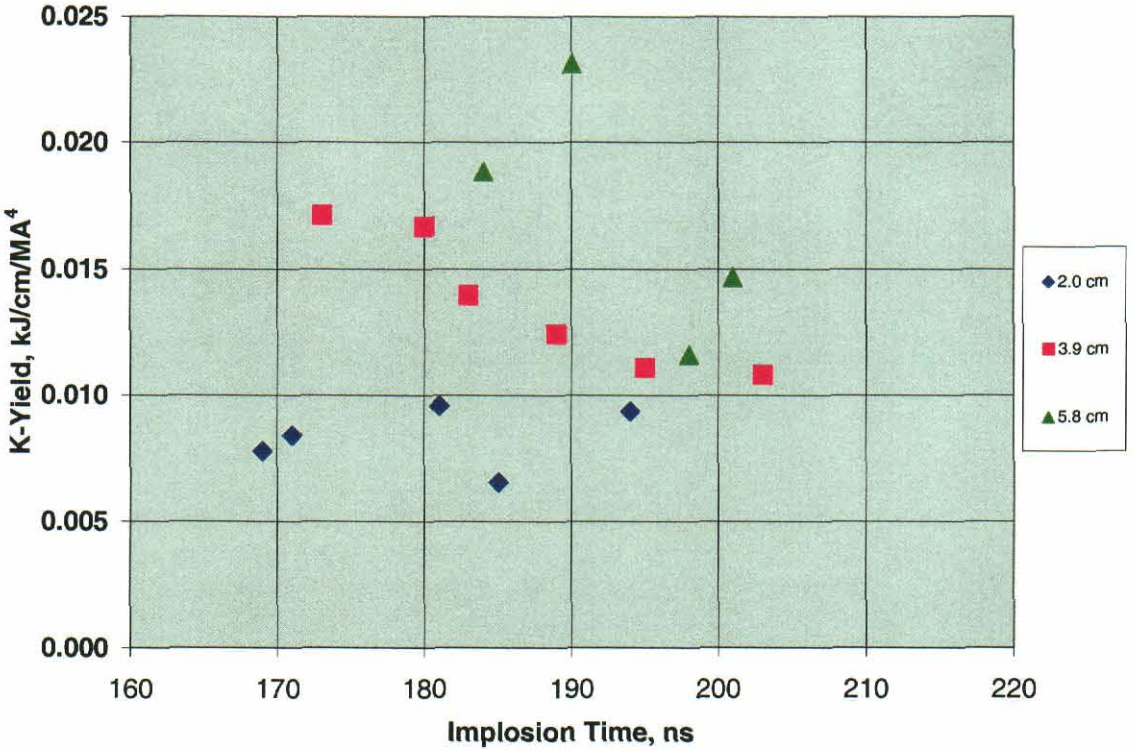

Figure 3-12. Yield per centimeter of pinch per current to the fourth power for the Double-EAGLE length scan. In the absence of instability losses for the shell-like gas flow near the nozzle, this parameter should be constant.

3.3 SATURN EXPERIMENTS WITH THE DOUBLE SHELL.

The lessons learned in our first long pulse gas puff tests on SATURN (Section 2.4) guided our design of the double shell test series on SATURN. We used the same valve (with a demonstrated breakdown pin), nozzle and circular pre-ionizer as employed on Double-EAGLE. With testing time limited, we kept the same fixed ratio of inner to outer plenum pressures as employed on most of the Double-EAGLE shots. The resulting test campaign was successful although we had to reduce the pinch length to 2 cm, i.e., reduced load inductance, to get good power flow.

In accordance with the usual kinematic arguments, we found that the product of peak current times implosion time (I*t) scaled as the square root of plenum pressure, i.e., as the square root of mass. Implosion time is well correlated with the mass inferred from the NRL density measurements, Figure 3-12.

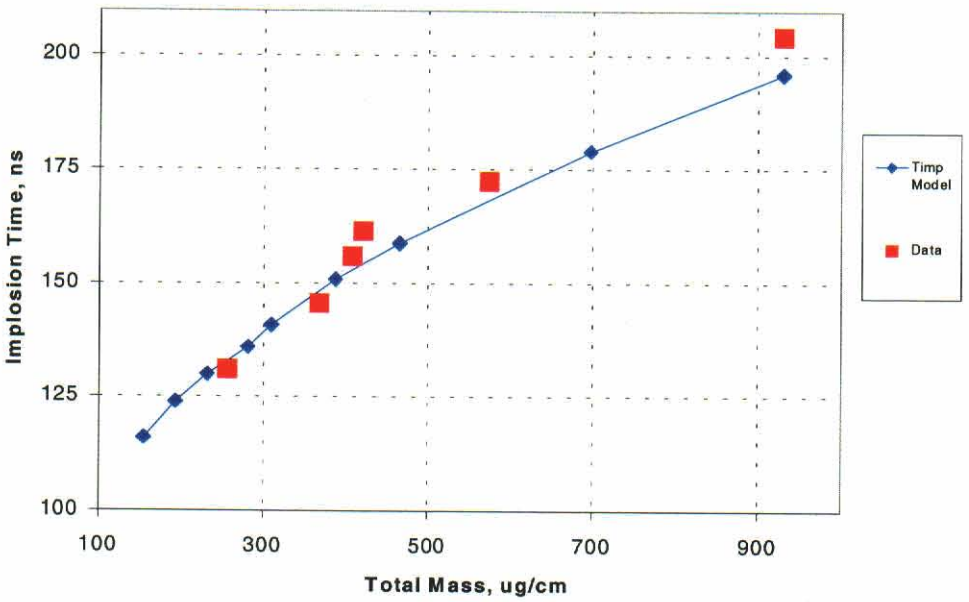

Figure 3-13. Implosion time vs. mass for the double shell on SATURN.

The sample current and K-power waveforms in Figure 3-13 hint at one important difference between the Double-EAGLE and SATURN tests; the optimum implosion time on SATURN was smaller. (The long pulse aluminum data also show this effect; see Section 4.) This is made even more evident in the yield summary of Figure 3-14.

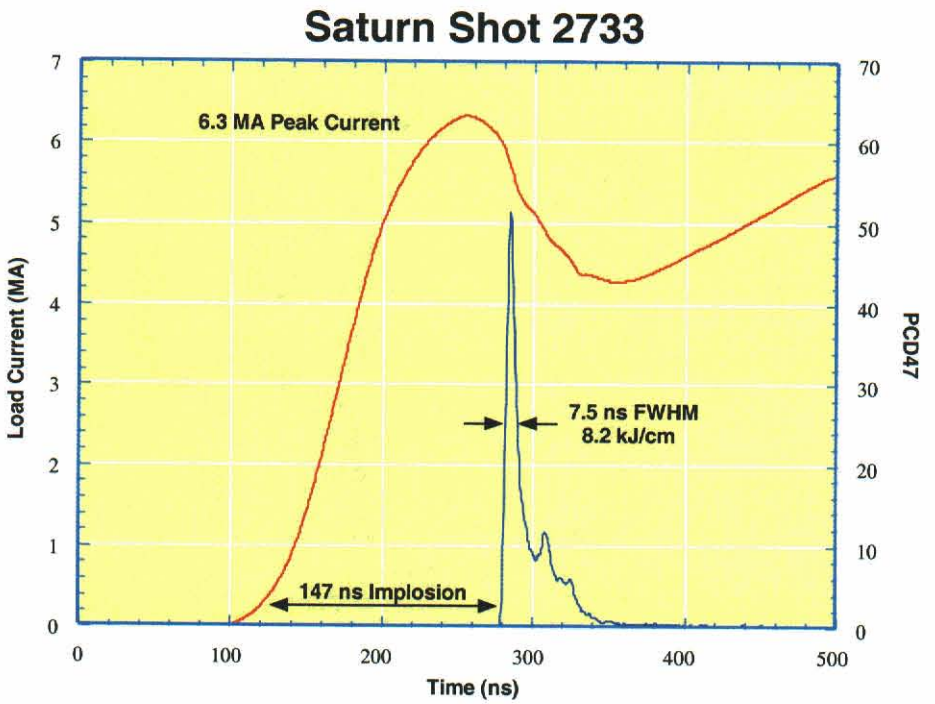

Figure 3-14. Example of SATURN current and double-shell K-power.

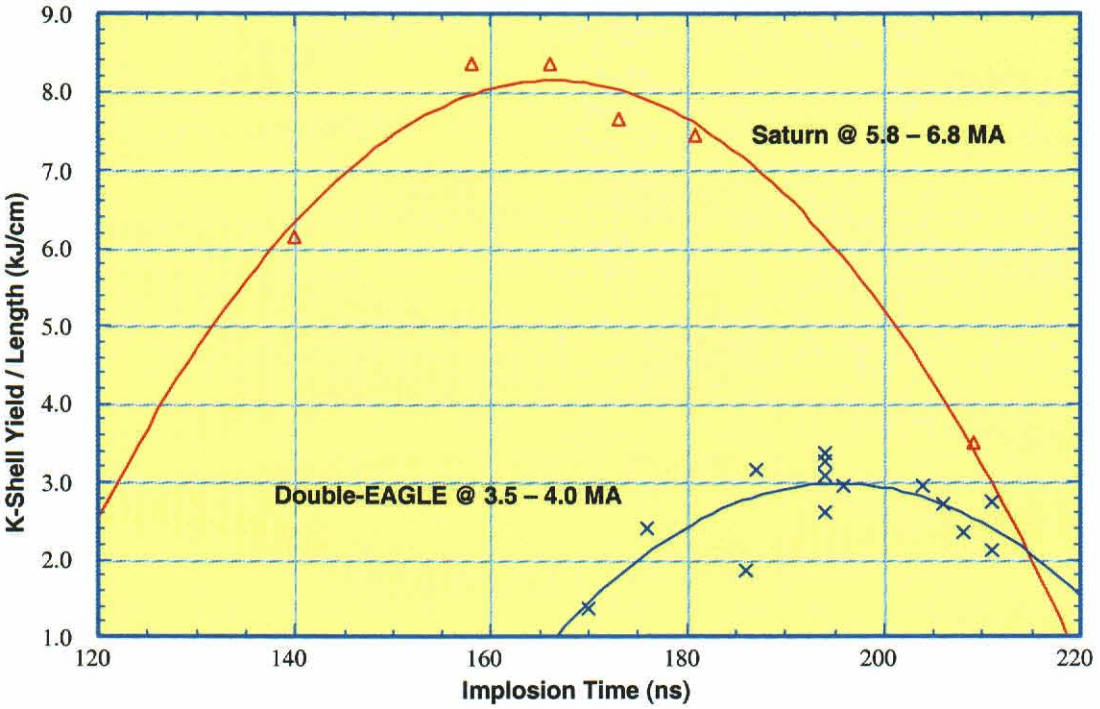

Figure 3-15. Double shell yield vs. implosion time for Double-EAGLE and SATURN.

The differences in the current waveforms of the two machines cannot explain this; see Figure 3-15. A possible explanation lies in the higher mass (roughly 3 times higher) needed for the SATURN shots. The main emission lines of argon are certainly optically thick in the SATURN shots. Reduced mass, hence reduced implosion time, may allow more of the K emission to be radiated. This is in accordance with the detailed 1-D rad-hydro calculations of NRL. They show that higher implosion velocity (higher η or lower implosion time) is favored as load mass increases.

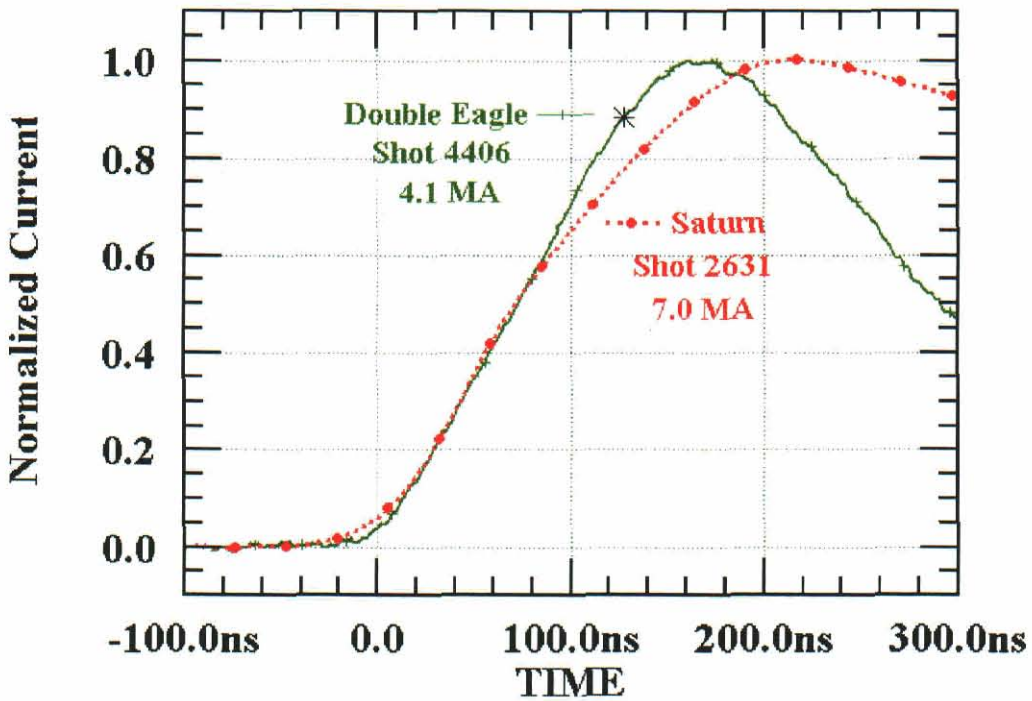

Figure 3-16. Normalized long pulse currents for Double-EAGLE and SATURN. Both shots were relatively high mass loads: 20 psia on Double-EAGLE and 60 psia on SATURN. Implosion times were 255 ns (Double-EAGLE) and 205 ns (SATURN).

3.4 SUMMARY.

In this section we have presented the results of argon z-pinch experiments using a double gas puff. The overall pinch quality and radiative characteristics of the double shell z-pinches are equal to the best observed to date for long (200 ns) uniform-fill implosions. Selective seeding of the shells demonstrates that the hottest mass of the pinch originates from the inner shell. This argues that mixing between the two plasma shells during their collision and final implosion is limited. An empirical review of these double shell results compared with other load styles is given in Section 5.

SECTION 4

WIRE ARRAY PRS EXPERIMENTS

Aluminum wire arrays have been studied for years in short pulse mode on many drivers and are a standard source of ≥ 1.6 keV x-rays for testing. Our efforts in this program were primarily to extend that knowledge base for long implosion time. Aluminum PRS experiments were all conducted under long-pulse conditions on DM2, SATURN, and Double-EAGLE with >140 ns implosion times. Molybdenum is also of interest because its L-shell transitions radiate above 2.3 keV, and it may be substituted for argon in mixed-element wire arrays for the high-fidelity PRS. The molybdenum PRS experiments were conducted only on Double-EAGLE, and only in short-pulse operation with ≈ 100 ns implosion times.

4.1 ALUMINUM PRS ON DM2.

A series of aluminum wire array shots was taken on DM2. All the arrays were 2 cm long and 4 cm in diameter, as shown in Figure 4-1. The number and diameter of the wires was varied to provide a 50 to 250 μg/cm range of masses. Peak current on all the shots was 2.5 MA. Implosion times varied from 260 to 380 ns, as shown in Figure 4-2, spanning the range of interest to Decade, though at substantially reduced current.

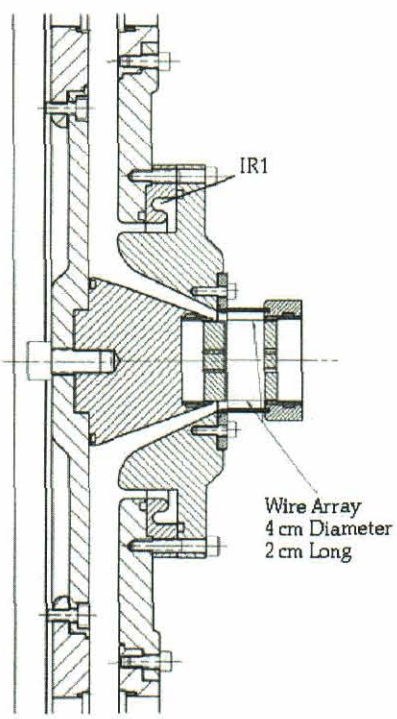

Figure 4-1. Wire array hardware for DM2.

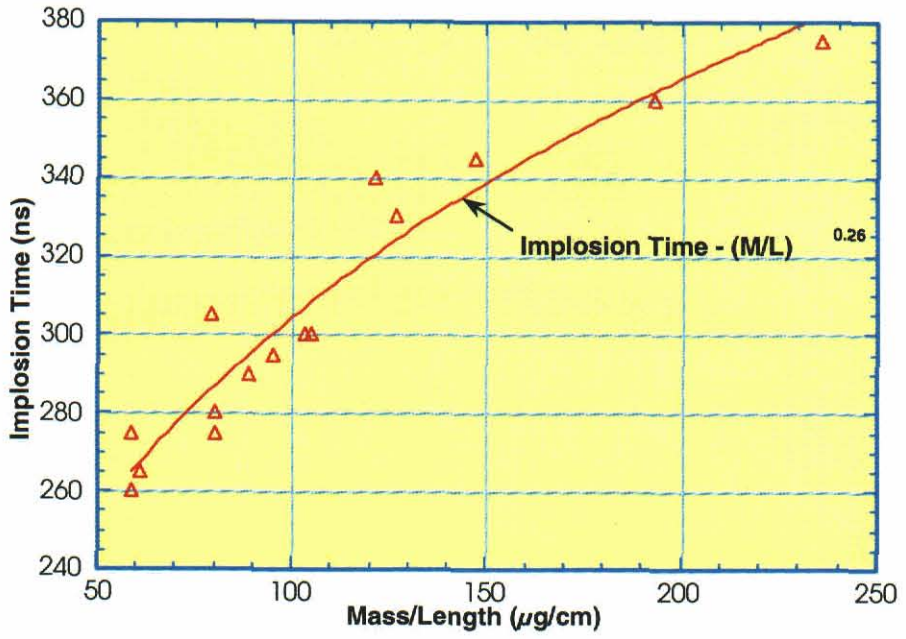

Figure 4-2. Implosion time as a function of load mass of aluminum wire arrays on DM2.

Typical current and K-shell power waveforms are shown in Figure 4-3. The yields, as a function of implosion times, are shown in Figure 4-4. Peak K-shell x-ray yields are ≈ 4 kJ, about 20% below the 5 kJ yield predicted by the Thornhill-Whitney-Giuliani model (Reference 28).

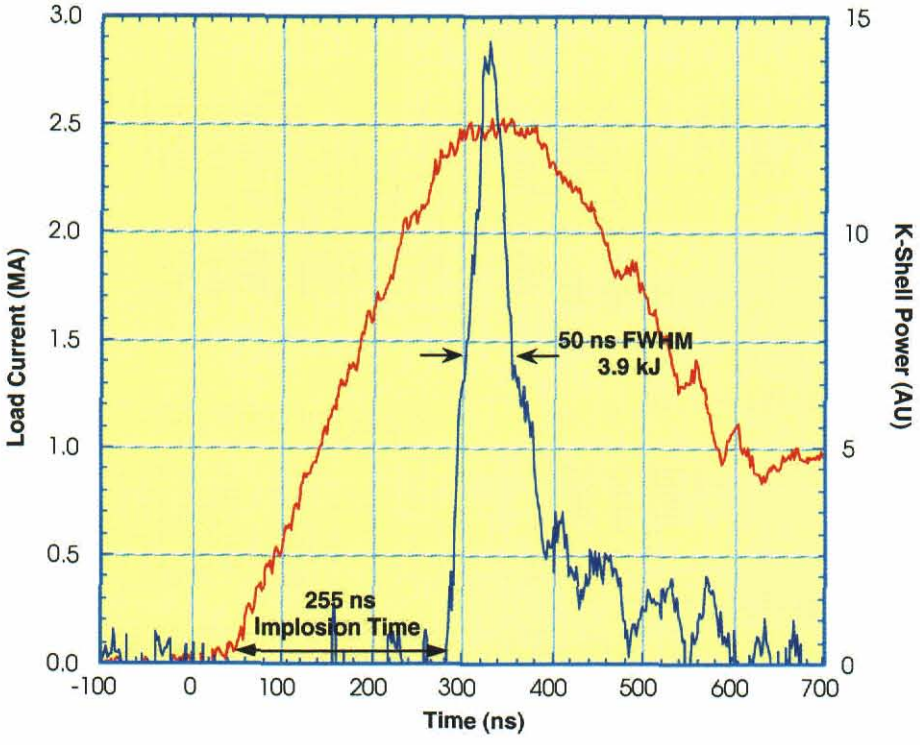

Figure 4-3. Load current and K-shell power pulse for aluminum wire array on DM2.

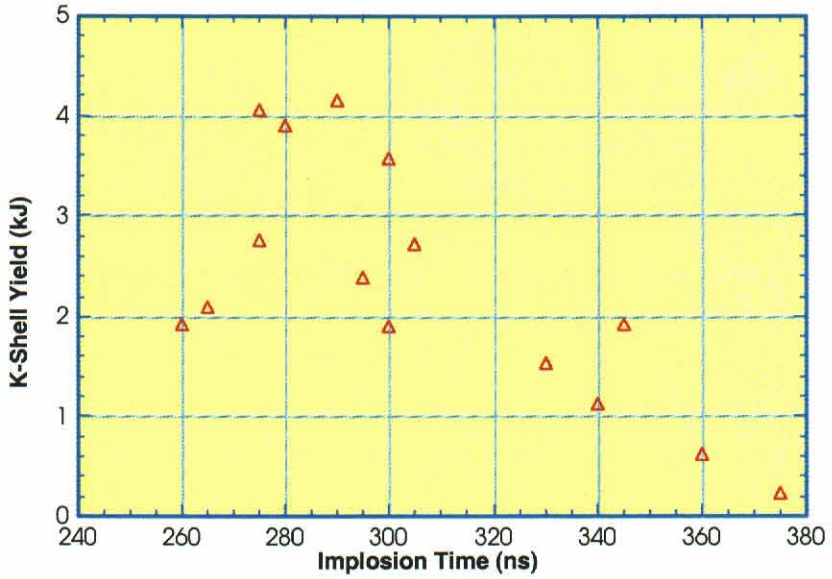

Figure 4-4. K-shell yield as a function of implosion time of aluminum wire arrays on DM2.

4.2 ALUMINUM PRS ON SATURN.

Because of this project's interest in long-pulse implosions, we participated in a series of long-pulse aluminum experiments that were designed and conducted at Sandia. The data discussed in this section are courtesy of C. Coverdale and C. Deeney of Sandia Labs.

Long pulse aluminum wire array shots were taken on SATURN in several campaigns during this project. Typical current and PCD waveforms are shown in Figure 4-5. The arrays were 4 cm in diameter, typically consisting of 180 0.5-mil-diameter wires, 2 cm long. Due to occlusion by the anode retainer, only a fraction (4 to 8 mm depending on the specific load) of the final pinch could be seen by the diagnostics. The reported yields are therefore scaled by factors of 2.5 to 5 from the observations, with the implicit assumption of axial uniformity.

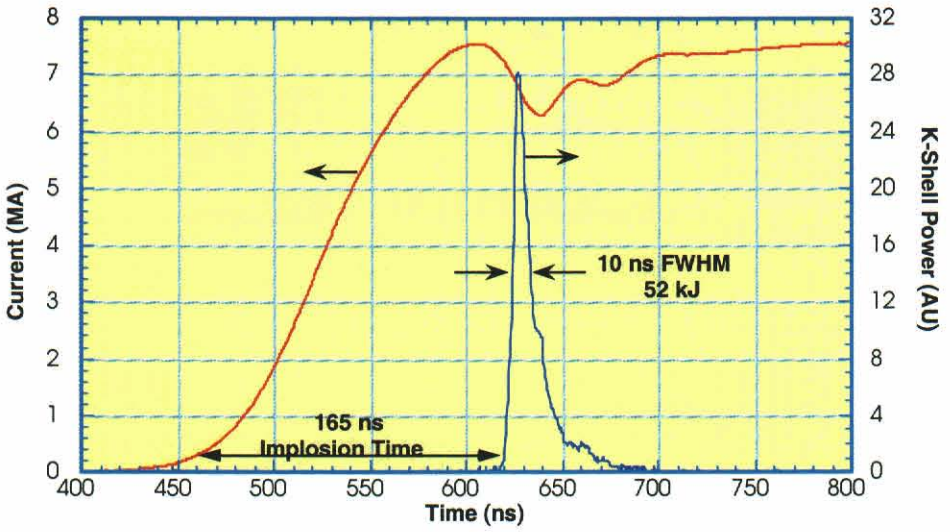

Figure 4-5. Current and PCD signal for SATURN long-pulse aluminum wire array shot #2480.

Figure 4-6 summarizes the variation of implosion time with mass. We see that at fixed mass, the implosion time varies by ± 4%.

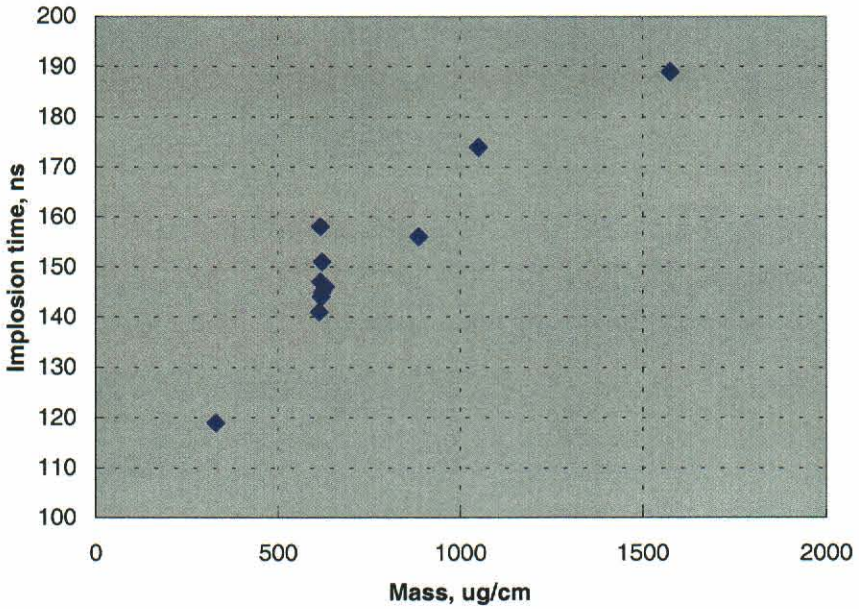

Figure 4-6. Implosion time vs. mass for long-pulse aluminum on SATURN.

The yield-implosion time variation appears in Figure 4-7. The best long implosion yield was > 60 kJ using the more reliable gold bolometer diagnostic. In short pulse operation, the highest reported aluminum K-yield on SATURN is 88 kJ with sub-30 ns FWHM pulses (Reference 29). See Section 5 for a review of the differences between long and short pulse aluminum pinches.

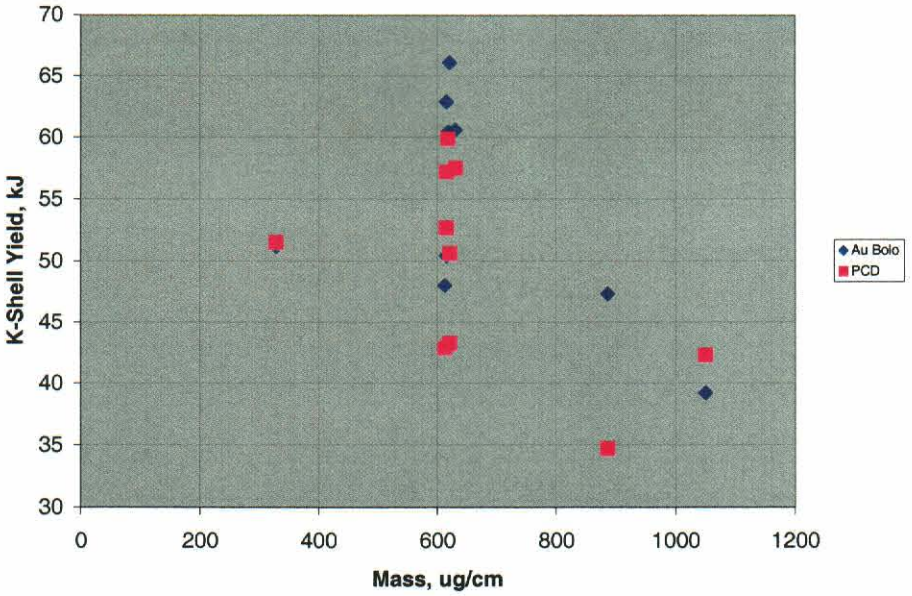

Figure 4-7. K-yield vs. mass for long-pulse aluminum on SATURN.

4.3 ALUMINUM PRS ON DOUBLE-EAGLE.

The emphasis of our investigation was to explore the effects of interwire spacing (i.e. wire number) at a given wire mass in long pulse operation, while demonstrating the efficacy of long pulse operation in the process. The procedure in this test series, therefore, was not to optimize the yield. The two wire masses selected were on either side of the nominal optimum mass as determined from our short pulse operation experience.

There were six load configurations tested (as shown in Table 4-1) that produced the two different load masses. All loads were 4 cm in diameter and 2 cm in length. The load hardware for Double-EAGLE (see Figure 4-8) was the same as used on DM2 with two modifications. First, the return cage diameter was increased to a 6-cm diameter to provide a more uniform magnetic field at the location of the wires. Second, the anode retainer was tapered to allow an unrestricted line of sight for the whole pinch length from the diagnostic lines, which are at a 68° angle from the pinch axis (eliminating the need to scale the observations for occlusion as at SATURN).

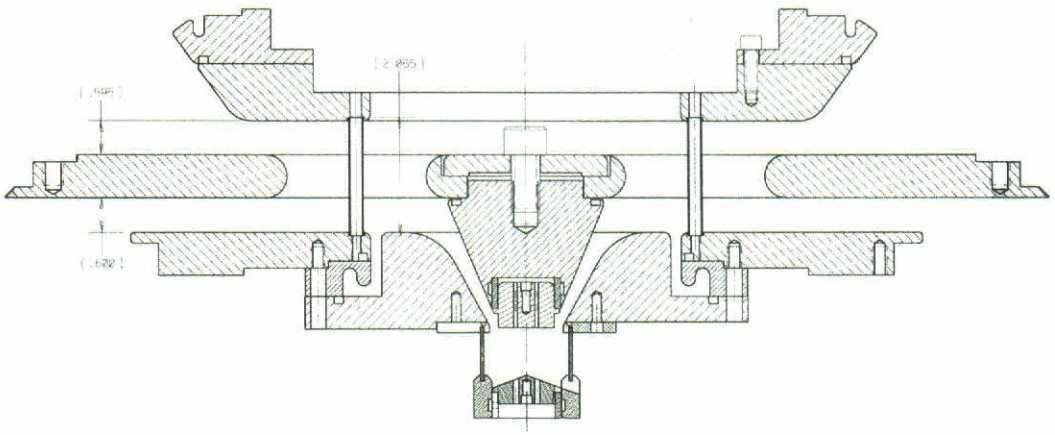

Figure 4-8. Wire load hardware for Double-EAGLE, shown here for the 25.5 mm array size (4-cm return cage) used for molybdenum experiments. Hardware for aluminum was similar with a 6-cm return cage.

Table 4-1. Aluminum wire configurations.

Number of Wires	Interwire Gap (mm)	Wire Diameter (mil)	Linear Mass Density (μg/cm)
30	4.2	0.7	201
23	5.5	0.8	201
50	2.5	0.7	335
38	3.3	0.8	333
30	4.2	0.9	332
24	5.2	1.0	328

Larger interwire gaps, i.e. fewer and heavier wires, produced sloppy implosions, as shown in Figure 4-9 for a 24 wire array of 1.0 mil wires, which radiated 12.9 kJ in a 38 ns FWHM pulse. Both the zipper array contour plot (Figure 4-9a) and the time-gated K-shell pinhole camera (Figure 4-9b), show substantial temporal and axial non-uniformities. Increasing the wire number, i.e. decreasing the interwire gap and the wire thickness, produces a much cleaner implosion (as shown in Figure 4-10) where the same yield (13.0 kJ) is radiated in a much narrower, 10 ns FWHM pulse.

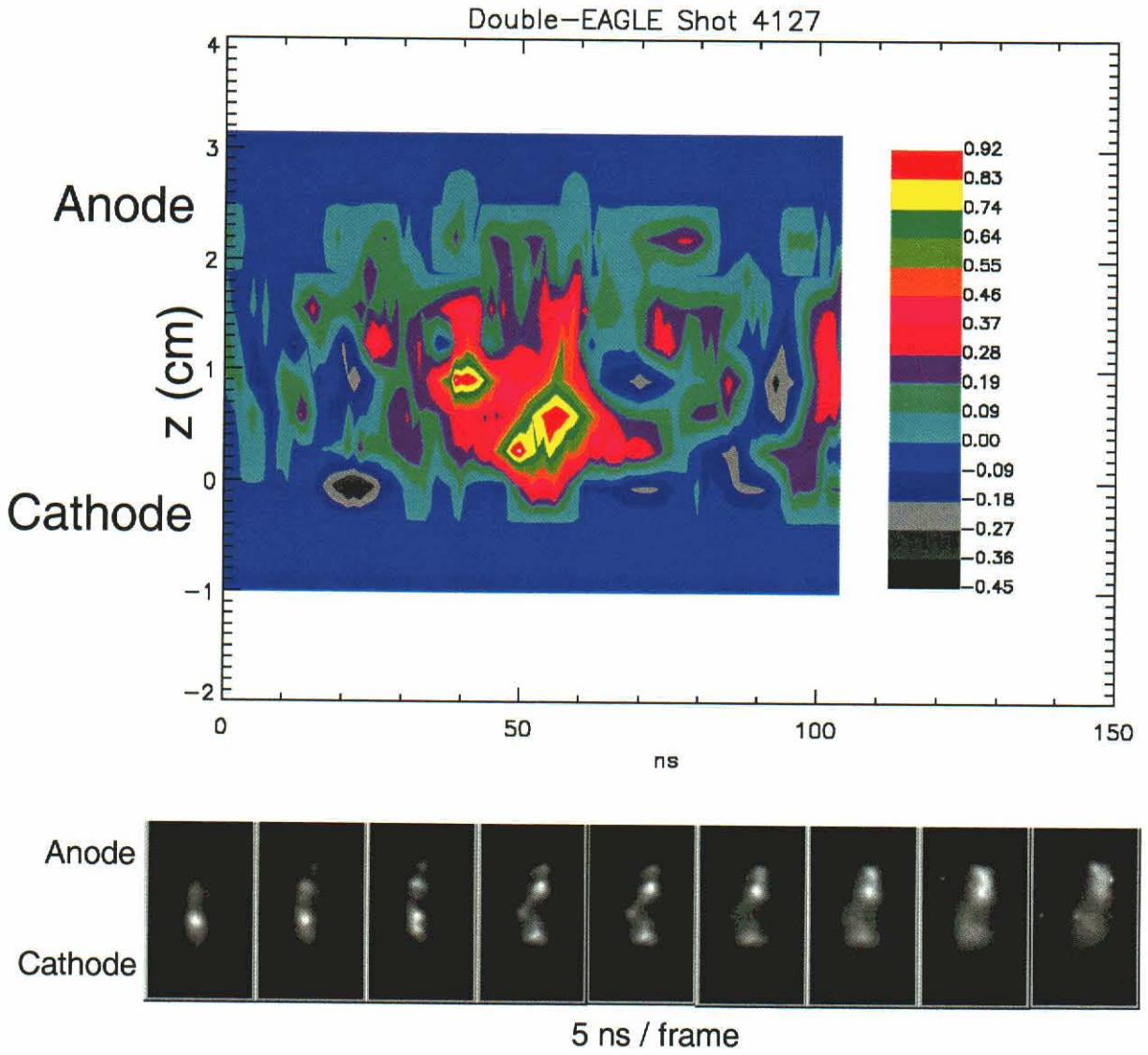

Figure 4-9. Zipper array contour plot and time-gated K-shell pinhole photograph for a low wire number shot.

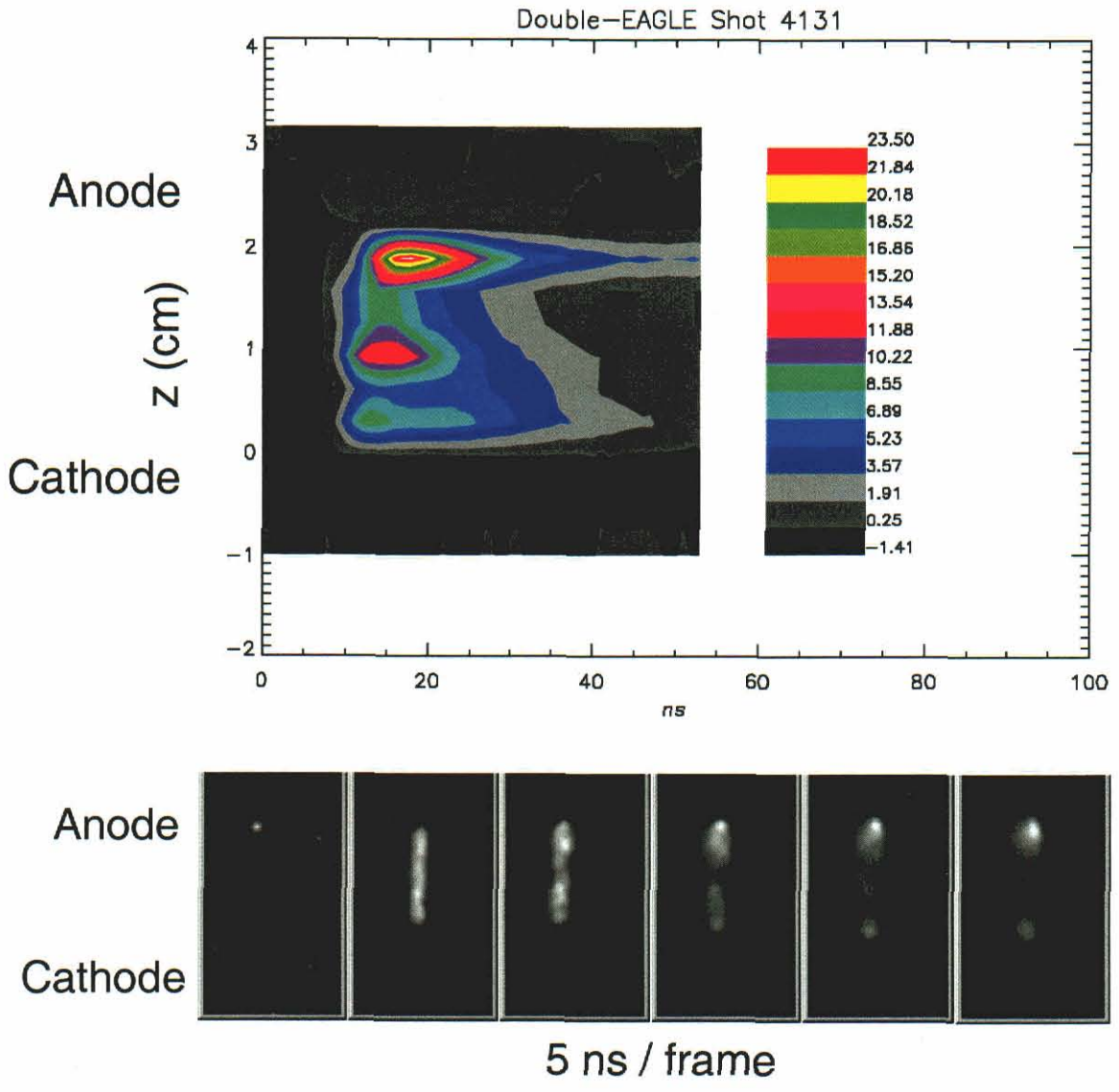

Figure 4-10. Zipper array contour plot and time-gated K-shell pinhole photograph for a high wire number shot.

As shown in Figures 4-11 to 4-16, below, the following trends occur with increasing wire(b) number at a given load mass: narrower, tighter, higher density pinches are produced at constant electron temperature and that radiate a constant amount of K-shell x-rays. These trends have been observed previously at short pulse (References 29 and 30). That they continue in long pulse is another indicator that new physics, e.g. higher levels of Rayleigh-Taylor instabilities, have not begun to interfere with the implosions.

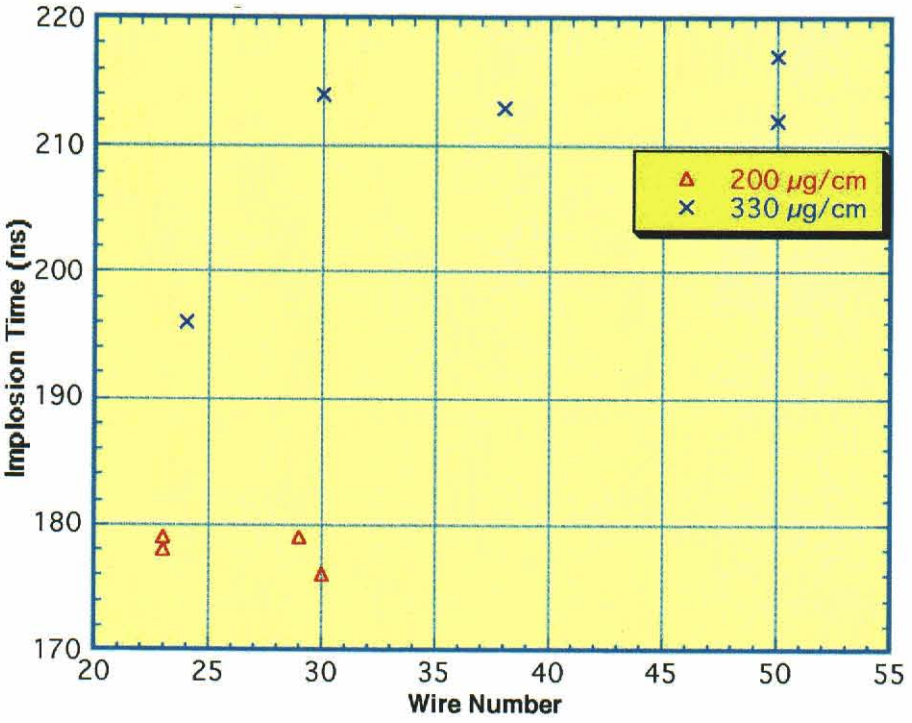

Figure 4-11. Data demonstrating that implosion time is almost invariant with wire number for a given wire mass.

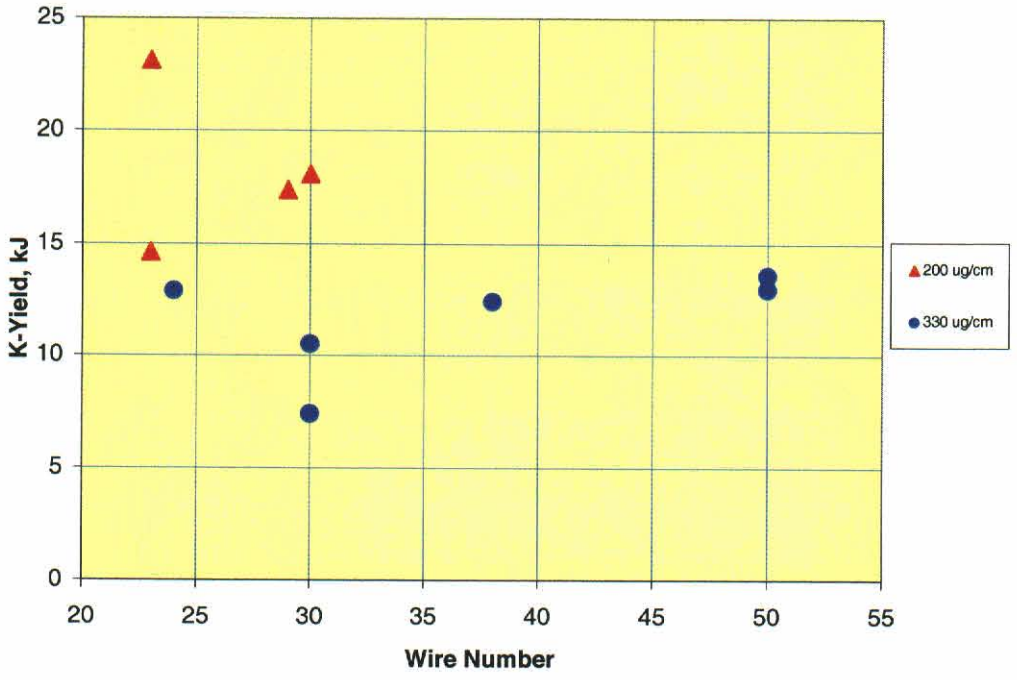

Figure 4-12. Data demonstrating that aluminum K-shell yield is insensitive to wire number for a given wire mass.

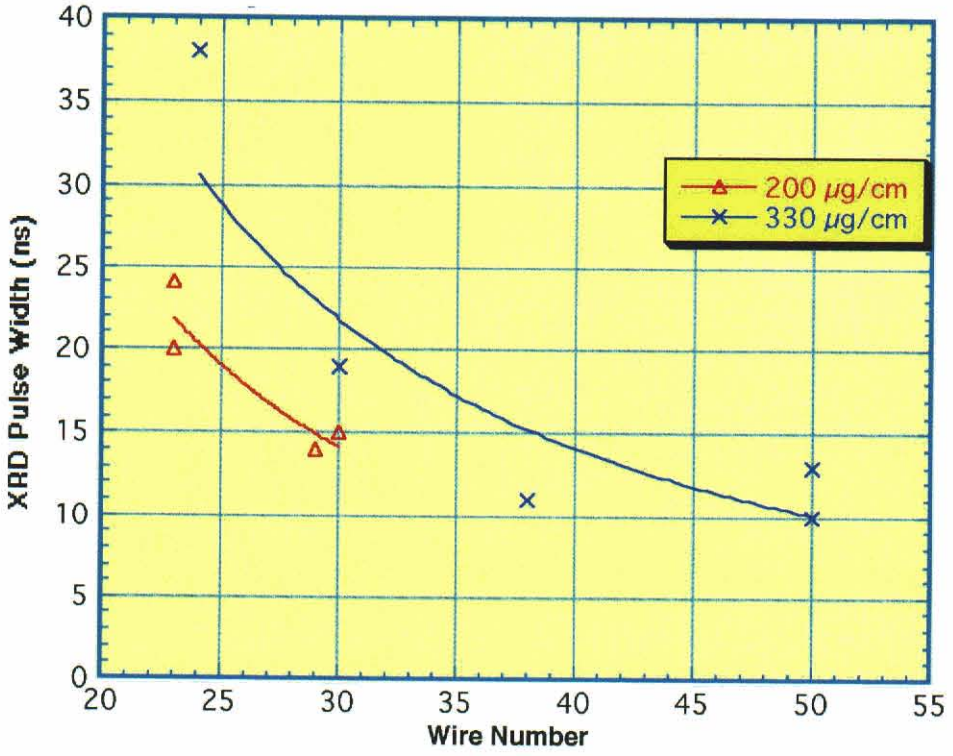

Figure 4-13. Data demonstrating that XRD pulse width (FWHM) decreases with increasing wire number for a given wire mass.

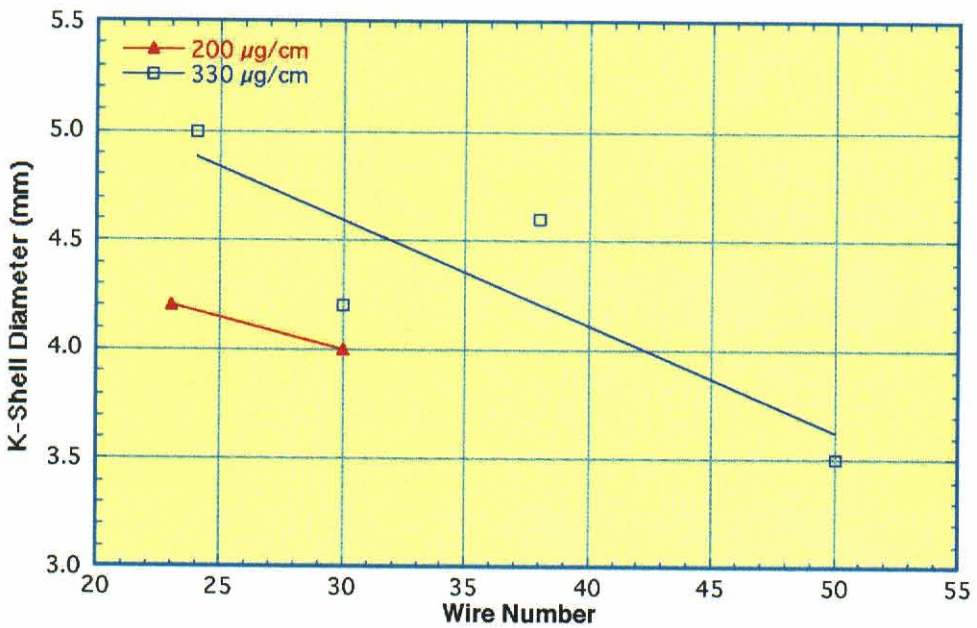

Figure 4-14. Data demonstrating that K-shell radiating diameter decreases with increasing wire number for a given wire mass.

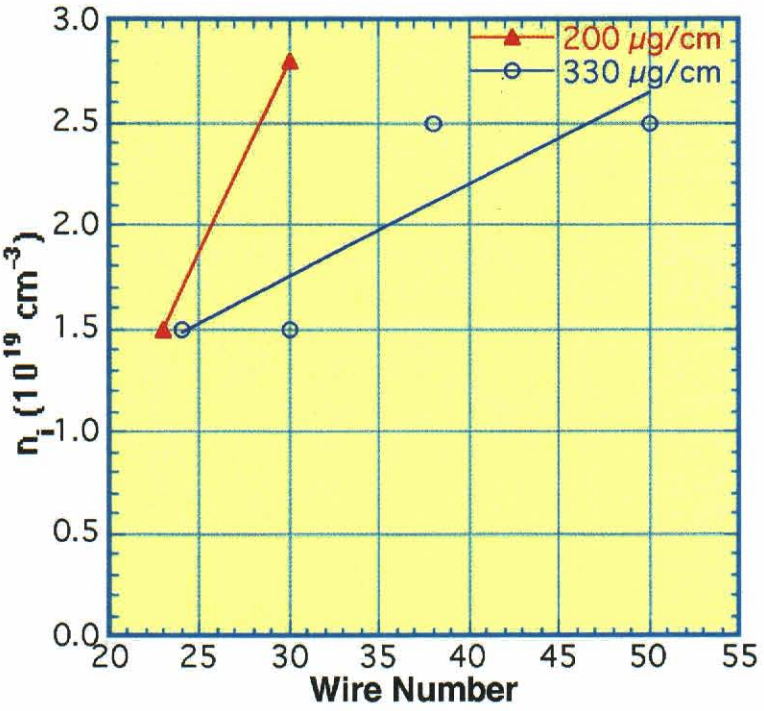

Figure 4-15. Data demonstrating that ion density within the radiating core increases with increasing wire number for a given wire mass.

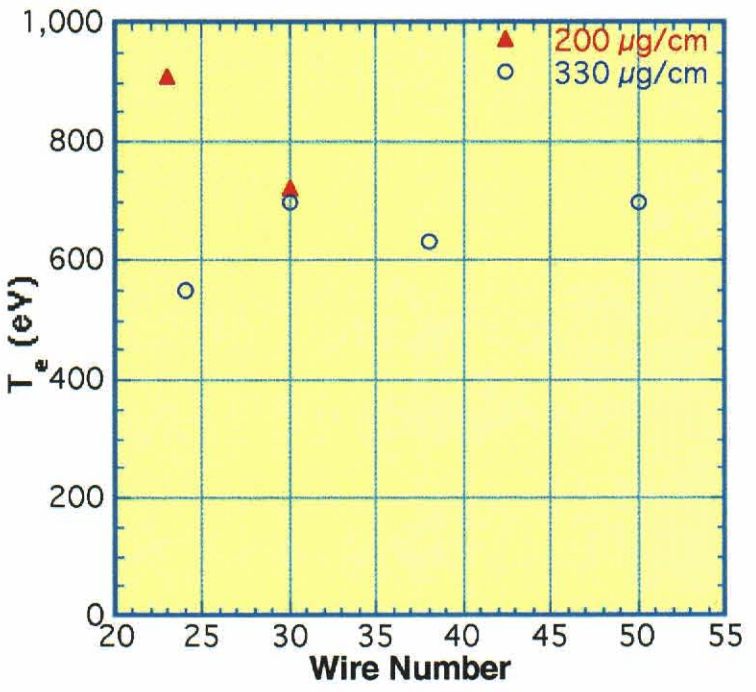

Figure 4-16. Data demonstrating that electron temperature is insensitive to wire number.

4.4 MOLYBDENUM PRS ON DOUBLE-EAGLE.

The production of radiation in the keV range has focussed mainly on K-shell radiators. This restricts the available sources, and therefore spectra, to a handful of choices. There are, however, a large number of potentially useful L-shell radiators in the keV range as well. Of these, we chose to investigate molybdenum due to the mechanical properties that it can be drawn into fine wires (0.3 mil diameter) strong enough to work with, so that arrays with many wires, *i.e.* good symmetry, can be constructed.

Our experimental configuration for this series of shots was a 2-cm length, either 2.55 or 4.0-cm diameter and short pulse operation. As shown in Figure 4-17, the molybdenum loads produced a clear implosion signature in the current trace after conducting up to 4.5 MA. The double spike XRD pulse was characteristic of lower mass loads; as the mass increased the first spike decreased in amplitude and merged into the second spike. The zipper array, shown in Figure 4-18, shows good axial uniformity and only slight zippering. A typical spectrum of the keV radiation is shown in Figure 4-19.

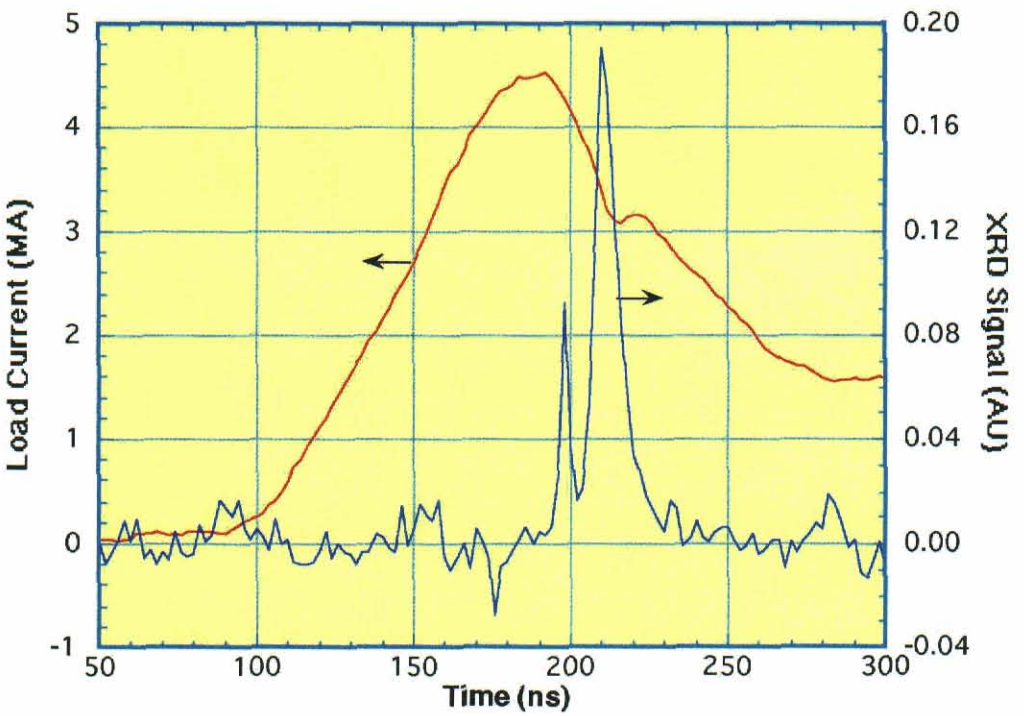

Figure 4-17. Current and XRD trace for a molybdenum wire shot.

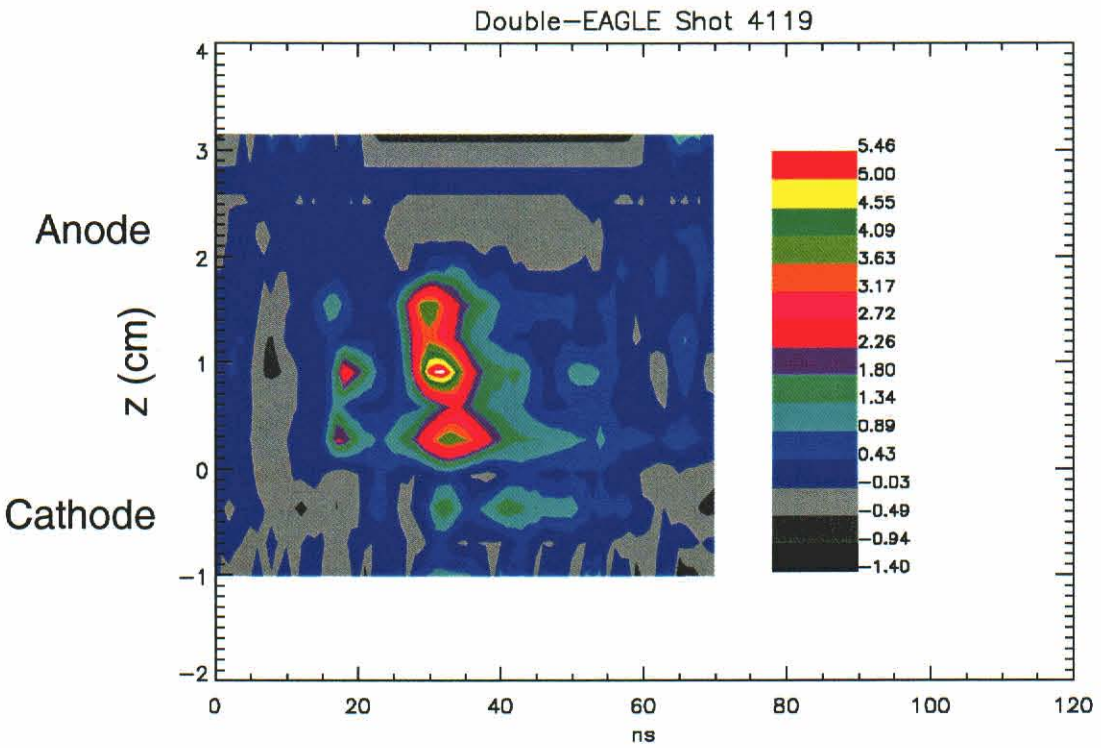

Figure 4-18. Zipper array contour plot for a molybdenum wire shot.

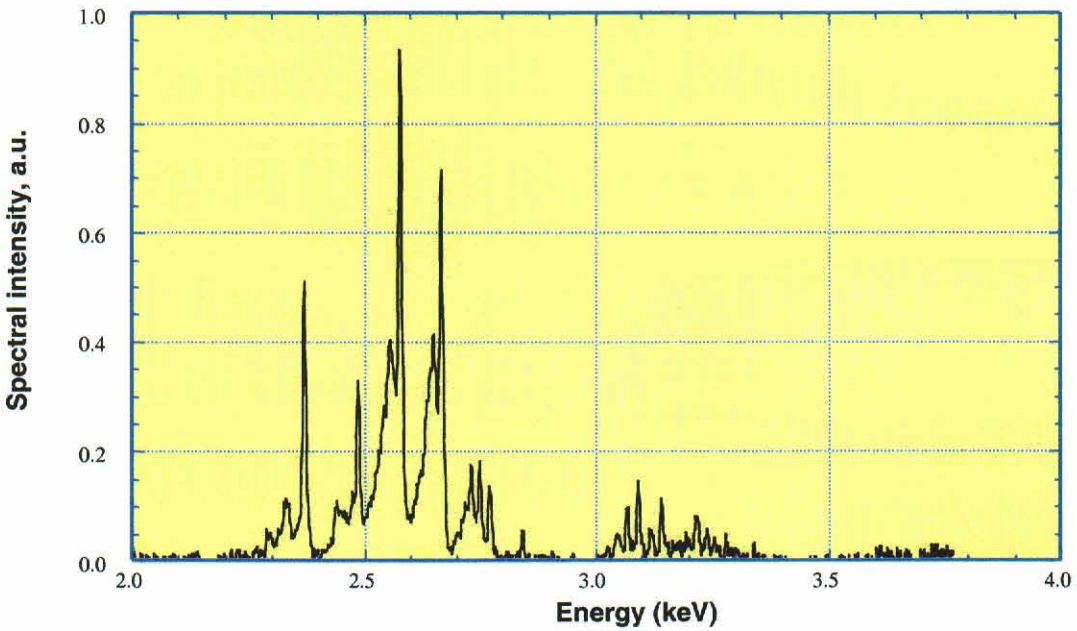

Figure 4-19. Spectrum of L-shell radiation from a molybdenum shot.

The yields, shown as a function of implosion time in Figure 4-20, were significantly reduced from a comparable K-shell radiator. Short-pulse Double-EAGLE typically produces 40 kJ of aluminum K-shell at 1.7 keV, and 20 kJ of argon K-shell at 3.1 keV.

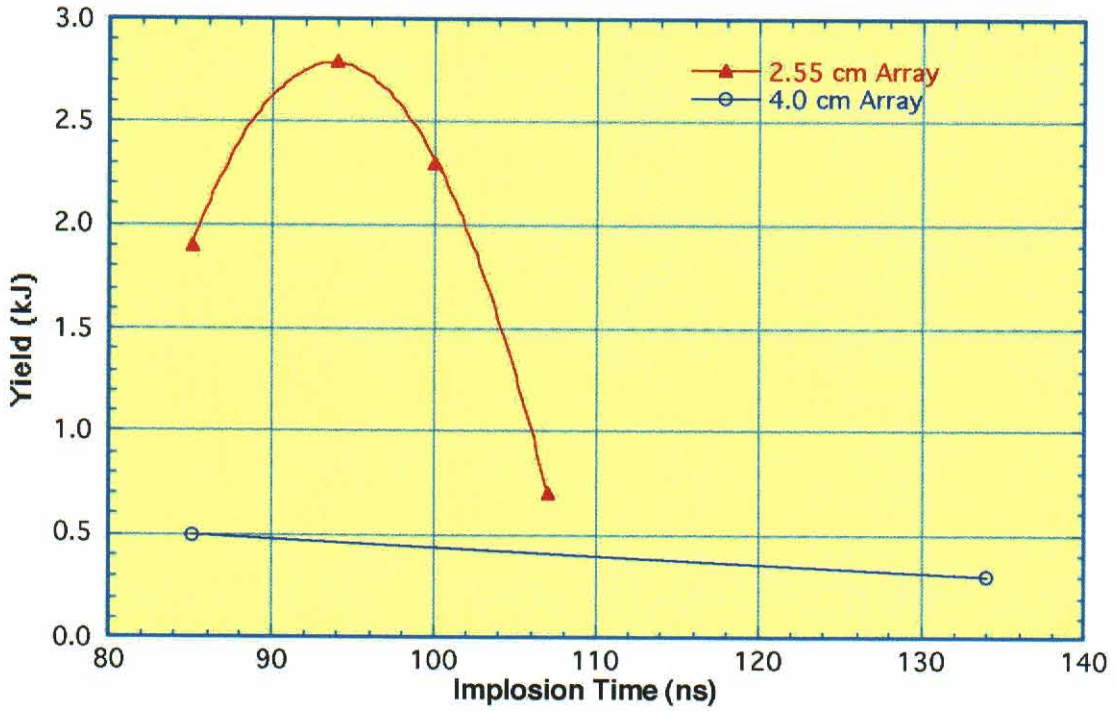

Figure 4-20. Yield as a function of implosion time for molybdenum wire arrays.

There are two effects contributing to the decreased yield. First, since the atomic weight of molybdenum is higher than a comparable K-shell radiator, there are fewer radiators at the same mass (which must be maintained to match to the pulse power driver). Second, the increased ionization necessary to strip the ion to the radiating shell (neon-like) drains too much of the available kinetic energy for the relatively small diameter of these arrays. These adverse energetics may be compensated for by a higher η implosion on a higher current driver.

SECTION 5

EMPIRICAL SUMMARY, ANALYSIS & SCALING TO DQ

5.1 EMPIRICAL REVIEW.

Earlier experiments on a number of different generators (SATURN, ACE 4, PITHON, DM2) have hinted that the x-ray yield from a PRS tends to decrease with longer implosion times. Adding the data from our experiments per Sections 2 and 3, Figure 5-1 indeed shows that the best yield per unit pinch length for "long" implosion times lies a factor of roughly 2 below the short-implosion scaling lines. The trend is, however, not exact. Note that at low currents on DM2 and GIT-12, 300 ns implosions seem to lie on the 200 ns trend line set by the ACE 4 and Double-EAGLE data. The SATURN data "long" pulse data actually refer to implosion times of 150 to 180 ns. And SATURN "short" pulse is actually 70 ns. (In view of the wide range of test beds and methods used at various laboratories, the correlation between their results as seen in Figure 5-1 is impressive. Each lab uses different types of yield and current sensors, calibrated in unique ways. Each lab analyzes their data in slightly different ways. And yield per centimeter is derived from the physical length of the anode-cathode gap, not the length of the pinch that actually lights up well.)

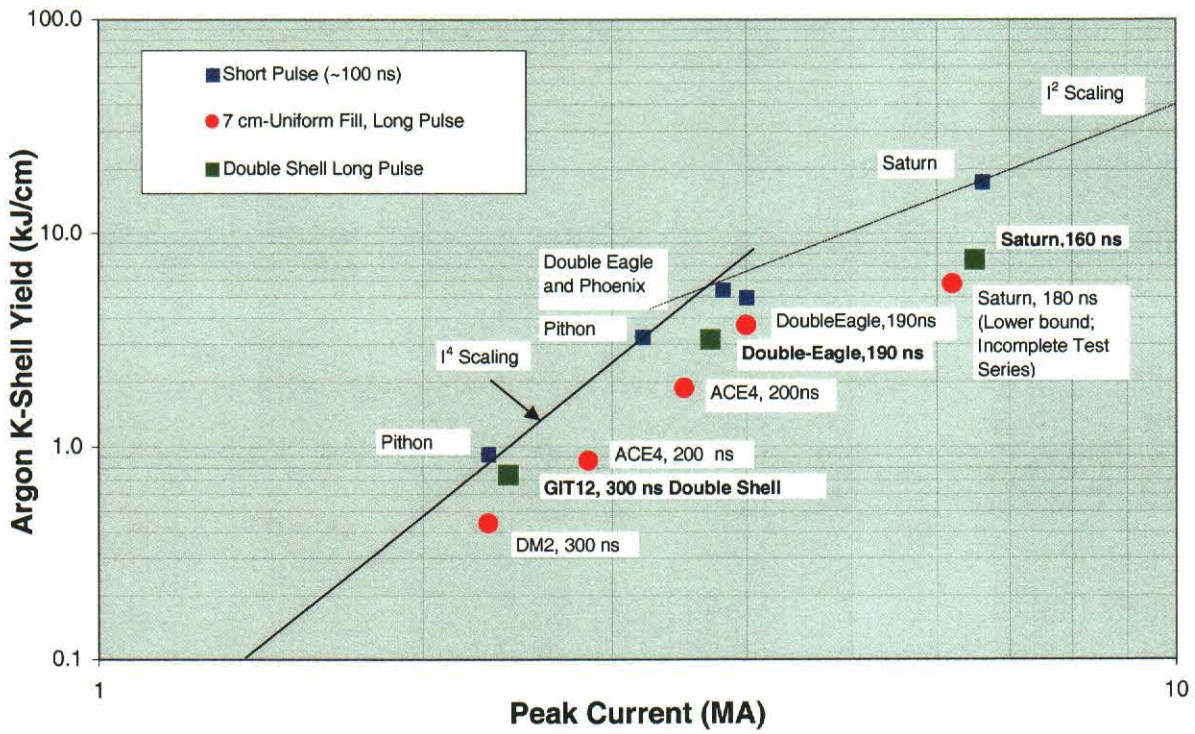

Figure 5-1. Argon K-shell yield scaling for short- and long-implosion PRSs.

This apparent implosion time "penalty" (Reference 31) can also be seen in the aluminum data as summarized in Figure 5-2. The surprising apparent linear relation between yield and current is due to two factors. First, the I^2 model assumes that each load is optimized for the generator it is used on, and that the implosion velocity (~ initial radius divided by implosion time) is held fixed. It is likely that neither SATURN (at 7 MA) nor Z (at 18 MA) has been so optimized. A plot of aluminum K-shell yield versus load mass (Figure 5-3) suggests that this is the case. Also, at the very high currents of Z, opacity effects (Reference 27) become very important for aluminum.

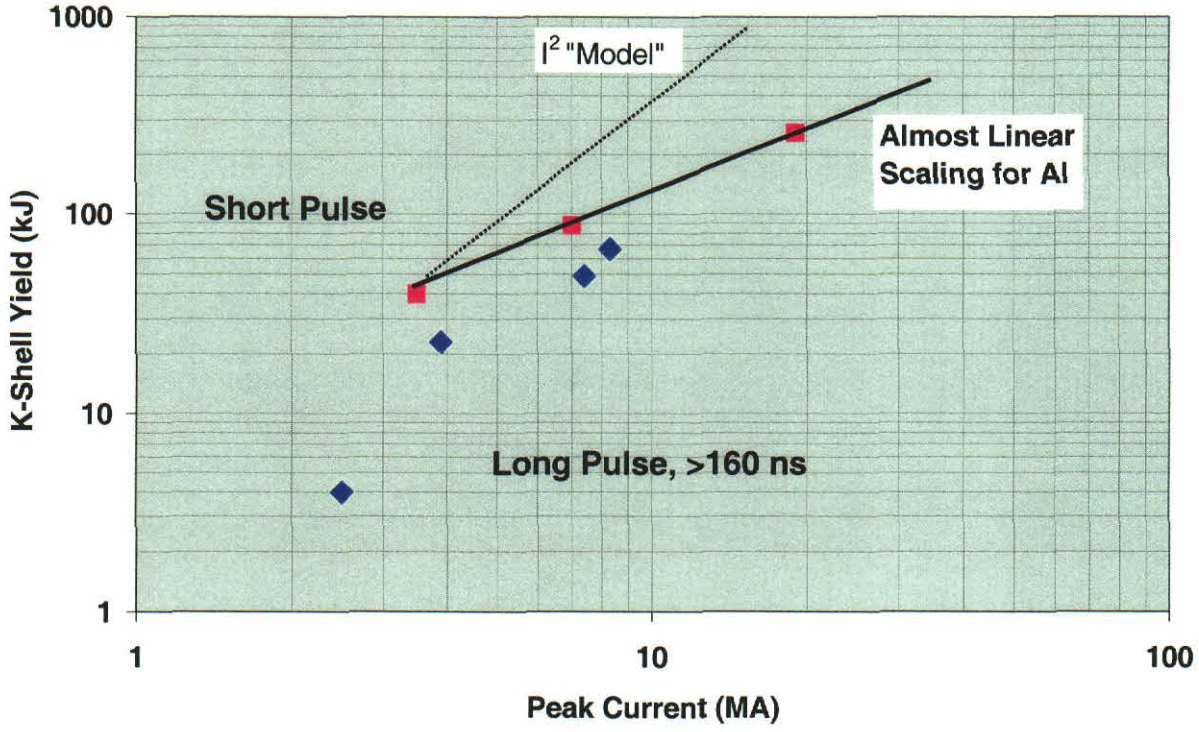

Figure 5-2. Aluminum yield scaling with current for short- and long-implosion PRSs.

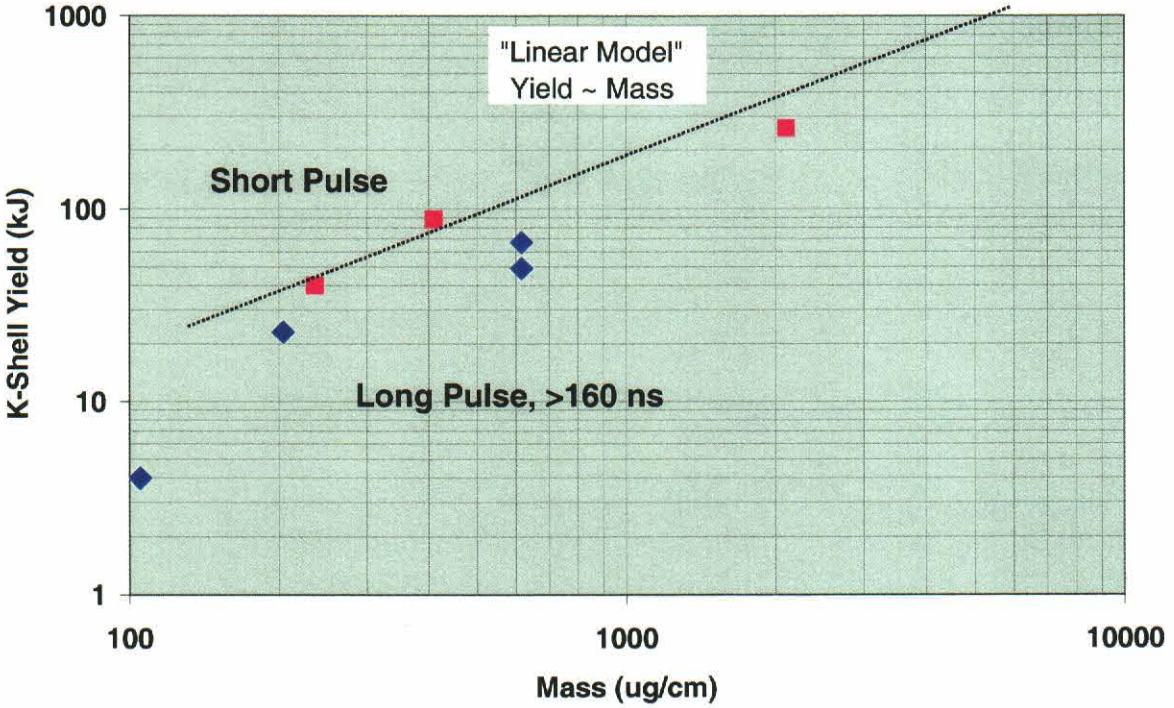

Figure 5-3. Aluminum yield scaling with load mass for short- and long-implosion PRSs.

This implosion time penalty evident in Figures 5-1 and 5-2 quantifies the challenge for the development of new z-pinch facilities. The lower cost of "slow" pulsed power like DQ must be balanced against the lower apparent yield of long implosion time PRS loads.

Finally, we note that pinch "quality" as measured by peak K-power (inverse of pulse width) is not so clearly compromised by long implosion time. Figure 5-4 shows that argon K-power is not simply correlated with implosion time. It is quite likely that details of the pinch geometry like the mounting diameter and number of return current posts affect pulse width as much as implosion time. Also, based on our experience (see Section 2 for example), modest levels of "zippering" have no effect on yield but they definitely increase pulse width and decrease peak power.

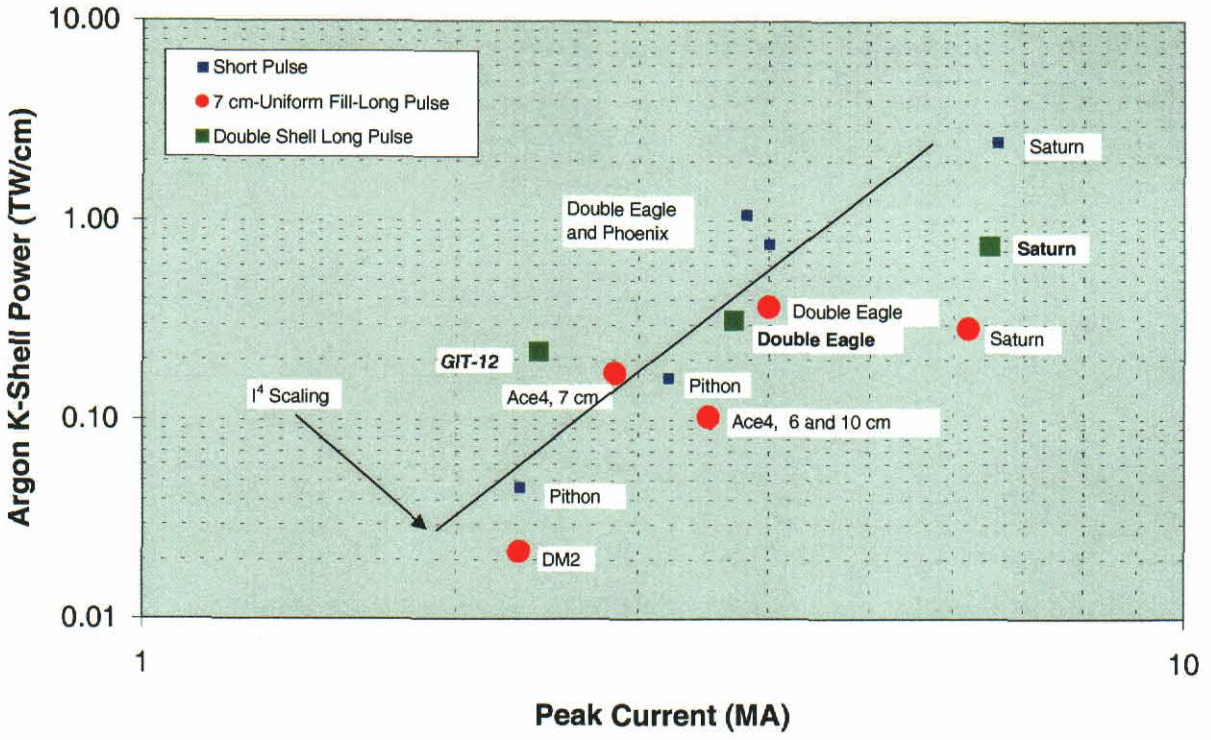

Figure 5-4. Argon K-power scaling with current for short- and long-implosion PRSs.

5.2 ANALYSIS.

Our experiments have also given us insights into the plasma conditions that underlie the decrease in yield with implosion time, so that future theory and experiment can be directed towards mitigating the physics that are presently limiting the x-ray output from long-implosion PRS.

As discussed in Section 2.3, the most significant difference in plasma conditions in the K-shell radiating core are the 2.5X decrease in density and 1.4X decrease in mass for long-implosion PRS compared to short implosion time tests. Within experimental error, the respective electron (and ion) temperatures show no significant difference. At constant temperature and neglecting opacity effects, the x-ray power then scales as the product of electron and ion densities with core plasma volume (V), or as the product of density and radiating mass:

$$P \propto n_e n_i V \propto n_e m_k$$

These factors account for most of the 4X reduction in power and 2X reduction in yield, allowing for the 2X increase in pulsewidth.

The decreased density of the long-implosion PRS is related to the requirement for higher compression ratio to achieve the same final radius as short-implosion PRSs, which have a smaller initial radius. Assuming that 2.5-cm "shell" and 7-cm solid-fill gas puffs have similar masses, then the 1.3X difference in final diameter accounts for most of the difference in density. It is illustrative to define the compression ratio as the ratio of the mass-weighted mean initial

diameter to the FWHM radiating diameter. The 7-cm solid-fill has mean initial and radiating diameters of ~ 40 mm and 2.1 mm, respectively, giving a compression ratio of 19. From the characterization of the 2.5-cm shell shown in Section 9, the initial mean diameter (defined per Section 1) at the 2-cm distance from the nozzle where it radiates best is 22 mm. Thus the 1.6-mm radiating diameter corresponds to a compression ratio of 14. We see that the long-implosion PRS has a higher compression ratio, but it needs to be higher still. Section 6 provides additional discussion of these points from a zero-dimensional perspective. Nevertheless, a higher dimensional treatment is needed to describe the physics of the radial temperature and density profiles that actually determine the radiating core.

The essence of the implosion time penalty then seems to be some limit on compression ratio or final pinch diameter. The origin of such a limit is not completely clear. One can imagine that the thickness of the imploding "sheath" may control the final pinch dimension. Perhaps sheath thickness does grow with time; see for example, Figure 8-8. But one would also expect that the radiation pulse width would also be correlated with the sheath thickness. The K-power data in Figure 5-4 show that pulse width is not uniquely controlled by implosion time.

The hydromagnetic Rayleigh-Taylor (RT) instability can broaden the sheath of an imploding z-pinch and thus limit the compression and density that can be achieved. A two-dimensional simulation of thick-shell and solid-fill gas puff PRSs with realistic density profiles shows that axial density gradients provide the initial perturbation (Reference 12). The RT instability grows only in the sheath between the magnetic piston and the shock front driven ahead of it, and mass accretion from the snowplow saturates the instability at small amplitude. Although exponential growth resumes in the shell when the snowplow reaches the inner surface, the RT modes continue to grow slowly (i.e., less than exponentially) for the solid fill. The saturated instability amplitude appears related to the sheath thickness, and thus to the final pinch density. Additional parameter studies need to be done to determine whether the longer implosion times and larger initial diameters lead to thicker sheaths and lower final density but not necessarily wider radiation pulses.

Time-resolved imaging diagnostics on the Double-EAGLE experiment indicate that two-dimensional effects are significant in both the short- and long-implosion PRS. Figure 5-5 shows a sequence of K-shell images for the short-implosion PRS and both shell and solid-fill long-implosion PRS; time increases to the right with a 5-ns interframe time. All the pinch images show significant two-dimensional effects (e.g., m= 0 "sausages"); the 5-cm shell also shows a kink mode near the cathode that may even be three-dimensional. These images suggest that the instabilities are not growing rapidly during the K-shell radiating phases and that they are probably saturated remnants of an imploding RT instability rather than a magnetohydrodynamic instability in the stagnated pinch. Additional measurements are needed to confirm this hypothesis, and to determine the dependence of the growth and broadening upon implosion time and initial diameter. This will require new visible and XUV imaging diagnostics with higher spatial and temporal resolution.

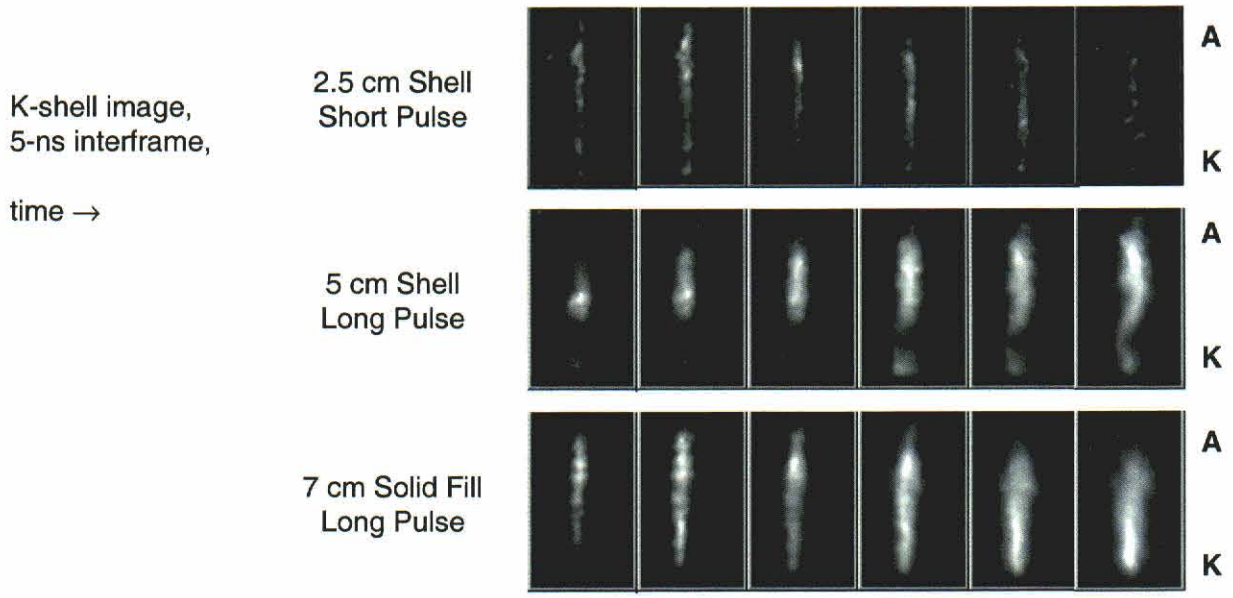

Figure 5-5. Time-gated x-ray images show evidence of 2-D and possibly 3-D effects.

It is also possible that one-dimensional physics, rather than the RT instability, is the cause of the reduced density observed in the long-implosion PRS. Shock heating and entrainment of the inner gas entering the sheath depends upon a characteristic collision length in the heated sheath, which in turn depends upon the density and temperature in the sheath. Larger-diameter annular and solid-fill gas puffs have lower initial density and longer collision length, and these differences may persist during the entire implosion. A combined theoretical and experimental effort is clearly needed to address the physics of sheath evolution.

5.3 SCALING TO DQ.

The most recent (January 2000) circuit model for the Decade Quad (using the planned water coupler) predicts that it should be capable of driving a peak current of 9.8 MA with 250-ns risetime into a very massive load; see Figure 5-6. For a 3-cm long, 7-cm ideal uniform-fill load with implosion times of 200 and 300 ns, the predicted peak currents are 6.3 and 8.6 MA respectively. The most conservative approach for estimating argon K-shell yields on DQ is to assume that an abrupt transition from I^4 to I^2 scaling occurs at the ~ 4-MA level. The Double-EAGLE yield at 4 MA is then extrapolated to DQ by using the circuit model to determine the peak currents on DQ that would produce the same implosion time (and η^*) as was achieved on Double-EAGLE, and then scaling the yields by the ratio of peak currents squared. On this basis, the Double-EAGLE result of 3.7 kJ/cm implies a DQ yield of 27 kJ for a 3-cm long pinch. Slightly more yield is predicted for longer pinches, but the higher inductance of the load might overstress the power feed. (The higher yield estimate given in Section 6 uses an earlier circuit model for DQ with significantly less generator inductance, hence higher current.)

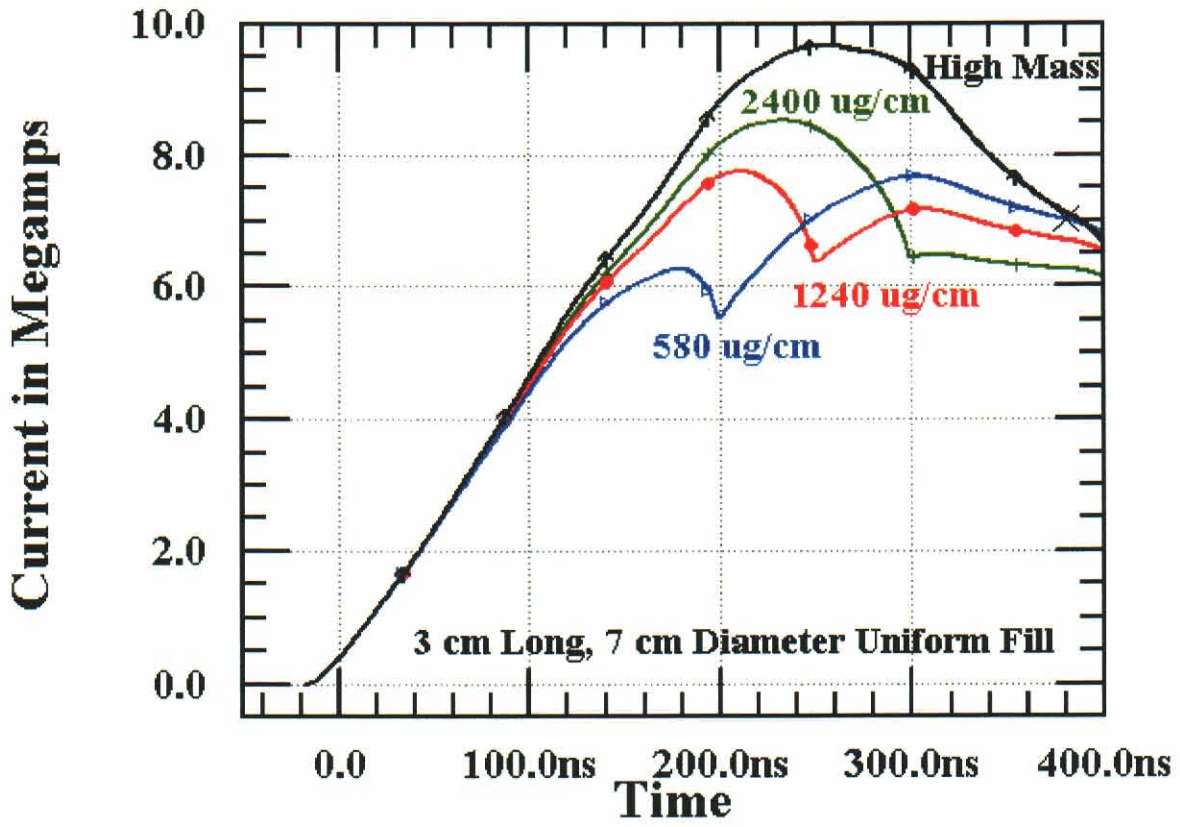

Figure 5-6. Decade Quad will deliver over 8 MA to a PRS load with 300-ns implosion time.

To take advantage of the full capability of DQ, i.e., > 8 MA at 300 ns, we will have to use a load that is optimized for longer implosion times than either the 7-cm uniform-fill or the 8-cm double shell. For example, the Mosher-Qi-Krishnan (Reference 14) and Whitney-Giuliani (Reference 28) models predict over 50 kJ for a 3-cm long, 10-cm diameter uniform-fill assuming a compression ratio of 15 as seen on Double-EAGLE. Our preliminary results with the 10-cm uniform-fill (Section 2.2.5) are quite encouraging that such large nozzles will work well.

SECTION 6

"ZERO"-DIMENSIONAL ANALYSIS FOR K-SHELL YIELD OF LONG-IMPLOSION PRS

6.1 INTRODUCTION.

The Mosher-Qi-Krishnan (MQK) model (Reference 14), while oversimplified, nevertheless captures the key physics of z-pinch implosions. In particular, it reproduces the main features (masses, implosion times, yields) of our experiments. Because of its explicit analytical form, it is easy to employ the model to elucidate radiation yield trends with current in the range of 2 to 10 MA and implosion times between 100 and 300 ns. In particular we use it to project the expected yield for Decade Quad (DQ).

The MQK model assumes thin K-shell radiation from a two-level atomic model. All of the mass in the final pinch of radius r_f is considered to be at a single temperature and density and to radiate for a time of the order of r_f/v_{th}, where v_{th} is the ion thermal speed in the pinch plasma. Electrons and ions are assumed to be at the same temperature. MQK also sets an energy balance in which the radiated yield plus the internal energy equals one-half of the kinetic energy imparted to the plasma in the implosion. The model treats the other half of the available energy as lost by various mechanisms not contained in the simplified description, e.g., M- and L-shell losses.

The MQK paper introduces constraints satisfied in the implosion dynamics between kinetic energy per unit length, K (J/cm), the peak current, I_0 (A), the implosion time τ (sec), the mass of the pinch per unit length, μ (g/cm), and the initial and final implosion radii r_0 (cm) and r_f (cm). They make the point that those constraints can be used for the ideal constant $\dot{I}$ (time derivative of current) case. By changing numerical values of some coefficients representing "current shape factors," the model can also be used for actual pulsed power generators, such as the typical water line kind. They treat thin shells in the slug approximation.

In Section 6.2 we use MQK to show the dependence of optimum yield as a function of implosion time and peak current for two very distinct cases: first for the case of constant Effective Compression Ratio (ECR) $v \equiv r_0/r_f$, and then for the case of constant final radius r_f. To establish trends in a clear way, we find the optima for the case of an ideal pulsed power generator delivering constant $\dot{I}$ for the implosion time τ.

Because in our experimental PRS program we have employed shells and uniform fills, we calculate optimal yields for both kinds of loads. To do that we derive K and τ formulas for uniform fills along the lines of what MQK derived for infinitely thin shells.

In Section 6.3 we discuss the application of the MQK model to circuit calculations for Double-EAGLE (DE) short- and long-implosion modes, and SATURN in the long implosion mode. We then project to DQ by taking the experimental DE long implosion results for the 7-cm uniform-

fill nozzle, fit the ECR to those results, and assume the same ECR to calculate the expected yield for DQ.

In Section 6.4 we discuss our conclusions.

6.2 YIELD OPTIMIZATION.

6.2.1 Expressions For The Kinetic Energy Per Unit Length And The Implosion Time.

First we discuss yield optimization for the case of an ideal constant $\dot{I}$ generator. The implosion equations of motion for the two types of load relevant to our experiment are:

$$(d^2/dx^2)y = -x^2/y \tag{6.1}$$

$$(d/dx)(1-y^2)dy/dx = -x^2/y \tag{6.2}$$

Equations 6.1 and 6.2 are for the slug and uniform fill cases, respectively. The slug is an infinitely thin shell of mass per unit length μ, and the uniform fill has a constant density ρ for $r_0>r>0$ and total mass per unit length $\mu=\pi r_0^2\rho$.

The variables x and y are the scaled time and radius; i.e.,

$$x=t/t_0, \text{ where } t_0= (100\mu)^{1/4}r_0^{1/2}/\dot{I}^{1/2} \tag{6.3}$$

$$y =r/r_0 \ . \tag{6.4}$$

From these equations we can obtain the kinetic energy per unit length and the implosion time τ as a function of the physical parameters $\dot{I}$, μ and r_0. We do this by numerical integration to any given final condition $y=1/v$. (Initial conditions are $y=1$ and $dy/dx=0$ for $x=0$, respectively).

The expression for τ follows immediately from Equation 6.3 and can be cast in the form;

$$\tau=\delta\mu^{1/2}r_0/I_0 \ . \tag{6.5}$$

For K we follow MQK in using the following approximation

$$K=\gamma I_0^2 \ln v \ . \tag{6.6}$$

In the preceding equations I_0 is simply $\tau\dot{I}$.

The numerical values for γ and δ for both types of loads are shown in Table 6-1. Those were calculated for $v=10$, and would vary by a few percent if we had taken another value of v. The selected values have indeed enough accuracy for our trend analysis approach.

Table 6-1. Value of coefficients vs. load type.

Load Type	δ	γ
Thin Shell	29	8.3e-10
Uniform Fill	20.9	6.7e-10

We remark that treating the uniform fills by just changing the values of γ and δ with respect to the thin shells puts both types of load on a same footing for the analysis.

6.2.2 Yield Optimization For Fixed ECR.

The yield and energy balance equations given by MQK are

$$Y= \alpha N^2 \exp(-T_0/T)/(r_f T) \quad \text{, where } \alpha=2.7\text{x}10^{-31}Z, \text{ and } T_0=10.2Z^2 \tag{6.7}$$

$$K/2= \beta NT+ Y \quad \text{, where } \beta=4.7\text{x}10^{-19}Z^{0.82} \quad . \tag{6.8}$$

In Equations 6.7 and 6.8, Y(J/cm) is the K-shell radiation yield per unit length. Equation 6.7 is the expression for Y in the two level thin radiation approximation, as given by MQK. Z is the atomic number, N is the ion number density per unit length; $N= \mu/m_{ion}$, where $m_{ion}(g)$ is the ion mass, and T(eV) is the PRS temperature. Equation 6.8 is MQK assumption on energy balance.

Using Equations 6.5 through 6.8 we can find (within each of the two types of loads we are considering) the load giving the optimal yields in two distinct cases. In the first case we seek the best possible yield for given $\dot{I}$ and τ, assuming fixed ν. In the second we consider instead that r_f is fixed. Finding the load which optimizes yield per unit length for an ideal generator characterized by $\dot{I}$ and τ, and the choice on the final implosion condition, means finding the values of initial radius and mass loading for that load. All other physical parameters at that point are also obtained, such as temperature, η (as commonly defined in this field), etc.

Using $\dot{I}$ and τ is a way of capturing the capability of a given generator of producing peak current I_0 and rise time τ. In that sense this idealization allows us to talk about all possible generators by varying those two parameters. We will see in the next section that this is a reasonable way to scope the problem. For studying actual pulsed power generators we employ circuit calculations, thus taking into account the actual I(t) resulting from the self-consistent interaction between generator and PRS load.

On the other hand, fixing either the ECR or the final radius is a much more radical assumption. Such assumptions ignore the known complexity of the z-pinch dynamics. In this sense assumptions of this kind can only be justified a-posteriori and judged by their utility; they are heuristic in nature.

We consider first fixed ECR. We have four relationships, Equations 6.5 through 6.8, between 8 quantities: Y, K, T, μ, r_0, r_f, τ, and I_0. For given (I_0, τ, ν) only one free variable remains; we can chose it to be T and, by algebraic manipulation of Equations 6.4 through 6.8, express Y as a function of only T and the fixed quantities (I_0, τ, ν):

$$Y = \alpha\, m_{ion}^{1/2}((\gamma I_0{}^2 \ln\nu - 2Y)/(2\beta))^{5/2}(\delta\nu/\tau I_0)\exp(-T_0/T)/T^{7/2} \quad . \tag{6.9}$$

Equation 6.9 is implicit with respect to Y. However it is straightforward to differentiate Y with respect to T, at constant (I_0, τ, ν) and obtain the value T^* that makes $(\partial Y/\partial T)=0$, thus maximizing Y, we find:

$$T^*=(2/7)T_0 \quad . \tag{6.10}$$

The optimal yield is easily found by using $T= T^*$ in Equation 6.9 and numerically solving the algebraic equation for Y^*. All other optimum quantities of interest, K^*, μ^*, $r_0{}^*$, and $r_f{}^*$, are easily obtainable as well. K^* is given by Equation 6.6 and is known directly even before optimization because it is just a function of I_0 and ν. The quantity μ^* is obtained by substituting the values of Y^* and T^* in Equation 6.8. Finally $r_0{}^*$ is obtained by substitution of μ^* in Equation 6.5, and $r_f{}^*$ follows from $r_f{}^* = r_0{}^*/\nu$.

It is interesting to notice that T^* is only a function of Z. In particular for Ar, at Z=18 we find T^*=944eV. A similar, yet different result was obtained by MQK by a different choice of quantities kept fixed, they obtain in their case $T^*=T_0/3$.

As a relevant example we plot in Figure 6-1 this optimal yield as a function of I_0 for different τs, both for the uniform fill and the thin shell cases, using ν=10. We remark that at a given ν and τ the transition from the inefficient I^4 scaling regime to the efficient one scaling as I^2, is smoothly contained in the optimal solution and can be seen in Figure 6-1 as a change in curvature in the log-log plot occurs as current increases. This transition is a consequence of Y being an increasingly larger fraction of K in the energy balance as the current goes up, for fixed ν and τ. This remark was already made in the MQK paper.

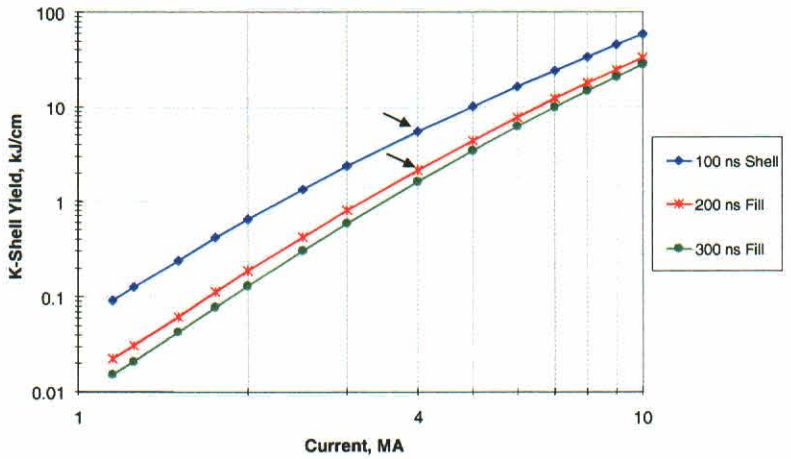

Figure 6-1. Optimized yield/cm vs. current for constant İ; ECR = 10.

6.2.3 Optimization For Fixed r_f.

Now we repeat the procedure of the last subsection, but keeping the set (I_0, τ, r_f) constant. The resulting algebraic problem is more involved, and we have chosen to introduce Lagrange multipliers to find the optimum yield.

We introduce the Lagrangian:

$$\mathcal{L} = Y(N,T,r_f) + \lambda_1(K/2 - \beta NT + Y) + \lambda_2(\tau - \delta\mu^{1/2} r_0/I_0) + \lambda_3(K - \gamma I_0^2 \ln\nu) \quad . \tag{6.11}$$

In Equation (6.11) the Lagrangian is a function of N, T, K, r_0, λ_1, λ_2, and λ_3 [if we keep (I_0, τ, r_f) constant]. The function Y(N, T, r_f) is Equation 6.7. Thus, its optimum, given the constraints of Equations 6.5, 6.6, and 6.8, is obtained by solving the seven simultaneous algebraic equations $\partial\mathcal{L}/\partial z_i = 0$, where the z_is symbolize the variables N, T, K, r_0, λ_1, λ_2, and λ_3. These partial derivatives are all taken at constant (I_0, τ, r_f).

We will spare in this report the details of the algebraic derivation; suffice it to say that one arrives at a set of two algebraic coupled equations, namely:

$$V^2 e^{-1/U}/U - a \ln\nu_0/V^{1/2} + bUV = 0 \quad , \tag{6.12a}$$

$$V = U^{-1}(1-U)/(3U-1) \quad , \tag{6.12b}$$

where $a \equiv 8\beta^2 r_f T_0^3/(\alpha\gamma I_0^2)$

$b \equiv 4\beta^3 r_f T_0^3/(\alpha\gamma I_0^2)$.

Simultaneous solution of Equations (6.12a) and (6.12b) gives the values (U^*, V^*) that optimize yield at constant (I_0,τ,r_f):

$$T^* = U^* T_0 \tag{6.13a}$$

$$Y^* = Y_0(V^{*2} e^{-1/U^*}/U^*) \tag{6.13b}$$

$$N^* = N_0 V^* \tag{6.13c}$$

$$K^* = 2(\beta N^* T + Y^*) \tag{6.13d}$$

$$r_0^* = \nu_0 r_f / V^{*1/2} \quad . \tag{6.13e}$$

where

$N_0 \equiv (\gamma I_0^2)/(4\beta T_0)$

$Y_0 \equiv (\alpha N_0^2)/(r_f T_0)$

$\nu_0 \equiv (I_0\tau)/(\delta N_0^{1/2} r_f)$,

and T_0 has already been defined in Equation 6.7.

We plot in Figure 6-2 this optimal yield as a function of I_0 for different τs, both for the uniform fill and the thin shell cases, using r_f=0.2 cm. As before, we remark that at a given r_f and τ the transition from the inefficient I^4 scaling regime to the efficient one scaling as I^2, is smoothly contained in the optimal solution. This can be seen in Figure 6-2 as a change in curvature occurs in the log-log plot as current increases.

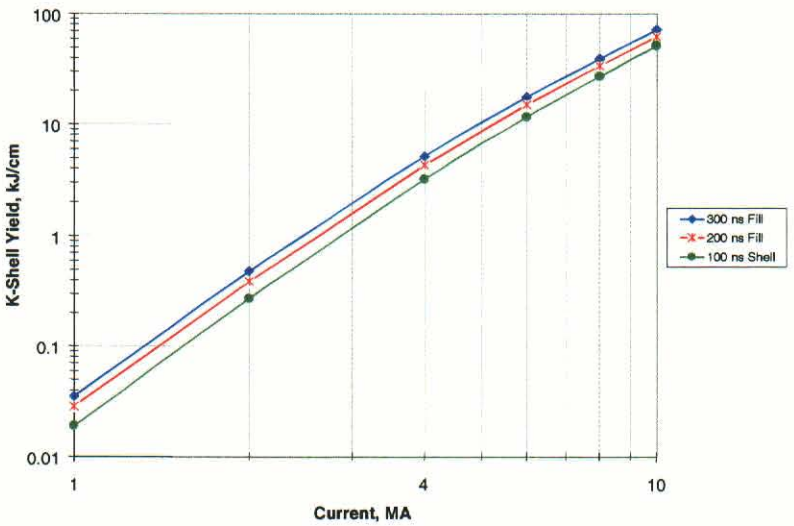

Figure 6-2. Optimized yield/cm vs. current for constant $\dot{I}$, final radius r_f = 0.2 cm.

By comparing Figure 6-1 with Figure 6-2 we also see that there is a profound difference in the way Y^* depends on peak current whether we fix ν or r_f. In fact the trends reverse; for fixed ν longer implosion time gives lower yield, while the opposite is true when r_f is assumed to be fixed. Also the uniform fill and thin shells become almost identical in performance for given (I_0, τ, r_f). This is not the case for constant ν, where the thin shell yield is larger than the uniform fill, at given (I_0, τ, ν). The largest ratio of thin shell to uniform fill yield at given (I_0, τ, ν) occurs in the I^4 regime, where the ratio is about a factor of 2.

In this 0-D model there is no way to discern which one of these two critical assumptions is better as a representation of experimental results. However, the evidence from our experiments is that fixed ν is most likely. And we must keep in mind that the value of ν, even if approximately fixed for given conditions in the experiment, may indeed change as we change experimental conditions; we do not have any way to predict it from fundamental physics at this point.

We must also keep in mind that saying, for instance as in the previous paragraph, that the thin shell does better than the uniform fill, is only meaningful within the assumption that when imploded they would attain the same ECR. In fact we have seen in our experiments that, perhaps due to the more stable behavior of uniform fills than thin shells with respect to the Raleigh-Taylor instability, that the opposite is true. A way to express this in the context of 0-D models is to say that the ECR is not attainable in that case. This makes the 0-D non-predictive in nature, unless other empirical and theoretical arguments are employed.

6.3 CIRCUIT CALCULATIONS FOR DE, SATURN, AND DQ.

We performed circuit calculations for DE, both in the short- and long-pulse mode, SATURN in the long-pulse, and DQ. We used simple circuits, rather than attempting to use more detailed models; for the purpose of assessing PRS performance trends they are certainly adequate. The circuits employed are shown in Figures 6-3 through 6-10, along with the driving V_{oc} and typical I(t) for relevant cases. The x-ray yield was calculated using the MQK model, but the circuit code also includes the Thornhill-Whitney-Guiliani model (Reference 28).

In the calculations, the generator and power delivery circuit drive the PRS load, either an infinitely thin shell or uniform fill. The implosion equation of motion is integrated in time, and the time dependent load inductance is fed back to the circuit solver. When using a circuit, Equations 6.5 and 6.6 are, naturally, no longer needed. The initial radius and mass loading are input parameters, while solving for the pinch motion gives at final time the necessary information to obtain all relevant quantities. Equations 6.7 and 6.8 are used to calculate yield.

A conceptual clarification of what constitutes optimization of K-shell radiation yield employing a 0-D model is in order here. In using a circuit code one parallels the experimental procedure. A load idealized in the calculation as thin shell or uniform fill, of given gas type and mass, initial radius, axial length and cage inductance is assumed, and the calculation is stopped, as explained in the previous paragraph, when the prescribed final radius is achieved. Three different procedures can thus be distinguished:

1. For a given experimental shot we adjust the mass and the final radius to get agreement with the experimental current trace and the observed yield. We call this "fitting a shot."

2. For a given load (nozzle) we do a suite of circuit calculations varying the mass and the pinch length to obtain the best possible yield at either fixed final radius or ECR for the generator in question. We call this "optimizing yield for a given load."

3. For a given generator we start with a type of load and do a suite of circuit calculations varying the initial radius (this is parallel to changing the nozzle in the machine). For each value of initial radius and pinch length we proceed exactly as in point 2 above. We then find the optimum of those optima by finding the values of initial radius and pinch length giving the highest Y. We call this "global optimization." This global optimization is the 0-D prediction for the absolute best yield that a machine can produce for a given Marx voltage, at the assumed ECR or final radius and load type.

The distinctions introduced in the previous paragraph are germane to how we conducted the analysis. In fact, for DE in the short-pulse mode, we found the value of ECR required to make the optimal yield for a thin shell of 2.5 initial diameter and 3.8 cm pinch length fit the best result obtained in the experimental campaign for that load.

We do the same for DE in the long-pulse mode with a 7-cm diameter uniform-fill with a 3.8-cm pinch length.

In reviewing these results, the reader should remember that the models used here use only idealized shells or uniform fills. As the data presented in Section 9 make clear, actual nozzles have mass distributions that are neither thin shell nor uniform fill.

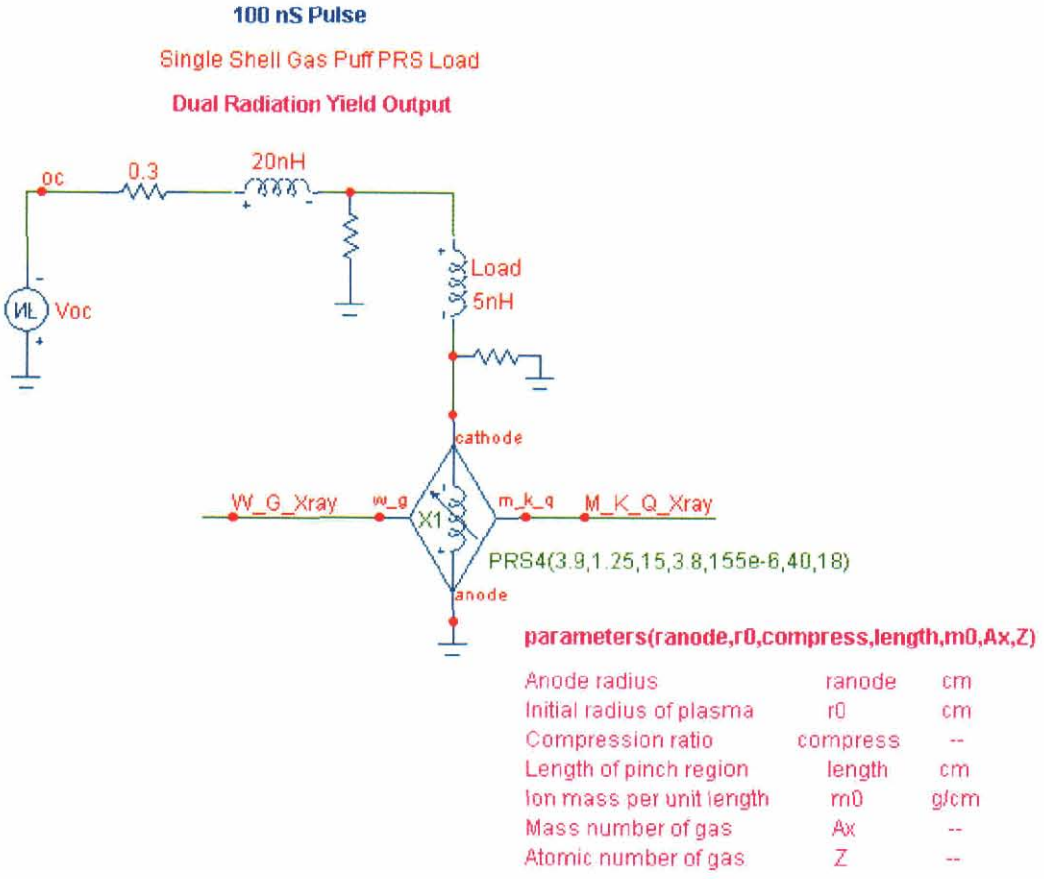

Figure 6-3. Circuit used for DE short pulse; PRS4 is a circuit element representing a thin shell with the displayed parameters.

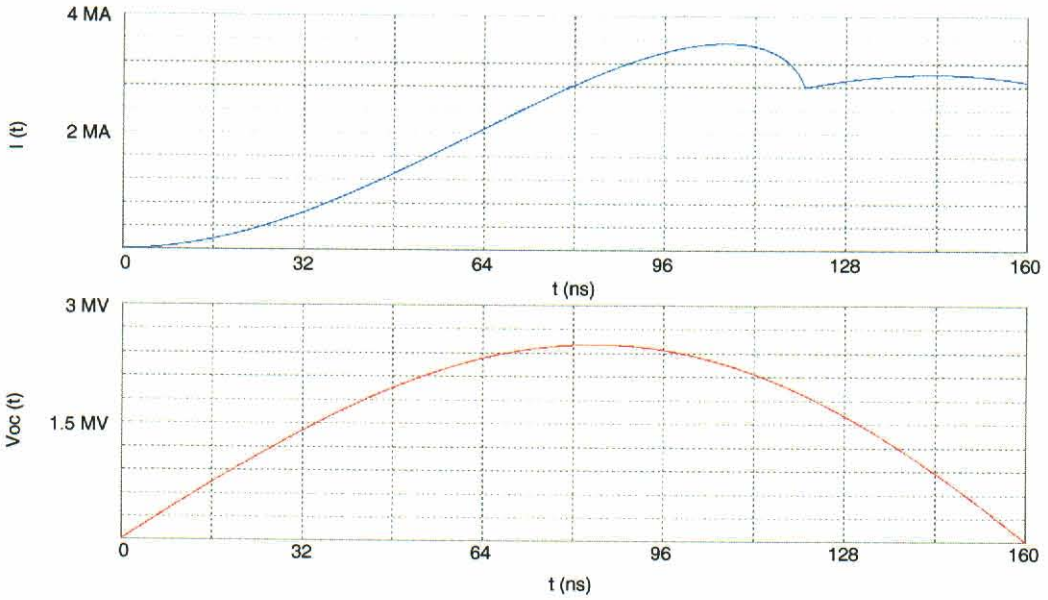

Figure 6-4. Current obtained in run of circuit of Figure 6-3. Voc(t) is the driving open circuit voltage corresponding to 60 kV Marx charge.

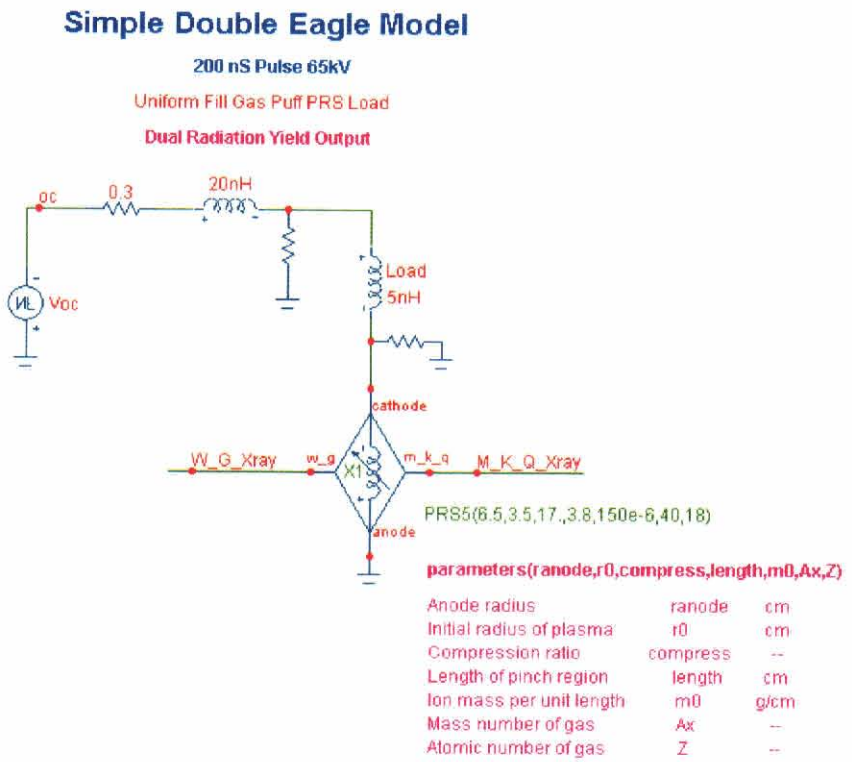

Figure 6-5. Circuit used for DE long pulse. PRS5 is a circuit element representing a uniform fill with the displayed parameters.

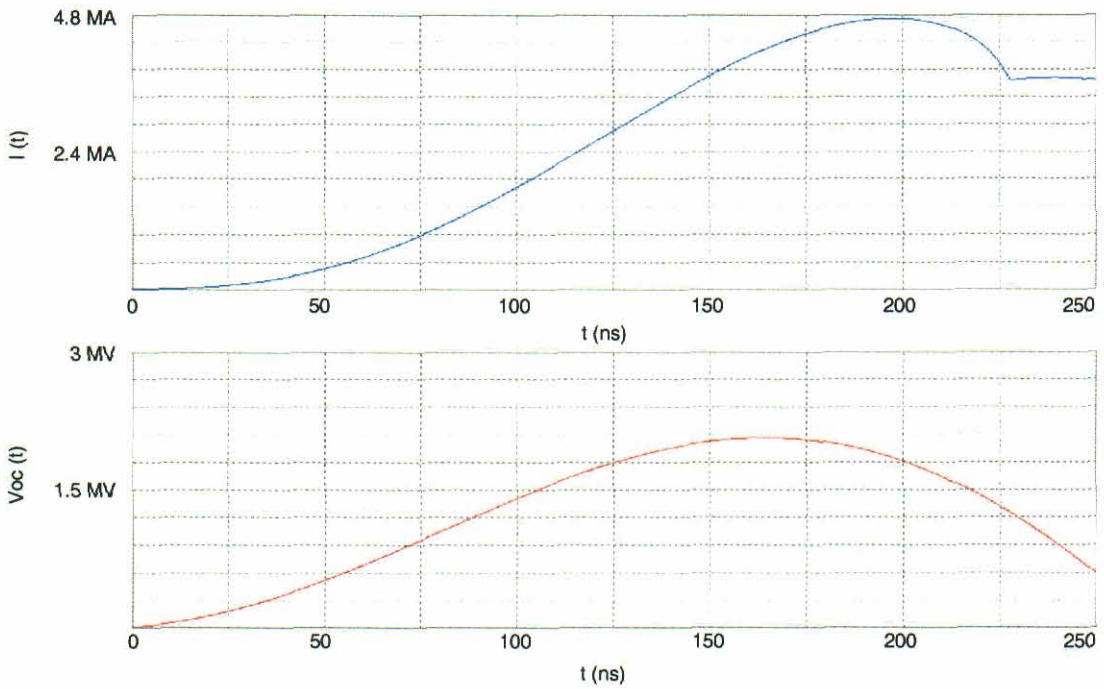

Figure 6-6. Current obtained in run of circuit of Figure 6-5. Voc(t) is the driving open circuit voltage corresponding to 65 kV Marx charge.

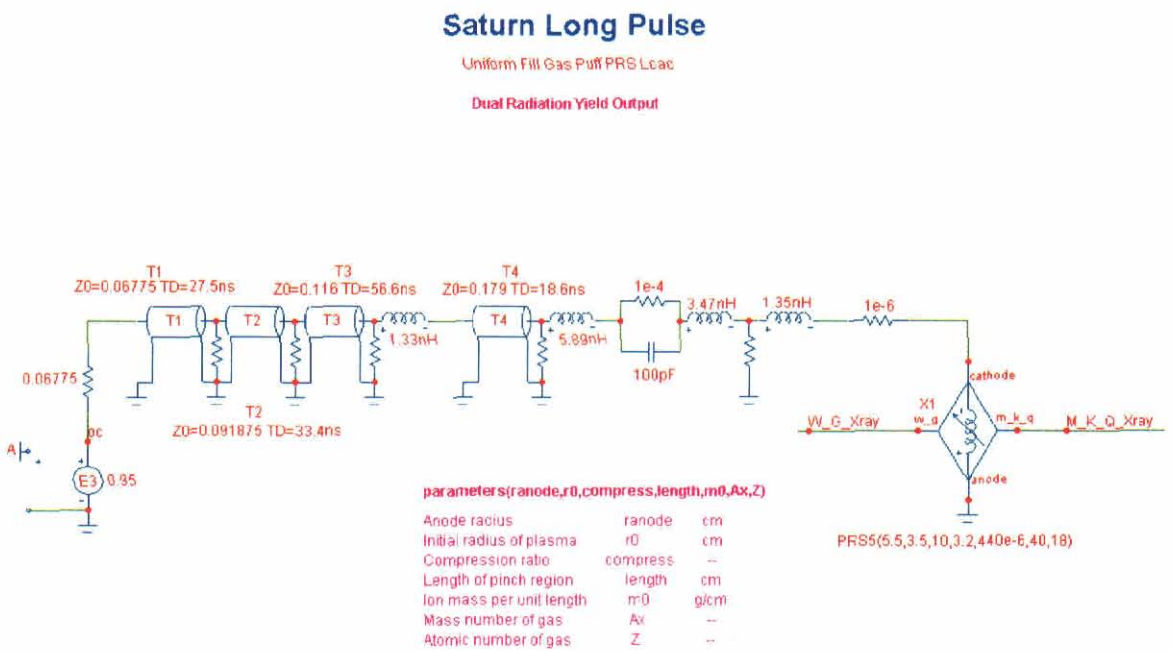

Figure 6-7. Circuit used for SATURN long pulse. PRS5 is a circuit element representing a uniform-fill with the displayed parameters.

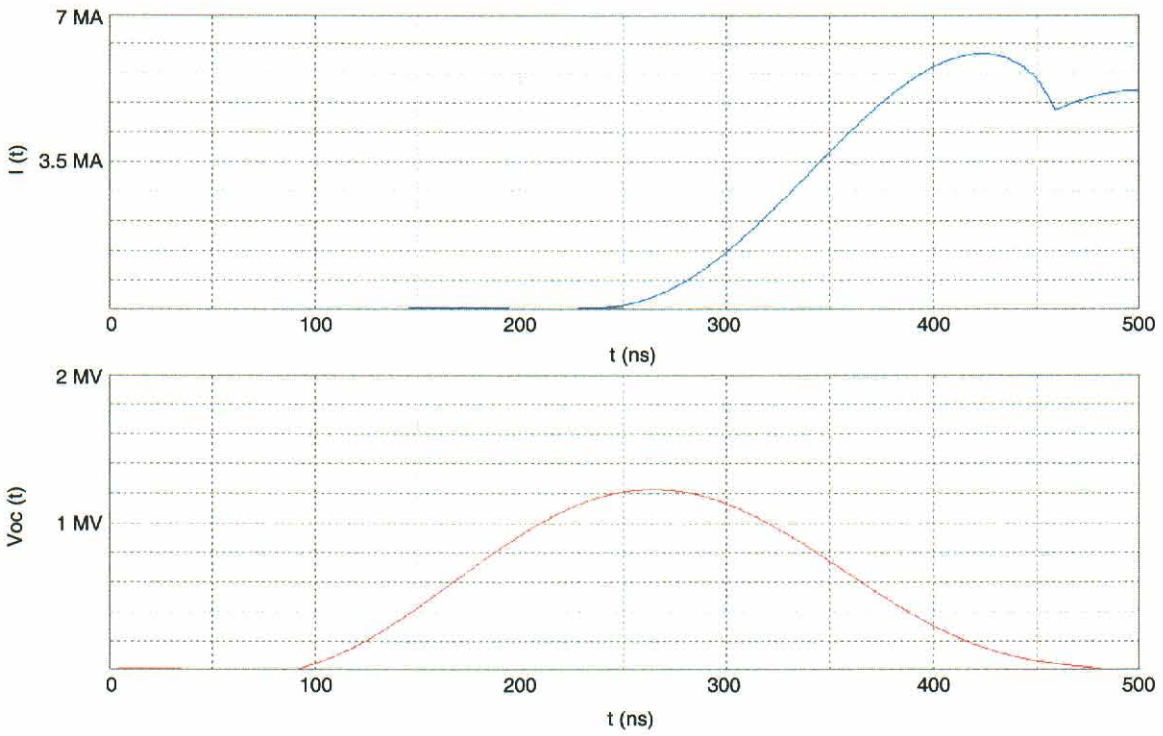

Figure 6-8. Current obtained in run of circuit of Figure 6-7. Voc(t) is the driving open circuit voltage, provided by Ken Struve of SNL, who also provided the circuit above.

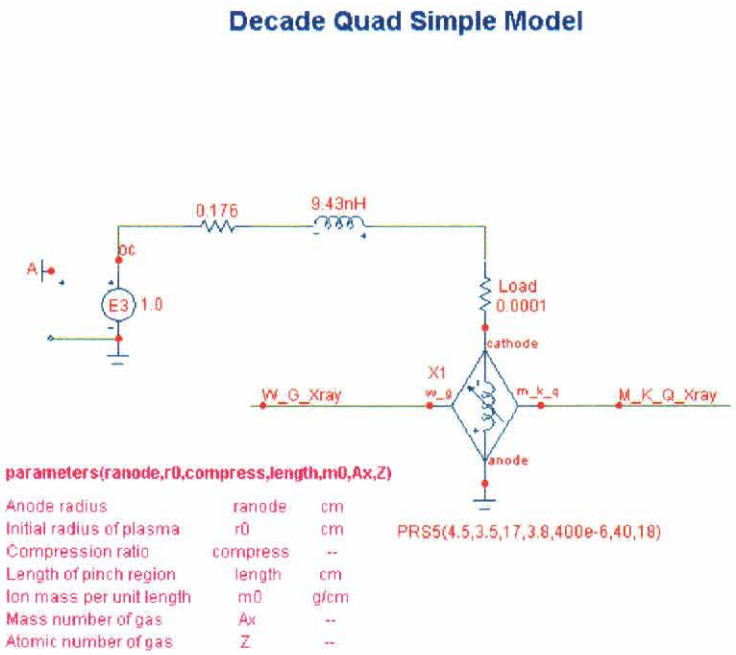

Figure 6-9. Circuit used to project DQ results. PRS5 a circuit element representing a uniform-fill with the displayed parameters.

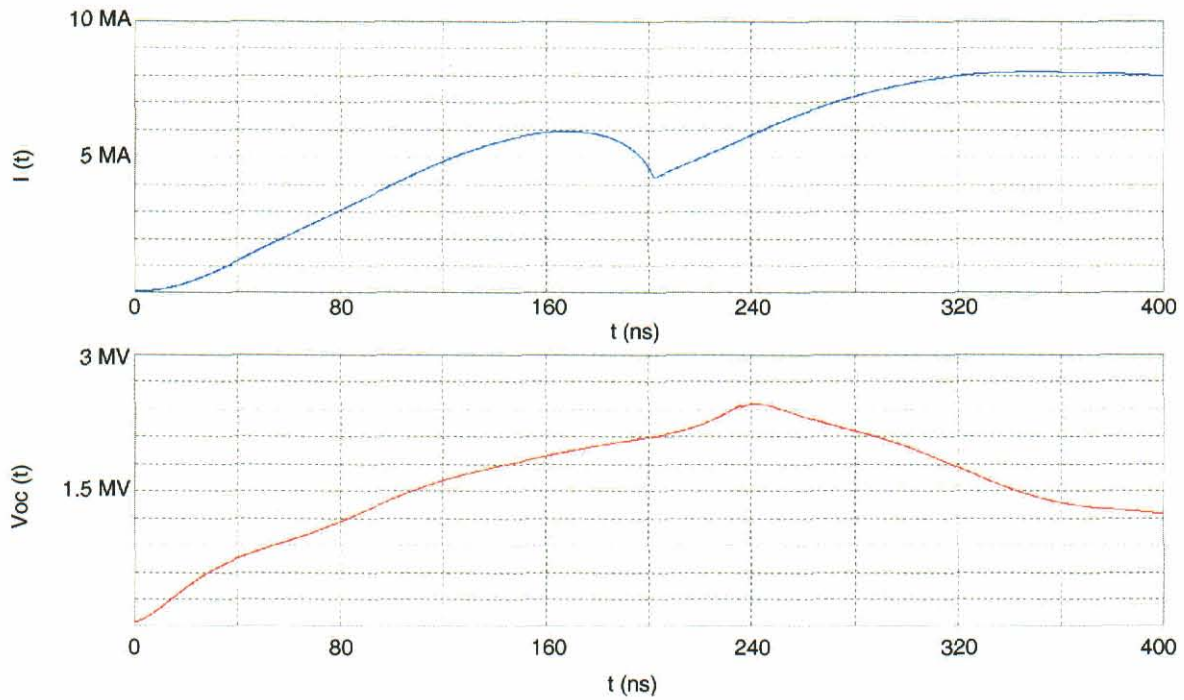

Figure 6-10. Current obtained in run of circuit of Figure 6-9. Voc(t) is the driving open circuit voltage, provided by Phil Spence of PSI, who also provided the circuit above.

For SATURN long pulse, only a few shots were taken. In that case, we found the values of mass and ECR that fits one of the shots for the same nozzle used in DE long-pulse mode.

Table 6-2 shows the results obtained in those calculations for DE, SATURN, and DQ. We see that we needed an ECR of 15 to fit the optimal results for the 2.5-cm diameter thin shell for DE short pulse. We needed to use 17 for the ECR value to fit the optimal DE long pulse yields (same ECR for the 60 and 65 kV Marx charge). We remark that an ECR of 17 for the uniform fill corresponds to an equivalent value of $17/1.4 \approx 12$ for a thin shell of the same mass imploding in the same time. From this point of view we see that the ECR for the thin shell in the DE short-pulse mode is comparable to the equivalent "mass weighted ECR" of the uniform fill.

Table 6-2. Results of circuit calculations, 0-D model compared with experiment. $\overline{Y}$ is total K-shell yield = $Y\Delta z$, Δz is the pinch length (see text).

	0-D μ (μg/cm)	0-D ν	0-D I_o (MA)	Experiment I_o (MA)	0-D τ (ns)	Experiment τ (ns)	0-D $\overline{Y}$ (kJ)	Experiment $\overline{Y}$ (kJ)
DE 60 kV 2.5-cm shell[1]	155	15	3.5	3.4	105	100	19.2	21.5
DE 60 kV 7-cm filled[1]	130	17	3.6	3.5	180	178	11.7	10.6
DE 65 kV 7-cm filled[1]	150	17	3.9	4.0	180	188	15.0	15.3
SATURN 7-cm filled[1]	350	17	5.8		180		34.4	
DQ 7-cm filled[1]	650	17	6.6		205		45.6	
DQ FIT[2] 7-cm filled	400	17	5.9		180		40.8	

[1]Optimized result at assumed ECR for the selected load.
[2]Fit to obtain τ = 180 ns.

The predicted SATURN result for the 7-cm uniform fill is well above the 18 kJ observed (Section 2.4). In view of the compromises made to conduct that limited test series, this disagreement can only be viewed as an impetus for further experiments.

We obtained the results shown in Table 6-2 for DQ by taking the ECR value obtained from fitting the optimal results for the 7-cm nozzle in DE long pulse, and using this value in calculating the optimal results for the same nozzle on DQ. We also repeated the calculation for DQ, but forcing the implosion time to 180 ns and keeping the same ECR of 17. Both calculations show over 40 kJ of Ar K-shell radiation predicted by this 0-D analysis.

In Figure 6-11 we show in a linear-log plot Y as a function of I_0 for DE short and long pulse, and SATURN experimental results. We show as well the two projected values for DQ mentioned in the previous paragraph. For orientation we also include the curves for the "İ ideal generators," for the 100 ns and 200 ns thin-shell and 200 ns and 300 ns uniform-fill. All those four curves are for ECR=10. We see that the DE data does better than the corresponding ideal generator curves, because as we discussed in relation to the data in Table 6-2, they exhibit ECR above 10 (for the same ECR actual water line generator yields would lie below the ideal generator case). On the other hand the SATURN short pulse data point exhibited is below its corresponding ideal curve. We also see that a large area in parameter space is available to improve on the projections of this report when DQ comes on line.

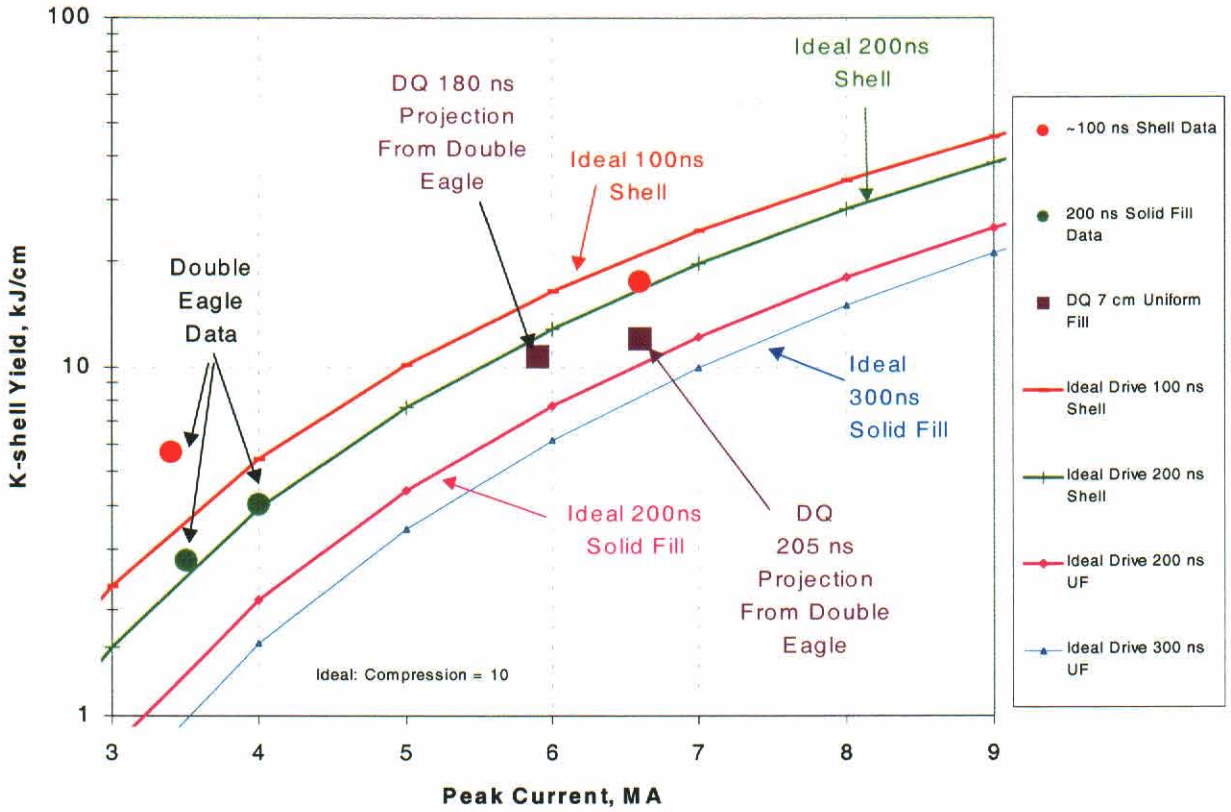

Figure 6-11. Data from DE, SATURN, DQ projections curves. Also presented here for comparison are 0-D global optimization for constant $\dot{I}$ and ECR = 10.

The critical aspect in obtaining the desired yields on DQ is to obtain ECRs about or above 15 for uniform fills of sufficiently large radius (3.5 cm and above) where the 0-D model predicts Ar K-shell yields in excess of 40 kJ.

6.4 CONCLUSIONS.

Application of the MQK 0-D model has proven useful in guiding experimental expectations and assessing trends in our DE campaign. We have generalized the MQK model to uniform fills, and derived from the model global optimization predictions for either fixed ECR or fixed final radius.

We had conjectured before the DE campaign that we would obtain 3 kJ/cm for I_{peak} between 3.5 and 4 MA. In fact we obtained experimentally 4 kJ/cm at 4 MA. We predicted that for comparable ECRs we would obtain yields about a factor of 2 lower for the 200 ns implosions with respect to the 100 ns implosions; indeed this was observed in the DE experimental campaign.

We project yields of ~ 40 kJ in DQ using this 0-D model for the 7-cm uniform-fill which provided successful results on DE. As DQ comes on line, we also need to experiment with larger diameter uniform fill loads; if their ECRs stay about or above 15 we should be able to obtain results exceeding 40 kJ.

If we assume that we should have gotten on SATURN the same ECR obtained in DE by using the same load, we come to the assessment that the results of SATURN are not optimal for the 7-cm uniform fill load used in the long pulse model.

Since 0-D models are not predictive we need to keep improving our modeling activities. Because of this and other valid R&D reasons, actual gas density profiles, obtained from either interferometric measurements or gas dynamic calculations, need to be employed as initial conditions in 2-D MHD calculations. We also need to include in the simulations a validated model of where current first strikes in the gas density profile. Modeling of this sort will help the experimental design and understanding, and may be conducive to improved simple 0-D like models. All of the necessary computational tools exist within the DTRA community, in particular at MPI.

SECTION 7

PLASMA CONDITIONS DERIVED FROM X-RAY SPECTRA

We have measured plasma conditions for both standard short (100 ns) and longer implosion (200 ns) time argon gas puff loads. Our objective is to understand the effect of implosion time on z-pinch performance. The plasma parameters of interest were electron temperature, ion temperature, and electron density. Measuring both electron and ion temperatures gives a measure of how well the ion kinetic energy has thermalized. This thermalization is assumed to be 100% in the calculation of the η required for efficient radiation production. High electron densities are important to thermalization and efficient radiation. For 100-ns implosions, the gas profile was a 2.5-cm diameter nominal shell, while both 5-cm shell and 7-cm solid-fill profiles were used for 200-ns implosions. Since the gas puff distributions vary both in r and z, spatially-resolved measurements are desired; our initial measurements look at variations in z.

We find that the average electron density is well correlated with the imploded mass; electron and ion temperatures are not equal, hence thermalization is incomplete. We also find that a larger axial extent of the pinch radiates in the K-shell for solid-fill profiles, and that the "shells" radiate most strongly in regions where their profiles approach a solid fill.

7.1 APPROACH.

We use x-ray spectroscopy to determine plasma conditions. Electron density and temperature can be estimated from a combination of different line ratios. The absolute source yield and plasma dimensions can also be used. Two spectrographs were fielded on these experiments, both using slits to resolve the data in z. One measured Ar emission, and the other Cl. The Ar He-α, Ly-α, and He-β lines were recorded with the first spectrograph, which used a PET crystal for dispersion and a P-20 phosphor to convert the x-rays to optical light. The light was lens coupled to and recorded with a cooled CCD camera. (See Section 8 for more details on the CCD systems.) Cl was introduced to the gas puff via CCl_2F_2, which was added to the Ar at the 2% molecular level (thus the puff was 4% atomic Cl). The Cl He-α, intercombination line (IC), jkl satellites, and Ly-α line were recorded with the second spectrograph, which used a Si(111) crystal for dispersion. The spectrum was recorded on DEF film and scanned with a PDS densitometer. The film densities were unfolded using the calibration data of Henke (Reference 32) included in the image analysis program, PDS Shrink.

The argon spectra were analyzed in the way suggested by Apruzese (Reference 18). The Ly-α to He-α line ratio, the absolute brightness of the pinch in the K-shell, and the K-shell diameter, measured from a pinhole camera photograph, are used to estimate electron densities and temperatures. The absolute pinch brightness is found by summing the lines, normalizing to the measured K-shell yield, and dividing by the measured x-ray pulse width. Both the line ratio and

K-shell brightness are resolved in z along the pinch axis. An atomic physics code must be used to predict temperatures and densities from the observed brightnesses and ratios because opacity effects are expected to be important.

The chlorine dopant provides a measurement that should be much less sensitive to opacity effects. Electron density can be estimated from the ratio of the resonance transition (He-α) of the helium-like ion Cl XVI to the intercombination line ($1s^2\ ^1S - 1s2p\ ^3P^0$). Because this ratio also depends on electron temperature, the temperature is estimated from the ratio of the He-α line to the dielectronic satellite transition ($1s^22p\ ^2P^0 - 1s2p^2\ ^2D$ or j,k,l satellites). If the Cl is optically thin, it could be Abel inverted to provide a radially-resolved measurement in the future. Glenzer (Reference 33) has used these ratios to diagnose plasmas with electron densities near 10^{21} e/cm^3 and electron temperatures between 1 and 3 keV. In our experiments, spectral dispersion is provided by a Bragg-diffracting crystal in the Johann geometry. A similar instrument was used by Wong to make measurements at the SATURN facility (Reference 34). The Johann geometry eliminates source size broadening of spectral lines. By keeping the dopant level sufficiently low, opacity should not broaden the lines either. The remaining broadening will be due to Doppler and Stark effects. Given the electron density and temperature, the Stark and opacity effects can be compensated for and the Doppler contribution determined, giving an estimate of the ion velocities in the plasma. We have assumed that the ion velocity distribution is Maxwellian, and have used the intercombination line width to estimate the ion temperature.

7.2 MEASUREMENTS.

Both Cl and Ar spectra were obtained for a number of shots. Table 7-1 lists the shot configurations. For more detail about the gas puff distributions see Section 9. The K-shell emission was more uniform from anode to cathode for the solid-fill loads. In the case of shell loads, the K-shell yield typically peaked between the center of the pinch and the anode, where the radial gas distribution was filled in. Plots of Ar K-shell emission and the Ar Ly-α to He-α line ratio as a function of z, the distance from cathode to anode are given for 3 different load configurations in Figures 7-1 through 7-3. Both the peak pinch brightness and line ratio are more than 3 times higher for short pulse than long-pulse implosions.

Table 7-1. Summary of the shots for which spectral data will be presented.

Shot number	Nozzle Diameter	Current Risetime	Peak Current	Ar Spectrum	Cl Spectrum
4045	2.5 cm shell	100 ns	3.5 MA	Yes	
4087	2.5 cm shell	100 ns	3.5 MA	Yes	
4090	2.5 cm shell	100 ns	3.5 MA	Yes	Yes
4069	5.0 cm shell	200 ns	3.5 MA	Yes	
4071	5.0 cm shell	200 ns	3.5 MA	Yes	Yes
4073	5.0 cm shell	200 ns	3.5 MA	Yes	
4080	7.0 cm solid-fill	200 ns	4.0 MA	Yes	
4083	7.0 cm solid-fill	200 ns	4.0 MA	Yes	Yes
4084	7.0 cm solid-fill	200 ns	4.0 MA	Yes	
4059	7.0 cm solid-fill	200 ns	3.5 MA	Yes	Yes

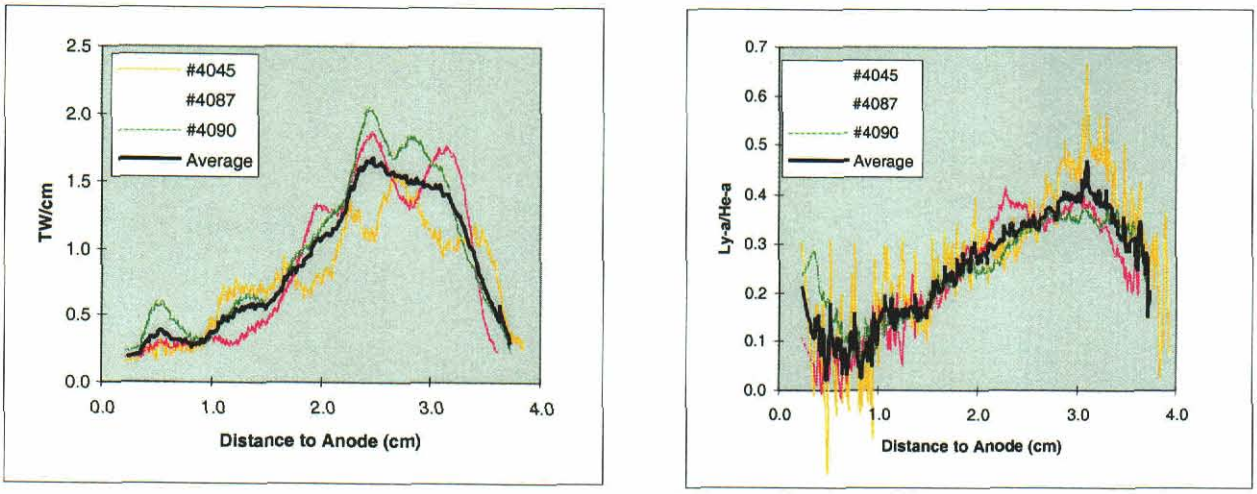

Figure 7-1. Emission and line ratio both peak toward anode for short pulse 2.5-cm shell.

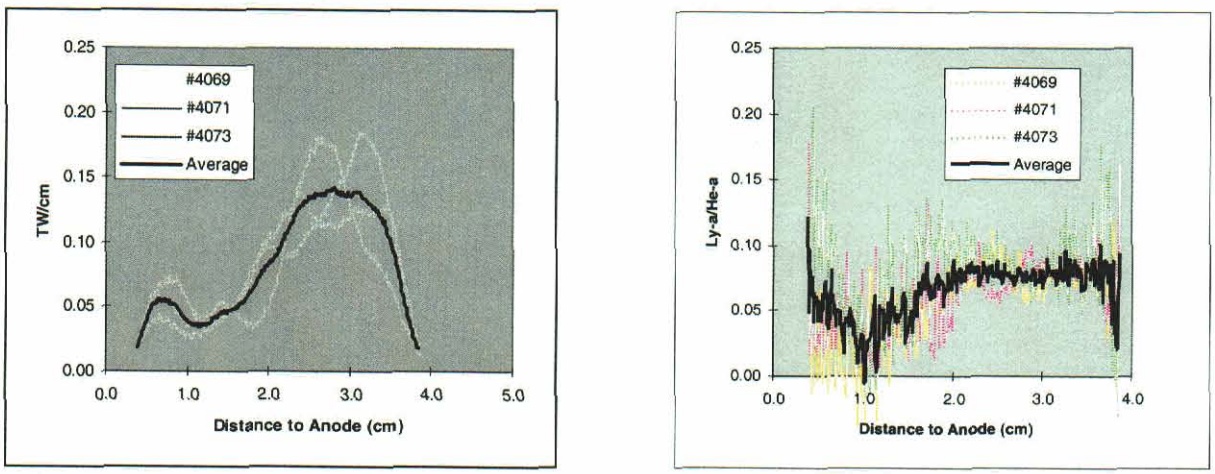

Figure 7-2. Emission and line ratio both peak toward anode for long pulse 5-cm shell.

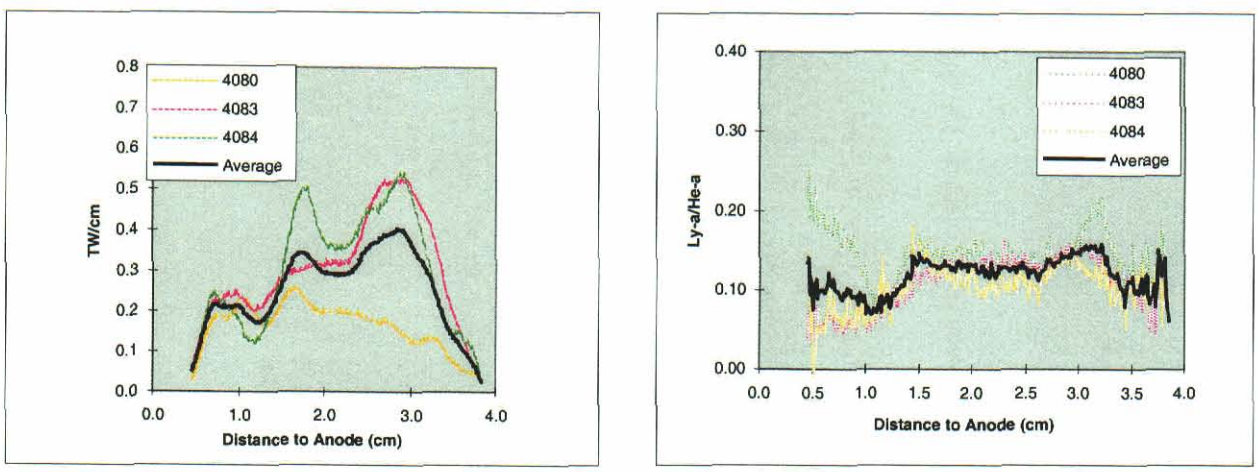

Figure 7-3. Emission and line ratio are both more uniform for long pulse 7-cm solid fill.

The same line ratio and relative brightness for Cl can be compared with the Ar results. In general the measurements, one recorded with x-ray film and the other with a phosphor/CCD combination, track each other well, as shown in Figures 7-4 through 7-6. The magnifications were calculated from the slit locations, and are slightly different (on the order of 5%). Also, because the direct x-ray film measurement is more sensitive, a narrower slit was used for the Cl, resulting in higher spatial resolution. The line ratios for the two long pulse shots agree very well, but there is a discrepancy for the short pulse shot—the Ar ratio is a factor of two higher in the region of brightest emission. This is consistent with increased opacity, since the absorption of the He-like line should be much greater than for the H-like one.

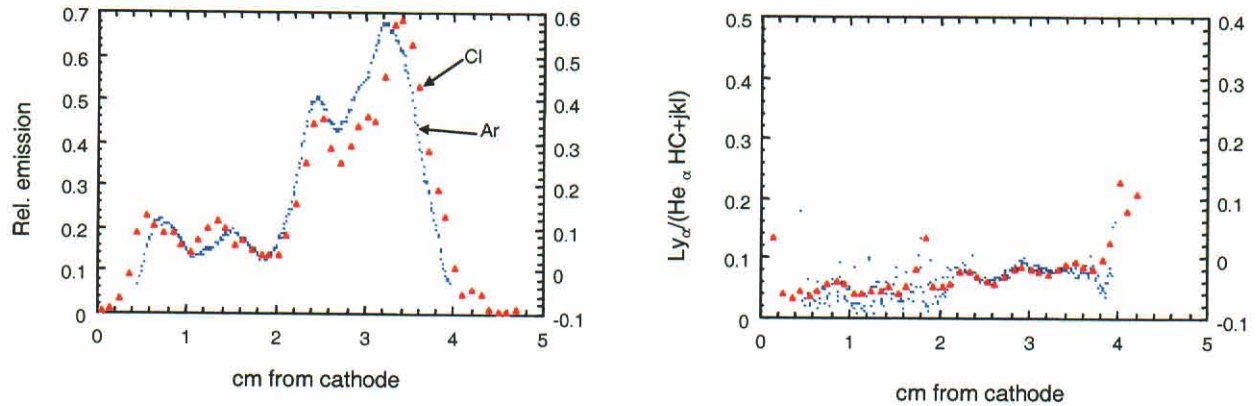

Figure 7-4. Long pulse 5-cm shell brightness and line ratio traces are consistent between Ar and Cl.

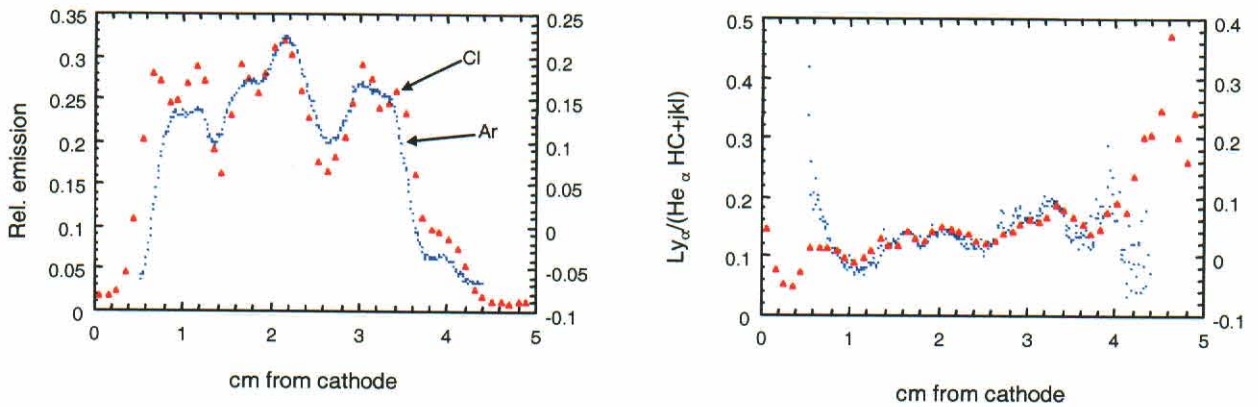

Figure 7-5. Long pulse 7-cm solid-fill brightness and line ratio traces are consistent between Ar and Cl.

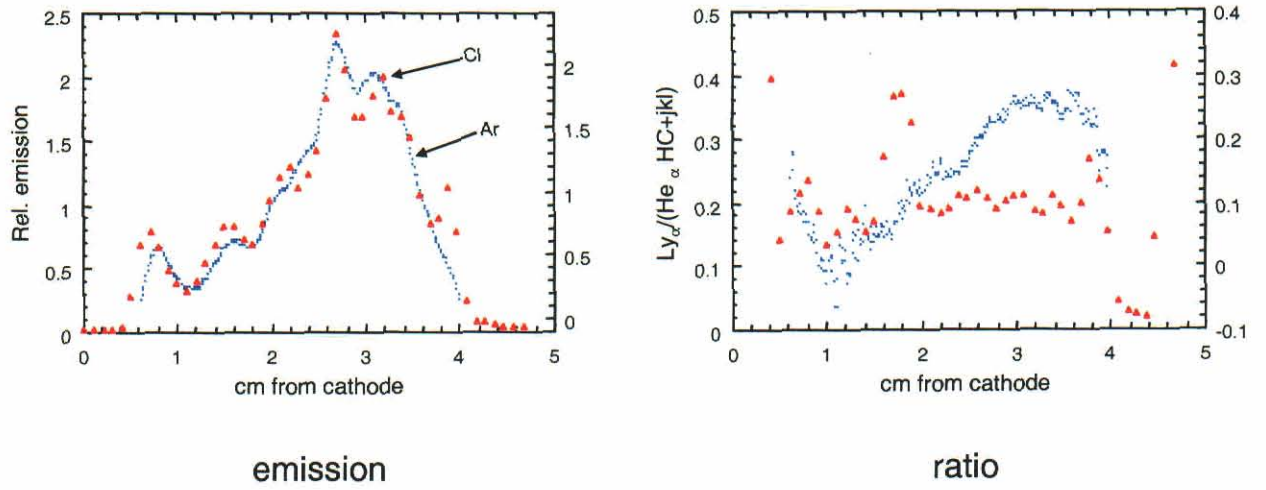

Figure 7-6. Short pulse 2.5-cm shell brightness and line ratio traces are not consistent between Ar and Cl.

We have used the Cl spectra to estimate plasma parameters as a function of z, the distance from cathode to anode, for four representative shots. In Figures 7-7 through 7-14, for each shot the electron and ion temperatures are shown on one plot, and the electron density and relative Cl emission are shown on the other. The error bars were estimated as follows. For electron temperature, the uncertainty in the He-α/jkl ratio was taken to be 5%. The resulting error bars in the temperature estimates are small, often not extending outside of the plot symbol used. For the ion temperature estimate, a FWHM uncertainty of 5% was used for the Doppler width, which results in an uncertainty in the ion temperature of 10%. Uncertainty estimates for the electron density are based on a 5% uncertainty in the inter-combination (IC) to He-α line ratio, and the uncertainty in the estimated electron temperature (since the ratio has some temperature as well as density dependence).

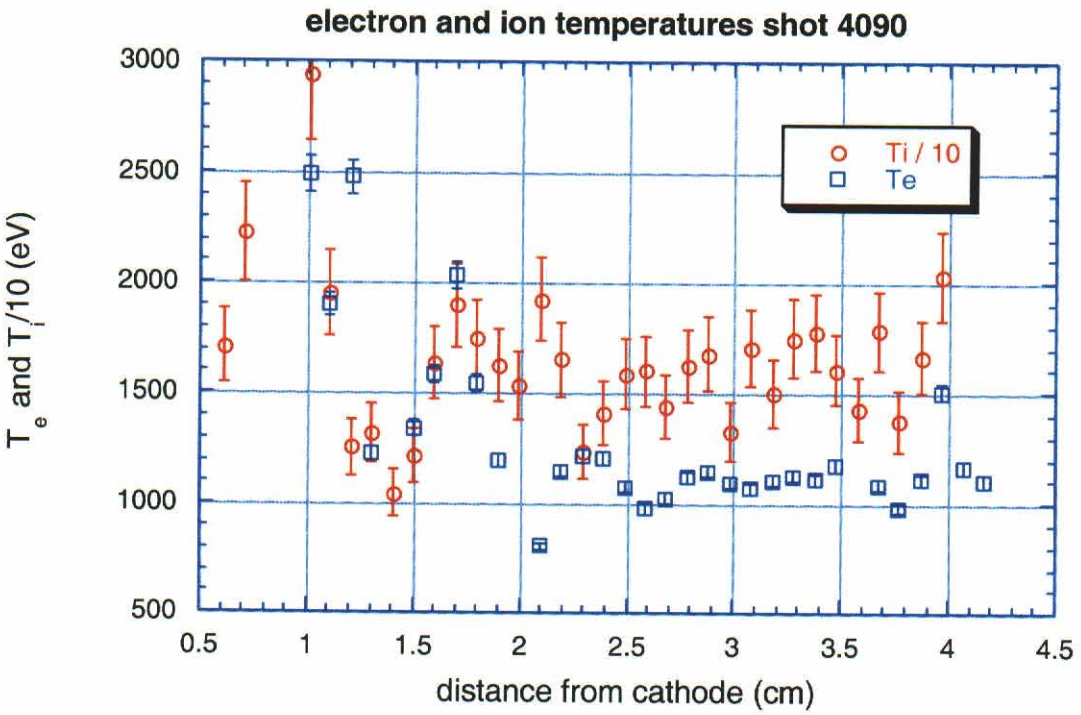

Figure 7-7. Short pulse (2.5 cm) temperatures are fairly uniform axially.

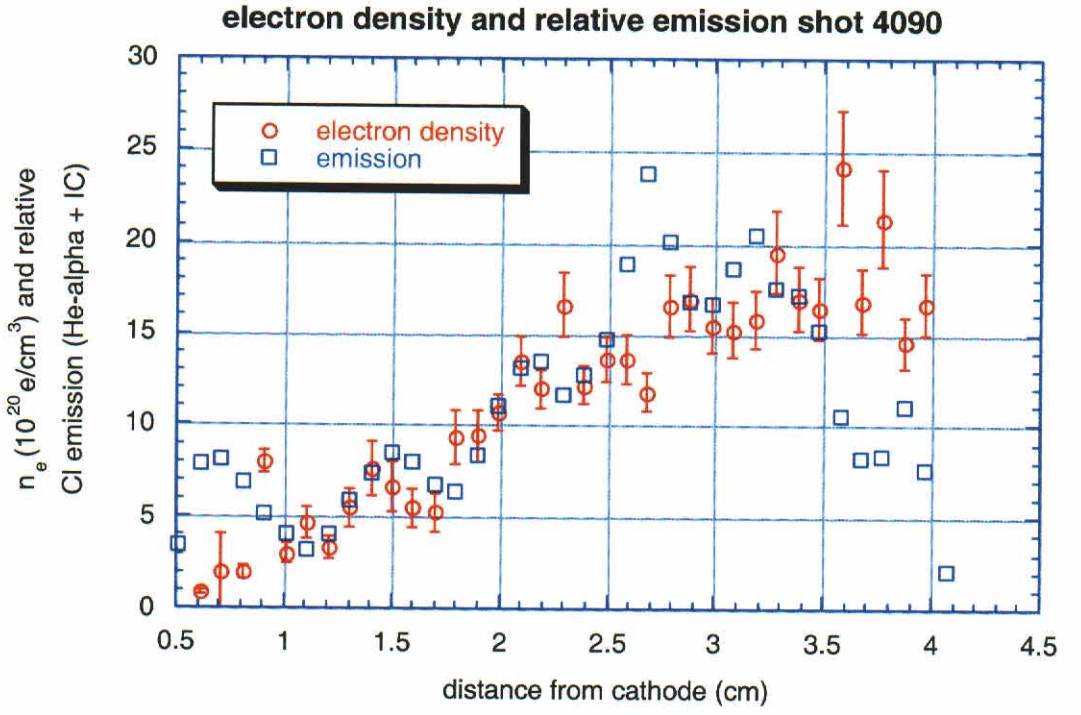

Figure 7-8. Short pulse (2.5 cm) emission and density peak toward anode, where gas profile is more filled in.

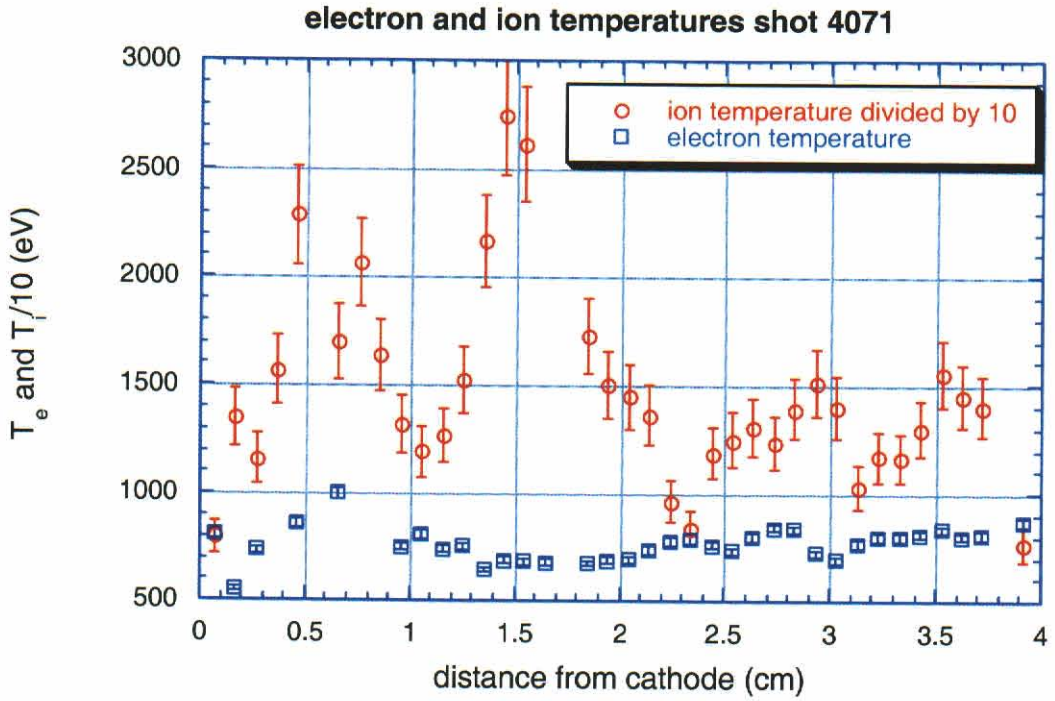

Figure 7-9. Long pulse 5-cm shell temperatures are lower than short pulse.

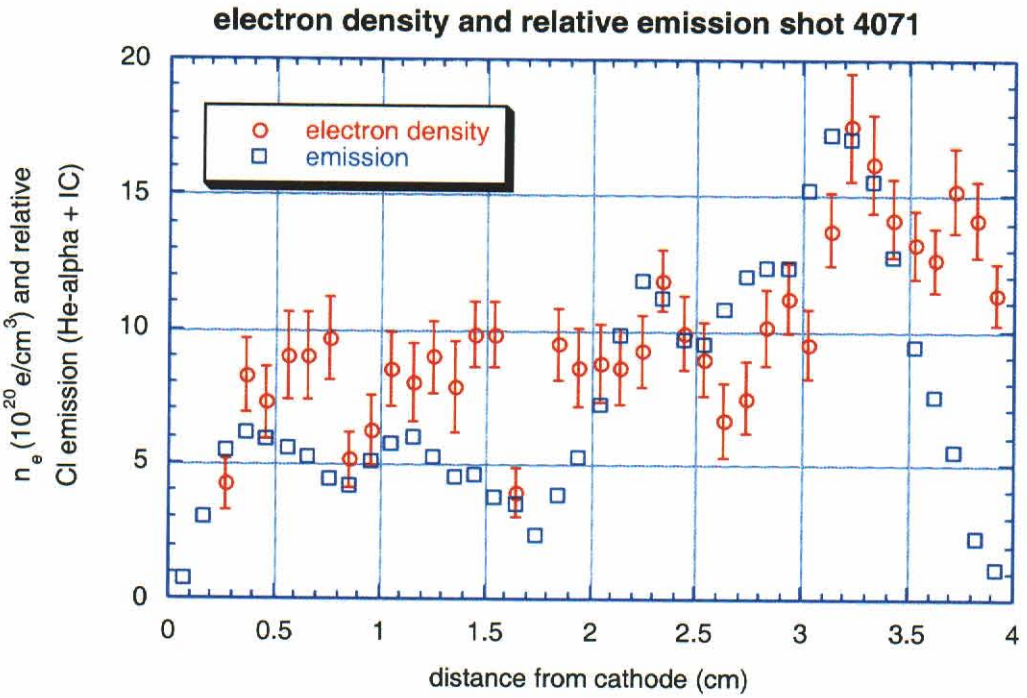

Figure 7-10. Long pulse 5-cm shell emission and density peak toward anode, where gas profile is more filled in.

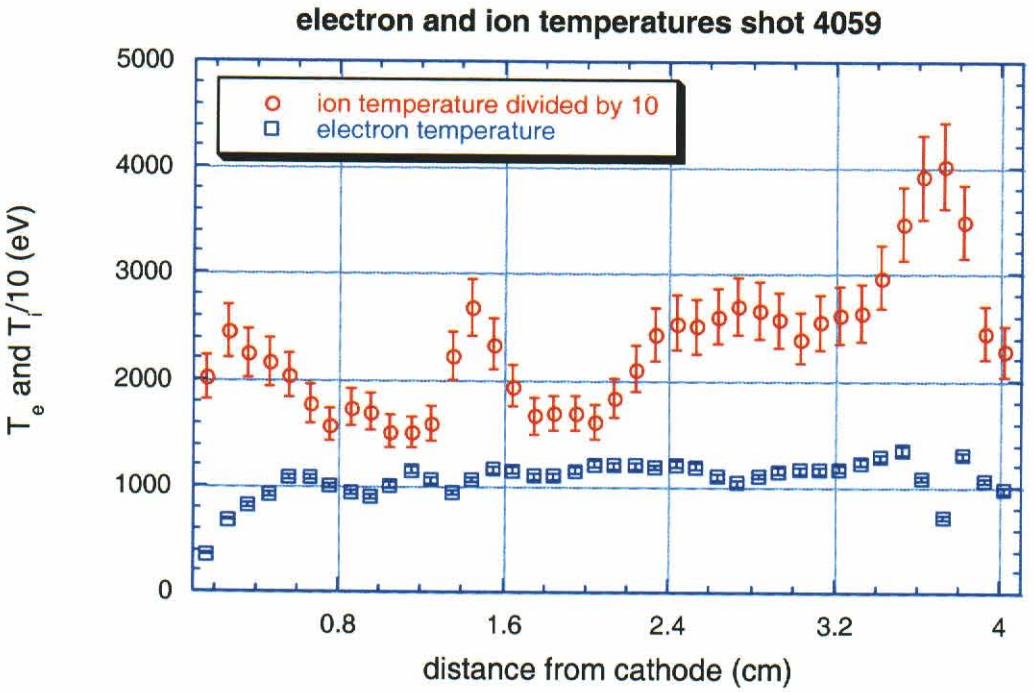

Figure 7-11. Long pulse 7-cm solid-fill Te is fairly uniform; Ti has more variations.

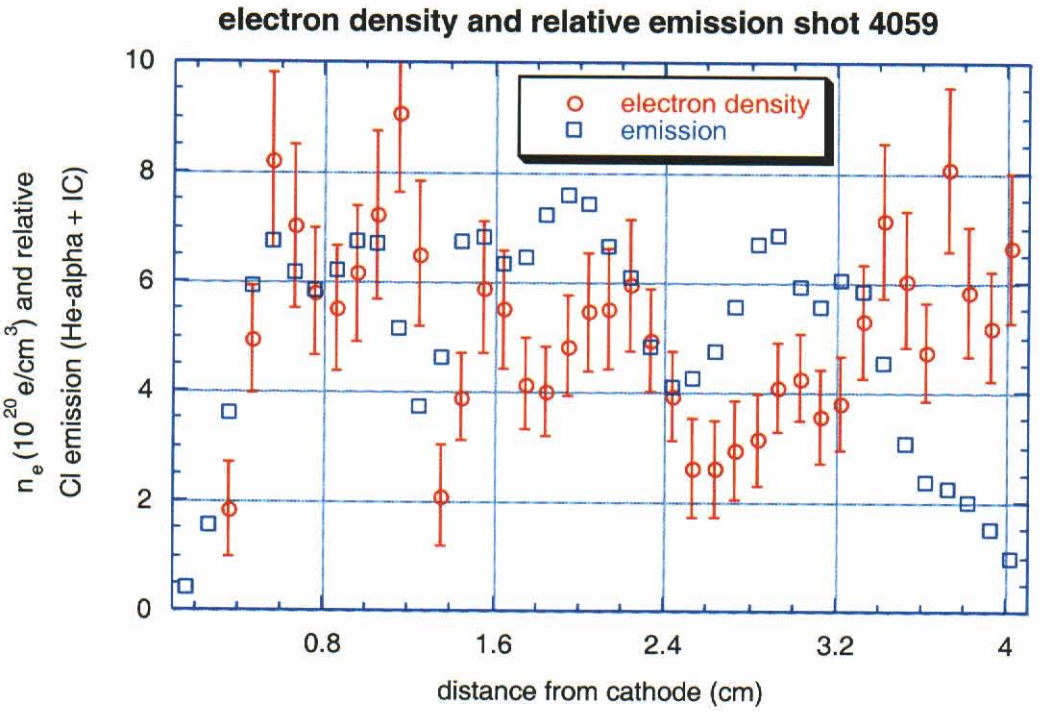

Figure 7-12. Long pulse 7-cm solid-fill density and emission are more uniform axially than shell.

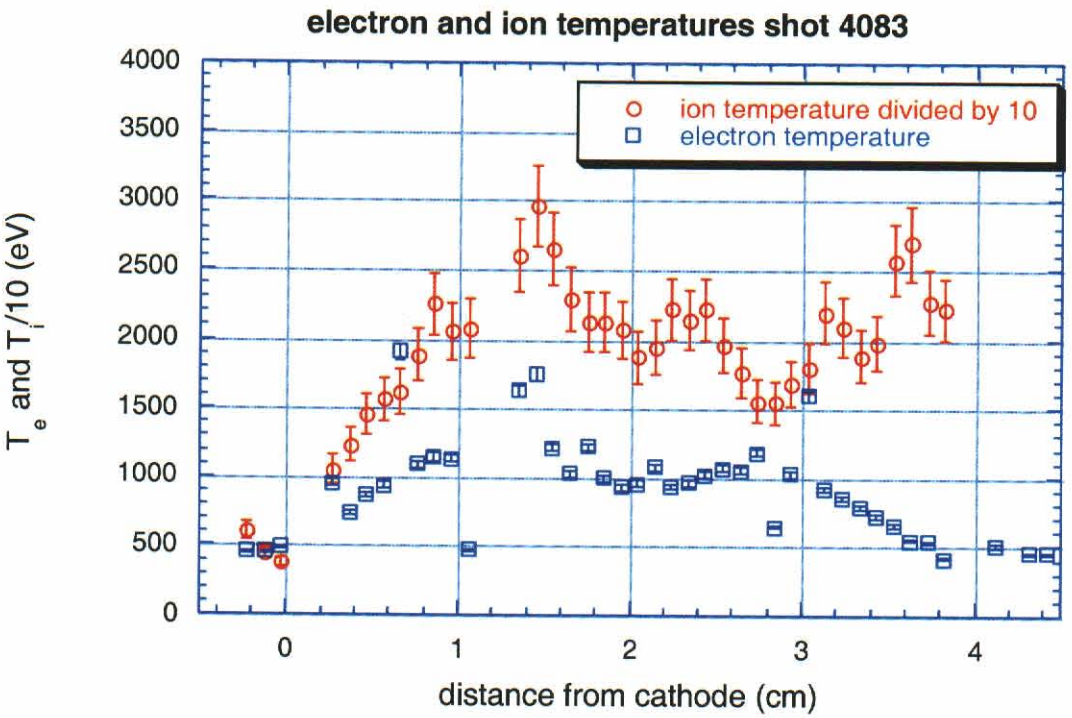

Figure 7-13. Temperatures for higher current, long pulse, 7-cm solid-fill are comparable to nominal current case.

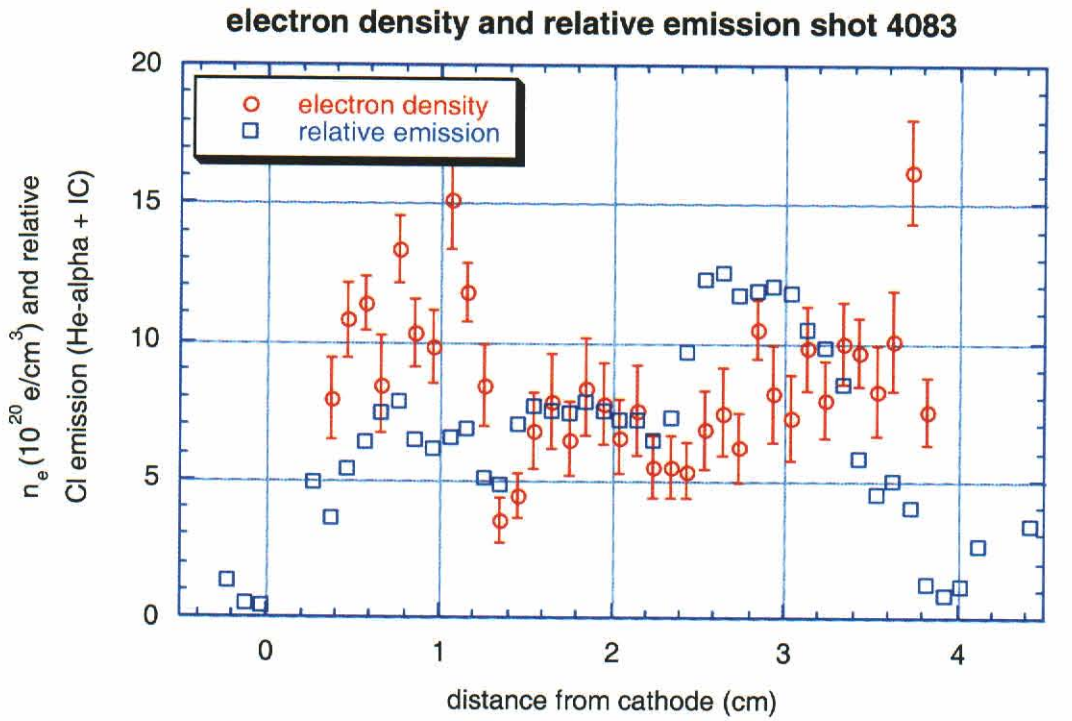

Figure 7-14. Density is higher for higher current, long pulse, 7-cm solid-fill.

The z-dependence of density and temperature depend on the load type. For the shell loads, the ion and electron temperatures are most stable between the center of the pinch and the anode, where the x-ray emission is strongest. Also, the estimated electron density ramps up in this region as well. For the solid-fill shots, the temperatures are more uniform over the full length of the pinch, with more variation in electron density. This variation and the larger error bars are due in part to the fact that the densities are lower for these large diameter loads and the IC line ratio is less density sensitive.

To easily compare one configuration with another, we have calculated source-averaged plasma parameters. These averages were weighted by the sum of the two dominant Cl lines—the He-α and intercombination lines. A summary of the source-averaged plasma parameters is given in Table 7-2, and plots of temperature and density versus nozzle diameter are given in Figures 7-15 and 7-16 respectively. The uncertainties in the source-averaged parameters are not due to measurement uncertainties, but rather variations in the parameters along the length of the pinch. The mean electron temperatures are comparable for the short pulse shot and the two 7 cm diameter long pulse shots, with the 5 cm shot coming in somewhat lower. The mean electron density of the K-shell emitting plasma increases nearly linearly with the injected mass, as shown in Figure 7-17. Because the K-shell x-ray emission on the shell shots is strongest from regions where the gas puff distribution is actually filled in, the relative injected mass (Figure 7-17) was calculated from only the nozzle outer diameter. Also, the degree of thermalization, given by the ratio of electron to ion temperature, is best for the highest density shots. (Shot 4083 was taken with a Marx charge of 65 kV; all other shots were taken at 60 kV. In Figures 7-15 through 7-17, shot 4083 is displaced to 7.1 cm for clarity.)

Table 7-2. Summary of plasma parameters from Cl spectra.

Shot #	**Nozzle Diameter**	**Current Risetime (ns)**	**Peak Current (MA)**	**$\langle T_i \rangle$ (keV)**	**$\langle T_e \rangle$ (keV)**	**$\langle T_e \rangle / \langle T_i \rangle$**	**$\langle n_e \rangle$ (10^{21} e/cm^3)**
4090	2.5-cm shell	100	3.5	16 ± 3	1.2 ± 0.3	$7.5 \pm 2.3\%$	1.3 ± 0.5
4071	5.0-cm shell	200	3.5	14 ± 4	0.77 ± 0.06	$5.5 \pm 1.6\%$	1.1 ± 0.3
4059	7.0-cm solid-fill	200	3.5	22 ± 5	1.1 ± 0.1	$5.0 \pm 1.2\%$	0.51 ± 0.16
4083	7.0-cm solid-fill	200	4.0	20 ± 4	1.0 ± 0.3	$5.0 \pm 1.8\%$	0.84 ± 0.25

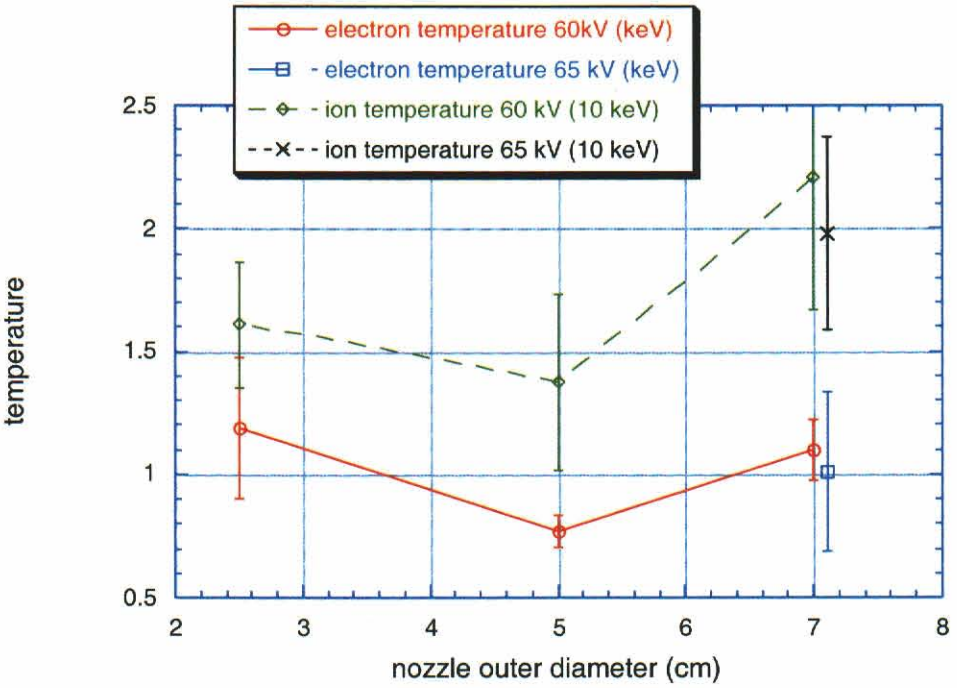

Figure 7-15. Temperature variations for the 3 load styles tested.

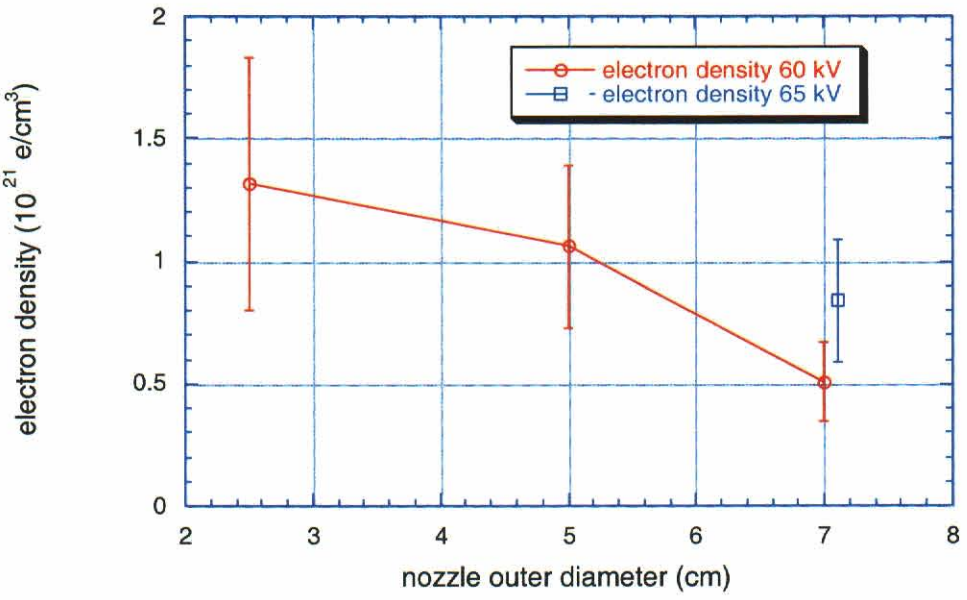

Figure 7-16. Density variations for the 3 load styles tested, current.

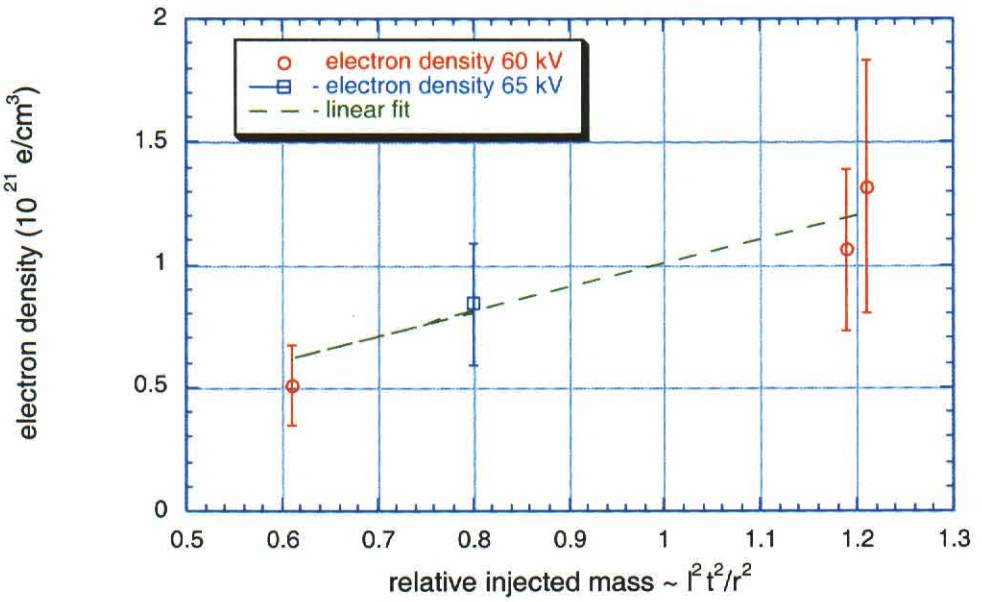

Figure 7-17. Estimated electron density increases with injected mass.

Comparing the K-shell power and yield with the estimated plasma parameters provides a consistency check that increases our confidence in the measurements. The relative emitted power for a transition to the ground state, I_{n0}, is given by

$$I_{n0} \propto \frac{\langle n_e^2 \rangle}{\sqrt{\langle T_e \rangle}} \exp\left(-\Delta E_{no} / \langle T_e \rangle\right) \quad ,$$

assuming that the ion charge state is not varying in the K-shell emitting region. The relative yield is found by multiplying I_{n0} by the radiation pulse width, $\langle\tau\rangle$, and the square of the K-shell emitting diameter, $\langle d\rangle$. Again, the pulse width and diameter used are averaged over the length of the source. As shown in Table 7-3, the estimated plasma parameters are consistent with the observed Ar yield (3.1 keV was used for ΔE_{n0}).

Table 7-3. Yield can be scaled from plasma parameters and dimensions.

Shot #	Nozzle Diameter	Current Risetime (ns)	Peak Current (MA)	$\langle T_e \rangle$ (keV)	$\langle n_e^2 \rangle$ (Relative)	$\langle d \rangle$ (mm)	$\langle \tau \rangle$ (ns)	K-shell yield (kJ)	Scaled K-shell yield (kJ)
4090	2.5-cm shell	100	3.5	1.2 ± 0.3	16.2	1.6	7 ± 1	20.0 ± 1.5	NA
4059	7.0-cm semi-solid	200	3.5	1.1 ± 0.1	2.3	2.1	19 ± 1	11.2 ± 0.8	11.0

7.3 SUMMARY.

Spectroscopic measurements have been used to estimate plasma temperatures and densities for Double-EAGLE Ar gas puff implosions. Implosions using both 100 and 200 ns rise time current pulses were analyzed. For some of the 200 ns implosions, the current was increased from 3.5 to 4.0 MA. For the shell nozzles, most of the yield was produced between the middle of the pinch and the anode, where the gas profile approaches a solid fill. Ion thermalization was better for the smaller diameter, higher mass implosions, and electron temperatures between 1.0 and 1.2 keV were achieved on both the 2.5-cm diameter, short-pulse and 7-cm, long-pulse shots. The mean electron density estimated for the K-shell emitting volume increased almost linearly with increasing load mass. A comparison between two shots indicates that the estimated densities and temperatures are consistent with the measured yield.

SECTION 8

DIAGNOSTICS DEVELOPMENT FOR LONG-IMPLOSION TIME LOADS: INITIATION & IMPLOSION IMAGING DIAGNOSTICS

With the success of small interwire gaps for high power wire array z-pinches, it has become even clearer that it is important to correlate the initial stages of a pinch with careful diagnostics of the radiation performance of the load. The initial mass distributions of our nozzles are discussed in Section 9. Here we cover three additional diagnostics that have increased our knowledge of initiation and implosion phase dynamics for the gas puffs. First we discuss the use of an optical framing camera to provide visible light images of the initiation and implosion of z-pinches on DM2 and on Double-EAGLE. Second, a "zipper" array was used to give a one-dimensional image of the K-shell emission as a function of time and distance along the pitch. We show that the zipper behavior can be correlated with the initial mass distributions. Third, CCDs (charge-coupled devices) have been configured for use in the severe environment of pulsed power machines (Double-EAGLE and SATURN). Our results demonstrate that CCDs can return high quality data and are an attractive replacement for conventional film to perform x-ray 2-D imaging or spatially resolved spectroscopy.

8.1 OPTICAL FRAMING CAMERA.

8.1.1 Diagnostic Features.

The IMACON optical framing camera uses fairly old technology. The scene is imaged with standard visible light optics onto a photocathode. Electron optics are used to provide the high speed shutter and to move the image to different regions of the output phosphor which is then photographed with conventional high speed (Type 57, ASA 3000) Polaroid film. In the camera's framing mode, 8 to 12 images can be captured with an interframe time of 21 ns. Each frame has an exposure time of 4 ns. The input photocathode is sensitive in the visible between about 450 and 600 nm.

From spectroscopic studies, we know that the argon puff gas initially radiates in the characteristic lines of its neutral and singly-ionized ions. Later in time, as the gas gets hotter and denser, the continuum becomes significant. The overall brightness of the pinching gas increases by many orders of magnitude during the implosion. Unfortunately, the camera has a limited dynamic range of roughly 100 at best. Hence it is difficult to capture good images of both the initiation of the pinch and its subsequent implosion. To a limited degree, the effective dynamic range of the camera may be improved by using a narrow band optical filter that is centered on a characteristic line of the emitting gas. Initially, the filter passes the dominant radiation with little attenuation as current begins to flow in the pinch. Later, the filter discriminates against the broad continuum.

For our experiments, we used a 10 nm FWHM filter centered on 480 nm which is reasonably matched to one of the dominant lines of singly-ionized argon (Ar II) at 480.6 nm. For other load materials, different optical filters would be appropriate. Singly ionized aluminum has lines at 490.0, 490.3 and especially at 466.7 nm (Al II); and at 490.4, 569.7 and 572.3 nm (doubly ionized, Al III). The only visible lines for molybdenum are due to neutral atoms. As a practical matter, the 480 nm filter was used for all the experiments reported here.

We have done some rough calibration of the sensitivity of the camera. Observations of a defocused 2 mW HeNe laser at 632 nm give a decent exposure (white but not overexposed) on the film for 0.4 mW incident per square millimeter of film. The bandpass of the camera is about 150 nm. Using this sensitivity, we predicted that a high brightness (>1 candela) red LED, overdriven by a 1 amp, 20 ns pulse should give usable images on the IMACON. The overdriven LED in fact worked well and was used to determine the timing of the optical response of the camera relative to the external trigger sent to the camera.

On DM2 argon PRS shots (≈ 1 kJ), good images of the implosion required 160 mm focal lengths, apertures of f/22 to f/32, and 2.0 neutral density in addition to the narrowband filter. With a demagnification of 4.2, the implied surface brightness during the later stages of implosion is ≈100 W/ster/ mm^2. At pinch time, surface brightness could exceed 1 kW/ster/ mm^2. For Double-EAGLE shots, the surface brightnesses are about a factor of 10 higher.

8.1.2 Optical Framing Images.

The primary purpose of the optical framing data is to document qualitative features of the initiation and implosion of the z-pinches. In particular, we are interested in perturbations that may seed instability growth leading to poor pinch compression and low radiation output. A typical image is shown in Figure 8-1. This single frame for Double-EAGLE shot 4070 shows the exit of the 5-cm shell nozzle, the anode return posts and the wire grid that defines the anode plane for the pinch. There are always 12 current return posts, but different nozzles have different bolt circle diameters for the posts. A pair of wires extends inward from the end of each post to define the anode plane. Like most diagnostics on Double-EAGLE, the camera usually viewed the pinch at an angle of 68 degrees from the pinch axis. For the DM2 tests, the camera had a more favorable view of almost 90 degrees to the axis. On some Double-EAGLE shots, the camera viewed the pinch end on (0 degrees); example images appear in Sections 2 and 3.

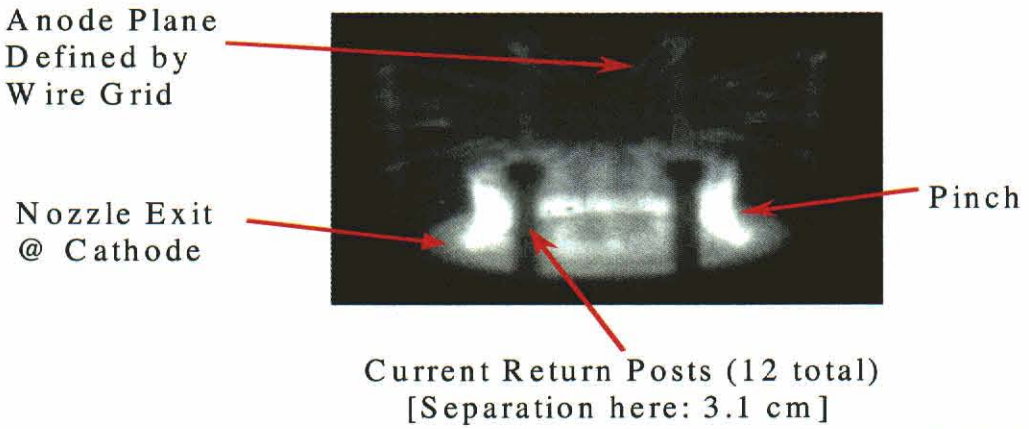

Figure 8-1. Sample frame for the optical imaging camera data on Double-EAGLE shot 4070.

The short pulse (100 ns) standard 2.5 cm diameter nozzle used on Double-EAGLE generally showed good symmetry in its optical images, even though only two discrete flashboards were used for pre-ionization of this load. Figures 8-2 through 8-4 show this load at 4 different times relative to the x-ray emission. For shot 4045, the camera caught the image even before the start of the nominal 99 ns implosion. In this case, Figure 8-2, the emission is presumably due to the "prepulse" of the current drive to the load.

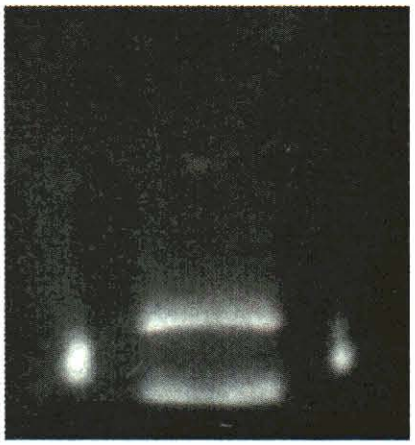

Figure 8-2. Optical image for 2.5 cm shell short pulse shot 4045; the frame occurred at –104 ns relative to peak K-power.

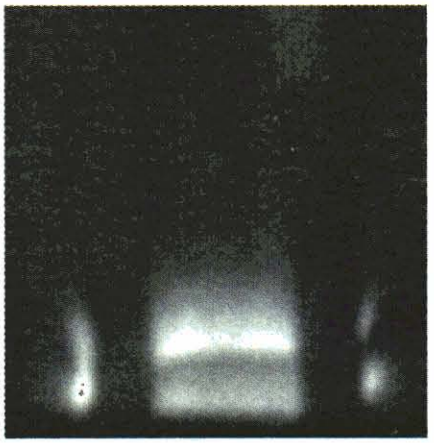

Figure 8-3. Optical image for 2.5 cm shell short pulse shot 4048; the frame occurred at –97 ns relative to peak K-power.

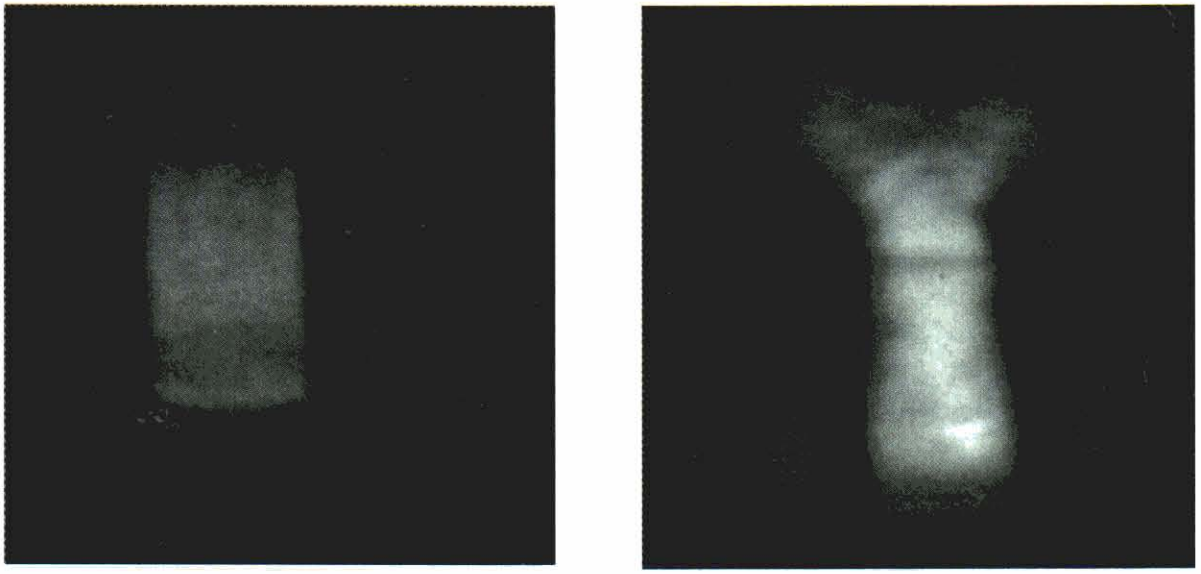

(a) 64 ns relative to peak K-power (b) -43 ns relative to peak K-power

Figure 8-4. Optical images for 2.5 cm shell short pulse shot 4029.

It is interesting to note that the light emission always grows from the cathode across the AK gap to the anode plane on a 25 to 50 ns time scale. This behavior was seen for all Double-EAGLE gas loads and also on DM2 and ACE 4 shots. The cause for this is not completely clear. Presumably the emission is a function of gas density, electron density and electron energy. While the gas density is highest near the cathode, it cannot change much on a sub-microsecond time scale. The electric field and current density are growing during these times. The sharp edge of the nozzle makes the electric field highest at the nozzle exit. Understanding this might contribute to our knowledge of the current initiation process for gas puffs. It is also possible that this time and space-dependent phenomenon could seed instability growth.

The image at –64 ns in Figure 8-4 also suggests axial filaments that are even more evident in Figures 8-5 and 8-6 below and Figure 8-1 above. The number of filaments, (≥20), is larger than the number of current return posts (12). The azimuths of the filaments are usually aligned with the pairs of chordal wires at the anode end of the pinch, which would produce 24 filaments. In this case the filaments may result from an initiation effect of the wires. Although the image resolution is not definitive, some filaments do not appear aligned with wires. Measurements at AASC (Section 9.2) showed that puff valve asymmetries can persist in the supersonic flow, so it is possible that the filaments are related to the 18 holes in the puff valve aperture plate upstream from the nozzle throat. Again, one must assume that the filaments are somehow related to gas and electron densities.

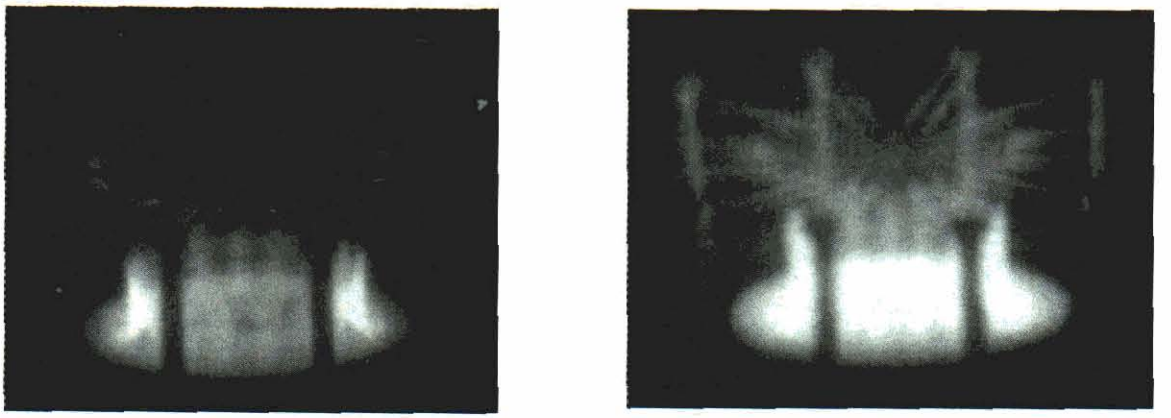

(a) –111 ns relative to peak K-power (b) –90 ns relative to peak K-power

Figure 8-5. Filaments evident in optical images for 5 cm shell long pulse shot 4075.

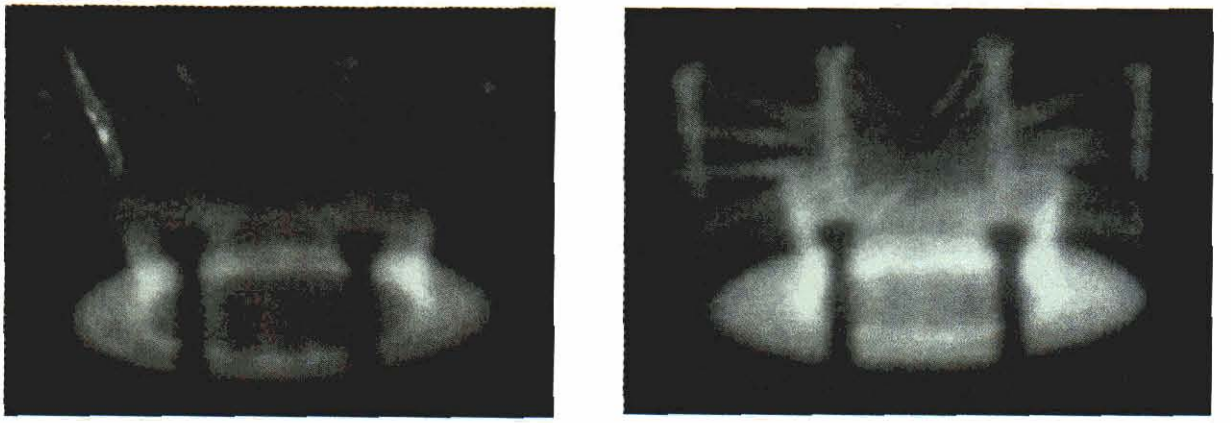

(a) -117ns relative to peak K-power (b) -96 ns relative to peak K-power

Figure 8-6. Filaments evident in optical images for 7-cm uniform-fill shot 4063.

Comparable images for loads on other machines like ACE 4 do not show the same filamentary structure. Hence we may assume that changes in puff valve and nozzle design can control the presence of the filaments and in particular minimize or eliminate them.

Most of these optical images give us mainly qualitative data on the pinch. In principle, we can get pinch diameter as a function of time for comparison with implosion calculations. Unfortunately, usually only one or two frames are well enough exposed to get good measurements. Also, there are the complications of non-orthogonal views on Double-EAGLE and time-dependent brightness variations across the AK gap

In a few cases, we can get quantitative data. Figure 8-7 is one example, showing four frames for a 7 cm uniform fill load. The width of the emission at the nozzle exit systematically increases with time. Perhaps this emission is a measure of the thickness of the current sheath. Lineouts across the diameter are shown in Figure 8-8. Such data might be useful constraints on detailed

MHD models of the implosion. (Also, the end-on views for some shots do give quantitative estimates of the pinch radius that correlates well with models; see Section 3 for an example.)

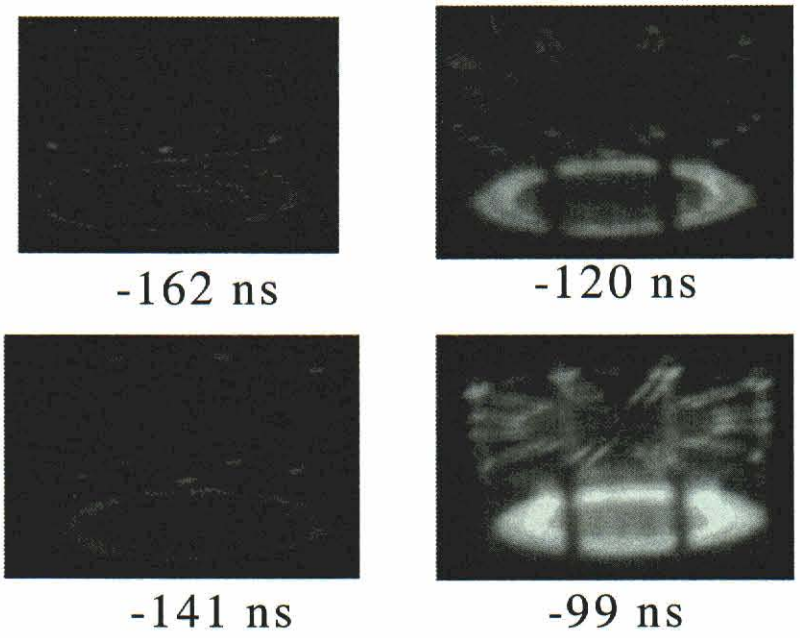

Figure 8-7. Optical images for 7-cm uniform-fill, long-pulse (165 ns) shot 4060.

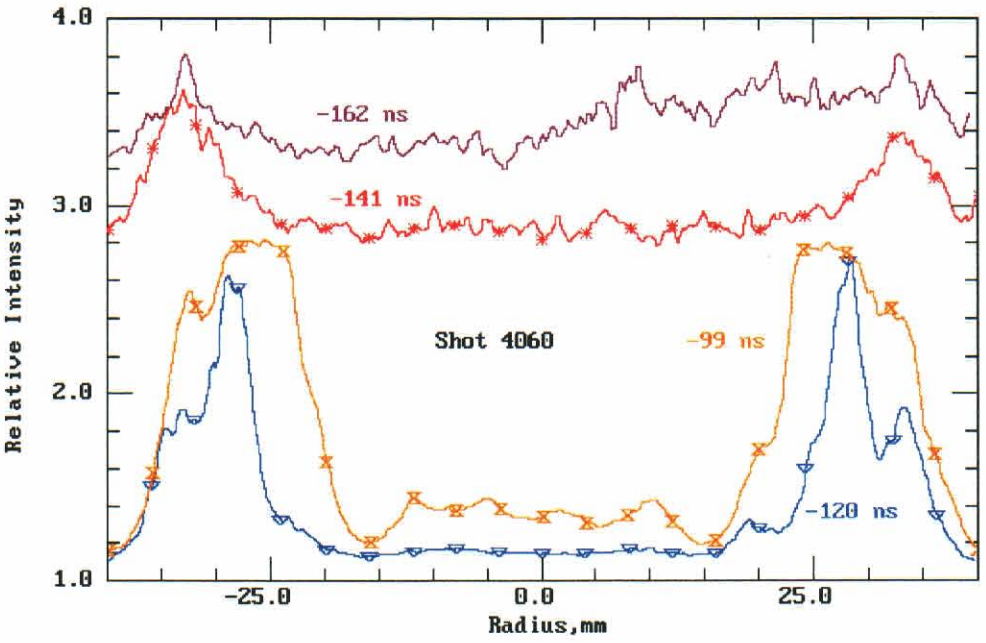

Figure 8-8. Lineouts for the optical images of shot 4060; the apparent sheath thickness increases from 3 mm at –120 ns to 6 mm at –99 ns.

A final example of optical imaging of gas puffs appears in Figure 8-9 for the 5 cm shell load as used on DM2. The near 90 degree view allowed us to clearly see the development of the instability as the implosion proceeded. The bubble and spike structure is quite evident with a characteristic wavelength of about 4 mm.

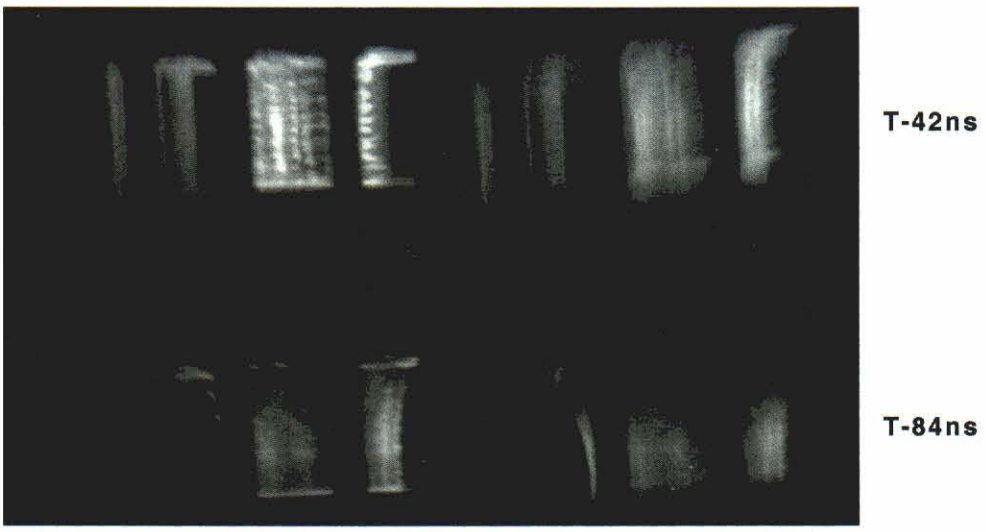

Figure 8-9. Optical images for the 5-cm shell load on DM2 shot 503.

Optical imaging of the aluminum wire shots proved somewhat less successful for a variety of reasons. The camera did need repair during some of the wire load testing, and the final stages of the pinch were often severely overexposed. A few shots gave good data; Figure 8-10 is a good exposure level for the initial part of the 213 ns implosion. In the second frame at –167 ns, one can almost count the individual 38 wires in the array. We also see bright-spot, on-axis emission in the last three frames. This is evidence for blowoff from the wires that implodes very early (≈100 ns) before the main implosion. The hot mass and perhaps some current that arrives on-axis early will likely affect the quality of the subsequent main implosion.

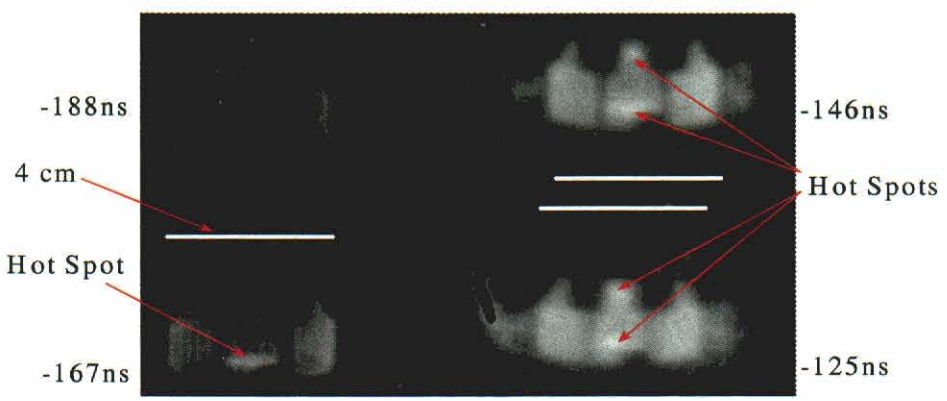

Figure 8-10. Optical images for a 4-cm aluminum wire array implosion, Double-EAGLE shot 4128.

8.1.3 Summary of Load Features Seen in Optical Images.

The short pulse (100 ns) argon puff load shows fairly good azimuthal symmetry. However, all gas loads on Double-EAGLE show axial filaments that may be related to details of the gas flow hardware. These filaments may affect the current sheath development and may be deleterious for the best quality implosions. It is likely that load refinements could eliminate the filaments.

All gas puffs show visible emission growing from the cathode side of the pinch on time scales of 10's of nanoseconds. This emission history may give us clues to the initiation process in gas loads and affect how we attempt to model the implosions with 2-D MHD codes.

Some images are good enough to give us quantitative data on current sheath thickness and diameter as a function of time. Again, such data could be useful in benchmarking detailed codes.

Optical imaging of the wire loads shows clear evidence of the arrival of hot emitting plasma on axis well before the main implosion. This observation is consistent with data from other experimenters who are studying the dynamics of individual wire explosions. It also contributes to the community's evolving understanding of wire arrays and their complexities.

In summary, optical imaging has given us useful clues to initial and run-in conditions. In particular, the optical data should guide improvements in gas flow hardware and geometry. To a limited degree, the data also can provide useful constraints for modeling of the z-pinches, especially current initiation and sheath development. Additional examples of the optical data appear in Sections 2 and 3.

8.2 1-D IMAGING ("ZIPPER") ARRAY.

8.2.1 Diagnostic Design and Features.

The zipper array gives us a time-resolved one-dimensional (1-D) image of the K-shell emission as a function of distance along the pinch. This diagnostic is especially useful in quantifying the "zippering" of the pinch, i.e., the systematic variation of on-axis assembly time along the length of the pinch. While the zipper array lacks the spatial details of a two-dimensional (2-D) microchannel plate (MCP) pinhole camera, the zipper array is very reliable, provides continuous time coverage, and is easy to use. Hence it is a good compliment to other pinch diagnostics.

Our zipper sensor uses a linear array of 14 silicon PIN diodes, positioned behind a perpendicular slit. The array axis is parallel to the pinch axis. The diodes are model AXUV-HS1 made by International Radiation Detectors (IRD). A very thin dead layer makes these diodes almost 100% quantum efficient for photons with energies between < 100 eV and > 5 keV. The low junction capacitance gives each diode a risetime of 0.5 ns. With 1 ns/sample recording, each diode provides a continuous record of the K-shell power from a thin slice normal to the pinch axis. Unlike a MCP, no special time-critical triggering is needed. The diodes are very stable. Once the array and slit are aligned towards the pinch, operation is easy and maintenance is minimal.

While the sensitivity of each diode is a fundamental property of silicon (3.6 eV per electron-hole pair), the effective area of each diode can depend on x-ray energy. This is because the nominal diode, 0.22 mm square, is contained on a 1 mm square die. Photoelectrons from higher energy photons stopping outside the nominal area can be collected as part of the signal. Thus the effective area of the diode is larger than the nominal 0.22 mm squared. To establish the relative responses of the diodes, we made a "flatfield" measurement: the imaging slit was replaced by a thick filter so that each diode had the same view of the pinch. This also let us measure the relative timing between channels (cable and delay for each digitizer) to 1 ns.

One complication is the very high sensitivity of the diodes, which are essentially 100 % quantum efficient. To keep peak signals below about 1.5 volts (30 ma into 50 ohms) for good linearity, heavy filtration is needed. For the ≈1 TW K-shell power of a Double-EAGLE argon pinch, we used a 5 micron silver foil over each diode. The L-edge of silver at 3.38 keV just passes the dominant argon lines, Ly-α at 3.32 keV and He-α at 3.14 keV; Figure 8-11 shows the transmission of the filter, consisting of 12.7 micron of Mylar, 5 micron of silver, and 60 micron of Kapton. The response decreases above 10 keV because of the 80 micron thickness of the silicon.

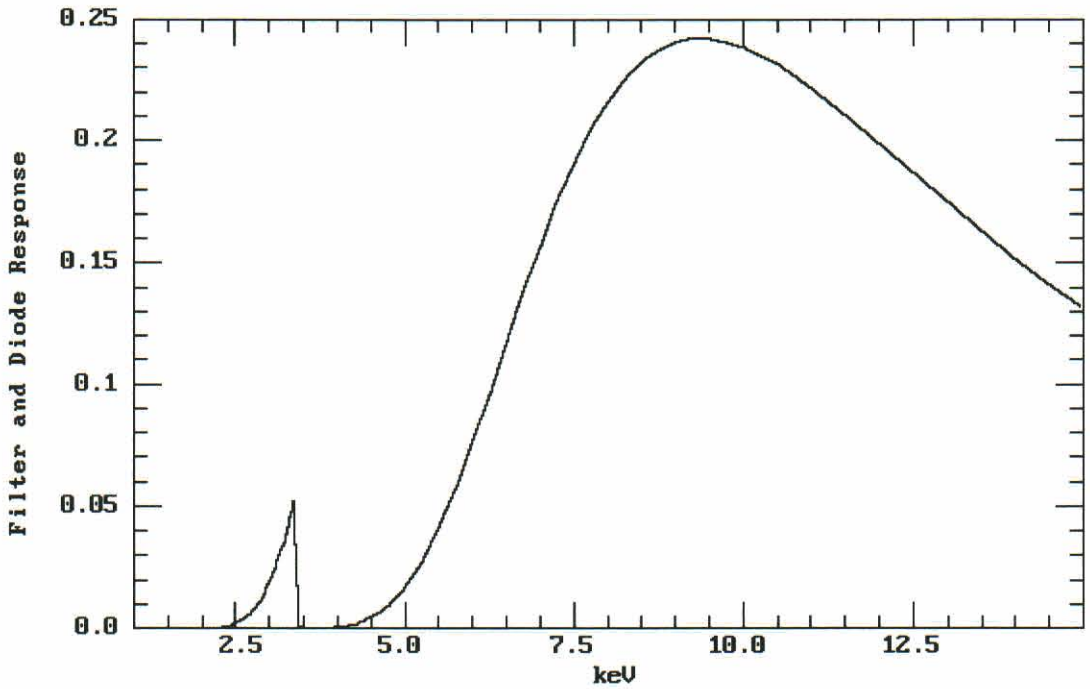

Figure 8-11. Filter transmission for zipper diodes.

The net response to the pinch is a convolution of this response curve with the x-ray spectrum. For a typical argon spectrum, Figure 8-12 shows the integral fraction of the response as a function of photon energy. We see that about half of the diode response is due to the K-shell lines. The rest of the response is due to the high-energy continuum above about 5 keV. Figure 8-13 is a comparable plot for an aluminum spectrum; about 75% of the PRS K-shell output is due to lines below 2 keV. In the later case, less than 1% of the zipper response is due to aluminum

K-lines; most is due to continuum above 2.5 keV. The net consequence for both argon and aluminum is that the zipper array is primarily sensitive to the very hottest parts of the pinch.

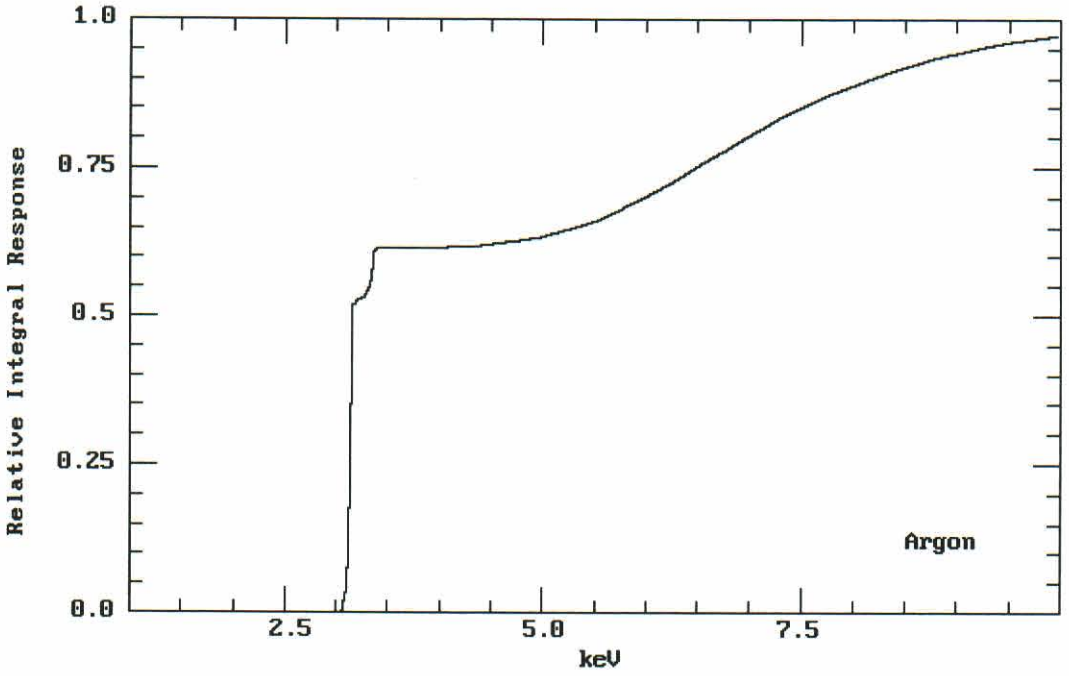

Figure 8-12. Integral normalized response of a zipper diode to an argon PRS.

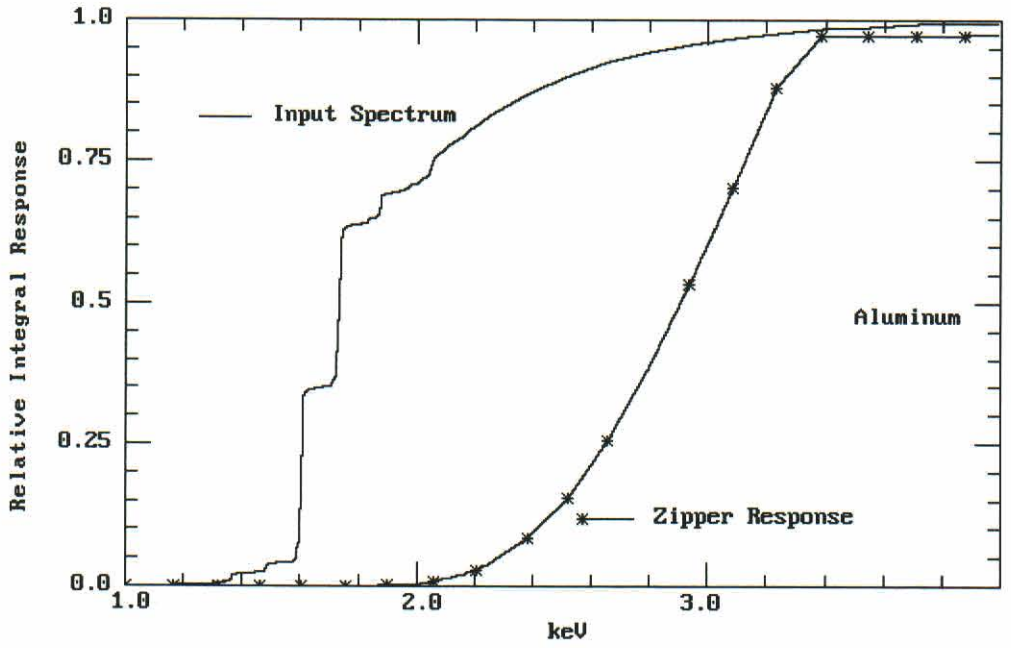

Figure 8-13. Integral normalized response of a zipper diode to an aluminum PRS.

The diodes must also be put at a sufficient range to reduce the signal level. On Double-EAGLE, the maximum practical range was 661 cm. The remaining design considerations are geometric optics. The position of the slit defines the elevation of each diode's view of the pinch. With 0.5 cm between each diode in the linear array and a slit range of 276 cm, the spatial resolution of the zipper array was 0.39 cm at the pinch. (This includes the effect of the 68-degree inclination of the diagnostic ports with respect to the pinch axis.) With 14 diodes, this allowed the array to cover an axial extent of 5.07 cm, i.e., the full 3.8 cm length of the pinch was visible. For the shorter wire array loads, the slit range was reduced to 244 cm to give a resolution of 0.32 cm between diodes.

Finally, the slit height was chosen to be 0.19 mm. Thus for argon loads, each diode could see a 0.41 cm high slice of the pinch; for aluminum, the viewed height was 0.37 cm. Hence, overall the array had a nearly contiguous view of the entire pinch.

8.2.2 Zipper Data Analysis.

Because the zipper diodes are so different from the usual PRS diagnostics (XRDs, PCDs, etc.), it is important to demonstrate that the zipper data are consistent with other measurements of x-ray output. As an example, Figure 8-14 compares the K-shell power waveforms as measured with XRDs, PCDs and the sum of the zipper diodes for Double-EAGLE shot 4072. The agreement in pulse shape is good. This result is typical so long as the each zipper diode's peak signal is kept below about 1.5 volts. Above that level, the zipper pulse width increases because the peak current level (≈30 ma) in the diode begins to saturate.

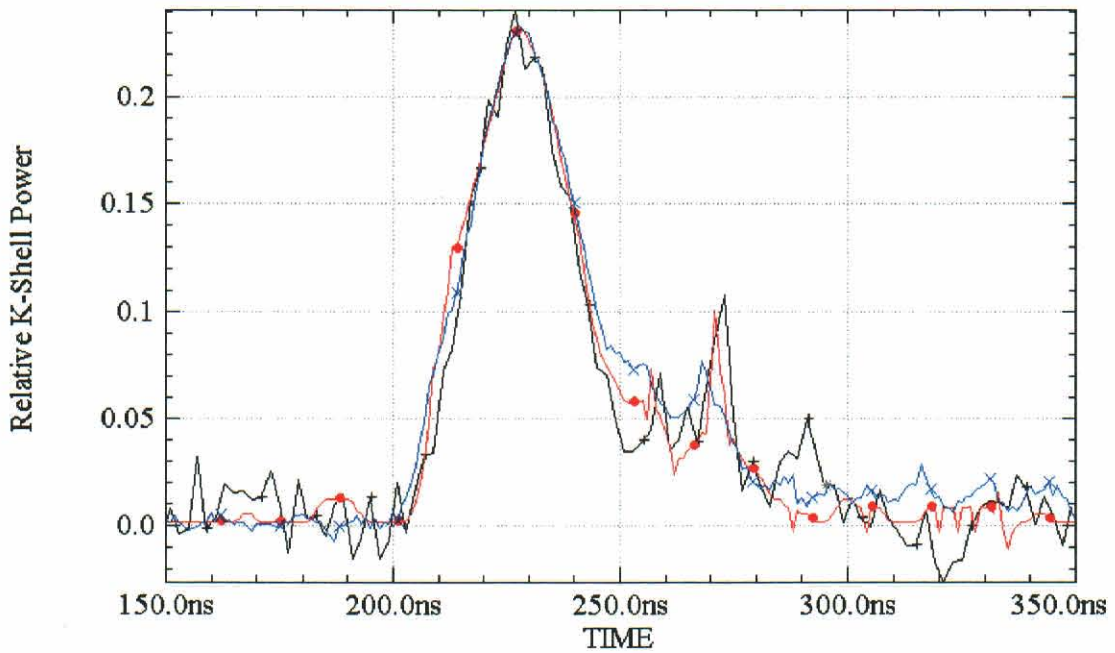

Figure 8-14. K-shell power for XRDs (plus), PCDs (dot), and the zipper array (x's) on shot 4072.

The 1-D image produced by the zipper array is also consistent with other views of the pinch. Figure 8-15 shows the zipper image as a 2-D color-coded map of x-ray power versus time on the horizontal axis and versus distance above the cathode on the vertical axis. Intensity, in relative units of K-shell power per unit length, is depicted by color. Five frames from the MCP pinhole camera also appear in Figure 8-15. Each 2-D frame's brightness has been adjusted for maximum contrast, so relative intensities between frames should not be compared. Both the zipper and MCP views show the pinch evolving: initially emission from most of the pinch to emission concentrated in the lower half of the pinch length.

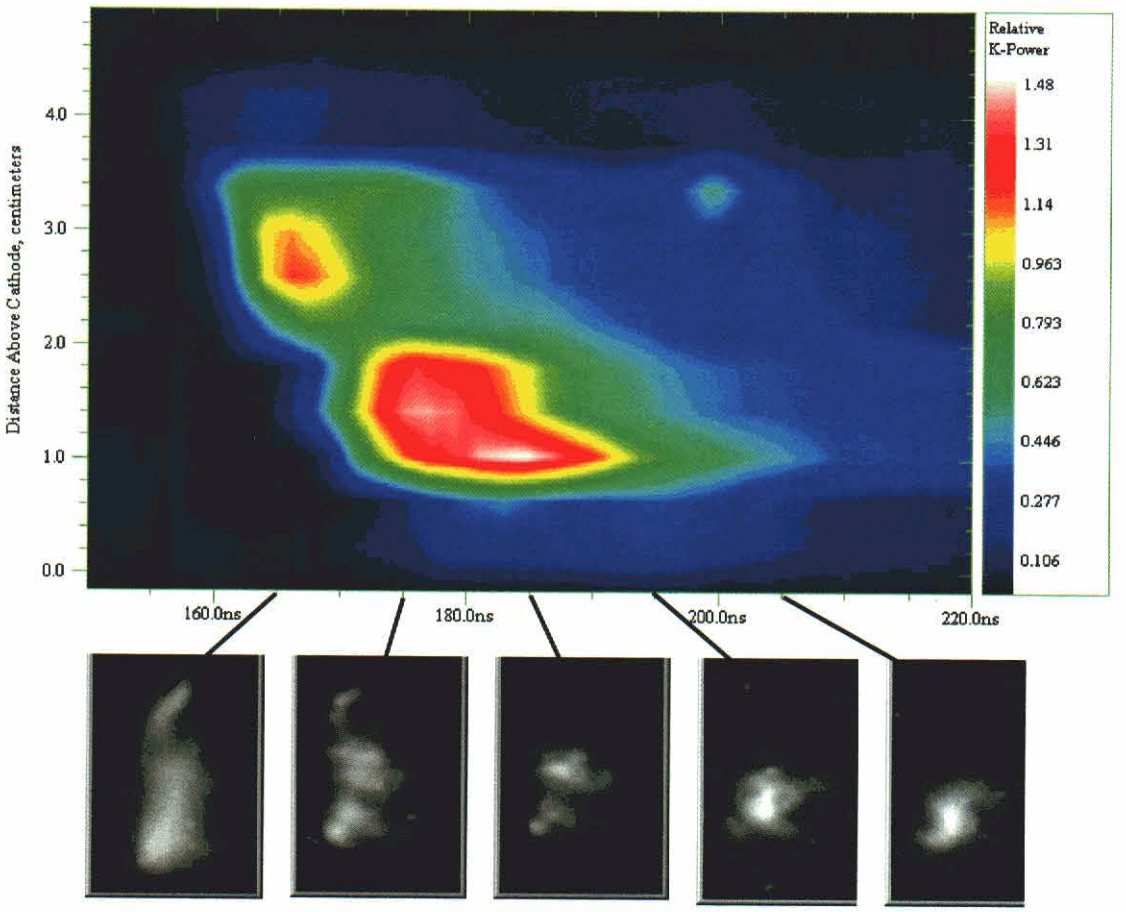

Figure 8-15. Comparison of 1-D zipper image (upper) and 2-D time-resolved pinhole images (lower) for shot 4079. The first frame occurred at about 165 ns; successive frames are 10 ns apart.

Having established some confidence in the performance of the zipper array, we turn to a review of its results. Figure 8-16 compares the zipper images for 4 consecutive shots with the short pulse, 2.5 cm nozzle. The objective of these shots was to hold gas injection constant and demonstrate the repeatability of the load. Gross features were indeed repeatable. The implosion time was 102 ± 2 ns. K-shell yield was 21.0 ± 1.0 kJ. The zipper data show that other features were also fairly reproducible. Only about 50% of the pinch length radiates well, typically the region farthest from the nozzle. As we show in Section 9, this is where the gas flow is actually relatively uniform rather than shell-like. The variation of implosion time with distance above the

cathode (the white line in each image) is almost constant, shot to shot. This implies that we have repeatable behavior in three different areas: gas injection and flow, gas breakdown and current initiation, and implosion dynamics.

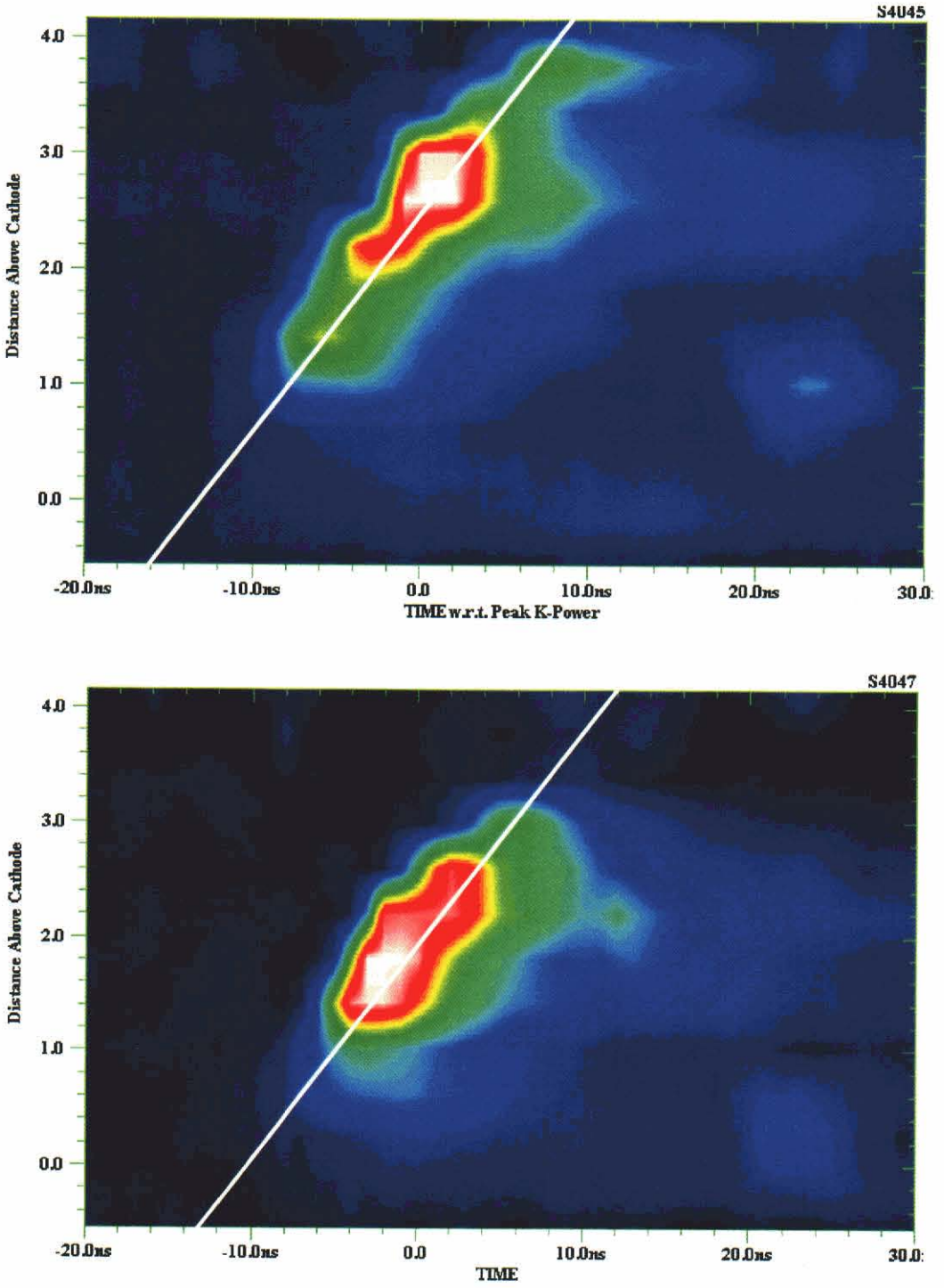

Figure 8-16. Zipper images for four consecutive shots, 4045-4048; relatively consistent zipper behavior argues for repeatable gas flow, initiation and implosion dynamics.

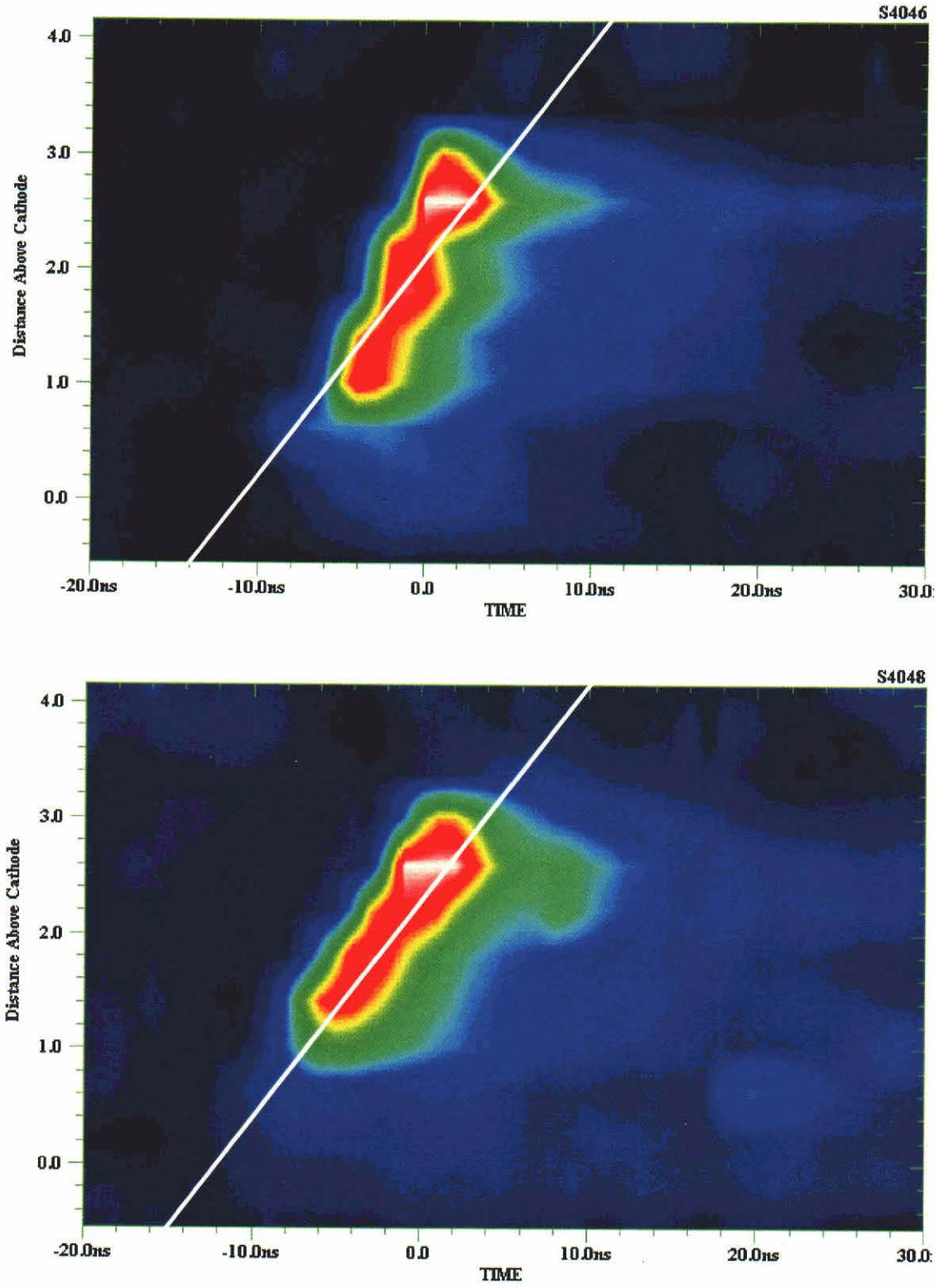

Figure 8-16 (con't). Zipper images for four consecutive shots, 4045-4048; relatively consistent zipper behavior argues for repeatable gas flow, initiation and implosion dynamics.

Our initial purpose for the zipper array was to see if zippering was compromising the radiation output of the long implosion time loads. Problems may arise if the differences in implosion time along the pinch axis are large compared to the thermalization time of each segment of the pinch. In that case, we would expect that the roughly spherical re-expansion of the first mass that arrives on axis will compromise the compression of adjacent parts of the pinch. The overall pulse width of such implosions would be controlled by the arrival time differences along the pinch axis rather than the intrinsic radiation time for a given element of compressed plasma.

Quantitatively, for a well-behaved implosion, we want the zipper "speed," i.e., the slope of the lines drawn in Figure 8-16, to be larger than the implosion velocity. This is in fact what we observe for most of the loads tested. The zipper speed is well above 100 cm/μs while the implosion velocity is below 100 cm/μs. While the zipper time, ≈10 ns, is comparable to the overall pulse width (≈15 ns), the zipper time is not dominant. The net result is that for the uniform fill loads of interest to the DQ objective, zippering is not limiting performance. In practice, for the range of zippering seen in our experiments, there is no clear correlation of K-power or yield with changes in zippering. Figure 8-17 shows examples for significant zipper changes with only modest yield variations.

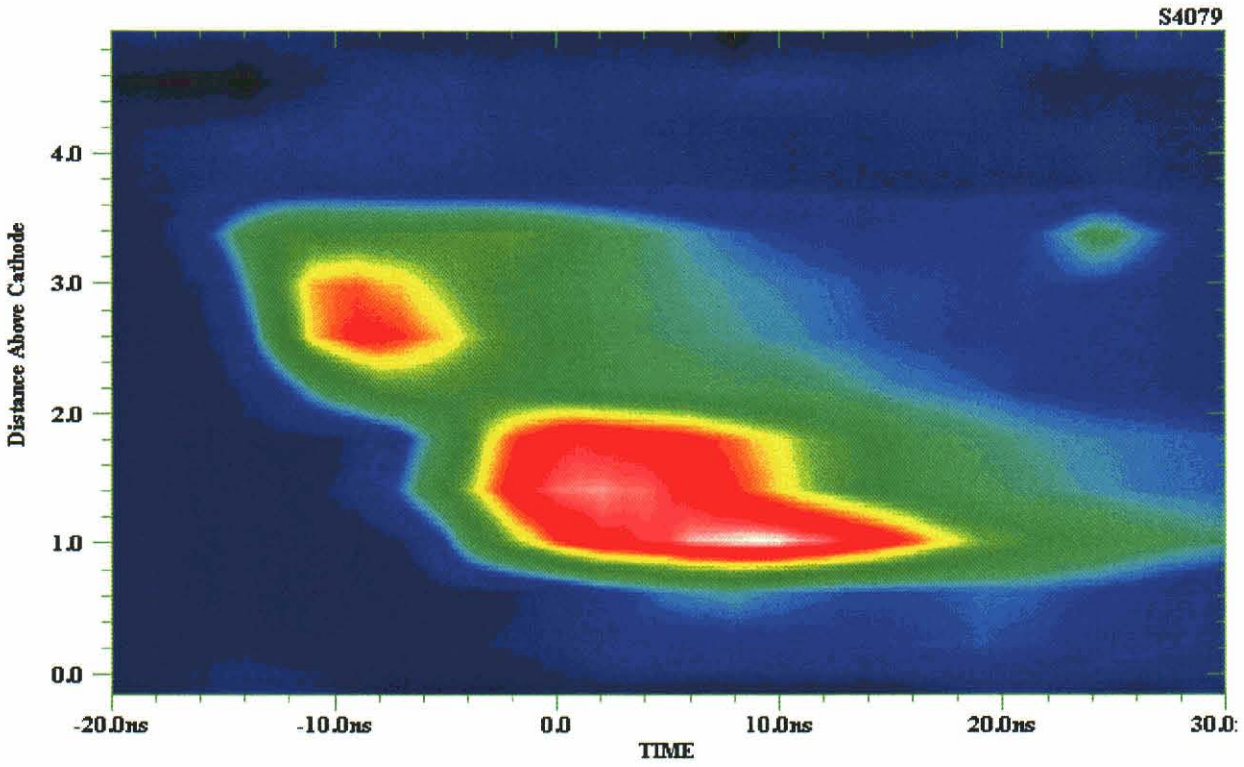

(a) 10.6 kJ, 70 psi, 125 us

Figure 8-17. Modest variations in zippering for 7-cm uniform-fill loads do not give large variations in radiation output: shots 4079 - 4081.

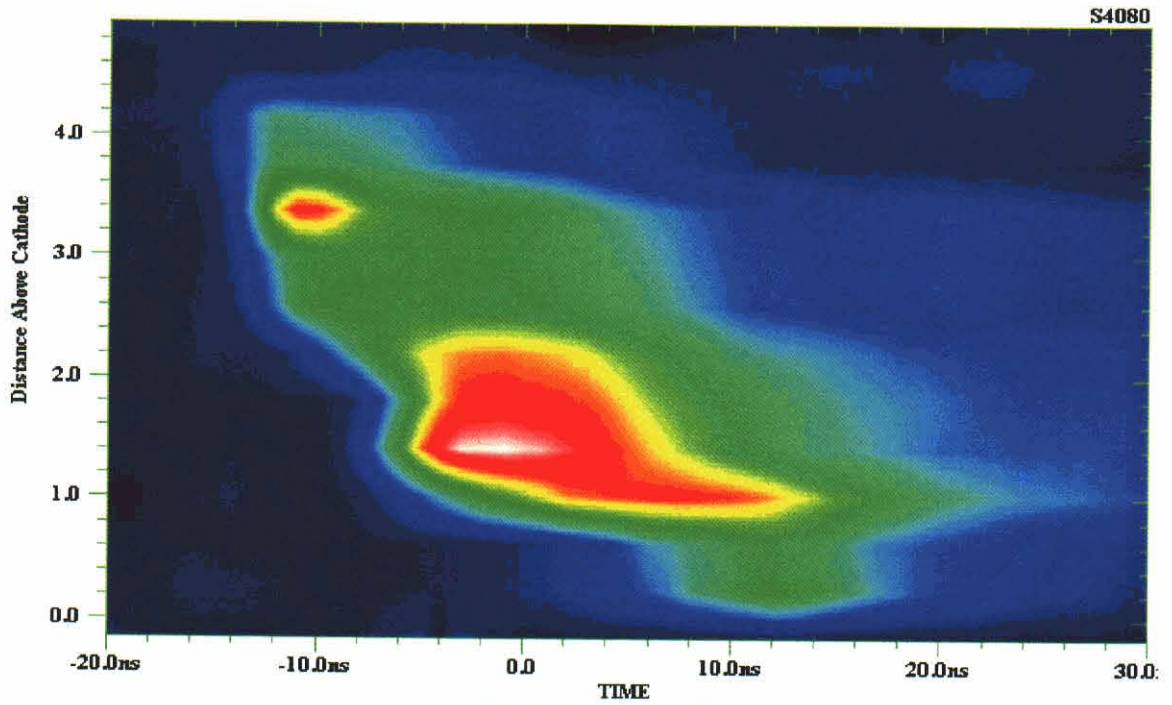

(b) 13.5 kJ, 80 psi, 150 us.

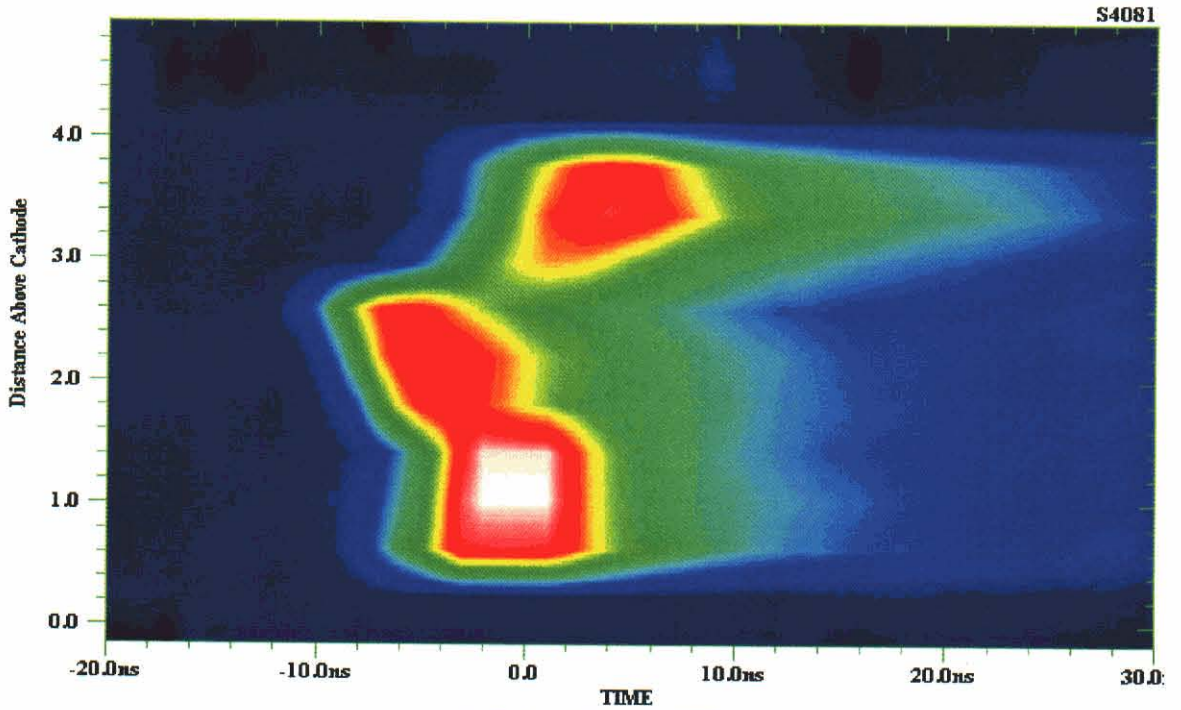

(c) 11.3 kJ, 100 psi, 175 us

Figure 8-17 continued. Modest variations in zippering for 7-cm uniform-fill loads do not give large variations in radiation output: shots 4079 - 4081.

A second objective for the zipper data was to help understand differences in performance for different load types. Data from Double-EAGLE, SATURN (Reference 35) and ACE 4 (Reference 13) all show that uniform fill gas loads perform much better than nominal shell gas loads. The qualitative explanation is snowplow stabilization: the constant addition of mass, as the implosion runs into a uniform fill, mitigates the growth of instabilities. The shell's losses due to instabilities far outweigh the ideally greater efficiency of an imploding shell as a converter of generator energy into radiation.

In practice, shell nozzles produce shell flows only near the nozzle as seen in Figures 9-1 and 9-3. Far from the nozzle, all flows tend to become more nearly uniform fills. Hence one might argue that true shell flows have not been given a chance to perform well, especially if there is significant zippering, i.e., if the uniform fill part of the flow implodes well before the shell portion arrives on axis.

But in fact, gas flow timing on Double-EAGLE was adjusted on some shots to give low zippering. Figure 8-18 shows three examples with zippering no larger than for the uniform fill loads; compare with Figure 8-17. Yet in all cases, the radiated K-power is more than a factor of two lower for the shell-like flow near the nozzle. It was always the more filled-in flow away from the nozzle that radiates best.

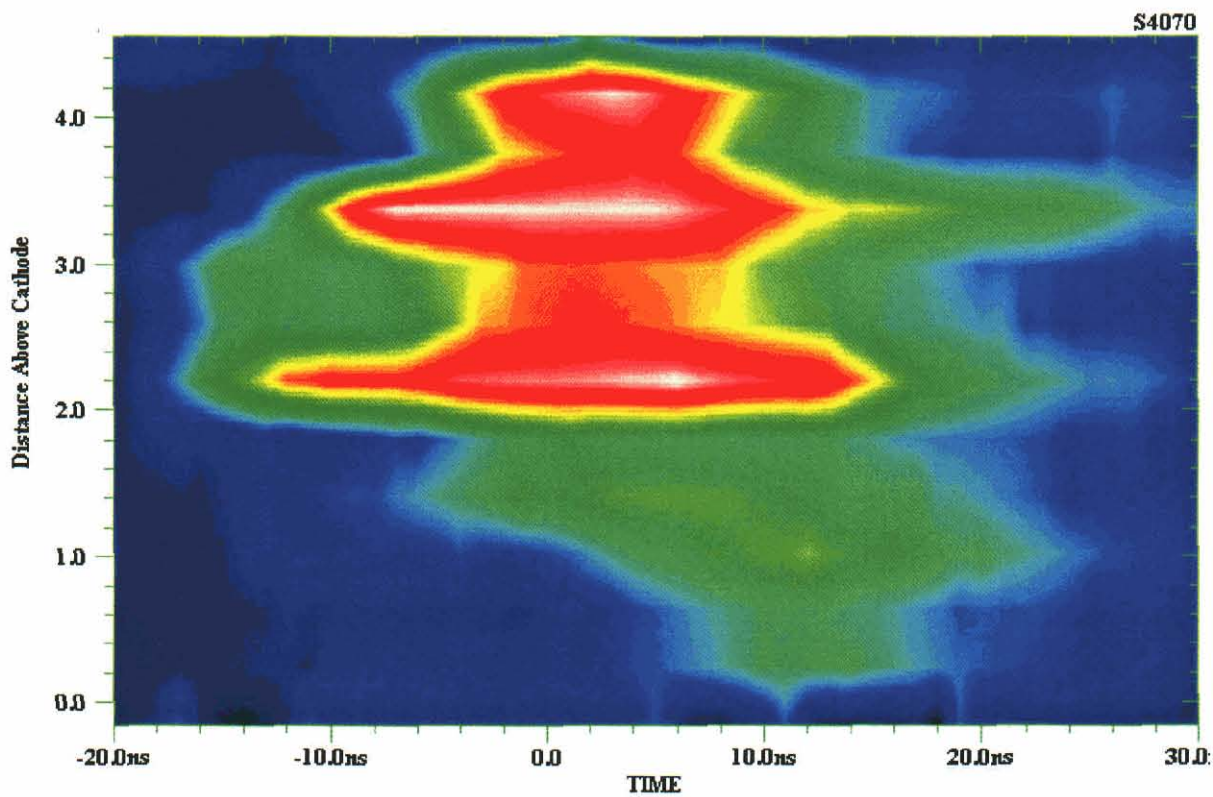

Figure 8-18. Zipper images for three shots (4070, 4072, and 4073) using the 5-cm shell nozzle.

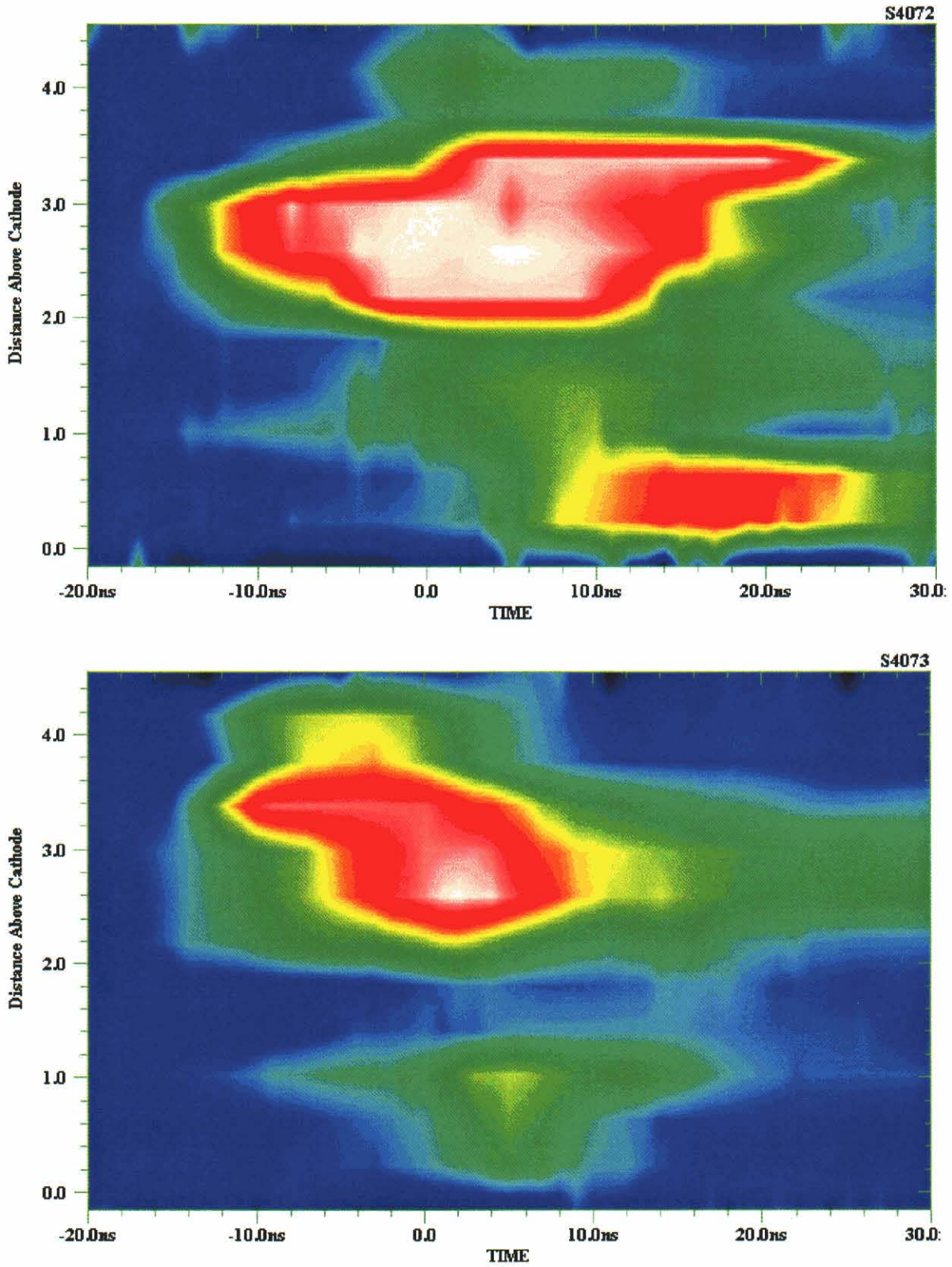

Figure 8-18 (con't). Zipper images for three shots (4070, 4072, and 4073) using the 5-cm shell nozzle.

8.2.3 Quantitative Interpretation of Zipper Timing.

Initial conditions in the z-pinch can affect the radiation output. Within the last few years, Sandia has demonstrated much higher radiated power as the interwire gap in wire arrays is decreased (References 29 and 30). Experiments and models are beginning to offer an explanation for this result. In particular, it is not sufficient that the wire array loads define the initial location of the cold mass. How the individual wires initially expand, the size and timing of the prepulse, and the surface conditions of the wires play significant roles. The better than expected performance of long implosion time wire arrays at Sandia (versus smaller diameter arrays) may be explained as follows. The time scale for merging of the perturbations in individual wires is fixed by the inter-wire gap and the properties of the wire material; the longer implosion time allows that merging to occur before significant radial inward acceleration occurs.

For the gas puff loads of interest for the DQ argon PRS, one might hope that there are comparable details of the initial conditions that, if controlled, would translate into better performance via an understanding of the implosion process. The demonstration of consistent zippering in Figure 8-16 implies some consistency of initial conditions but not true control.

Now, however, we have neutral gas interferometry data that tell us where the cold gas is at the beginning and how reproducible the flow is. Optical techniques (see Section 8.1) may show us how the current initially flows. We may posit that such possible features or information will have consequences for the radiation output. Do we have any reason to believe that details of the gas flow really matter that much?

The best way to address that question would be to use the measured gas flows in 2-D MHD calculations of the implosion coupled to detailed radiation models. But to begin the process and argue that there is hope, we have used the gas flow data from NRL (Reference 16; see Figures 9-1 and 9-2) in simple 1-D snowplow calculations. The measured load currents for actual Double-EAGLE shots were used to drive the implosions. Implicitly, this approach ignores mass flows in the axial (z) direction and it ignores losses due to instabilities. We also assumed that the measured gas densities can be scaled by plenum pressure and, for the 7 cm nozzle, that the screen actually used for the Double-EAGLE shots at the nozzle exhaust was unimportant. (The 7 cm flows were measured by NRL without the screen in place. Subsequent measurements of the 7 cm nozzle by AASC did use a screen, but unfortunately, misalignment of the puff valve parts made the measured flow not axi-symmetric.)

For both the 5 cm shell nozzle and the 7 cm solid-fill, we looked at cases with low gas flow time and a larger flow time. As Figures 8-19 and 8-20 show, the relative variation in imploding mass (versus axial distance) is large for low flow times. Because the implosion time increases monotonically with mass/length, we would expect zippering to be larger with low flow time, when the anode-to-cathode mass difference is greatest.

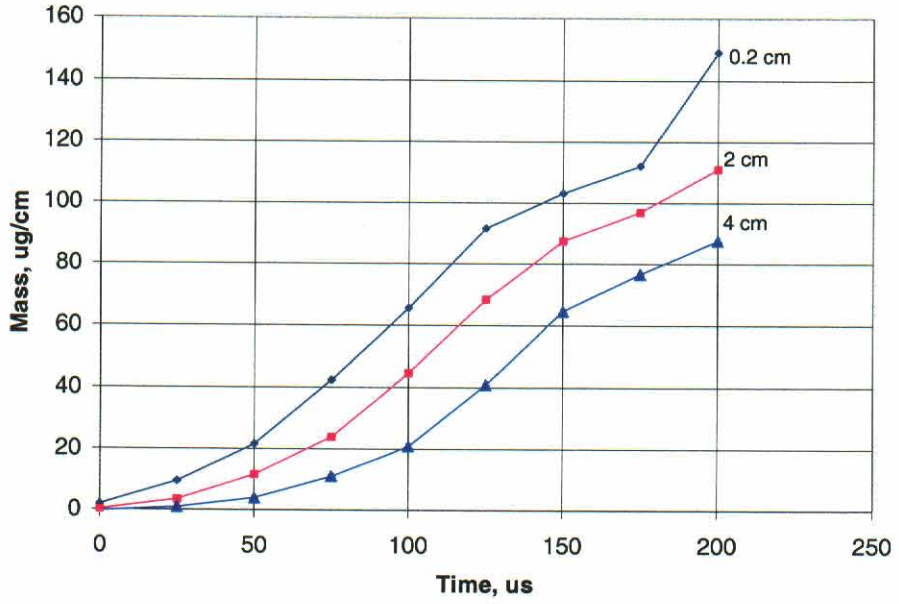

Figure 8-19. Mass loading versus time at 3 axial distances for the 7-cm solid-fill nozzle; the gas flow data were measured for a plenum pressure of 36 psia.

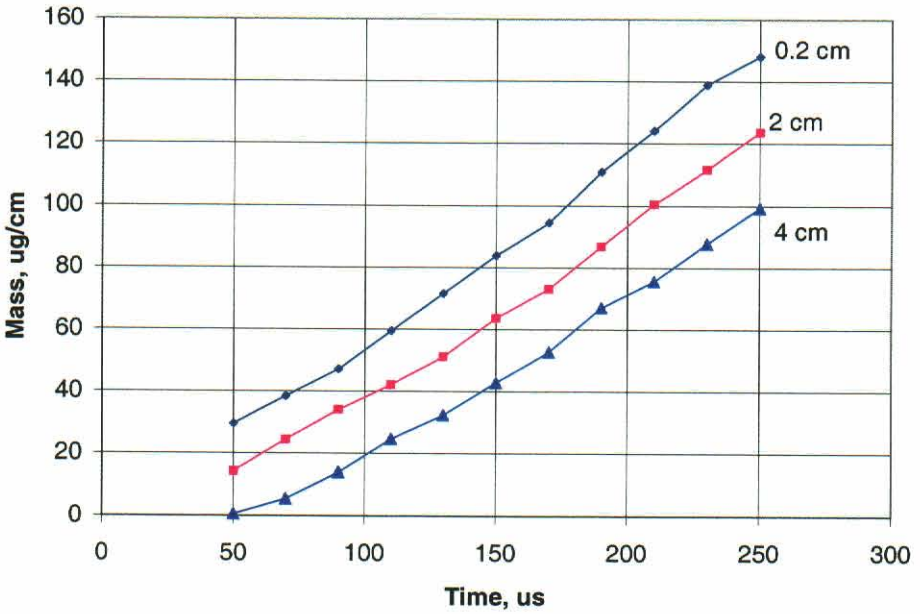

Figure 8-20. Mass loading versus time at 3 axial distances for the 5-cm shell fill nozzle; the gas flow data were measured for a plenum pressure of 15 psia.

The first zippering example, Figure 8-21, is for a 7 cm nozzle shot with long flow time, shot #4081. The heavy black line is the predicted implosion time based on the gas density data at 2 mm, 2 cm and 4 cm elevations. The actual zipper data show virtually no zipper. The

prediction for implosion times of the simple model is remarkably good although about 10 ns early at the anode side of the AK gap.

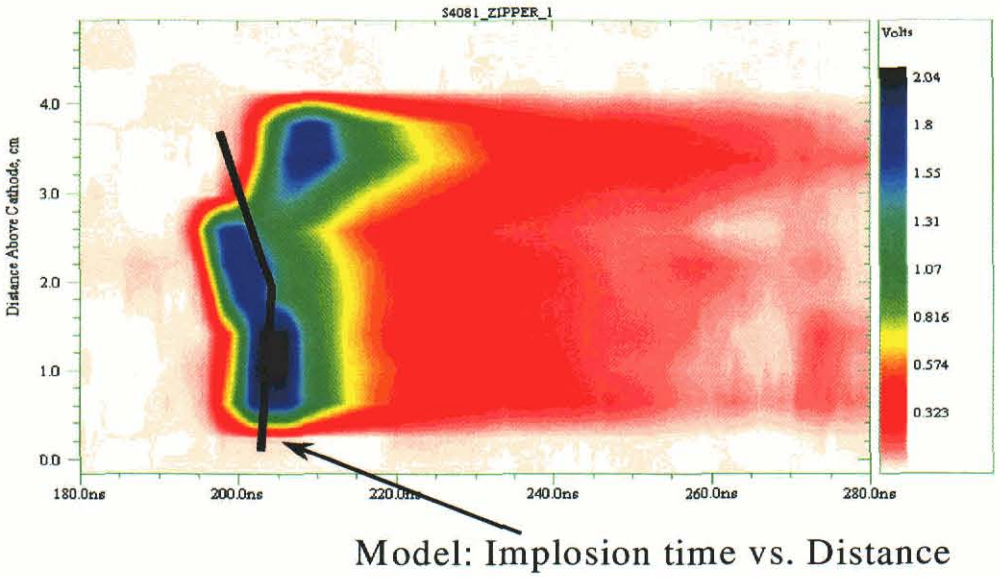

Figure 8-21. Comparison of zipper data and simple model of implosion time for 7-cm shot 4081, 175 μs flow time, 100 psia plenum pressure.

The second example, Figure 8-22, is for a 7-cm nozzle shot with short flow time, shot #4079. As expected from the axial mass gradient data, Figure 8-19, there was more zippering in the shot. The prediction for implosion time also predicts systematic zippering but is consistently about 10 ns late. This may be due to the screen's influence on the true flow or because gas density is not exactly proportional to plenum pressure. Still, the qualitative character of the observed zippering is reproduced by the calculation.

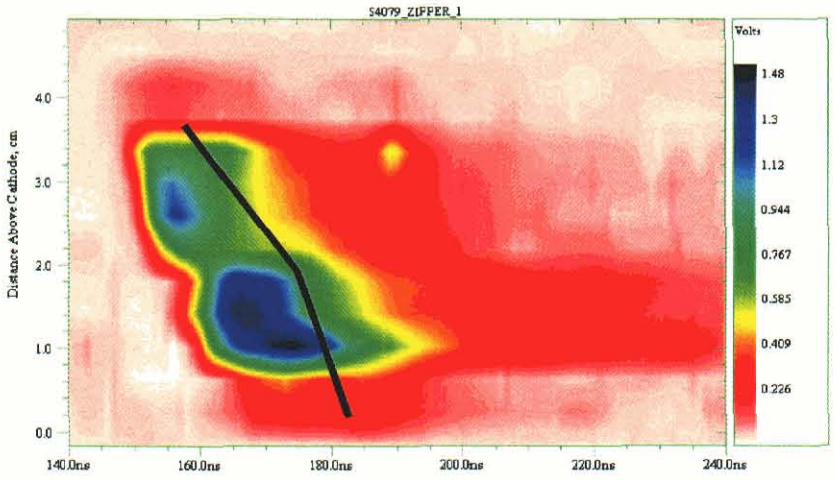

Figure 8-22. Comparison of zipper data and simple model of implosion time for 7-cm shot 4079, 125 μs flow time, 70 psia plenum pressure.

A third example, Figure 8-23, is for a 5 cm shell nozzle shot with long flow time, shot #4073. The data show low zippering as expected, although K-shell power near the nozzle (cathode) end is low. The model does a good job of predicting arrival time, especially far from cathode where the flow is more nearly a uniform fill.

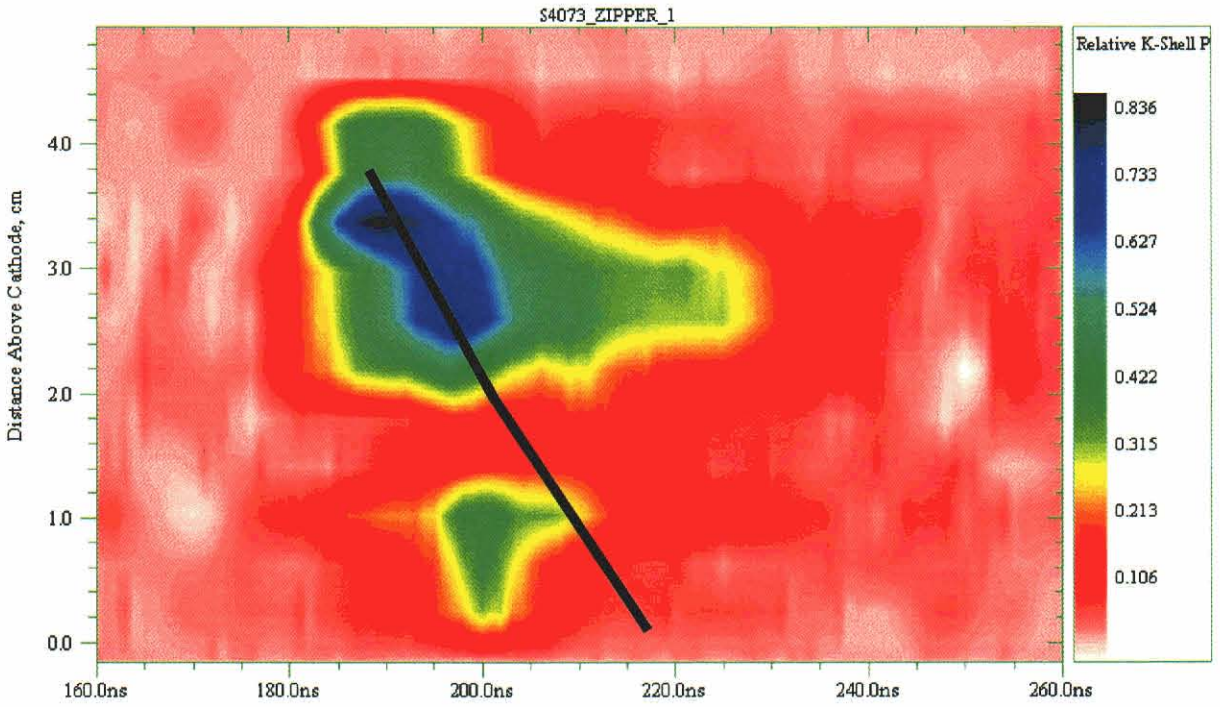

Figure 8-23. Comparison of zipper data and simple model of implosion time for 5-cm shot 4073, 235 μs flow time, 22 psia plenum pressure.

Finally, a fourth example, Figure 8-24, is for a 5 cm shell nozzle shot with low flow time, shot #4068. The data show high zipper as expected with very weak K-shell power near the cathode end. Again, the model does a good job of predicting arrival time, especially far from the cathode where the flow is more nearly a uniform fill. Even near the cathode, the model is consistent with the low level, late emission seen in the zipper data.

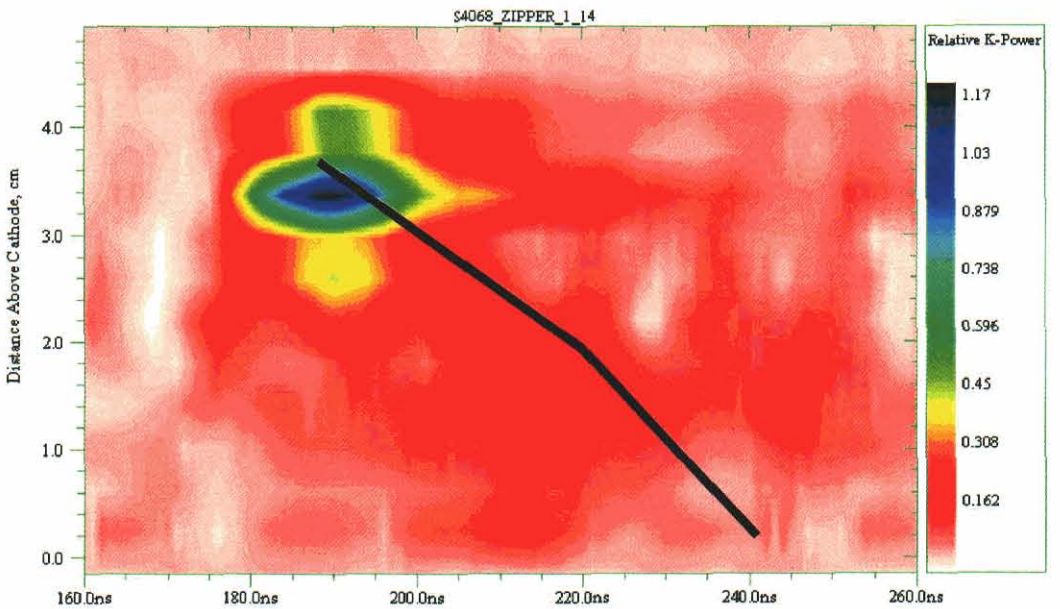

Figure 8-24. Comparison of zipper data and simple model of implosion time for 5-cm shot 4068, 135 μs flow time, 60 psia plenum pressure.

These four examples strongly argue that we have some basic understanding of the initial conditions, initiation and implosion of the gas puff pinches. In particular, we can model the gas puff implosion times with an accuracy that is the equal of wire array loads. In the future, real MHD models should be used to see if they can predict the variation of radiated power with axial position.

8.2.4 Zipper Data for Wire Loads.

In principle, the zipper effect is due to a systematic variation in mass loading (mass per unit length) and radial extent across the AK gap. For gas puffs, this mass gradient can be well documented as in Figures 8-19 and 8-20. But for wire loads, there is no mass gradient, so there should be no zipper. However, as Figures 8-25 and 8-26 show, while wire loads show no systematic zipper, they do show significant power variations along their length. Even modestly high wire count arrays (Figure 8-26), which have shorter pulse widths and higher powers, have more than factor of 2 variations in K-shell power density (W/cm) along their length. It is likely that these variations are due to instability growth that produces "bubble and spike" structures. The dominant wavelength of those structures is roughly 5 mm, although shorter wavelengths might be missed given the 3 mm spatial resolution of the zipper array.

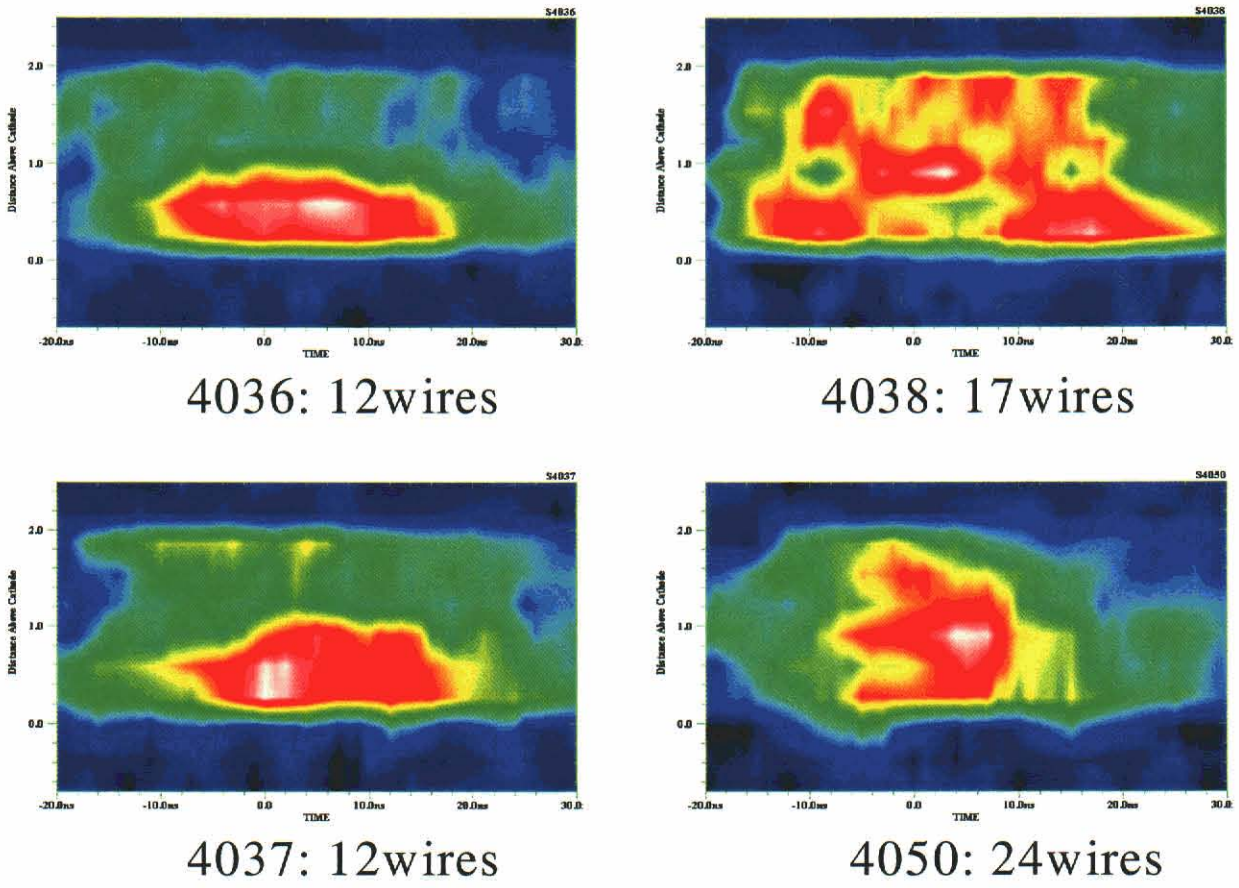

Figure 8-25. Zipper data for short pulse aluminum shots: #4036 @ 85 ns; #4037 @ 82 ns; #4038 @ 93 ns; and #4050 @ 107 ns; each array used a diameter of 2.5 cm.

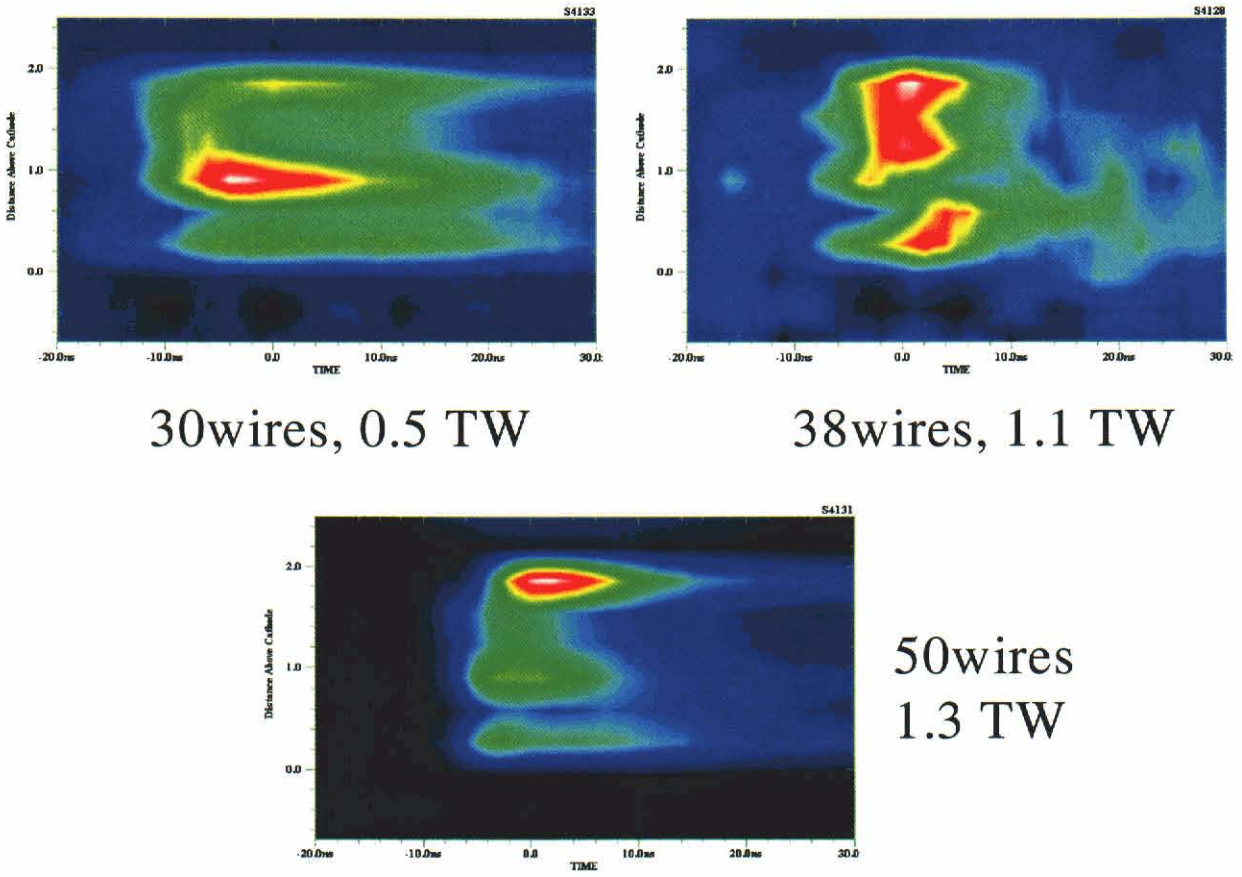

Figure 8-26. Zipper data for 3 long pulse (214 ns) aluminum shots: #4133 with 30 wires, 0.5 TW peak K-shell power; #4128 with 38 wires, 1.1 TW; #4131 with 50 wires, 1.3 TW. Each array used a diameter of 4.0 cm.

8.2.5 Summary of Load Features Seen with the Zipper Array.

For short (100 ns) and long (200 ns) pulse aluminum wire arrays, there is no systematic zipper. But large (> 2x) variations in K-shell power are still present on a random length scale of about 0.5 cm. Reducing interwire gaps to 0.25 cm improves peak power but does not eliminate large axial variations in the power.

In contrast, the gas puff loads do show a systematic zipper. However, it is not large enough in most cases to upset the performance of the pinch. For both short pulse and long pulse shell flows, the truly annular flow near the nozzle is seen to radiate poorly. The more filled-in flow far from the nozzle radiates best.

The solid-fill flows tend to radiate more uniformly along their entire length. Gas flow timing and plenum pressure can be adjusted to significantly change the zippering behavior. As noted above, for the range of zippering times explored in the experiments presented here, the magnitude of the zipper is not important for radiated K-shell yield.

There is growing evidence that we can be quantitative in our understanding of gas puff loads. Gas density measurements can be coupled with the measured current drive to predict the observed implosion time of a load as a function of position across the AK gap. This implies reproducible and plausible behavior for the gas flow, current initiation, and implosion dynamics of these loads.

In summary, the zipper data show that even good pinches show significant variations with axial distance. Hence simple comparisons of global data (K-shell power waveforms, a pinch diameter, a single temperature, etc.) with 0-D, 1-D models should proceed with caution.

8.3 USE OF CCDS FOR X-RAY IMAGING ON Z-PINCHES.

8.3.1 Introduction.

Several key z-pinch diagnostics produce 1-D and 2-D images: spatially resolved spectrographs and pinhole cameras. These diagnostics routinely use film to detect and record the image. Film is compact and relatively inexpensive for qualitative use. But it has high facility costs (dark room and microdensitometer upkeep), and "hidden" expenses (film and processing chemicals acquisition plus hazardous waste disposal). Scientifically, the "costs" are also high. Accurate quantitative information requires operators trained in carefully-controlled film development and digitization, capital investment in expensive (~$100k) equipment, such as a microdensitometer, and significant labor (i.e., time). Typically the developed film is not available for qualitative inspection until hours after a test. Quantitative data from the image requires additional hours or days for microdensitometer scanning.

Under a separate DTRA contract, we have successfully demonstrated the use of charge-coupled devices (CCD) as a replacement for film. During the long implosion time development effort discussed in this report, we made use of the CCDs to improve data quality and reduce analysis time. With a CCD, the qualitative image can be viewed within seconds of a test. We get quantitative image and spectral data within 30 minutes of a shot. This has allowed us to make decisions about the configuration of the next shot based on quantitative interpretation from the most recent shots, thus enabling more effective load development.

The hardware used included 4 CCD camera image recording systems and a soft x-ray calibration facility. Two of the four CCD image recording systems have been configured to detect x rays directly: one records time-integrated x-ray pinhole images and the other spatially-resolved but time-integrated x-ray spectra. The other two CCD systems record optical images produced by phosphors in an x-ray streak camera mounted on a spectrograph and an x-ray framing camera used in a pinhole camera. The soft x-ray calibration facility is used to confirm the operation of diagnostics before being fielded on a test. Characteristic x-ray lines from aluminum, palladium, and titanium anodes are used to confirm crystal alignment in spectrographs and the transmission of x-ray pinholes. A gas proportional counter monitors the x-ray source output during diagnostic checkout.

We also used newly developed software to analyze the CCD image data. The x-ray pinhole camera routine generates plots of brightness, plasma diameter, and the radial offset of peak emission (a measure of pinch "kinking") versus axial position; it also produces a plot of the axially-averaged radial profile. The spatially-resolved spectrum routine generates plots of the line brightness and Ly_α to He_α ratio versus axial position, and also an axially-averaged x-ray spectrum. These data, combined with the usual x-ray yield and power diagnostics give us very good measures of the overall performance of the PRS load.

8.3.2 Environmental Considerations.

To use CCDs, we had to consider the challenges associated with the harsh z-pinch pulsed power environment, which include RF noise, x-ray bremsstrahlung, and mechanical shock. RF noise is produced in high current switches and transmission lines inside the experimental facility. It can produce ground loop voltages that upset sensitive electrical equipment and integrated circuits. X-ray bremsstrahlung, with energies extending to above 1 MV, results when energetic electrons are lost at different points in the electrical transmission line near the z-pinch load. X-ray fluxes can generate spurious currents that upset electrical instrumentation and also "fog" the recording medium. Finally, the z-pinch vacuum chamber "jumps," that is, physically moves, during a shot, which means that anything rigidly attached to it will experience a rapid acceleration. Such acceleration could damage delicate equipment.

Our testing has demonstrated that these challenges can be met for CCD systems. Thorough RFI shielding of the camera, it's nearby controller electronics and intervening cables prevents electrical "upset". Hard x-ray bremsstrahlung is indeed a potential noise source. It produces single pixel counts in the CCD camera as high as 4000, which corresponds to an absorbed pixel x-ray energy of ~100 keV. The voltage between the anode and cathode on Double-EAGLE is as high as 1.5 MV for z-pinch loads, so an electron lost to the anode with that much energy could easily produce 100 keV x rays. In most cases, acceptable signal to noise ratios have been obtained in spite of this hard x-ray background. Where feasible, we have located the CCD camera heads as far from the source as possible, reducing the background as the reciprocal of distance squared. We have also reduced noise by surrounding the camera head RF shielding boxes with 1/8-inch thick sheets of lead. With such steps, signal to noise ratios have proven quite good. Finally, use of the CCDs on both Double-EAGLE and SATURN have shown that the mechanical shock is not a serious hazard to the cameras.

8.3.3 System Description.

We used a CCD camera system that has recently been characterized in the 1 eV to 9 keV spectral region (Reference 36). The CCD chip, produced by Scientific Imaging Technologies, has 24-micron square pixels in a 512 x 512 array; thus the sensitive area is 12.3 mm square. The chips can be coated with anti-reflective (AR) coatings by the manufacturer, and in our case we requested chips with both visible (VIS) and ultraviolet (UV) AR coatings since we wanted to be able to record images from both P-20 and P-11 phosphors, and also UV plasma self-emission. These AR coatings were considered proprietary by the manufacturer, so the chemical formulas were not available for use in x-ray absorption calculations. But the coatings are expected to be a

few light wavelengths thick, and we did not see unexpected x-ray absorption features in the spectrum when the cameras were used to detect multi-keV x-rays directly. To improve sensitivity, the chip back was thinned by additional etching, and then mounted so that illumination strikes the back of the chip. The chip is mounted in a camera head provided by Princeton Instruments (Reference 37). A Peltier device provides cooling to reduce the pixel dark current; typical levels were about 1 count per pixel per second. Because the camera head was located in a metal box to provide RF shielding and air flow was limited, water flow was used to remove the excess heat. The pixel data was digitized to 16 bits (corresponding to a full pixel well of 350,000 electrons) at a rate of 100 kHz using correlated double sampling to reduce the read noise.

We used the CCD cameras to either detect optical light produced in a phosphor as a result of the z-pinch x-rays, or the x-rays themselves, directly. For optical measurements, the camera nose was vacuum sealed with a cap that had an optical window on it. For x-ray measurements, the camera nose was either open to the diagnostic vacuum system, or was vacuum sealed with a 10 mil Be window. The vacuum sealed heads allowed the camera cooling to be run continuously, without fear of a diagnostic vacuum failure. Because the chip detects 3 keV x-rays with 80% efficiency, and 3.65 eV is required to produce an electron-hole pair, a pixel will saturate at a fluence of about 1 photon/μm^2 or 530 photons per pixel. If detected in a single pixel, a single 3keV photon will produce a digitized signal of 150 counts.

The camera system, as supplied by the manufacturer, consisted of a camera head, camera controller, peripheral component interconnect (PCI) card, and cables to connect between the head and the controller, and the controller and the PCI card. The PCI card was installed in a computer running the Windows95 operating system. The manufacturer's software program, which ran on the computer, provided control of the camera operation and the ability to acquire, view, manipulate, and save the raw camera images to disk files. The controller box was supplied with filtered AC power. A fiber optic cable connected the controller with the PCI card in the computer, which was located in a screen room outside of the test cell.

Since the camera dark current noise level was 1 count/pixel/second, signal to noise was not strongly affected by integration times up to 10-20 seconds. Normally we use triggers from the facility master timing system to enable and trigger the camera 0.5 seconds before firing the machine. The image integration time is typically 3 seconds.

As noted above, the CCD camera can be used to record either optical light emission from a phosphor, or x-rays directly. Since the intrinsic image readout time is many microseconds, the CCD can not be used for direct time-resolved x-ray imaging.

Thus for x-ray framing or streak systems, our approach was to collect optical light emission from the x-ray sensing phosphor with a fast lens imaging on to the CCD. This combination simply replaces the Kodak 2484 film backs we had been using (which were mounted in contact with the fiber optic outputs of the diagnostics).

For the time-integrated systems, we chose to record x-rays directly with the CCD to increase sensitivity over the use of a lens to image a phosphor. This is because if the lens collects 5% of

the phosphor light, and the phosphor is 5% efficient in absorbing x-rays and emitting the x-ray energy as optical light, then there is a potential signal gain of 400. This increased signal can be used to improve the signal to noise ratio and/or improve the spatial resolution of the measurement (by allowing a smaller pinhole or narrower imaging slit to be used). The spatial resolution should also improve with direct x-ray detection because the fast optical lens, which was needed to couple the phosphor light to the CCD, has been eliminated.

8.3.4 Results.

In adopting CCDs for z-pinch diagnosis, it is important to demonstrate that the promise of higher quality data is actually achieved. Figure 8-27 is one example. Here the integrated brightness of time-integrated CCD pinhole images is compared with the argon K-shell yield derived from calorimeters. We see that there is an excellent linear correlation.

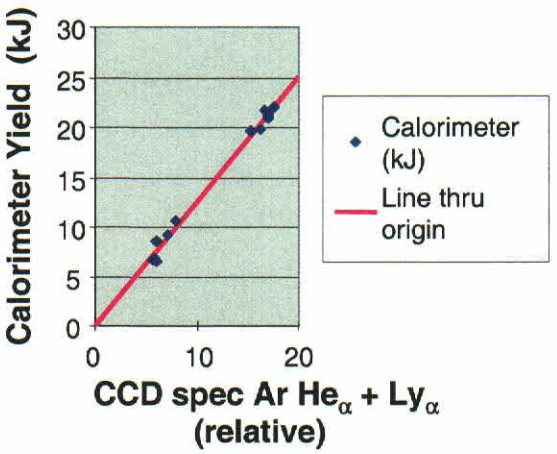

Figure 8-27. Calorimeter yield versus integral CCD response.

A second example compares the performance of film and CCD from some aluminum wire experiments on SATURN. The goal of the SATURN measurements was to determine plasma density and temperature from magnesium dopant line brightnesses and ratios. For this reason the film and CCD radially resolved spectrographs were set up to record the He_α and Ly_α lines of magnesium. Figure 8-28 shows a comparison between the CCD and 2497 film recorded spectra. The 2497 film data was digitized with a microdensitometer and then converted from film density to exposure using a computer program. The geometry of the two radially resolved spectrographs were similar, as shown in Table 8-1, with the CCD version having 30% higher spatial resolution because the CCD is located further from the source than the film. Both spectrographs used KAP crystals to disperse the spectrum, and the signal to noise, defined in this case as the ratio of the peak signal to the standard deviation of the background, was about 25 in both cases.

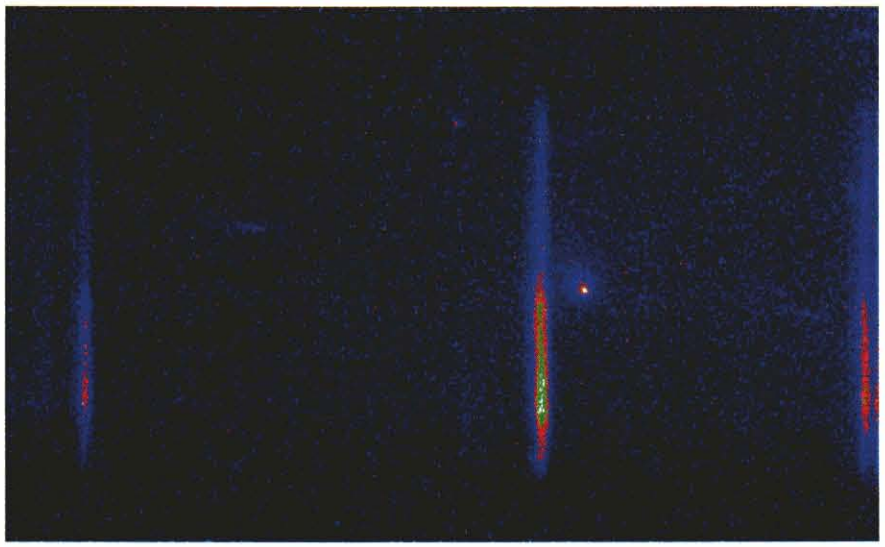

(a) X-ray CCD Spectrum

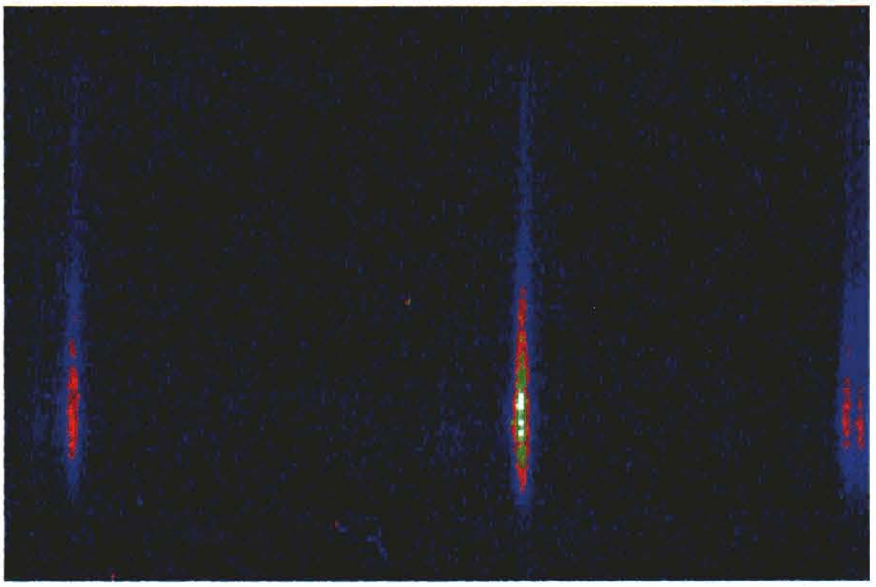

(b) 2497 Film Spectrum

Figure 8-28. Spectrum for aluminum, doped with magnesium, SATURN long pulse shot 2640. (a) CCD recorded spectrum. (b) Data from 2497 film that was digitized with a microdensitometer and then converted from film density to exposure.

Table 8-1. Parameters for CCD and 2497 film comparison. The spectrograph geometries are similar, the main difference being the slit to CCD camera distance.

Spectrograph type	CCD	2497 Film
Source to slit distance	417 cm	400 cm
Slit to CCD or film distance	234 cm	100 cm
Source to CCD or film distance	651 cm	500 cm
Slit width	140 μm	114 μm
Radial resolution on source	390 μm	570 μm

We did quantitative comparisons between the spectral and spatial profiles recorded by the two spectrographs. Spectrally, we determined the line width of the Mg Ly_α line, and the Ly_α to He_α line ratio (see Figure 8-29). We found the CCD camera gave somewhat higher quality data: the line width was 23% narrower and the line ratio had 11% less scatter. Spatially, we looked at the radial profiles of the Mg Ly_α and He_α lines. Comparisons of the Ly_α radial profiles for two shots are shown in Figure 8-30. There is excellent agreement for one shot, and good agreement for the other; the same calibration factor for the CCD camera was used for both shots, indicating consistency between the CCD response and the film processing and digitization. The differences seen in the shot 2640 data may be the result of slightly differing fields of view for the two spectrographs.

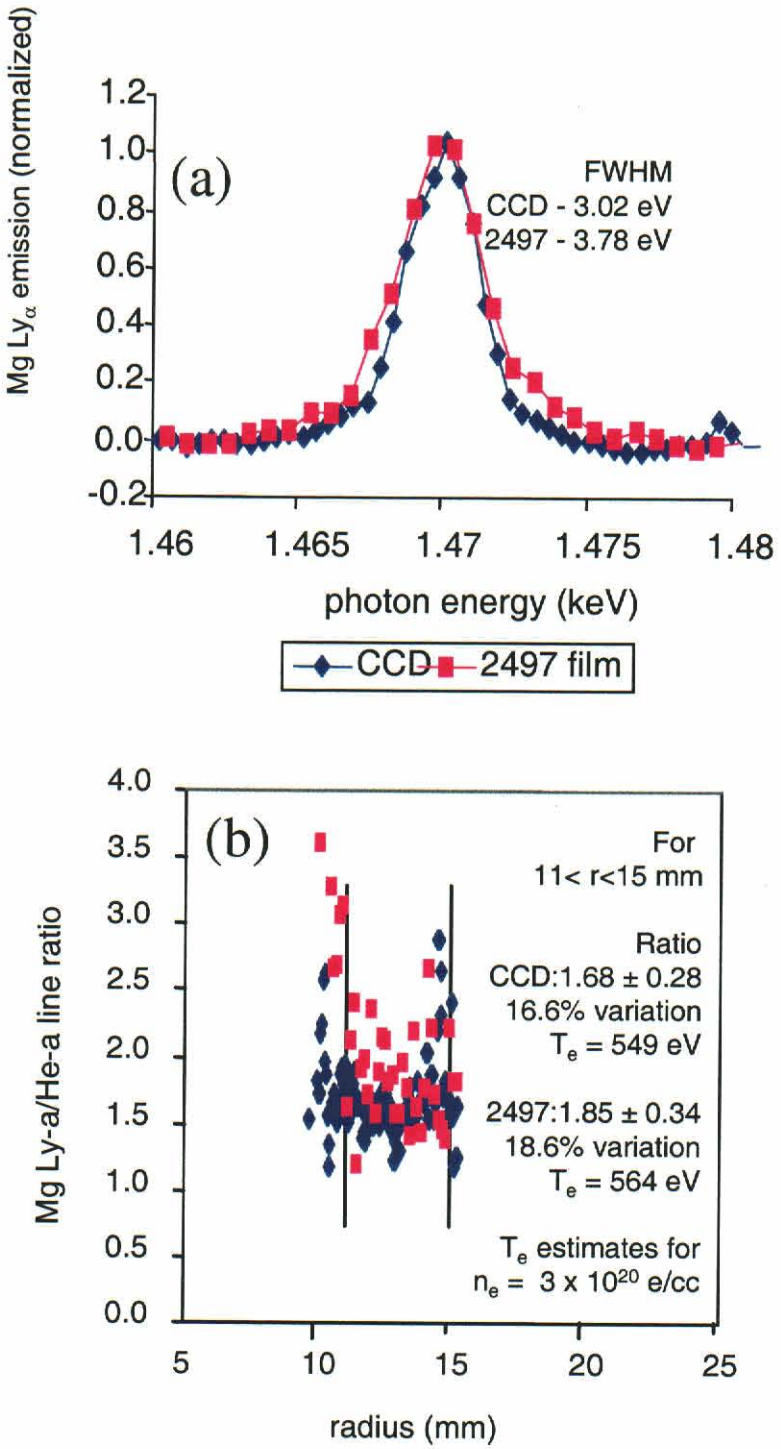

Figure 8-29. Spectral comparison between the CCD and film-recorded data. (a)The FWHM of the CCD-recorded Mg Ly$_\alpha$ line is slightly smaller than the corresponding film-recorded value. (b)The CCD-recorded line ratio has slightly less uncertainty than the film-recorded one. Estimated temperatures differ by 1-2 percent.

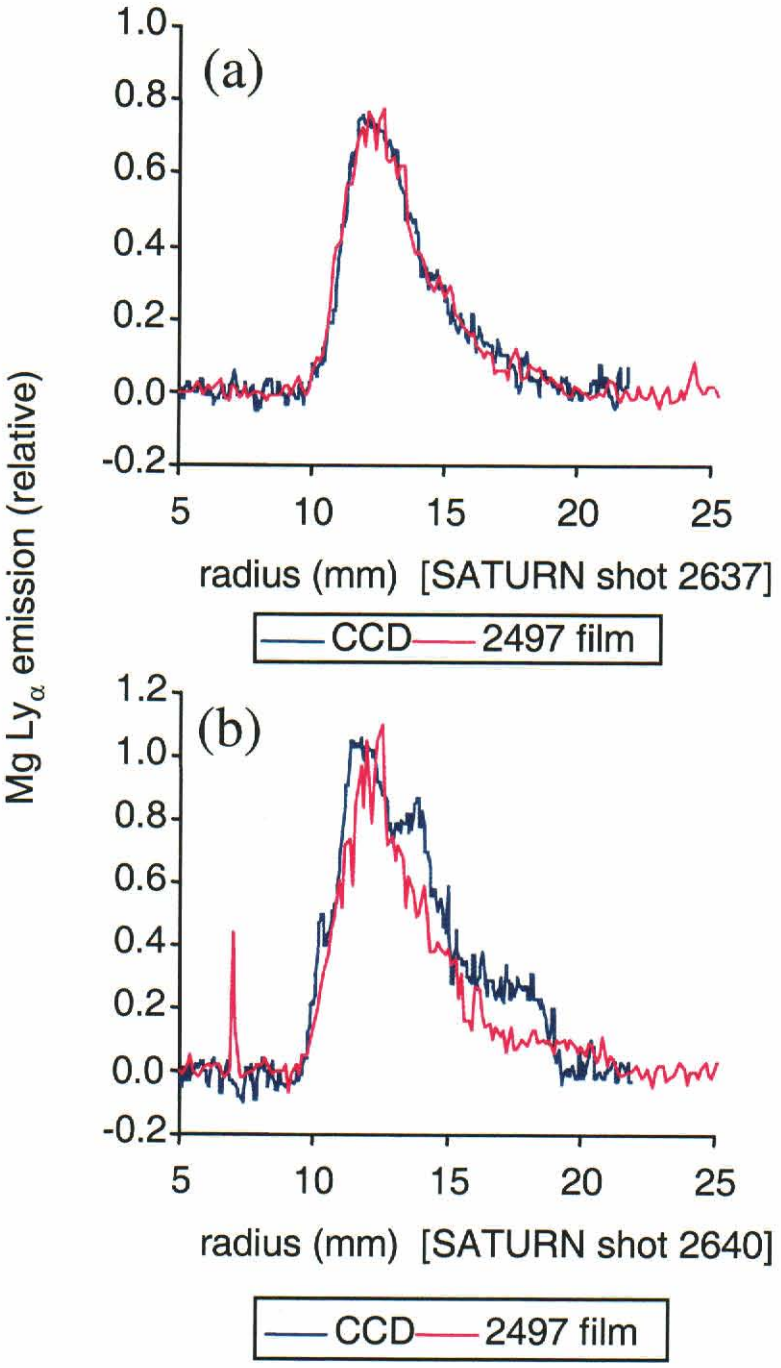

Figure 8-30. Agreement between CCD and film-recorded radial profiles for the Mg Ly$_\alpha$ line are either (a) excellent or (b) good.

The spectrograph data can be used to estimate the relative sensitivities of the 2497 film and the CCD. Using the data from shot 2637 (see the previous figure), 2497 film density can be compared with CCD response; see Figure 8-31. The CCD counts have been scaled as the square of the distance from the source and the reciprocal of the slit width to compensate for geometric differences between the measurements (we assume that the KAP crystal integrated reflectivities

are equal). Also shown in the figure is a curve based on the film model of Henke (Reference 32); a CCD count of 10,000 corresponds to a photon flux of 1.8 photons/μm^2 at 1.47 keV. Two observations from this data are: (1) assuming linear CCD response, the CCD sensitivity threshold is at least 10 times lower than that of the film, and (2) the CCD will saturate at specular film densities in the range 0.8 to 1.2.

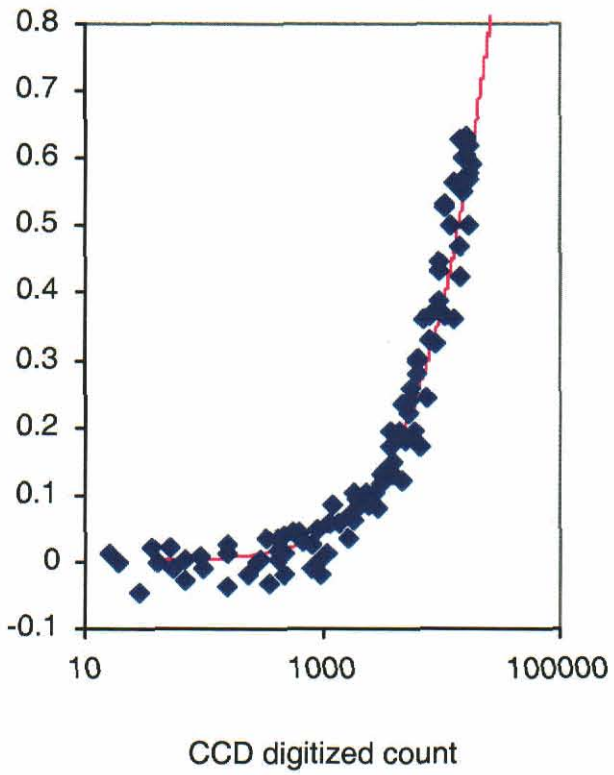

Figure 8-31. 2497 film density versus log CCD count found from the radial profile data of Figure 8-30(a).

Another advantage of a CCD is its wide dynamic range. With a thermal background of under 10 counts per pixel, the 16 bit resolution of the CCD corresponds to a dynamic range of more than 6000. In contrast, film typically has at best a dynamic range of less than 1000 and is linear in its response over a dynamic range of only 100 to 200. The example in Figure 8-32 shows that the CCD camera has sufficient dynamic range to record both the bright K-shell lines of argon as well as the helium and hydrogen-like continua.

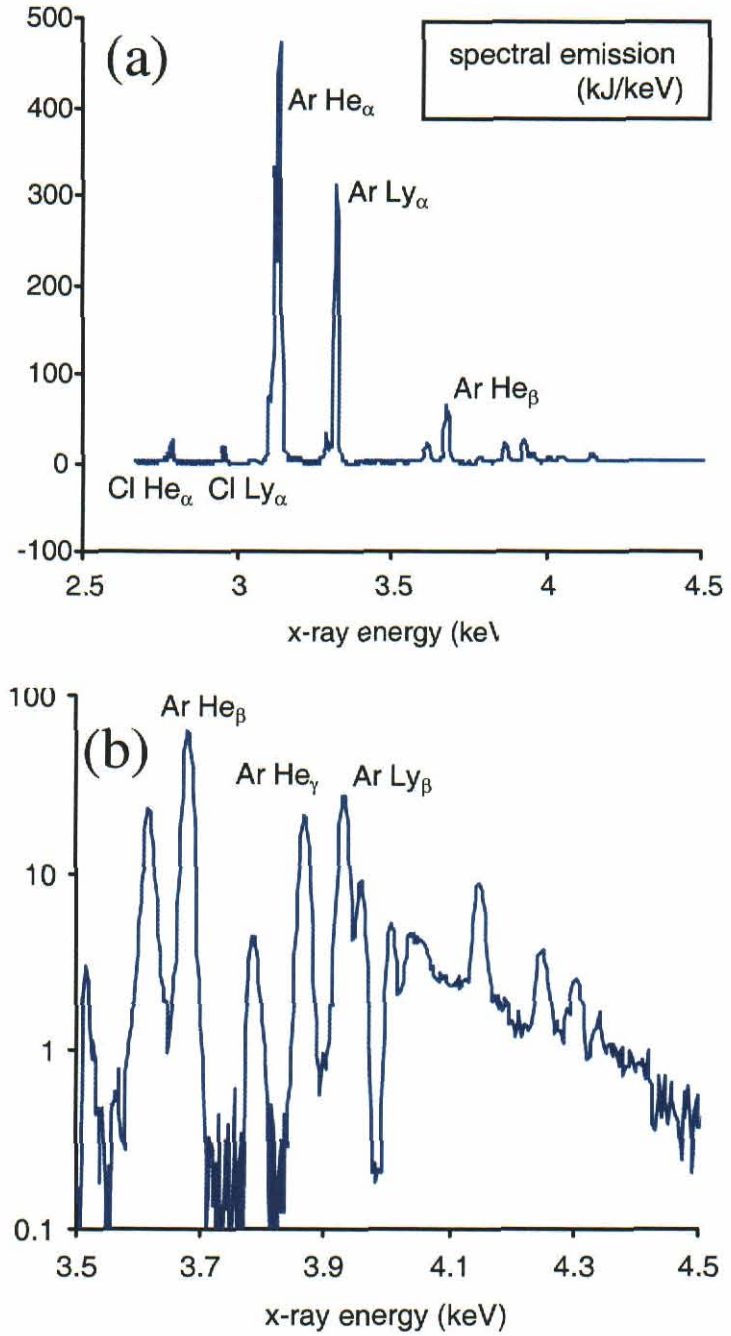

Figure 8-32. Example of time-integrated K-shell spectrum recorded directly with CCD camera. The large CCD dynamic range allows both the (a) brightest lines and (b) the continuum to be measured simultaneously. Spectrum is from a standard argon puff z-pinch on Double-EAGLE.

8.3.5 Summary.

We have demonstrated the use of CCD cameras to acquire 2-D image and spectral data in the severe EMP/radiation environments of large pulsed power machines like Double-EAGLE and SATURN. Over 100 CCD images have been acquired without an instrumental failure requiring electronic repairs, although RF shielding is required to prevent camera lockup. The primary source of background noise is hard x-ray bremsstrahlung due to electron losses in the vacuum transmission line near the z-pinch load. Sheets of lead shielding reduce this background.

The CCD cameras have been used to detect both optical light and kilovolt x-rays. For time-integrated measurements, x-ray recording of images and spectra is preferred to lens-coupling of phosphor optical light because of improved signal to noise levels and better spatial resolution. We have compared x-ray CCD measurements with 2497 film records and find them in satisfactory quantitative agreement. The CCD recorded line widths and line ratios show some improvement over the corresponding film measurements, but the recording area available with film (35 mm wide and more than 100 mm long) is many times larger than that of the CCD camera (12.3 mm square) used in the comparison. The estimated signal threshold for the CCD camera was at least 10X lower than the film, and the CCD saturation should occur at specular film densities of ~ 1.

Optical light recording is needed for time-resolved measurements, such as the time-resolved spectrograph and pinhole cameras. In the case of the spectrograph, the streak camera has sufficient gain to provide a good signal to noise ratio. In the case of the pinhole camera, nonlinearity of the output image can be an issue if the x-ray framing camera is run at too high a gain. If we were to replace the imaging lens with a fiber optic light coupler, we would improve the signal level 10X, at the same time reducing the overall dimensions of the RF and x-ray shielding required.

SECTION 9

GAS PUFF TESTING AND NOZZLE DEVELOPMENT

The gas puff argon PRS experiments described in previous sections have all used a supersonic nozzle coupled with a fast-opening valve to create the initial density distributions. Understanding of the performance of the z-pinches, as in the 0-D analysis of Section 6 and the zipper behavior of Section 8, requires knowledge of the detailed distribution of gas mass produced by the nozzles. This section begins with a discussion of the use of precision interferometers to measure the density profiles of our nozzles.

The 5 and 7-cm nozzle/valve configurations used on DM2 were characterized at the Naval Research Laboratory (Reference 17); see Section 9.1. The nozzle configuration used on Double-EAGLE was also characterized at Alameda Applied Science Corporation (AASC) (Reference 38) using their fiber optic interferometer; see Section 9.2 for details. Brief comments about the valve/nozzle used for our initial long pulse testing at SATURN appear in Section 9.3. Section 9.4 concludes with a discussion of the development of the double shell nozzle that was tested as described in Section 3.

To summarize all of these results, Figures 9-1 and 9-2 compare density maps for the shell and uniform nozzles. While the shell nozzle does have a well-collimated flow near the nozzle, it is interesting to note that the flow becomes much more filled in only a few centimeters from the nozzle exit. As the zipper data show (Figures 8-23 and 8-24), the 5-cm shell nozzle radiates best away from the nozzle where in fact the gas density distribution is more uniform than shell-like. This behavior is even true for the 2.5-cm shell nozzle that is used for short 100 ns operation on Double-EAGLE. Compare that nozzle's gas distribution as measured by NRL (Figure 9-3) and the zipper data (Figure 8-16).

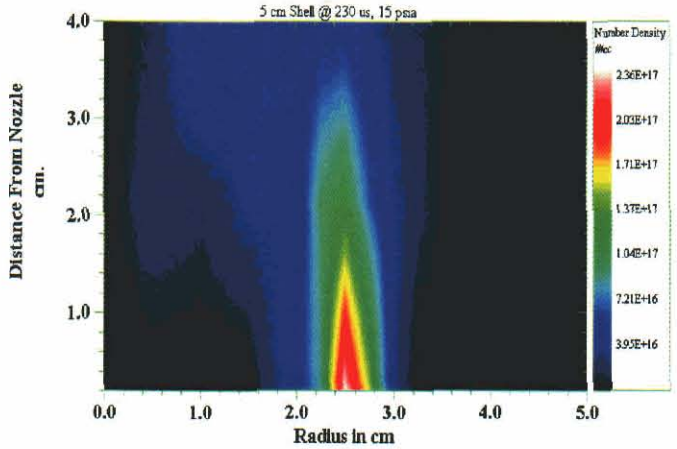

Figure 9-1. Gas density map for the 5-cm shell nozzle.

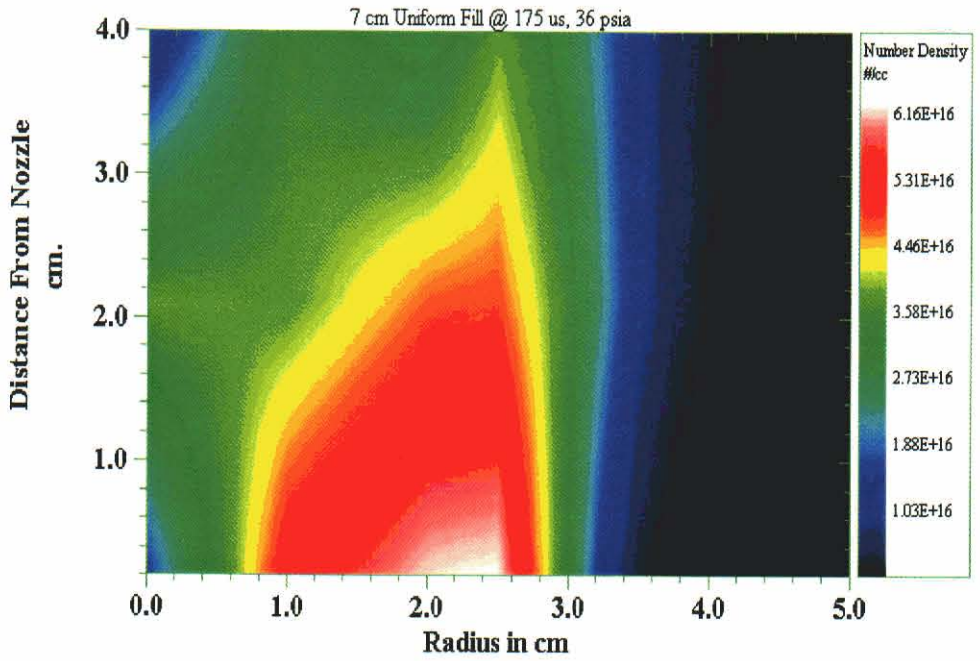

Figure 9-2. Gas density map for the 7-cm uniform-fill nozzle.

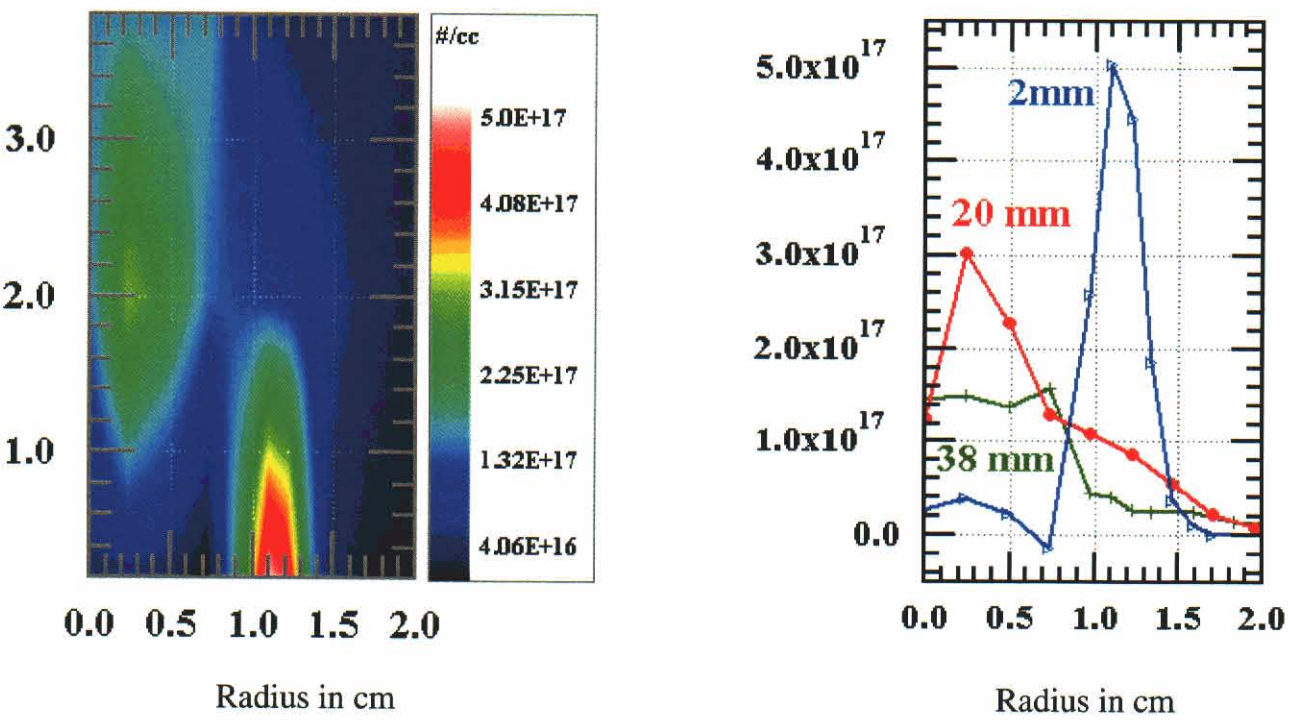

Figure 9-3. Gas density contour map and radial lineouts for the 2.5-cm shell. The gas pressure was 15 psia and flow time was 240 μs.

9.1 GAS DENSITY MEASUREMENTS AT NRL.

Gas density measurements were performed at the Naval Research Laboratory using high-sensitivity interferometry. The Nd-YAG laser driven Mach-Zender interferometer is sensitive to fringe shifts as small as 2×10^{-5} waves at bandwidths of up to 100 MHz (Reference 39). The interferometer system employs two coincident laser beams at wavelengths of 532 nm and 1064 nm. The measurable line density (atoms/unit area) of a neutral argon gas ranges from 10^{14} cm^{-2} to over 10^{18} cm^{-2}. The laser beam diameter, ~0.5 mm, is small enough to allow sub-millimeter spatial resolution

The nozzle was installed on top of a specially built cradle, which in turn was attached onto a movable carriage. The carriage could be moved axially (parallel to the nozzle axis) as well as transversely (up and down relative to the axis) from outside the vacuum chamber. The relative location of the nozzle in these two directions was known to better than 1 mm. The carriage/nozzle assembly rested at the bottom of a 50 cm-diameter vacuum tank the length of which was such that the nozzle exit was never closer than 37 cm from the chamber end plate. The scene beam of the laser interferometer entered and exited the vacuum chamber through quartz windows along a line perpendicular (left and right) to the nozzle axis. The chamber was typically evacuated to $< 4\times10^{-4}$ Torr.

For the gas flow measurements, the nozzle is aligned with its face parallel to the laser beam. Each firing of the gas puff gives the time history of the line density. The breakdown pin signal defines time zero. Multiple shots are taken to establish the experimental uncertainties. Then the nozzle is translated in the y direction (normal to the nozzle's axis) to get the line density on a different chord. Numerical integration over a range of chordal distances (0 to well beyond the outer radius of the nozzle) gives the linear mass function (mass per unit length as a function of z). Abel inversion of the chordal data gives the gas density as a function of radius and axial distance z.

Additional details are given in Reference 17, from which most of the material below is excerpted.

Two 7 cm nozzles, one new and one used, were calibrated during the study to check whether that the basic gas flow characteristics change significantly with normal use. Figure 9-4 is a scale drawing of the nozzle with the axial and chordal measurement positions indicated. The circles and the solid dots indicate the measurement locations of the new and used nozzles, respectively. Note that the nozzle is not totally "solid fill" since it incorporates a 1cm diameter center stalk. All data were taken with 36 psia argon plenum. A breakdown pin designed and installed by NRL was employed on all shots for triggering of the digitizers and served as a reliable time marker for the data.

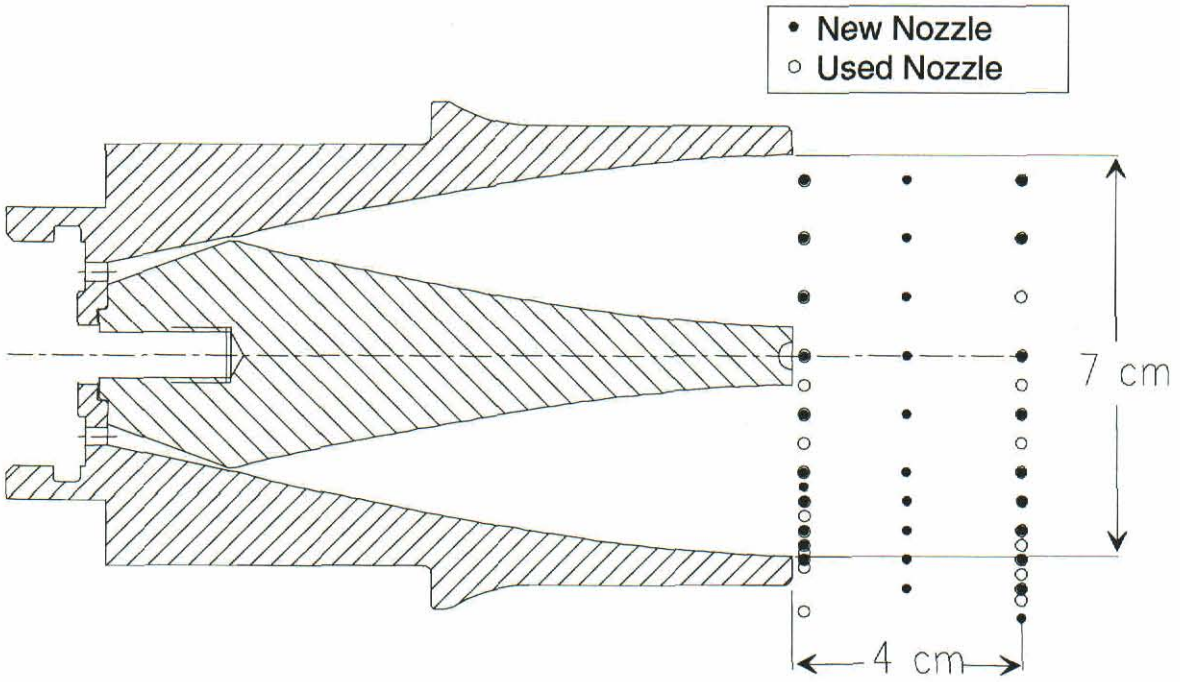

Figure 9-4. MPI 7-cm solid-fill nozzle and measurement locations.

The interferometer provides a measurement of linear (or "areal") density.

$$nL \equiv \int n \cdot dL \quad ,$$

where n is the argon gas density integrated over a path L along the laser trajectory through the gas. Examples of nL (cm^{-2}) as a function of time are shown in Figure 9-5, for an axial distance of 2 mm from the used nozzle exit (z = 2 mm). Each curve represents the average of 2-3 shots at a transverse position y at which the chordal measurement was taken. Note that at y = 3.56 cm, the limit of detectability is being approached for this particular set of tests. This limit is reached when the shot-to-shot standard deviation becomes comparable to the average signal magnitude. No smoothing has been applied to this data. This family of curves is representative of all the data and will only be shown for this nozzle and this z position for the sake of brevity. Slices of these data at 5 pertinent points in time result in the chordal profiles shown in Figure 9-6. The times chosen are based on the gas flow times used on DM2. Here the error bars shown represent ± one standard deviation calculated for all the shots at each position.

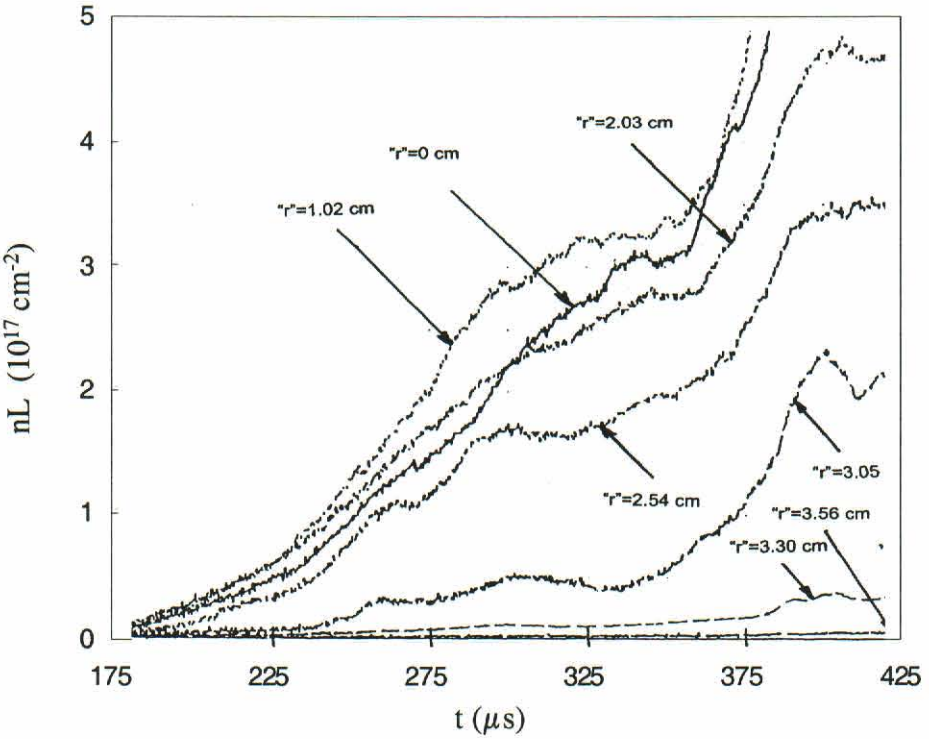

Figure 9-5. Averaged linear density plots as function of time.

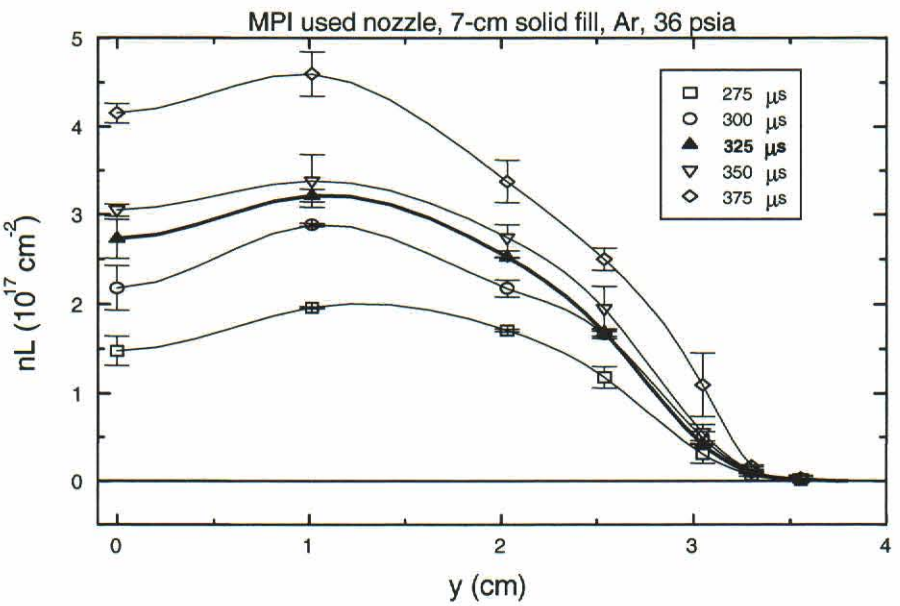

Figure 9-6. Chordal plots of linear density at z=0.2 cm.

An Abel inversion must be performed to determine the density profile of the gas at each time. The density as a function of radial position (n vs. r) for the five selected times are shown in Figure 9-7. They reveal a wide distribution of almost constant density of $3 - 6\times10^{16}$ cm^{-3} over a

range of radii of 0.6 – 2.8 cm with a fall-off at larger and smaller radii due to the outer extent of the exit aperture and the presence of the center stalk respectively. The density spikes at the inner and outer radii predicted by the gas-dynamic design code (Reference 15) were not observed.

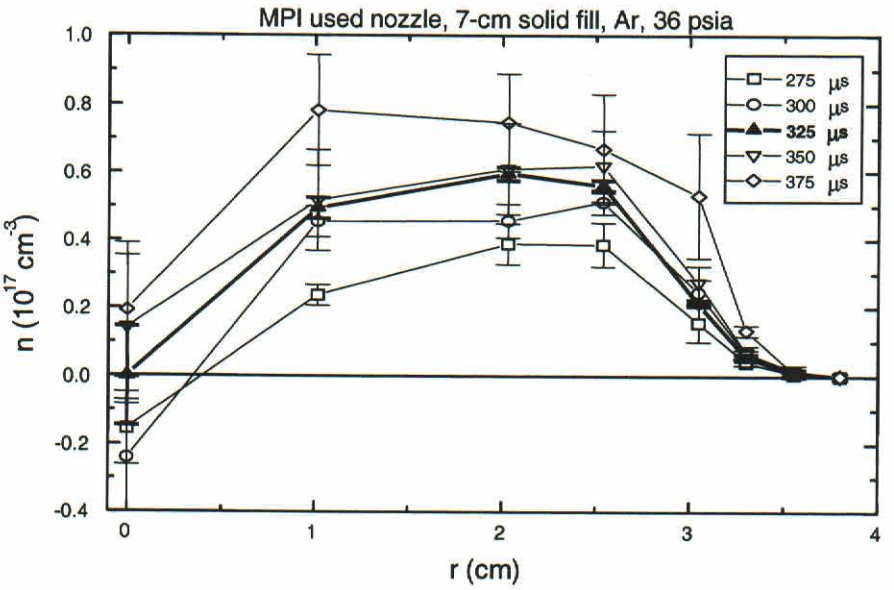

Figure 9-7. Argon density vs. r at z=0.2 cm.

Figure 9-8 and Figure 9-9 show the corresponding nL vs. y and n vs. r curves, respectively at z = 2 cm. Note that the peak density exhibits a slight drop, the outer wing extends out to r = 4 cm and the center hole is starting to fill in especially at later times.

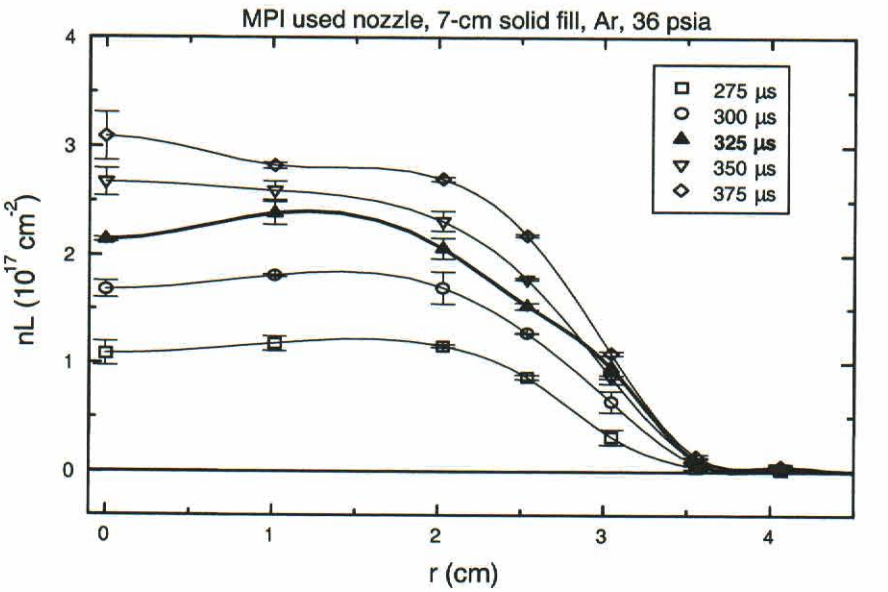

Figure 9-8. Chordal plots of linear density at z=2.0 cm.

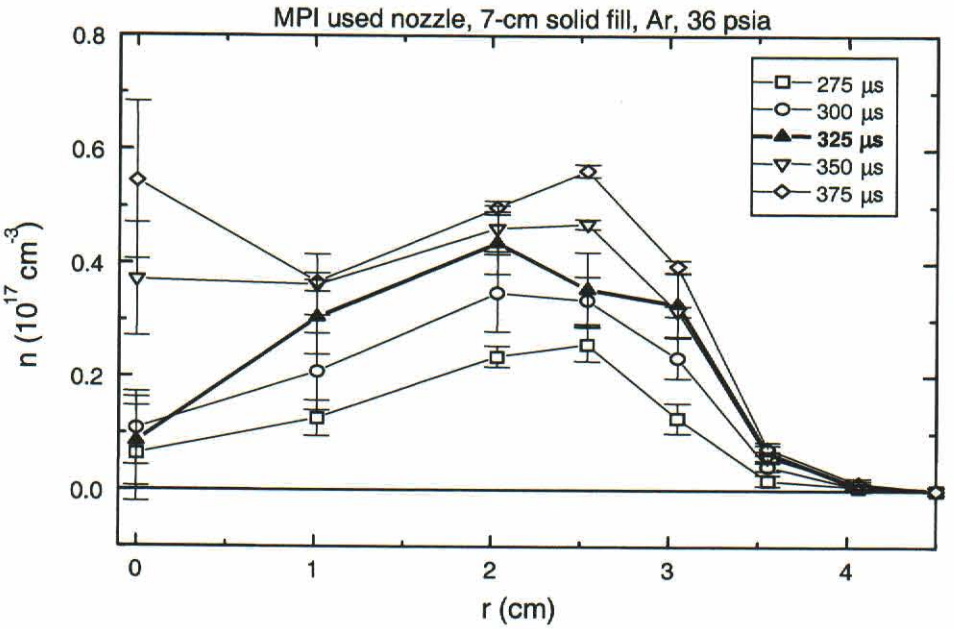

Figure 9-9. Argon density vs. r at z=2.0 cm.

Comparable data were also taken at the 4-cm range from the nozzle.

Figure 9-10 summarizes the results. For each axial position, the corresponding mass per unit length (m/l) is designated in parentheses. Note that m/l decreases with increasing z. This drop-off in mass with z is more clearly illustrated in Figure 9-11 where the mass per unit length is plotted as a function of time. This phenomenon is not unexpected considering the finite time required for the gas to traverse the axial distances involved. Thus, to design an experiment based on these data, one should probably calculate implosion times based on the axially-averaged mass, in this case 80 µg/cm.

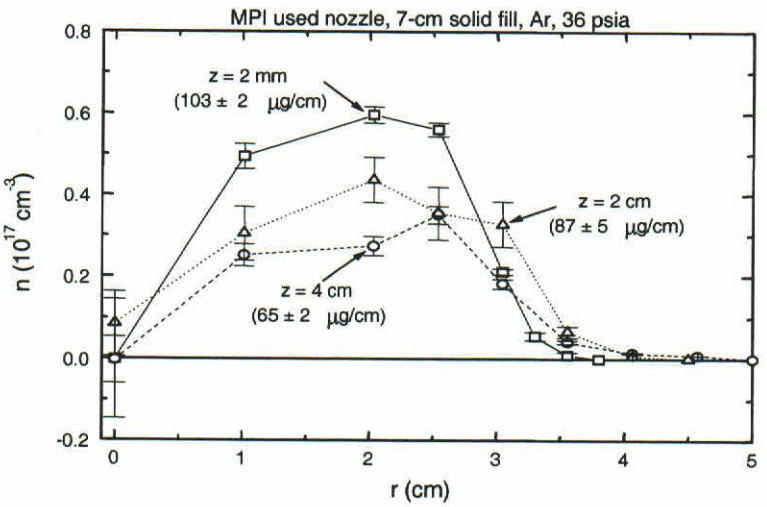

Figure 9-10. Density distribution comparison at different axial locations, 325 μs after breakdown pin (150 μs after gas onset).

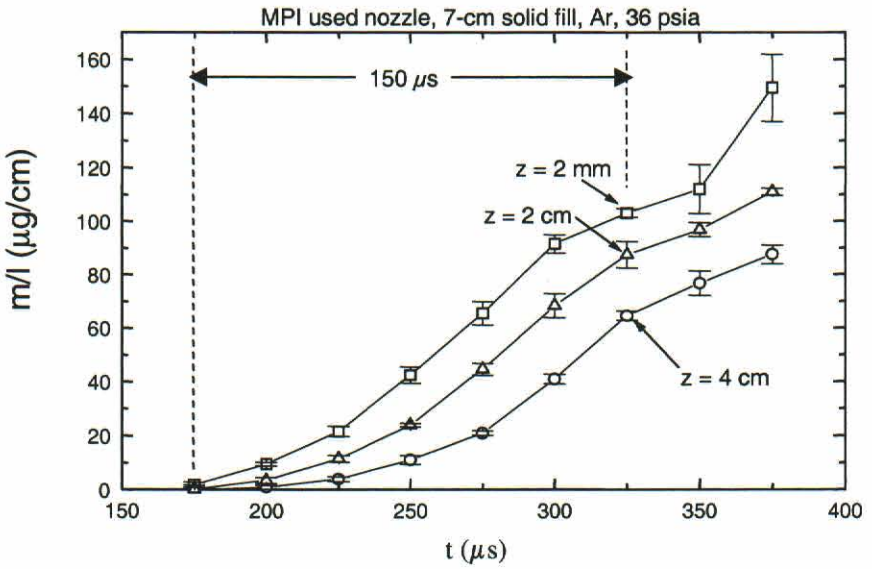

Figure 9-11. Mass per length at different axial locations.

Similar measurements of the new nozzle were also made. Figure 9-12 compares the density distributions of the new and used nozzles at z = 2 mm. It shows some differences in the details, but, except for r = 2.54 cm, the two distributions lie within each other's error bars. The somewhat higher density that the new nozzle exhibits at large radii results in a higher mass (of order 10%). Figure 9-13 shows a similar comparison at z = 4 cm. Again, some differences are apparent. In particular, note that the new nozzle seems filled-in at the center while the used one is hollow. In this case however, since the main differences occur at relatively small radii, their effect on the mass loading is insignificant (66 vs. 65 μg/cm). It should be emphasized that Figure 9-12 and Figure 9-13 represent one point in time and are not necessarily representative of all the data (as seen in Figure 9-5) which tend to have some fluctuations in the few microsecond time scale. Figure 9-14 summarizes the comparison indicating that the two nozzles are essentially identical, in terms of mass loading, for the first 125 μs after the gas exits the nozzle. At later times, the new nozzle puts out more mass than the old nozzle, a difference that becomes apparent earlier at the 2 mm than the 4 cm position. It is not clear that this difference is really due to nozzle differences, since the two sets of measurements were also done with different gas puff valves that may have slightly different valve opening speeds.

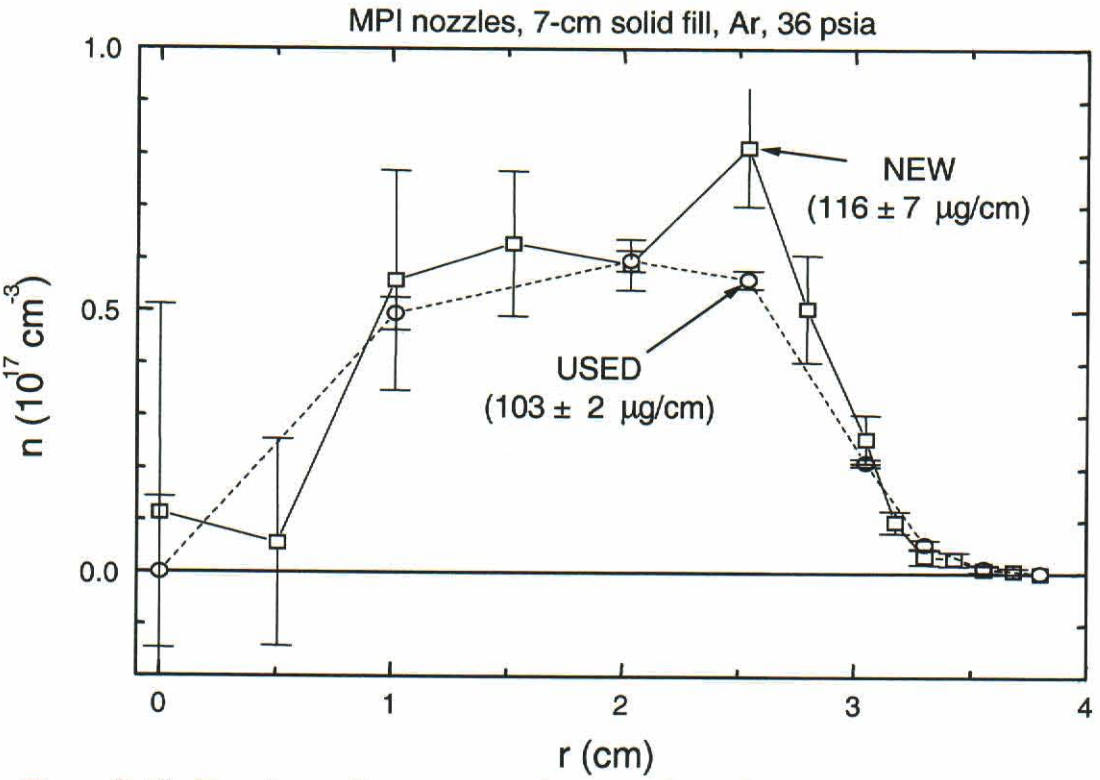

Figure 9-12. Density profiles; new nozzle vs. used nozzle. z = 0.2 cm, t=325 μs.

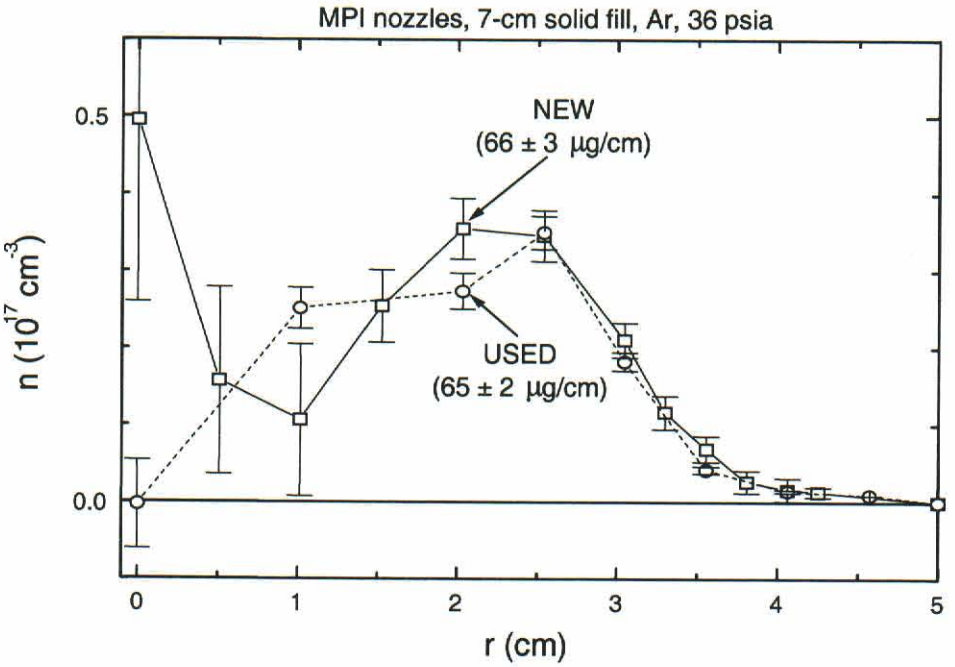

Figure 9-13. Density profiles, new nozzle vs. used nozzle, z = 4.0 cm, t=325 μs.

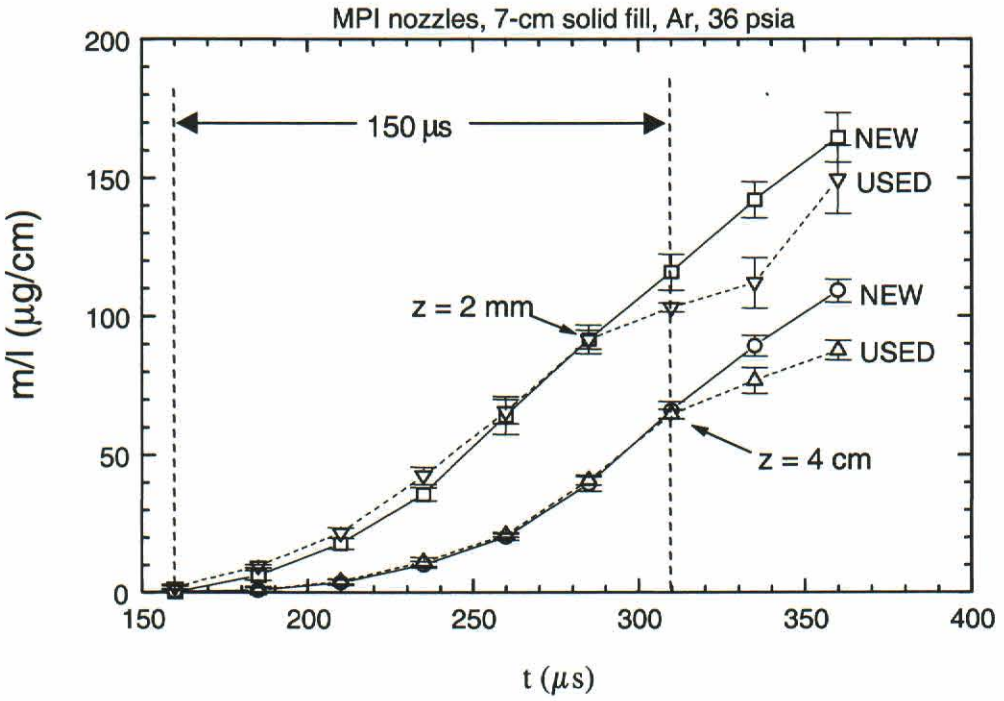

Figure 9-14. Flow mass vs. time; new nozzle and used nozzle, z = 0.2, 4 cm.

9.2 GAS DENSITY MEASUREMENTS BY AASC.

The valve and nozzle used during the Double-EAGLE PRS experiment are nominally the same ones used during the DM2 PRS experiment, i.e., the MPI gas valve and the MPI 7-cm diameter solid-fill nozzle. But there are two differences between these cases. First, the valve's plenum pressure on Double-EAGLE was higher than that on DM2. Second, on Double-EAGLE there was a 90% transparent tungsten mesh on the nozzle exit, while on DM2 a 12-spoke pattern of aluminum wires was sometimes used to define the electrical cathode plane of the pinch.

This valve/nozzle assembly was characterized using the AASC fiber optic interferometer (FOI) which has 10^{-3} (or better) wave sensitivity (Reference 38). The initial test setup was modified to eliminate the coupling of mechanical vibration from the puff valve to the interferometer. In the new set-up, shown schematically in Figure 9-15, the interferometer and the vacuum chamber are mounted on two separate tables, and the optical fibers are detached from the vacuum chamber. The probing leg of the interferometer is fixed on a specially built jack that can move axially and vertically relative to the vacuum chamber. The valve/nozzle assembly is attached rigidly to the chamber. The laser beam enters and exits the chamber though a pair of high transparency quartz windows. The chamber is typically evacuated to $<10^{-5}$ Torr. During the measurement, the valve's plenum pressure was maintained at 80 psia. A breakdown pin was employed to serve as a reliable time marker for the data.

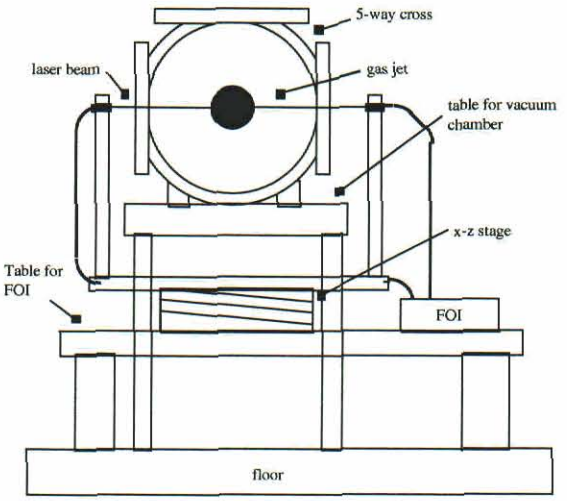

Figure 9-15. Set-up of the FOI.

The linear density, (nL) was scanned vertically at an interval $\Delta y = 2$ mm. The axial positions are chosen to represent the three points in a Double-EAGLE PRS load: near the cathode, at the middle plane and near the anode. Figure 9-16 shows the waveforms of six identical shots where the laser beam was located at y = 0 mm and z = 38 mm relative to the center of the nozzle. The valve had good reproducibility and the breakdown pin had little jitter. The risetime of the gas flow is about 400 μs which is longer than the risetime measured at NRL (≈300 μs). This is explained by the higher plenum pressure. A higher plenum pressure will slow valve opening speed. Figure 9-17 shows nL measured at z = 20 mm and at a few y positions. As in Section 9.1, this family of curves is representative of all the data taken and only a sampling are shown here for the sake of brevity.

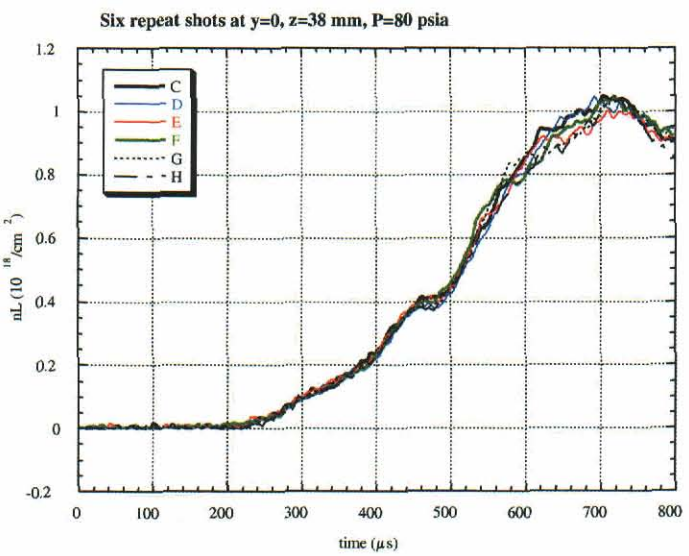

Figure 9-16. Linear density waveforms for 6 repeat shots of the FOI.

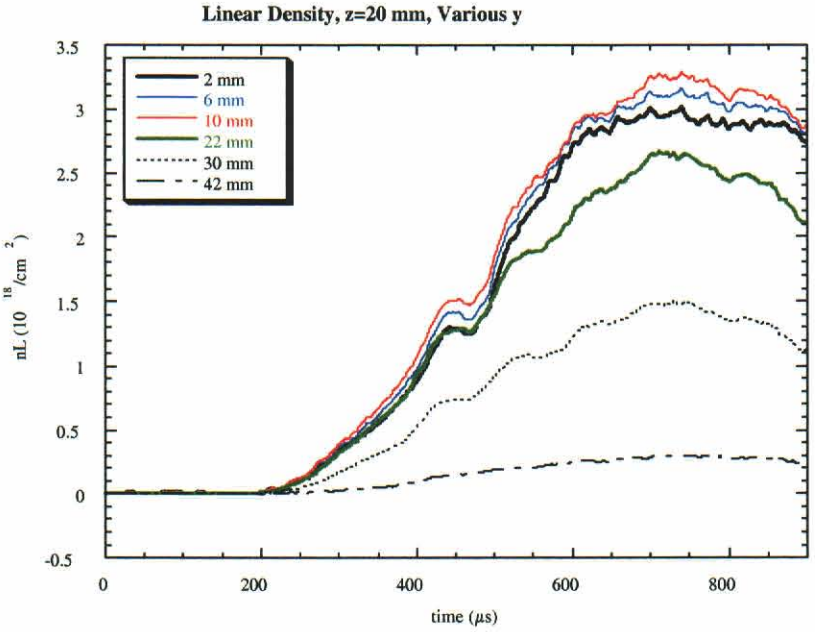

Figure 9-17. Linear density as a function of time and chordal distance.

Plots of nL as a function of y at z = 2 mm and at seven pertinent times are shown in Figure 9-18. Double-EAGLE was fired at a time corresponding to 300 μs on this plot.

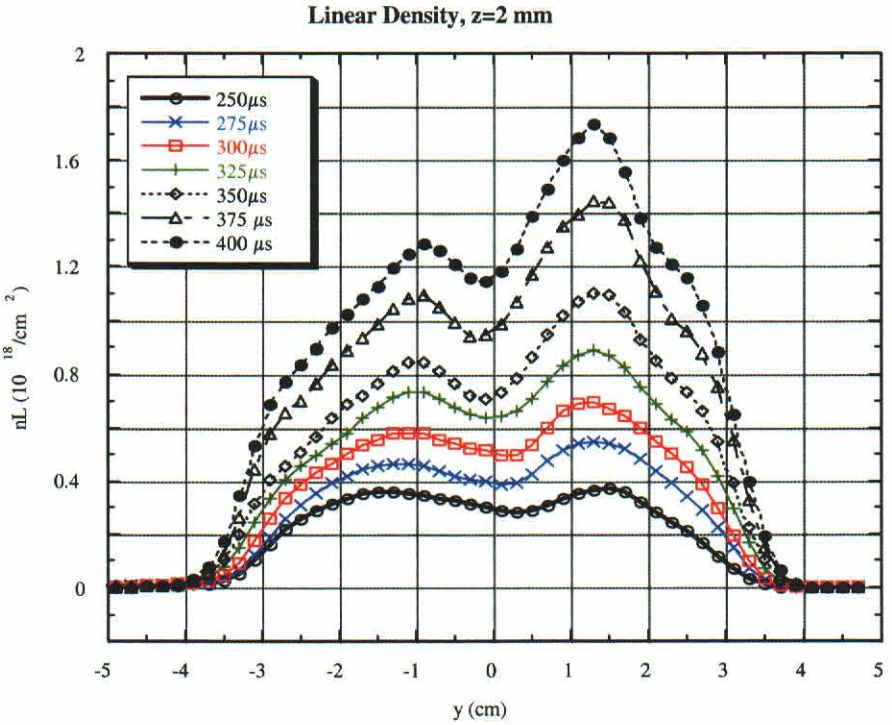

Figure 9-18. Linear density vs. y at z=2 mm.

The data in Figure 9-18 show that the linear densities measured in the upper half of the nozzle ($y>0$) are higher that their counterparts in the lower half of the nozzle ($y<0$), indicating that the gas flow of this nozzle is azimuthally asymmetric. This phenomenon was also observed to a lesser degree during the DM2 nozzle calibration at NRL. We subsequently determined that this problem was caused by asymmetric friction on the movable part of the valve. Based on this experience, we modified our valve designs to minimize the opportunities for such problems to develop. More recent testing (for example, see Figure 9-24) shows that we can achieve good azimuthal symmetry.

9.3 SATURN GAS PUFF.

For practical and scheduling reasons, the initial long-implosion argon PRS experiments on SATURN (Section 2.3) used the 7-cm solid-fill nozzle but with the standard Sandia puff valve rather than the MPI puff valve. The Sandia breakdown pin is housed in a valve-to-nozzle adapter, whose "dead" volume increases the gas puff risetime to about 600 μs (approximately twice that on DM2 and Double-EAGLE). To achieve the higher load mass required for the SATURN currents, we had to operate at higher plenum and longer flow times than in the other long-implosion argon PRS experiments.

We suspect that the 7-cm density profiles on SATURN were substantially different from those on DM2 and Double-EAGLE, but we were unable to measure SATURN density profiles at NRL because of jitter problems. The jitter results from the location of the breakdown pin down a long, narrow channel off the main gas flow path, where the density is much lower. Measurements of the pressure pulse showed a jitter of ~100 μs, even after the breakdown pin bias was doubled from the -700 V value used on SATURN. Because the jitter is a significant fraction of the flow time, the measurement statistics were inadequate to perform the Abel inversion required for the radial density profiles.

The NRL tests uncovered another problem with the SATURN valve. We found that the Sandia valve poppet failed to reseal after being pulsed at NRL: the o-ring had come out its groove during poppet opening. Because NRL oriented the valve axis horizontally, the o-ring fell vertically before the poppet reclosed. This situation would not have been noticed at SATURN, where the valve is vertically aligned, because the poppet would recapture the o-ring as it closes. It is likely that the o-ring inertia will cause the o-ring to pop out at SATURN also, and that its frictional retaining force will make the process non-reproducible.

Experience with all of the valve/nozzle problems discussed above helped guide our efforts when we began the development of the double plenum, double shell nozzle. That valve/nozzle combination was successfully tested on Double-EAGLE and SATURN as discussed earlier in Section 3. Details follow here.

9.4 DEVELOPMENT OF THE DOUBLE SHELL NOZZLE.

9.4.1 Introduction

We review here the development of the shell-on-shell structured load. As reported in Section 3, PRS experiments on the Double-EAGLE and SATURN accelerators demonstrated that such a load performs at least as well as a uniform fill distribution. Section 9.4.2 describes the design of the double puff gas valve and its matching nested pair of supersonic nozzles. The characterization of the gas flow of the shell-on-shell valve/nozzle is shown in Section 9.4.3, followed by a brief summary in Section 9.4.4.

9.4.2 Design of the shell-on-shell valve/nozzle.

Figure 3-1a is a photograph of the shell-on-shell valve/nozzle assembly. Figure 9-19 is a schematic diagram, illustrating the inner structures and dimensions of the shell-on-shell valve/nozzle. The major components of the valve are the electrical solenoid, the hammer, and the poppet. The solenoid is very robust, made with a fabric re-enforced copper coil cast in epoxy. The inductance of the solenoid is about 90 μH. The hammer is made of copper and sits on top of the solenoid. The solenoid is connected to a 1 mF capacitor bank through a switching SCR. When the capacitor bank is discharged, the current in the solenoid induces an eddy current in the hammer, resulting in the latter being pushed away from the solenoid. The flying hammer hits the lifting plate of the poppet, and causes the valve to open. A hammer-reset spring automatically reseats the hammer on the solenoid surface after each valve opening. This allows the valve to be operated in any orientation. A reseating spring for the poppet closes the valve a few milliseconds after it opens. Quick reseal of the valve prevents the remaining gas in the plenums from flooding the vacuum system unnecessarily.

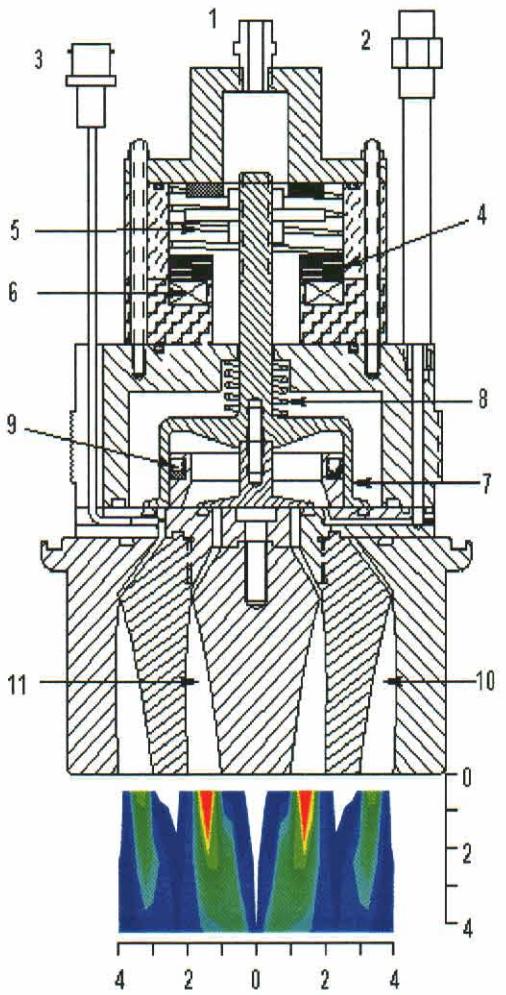

Figure 9-19. Schematic diagram of the shell-on-shell valve/nozzle, illustrating the inner structures and dimensions: 1) outer plenum gas inlet, 2) inner plenum gas inlet, 3) break-down pin output, 4) hammer, 5) hammer reset spring, 6) solenoid, 7) poppet, 8) poppet reset spring, 9) sliding seal, 10) outer nozzle, and 11) inner nozzle. The gas density contours are shown under the nozzle sketch. Scales are in cm.

The poppet is made of 6061T6 aluminum for its light weight and high strength. The poppet has two sealing surfaces: an inner disc and an outer coaxial cup. The outer cup also serves as the boundary between the inner and outer gas plenums. The outer cup slides on a low-friction U-cup piston seal (PSP Inc.). This sliding seal prevents the gas in the inner plenum from leaking into the outer plenum whether the valve is open or close. There are two benefits to this design. First, the two plenums can be set at different pressures to alter the mass-ratio of the two gas puffs. Second, it allows the two plenums to use different gases. The latter benefit is potentially useful in implosion diagnostics (each plenum can be seeded with a unique tracer) and in PRS experiments that use gases with different atomic numbers for increased spectral content. From Figure 9-19, one can see that the pressure in the outer plenum, P_{out}, helps to seal the poppet while the pressure in the inner plenum, P_{in}, tends to open the poppet. The dimensions of the inner disc

and the outer cup need to be chosen properly to maximize the usable ratio P_{in}/P_{out} while keeping the plenums sealed until the solenoid is pulsed. The usable range of P_{in}/P_{out} is 0~2.5 under the current design.

The shell-on-shell nozzles are attached to the valve through an adapter plate. A breakdown pin is also installed in the adapter plate, as shown in Figure 9-19. The pin is made from a piece of semi-rigid coaxial cable with the exposed center conductor at one end being inserted into the gas path of the outer gas puff. The pin is DC biased at -1 kV. Before the valve opens, the ambient vacuum keeps the pin from breaking down. When the valve opens, the emerging gas will cause the center conductor to arc to the adjacent metal, producing a voltage pulse in the coaxial cable. This pulse serves as the time marker of the valve's opening and can be used to trigger the pulsed power system. The gas flow measurements discussed below show that this scheme makes experiment timing insensitive to any mechanical jitter of the valve. The on-set of gas flow is defined by the breakdown pin with a jitter of a few microseconds. This is small compared to the typical gas flow times of hundreds of microseconds that are used for the z-pinch experiments.

The shell-on-shell nozzle is comprised of three separate parts mounted on the common adapter plate. The inner and outer radii of the outer nozzle, measured at the gas exit, are 3 cm and 4 cm. The corresponding radii of the inner nozzle are 1 cm and 2 cm. The dimensions of the outer nozzle were determined by the geometry and peak current of Double-EAGLE and SATURN. That is, for a given current drive, the implosion time is controlled mainly by the outer mass and its initial radius.

In choosing the radii of the inner nozzle, we have taken into consideration the results of two-dimensional radiation magneto-hydrodynamics (MHD) code (Reference 40) calculations and fluid code (Reference 41) gas flow calculations. The MHD calculations were performed to optimize the shell-on-shell geometry for mitigation of RT instabilities during the implosion compared with a simple single-shell load. The calculations indicated that for the planned outer shell radii, i.e., 3 cm and 4 cm, inner shell radii of 1.5 cm and 2.5 cm would give optimum results, that is, a stabilized implosion and enhanced x-ray yield. However, the MHD calculations were based on an idealized initial gas distribution: the two shells were perfect gas cylinders. In reality, a gas shell generated by a supersonic nozzle always has radial and axial divergence. According to the fluid code calculations, if the radial separation between the two nozzles is too small, the gas puffs will quickly expand into each other, forming one thick shell rather than two separate shells. Therefore, the final radii of the inner shell were chosen based on considerations of having both instability mitigation and a practical shell-on-shell gas distribution.

The contours of each nozzle were designed according to the fluid code to minimize the radial expansion or "flaring" of the gas flows. The nominal Mach numbers of the inner and outer flows are 6 and 8 respectively. It is also important to minimize the "dead volumes" between the gas exit of each valve and the throat of its nozzle. Calculations using a simplified gas flow "circuit" model show that reducing the dead volume will shorten the rise time of the gas puff ejected from a supersonic nozzle. The throat dimensions of the inner and outer nozzles, 0.38 and 0.19 mm respectively, were also selected based on the gas dynamics calculations. Figure 9-20 shows the two dimensional (r-z) gas flow-patterns calculated by the fluid code at several times after the opening of the valve.

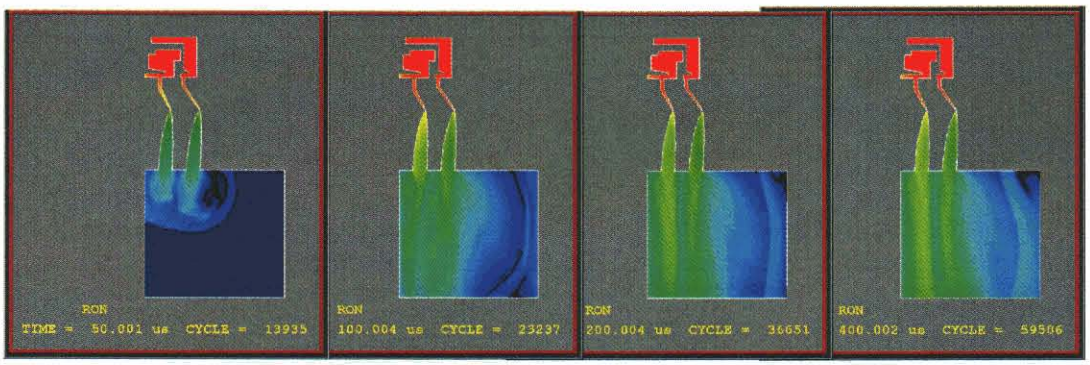

Figure 9-20. Two-dimensional (r-z) gas flow-patterns calculated by the fluid code at 50, 100, 200, and 400 μs following the opening of the poppet.

9.4.3 Characterization of the Shell-on-Shell Valve/Nozzle.

With the valve case removed, we estimated the poppet opening speed by observing the height to which it was thrown as the solenoid was energized. For charge voltages up to 1000 volts, the opening speed of the valve is linearly proportional to the charge voltage. Typical values are 5 m/s at 500 V and 10 m/s at 800 V.

Gas distributions for the shell-on-shell nozzle were measured at NRL as described in Section 9.1 for the 7-cm uniform-fill nozzle.

The following sections describe measurements of azimuthal symmetry, density distributions for individual shells and both shells, density distributions at t = 500 μs (the timing used for most of the z-pinch shots), mass loading, and pressure scaling.

9.4.3.1 Measurements With Individual Shells And Both Shells. The gas distributions from the inner shell and the outer shell were measured independently, and compared with the measurements when both shells were operating simultaneously. To make this comparison, it is necessary to have pressure in the outer shell so that the breakdown pin operates. Thus in order to diagnose the inner shell, the outer shell exit was blocked using 3/8 inch o-ring material, wedged into the outer nozzle with a small break where the ends met to allow the gas to be pumped out of the outer nozzle for subsequent shots. A small piece of Mylar served as a deflector to help keep gas from this exit hole from affecting the inner shell measurements. Test shots with no gas in the inner shell showed negligible gas from the outer shell in this configuration.

The outer shell was diagnosed by simply evacuating the plenum of the inner shell. In principle, this technique is not ideal because the net force applied by the gas on the poppet increases when the inner shell pressure is zero. The valve might open more slowly in this case, possibly affecting the rate of rise of the gas flow. A better technique would be an o-ring seal in the inner nozzle and a static fill in the inner shell plenum. (Note that a delay in the valve opening is not a problem since the breakdown pin is the time reference.) However, in view of the data presented below, this concern does not seem to have materialized.

Figure 9-21 compares the line-masses from the individual shells and their sum with the line-mass measured when both shells are pressured. The sum of the inner and outer shell masses agrees with the combined shell mass to within 5%. This small discrepancy is probably a measurement error since the two shells are completely independent at this small distance, 0.2 cm from the nozzle. Another cause might be the wobble in the mechanism used to raise and lower the nozzle (relative to the interferometer beam) resulting in small errors in the y positions. This problem was detected and corrected during the measurement series and some (but not all) of the measurements were repeated. The measurements for the individual shells are more reliable in this case.

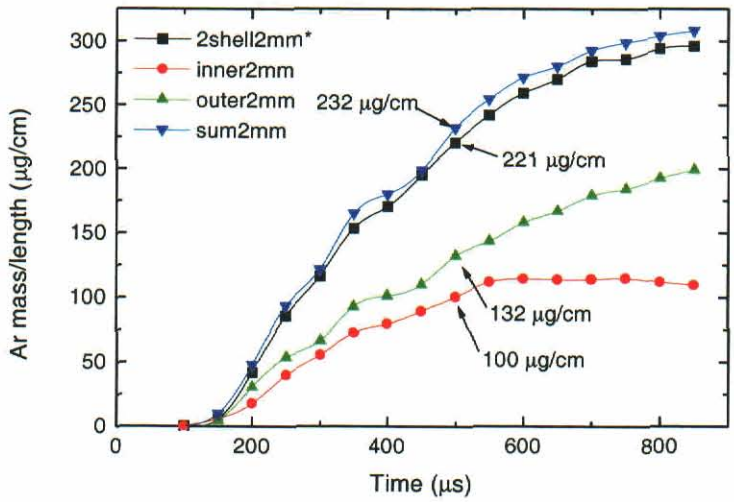

Figure 9-21. Mass per-unit-length at $z = 0.2$ cm for both shells, inner and outer shells separately, and the sum of inner and outer shells. The asterisk indicates there is some uncertainty in the measurement because of wobble in the nozzle positioning mechanism.

9.4.3.2 Density Distributions at the Time of Pinch Initiation. When the shell-on-shell valve/nozzle was fielded on Double-EAGLE and SATURN, the pinch was normally initiated 500 µs after the breakdown pin pulse. The Abel-inverted density $n(r)$ distributions at $t = 500$ µs are shown in Figure 9-22, where the individual shell densities are compared with the combined shell densities, including error bars derived from the shot-to-shot variations in the measurements. The error bar magnitudes increase as $r \rightarrow 0$, an unavoidable property of Abel inversion. The apparent finite densities (both positive and negative) at $r = 0$ are probably wrong, based on the neighboring $r > 0$ points and error bars.

Figure 9-22 shows that combined shell density distributions agree well with the sum of the densities of the two individual shell at all three axial locations. The data indicate that the gas puffs from the two shells are well separated near the nozzle exit and only start to overlap as the axial distance reaches several centimeters. The density contour plot shown in Figure 9-19 gives a good qualitative impression of the gas flow at this time.

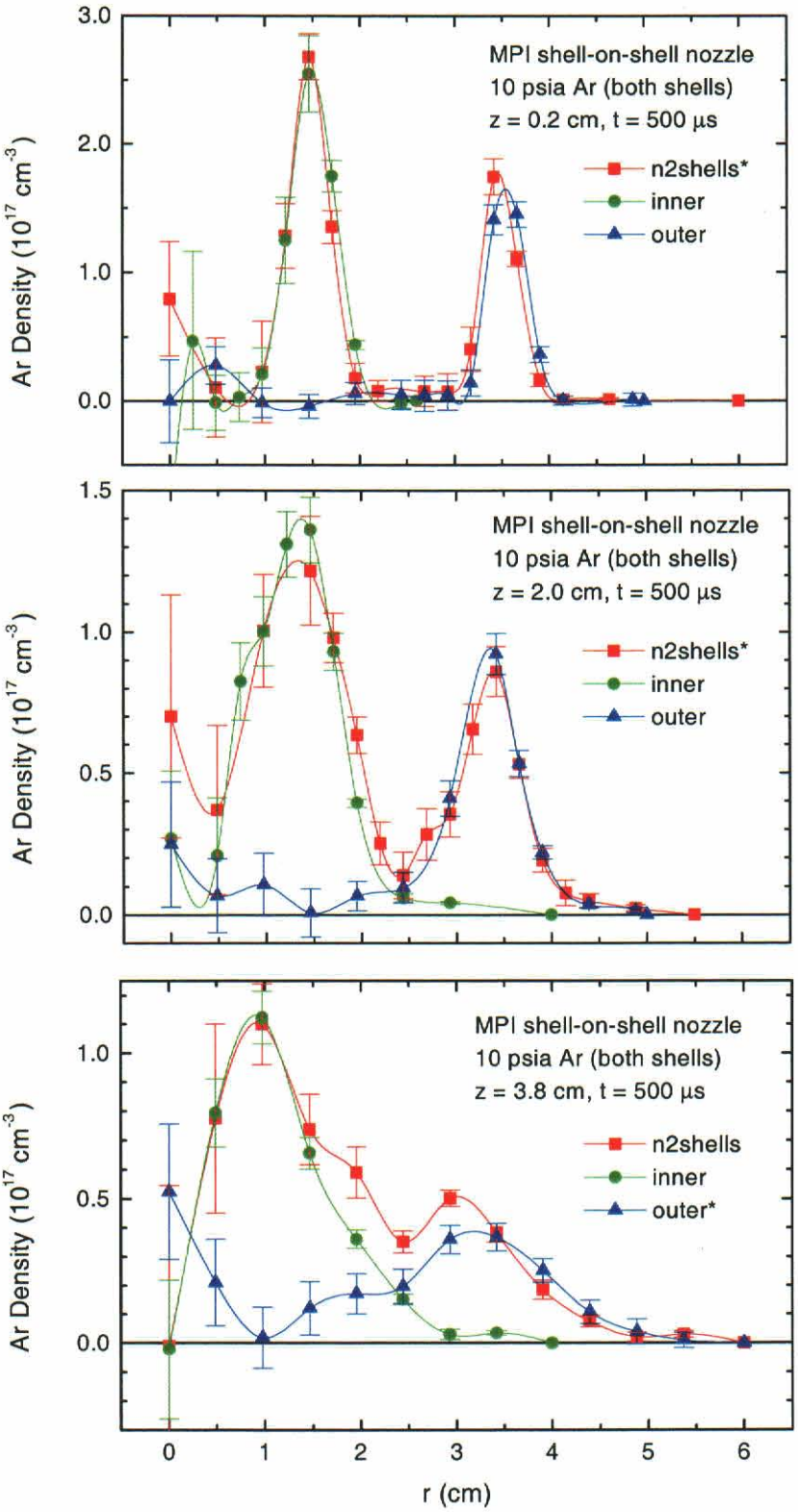

Figure 9-22. Density distributions of individual shells and the 2-shell at (a) z = 0.2 cm, (b) z=2 cm, and (c) z=3.8 cm. * denotes possible problems with the nozzle positioning hardware.

9.4.3.3 Mass Loading and Pressure Scaling. The plenum pressure p in the valve was varied to test the expected linear scaling of mass with pressure. The linear masses close to the nozzle (z = 0.2 cm) for pressures of 34 to 276 kPa (5 to 40 psia) are plotted in Figure 9-23. (As the pressure was increased above 138 kPa, the phase shift of the green beam became too large and the higher pressures were diagnosed with the IR beam. The green and IR measurements compare well at 138 kPa.)

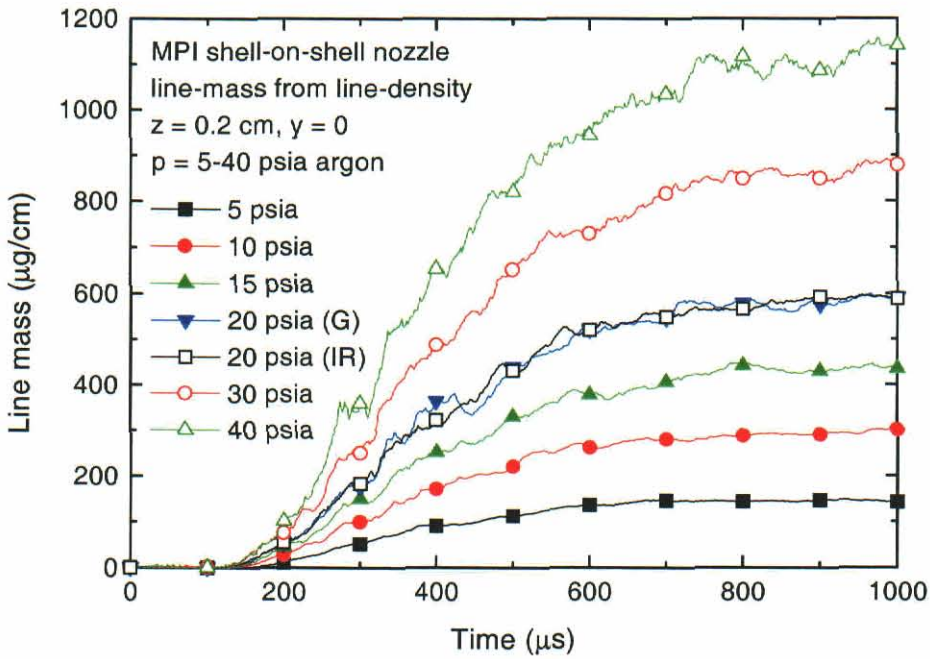

Figure 9-23. Line-masses of the shell-on-shell nozzle at various plenum pressures.

Up to pressures of about 200 kPa (29 psia), the mass is closely proportional to the plenum pressure. At higher pressures, the mass is somewhat less than expected from linear scaling. It is likely that the higher pressures do affect the valve opening velocity.

9.4.3.4 Azimuthal Symmetry. Due to its small throat width (0.19 mm), tight tolerances had to be put on the fabrication of the outer nozzle to ensure that the throat gap (and gas flow) would be uniform azimuthally. The symmetry of the outer shell was tested by repeated line density measurements at an axial distance z of 2 mm as the nozzle was rotated about its axis of symmetry. Six probing orientations were used. The plenum pressure of argon for the outer nozzle was 69 kPa (10 psia). Figure 9-24 shows the measurements at various gas flow times. The error bars in the figure are ± one standard deviation and the horizontal dashed lines are drawn to indicate ideal azimuthal symmetry. The data are close to this ideal, considering the shot-to-shot reproducibility indicated by the error bars.

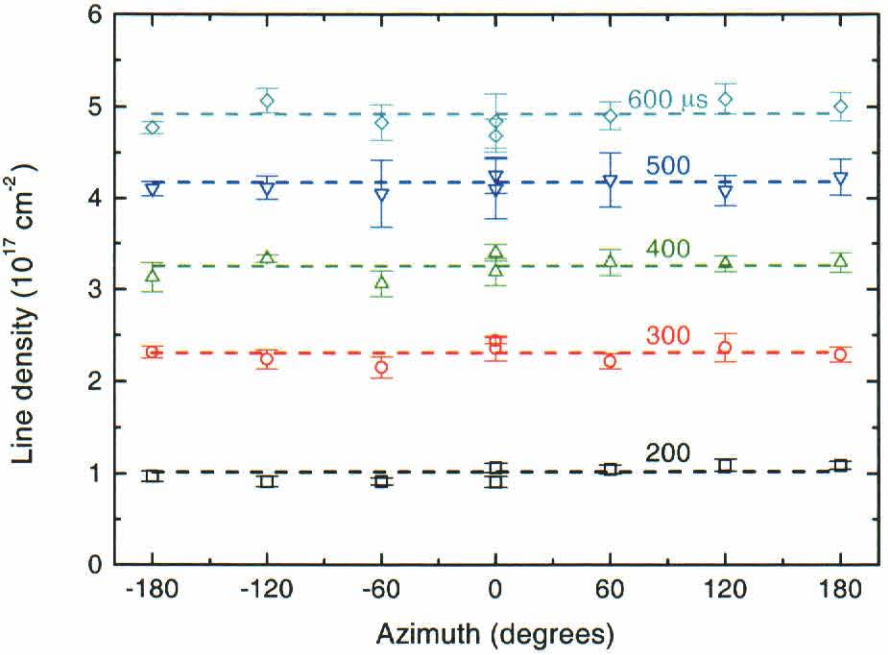

Figure 9-24. Line density as a function of azimuthal angle at various times for the double-shell nozzle.

9.5 SUMMARY.

We have developed and characterized a valve/nozzle to generate shell-on-shell gas-puff loads for z-pinch PRS experiments. Long-implosion-time PRS experiments on Double-EAGLE and SATURN using this shell-on-shell nozzle have generated K-shell yields and pulse widths equivalent to a solid-fill nozzle. Diagnostics showed good pinch quality in terms of pinch diameter and uniformity along the pinch length. The opportunity to selectively seed the shells with a tracer has already led to insights into the pinch dynamics; see Section 3. There is potential for further improvement since we have not yet determined the optimum mass ratio between the two shells nor have we explored the use of different types of gases in the individual shells.

SECTION 10

ULTRAVIOLET PRE-IONIZATION SOURCES

10.1 INTRODUCTION.

This section describes the development of ultraviolet (UV) pre-ionization sources for use with our long implosion time loads. These sources had the specific objective of being much more uniform than is common practice. The idea is that instability development during an implosion is seeded in part by the level of non-uniformity in the initial conditions of the pinch. More uniform pre-ionization of the gas should promote more uniform current flow on the gas column, i.e., more uniform initiation will reduce the seed for the instability.

Two UV pre-ionization sources have been designed and constructed. The first one, called here the DM2 pre-ionizer, was developed by the NRL Pulsed Power Physics Group (Reference 42) and fielded on DM2 during the PRS experiment in the spring of 1998. Ionization levels > 1% were measured at the outer edge of the flow, with penetration consistent with $\geq 100\ \mu J/cm^2/\mu s$ of 16-27 eV radiation. Data from the DM2 PRS experiment suggest that pre-ionization helps to eliminate the low yield shots and reduce shot-to-shot variation. However, the DM2 experiment also revealed that the DM2 pre-ionizer was vulnerable to damage. Maintenance and repair slowed down the experimental shot-rate significantly. Therefore, in order to field this type of pre-ionizer on an even higher power generator such as Double-EAGLE or Decade Quad, the issue of survivability or easy replaceability had to be addressed.

The second UV pre-ionizer was fabricated at MPI based on the experience with the first one. This pre-ionizer, called the DE pre-ionizer, has now been successfully fielded on Double-EAGLE and Saturn. The performance of the DE pre-ionizer indicates that it has successfully addressed the issues of survivability and replaceability: it is robust and reliable; fabrication and replacement of its components can be easily done.

This section documents the development of those two pre-ionizers. Section 10.2 describes the characteristics of the DM2 pre-ionizer and its performance in the DM2 PRS experiment. Section 10.3 presents the changes made in the design of the DE Pre-ionizer to address the issues of survivability and replaceability, as well as the improvements in performance shown by this pre-ionizer over the DM2 pre-ionizer. A summary is given in Section 10.4.

10.2 DM2 PRE-IONIZER.

Flashboard-generated UV light is a suitable source for pre-ionizing argon gas puffs. The photoionization cross-section for neutral argon exhibits a broad maximum in the $h\nu$ = 16-27 eV range (Reference 43). Earlier experiments indicate that over 60% of the UV emission from such flashboard sources is in the 10-20 eV range with the remainder emitted primarily between 20 and 70 eV (Reference 44). Thus, there exists a good match between the range over which the UV

source is most powerful and that over which argon is most susceptible to ionization by UV radiation.

The working principle of the DM2 pre-ionizer is illustrated in Figure 10-1. In order to generate an azimuthally symmetric ionization source, two semicircular flashboards are used. Each of the flashboards is independently driven by a pulser, which consists of a capacitor bank with a spark gap switch. When triggered, the electric energy stored in the capacitor bank is delivered to the flashboard through the transmission line. Surface breakdown on the flashboard generates the UV emission. Figure 10-2 is a photo of the flashboards and partial transmission lines.

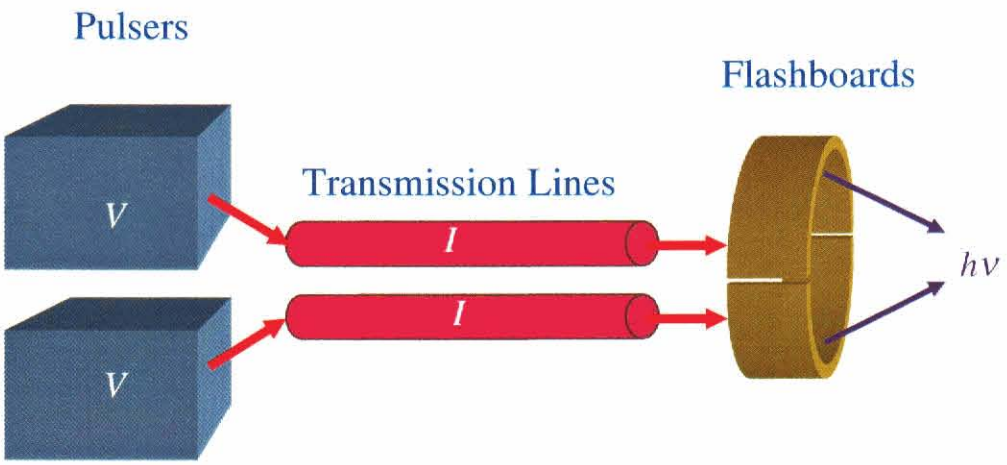

Figure 10-1. Schematic of a UV pre-ionizer.

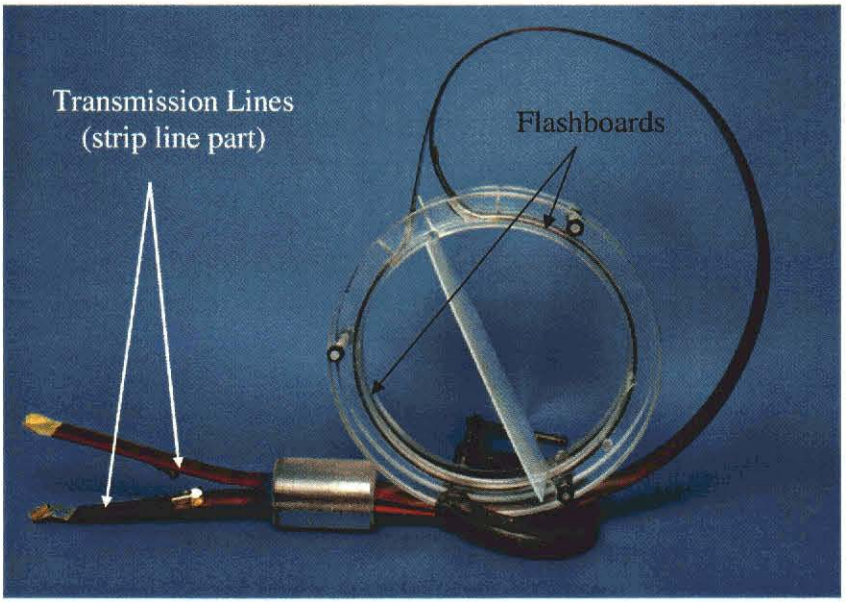

Figure 10-2. The DM2 pre-ionizer.

The flashboards were made of Kapton sheets imprinted with copper pads, as shown in Figure 10-3. Each flashboard has two sections of imprinted Kapton sheets in series, with two rows of copper pads on each section. There is a piece of brass shim on the back of the Kapton sheets to provide capacitive coupling to the copper pads during breakdown as well as to serve as a return current path.

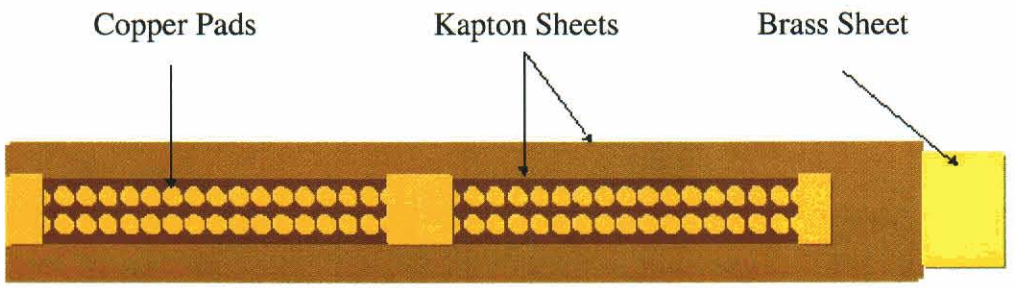

Figure 10-3. Flashboard of the DM2 pre-ionizer.

One of the transmission lines of the DM2 pre-ionizer is shown schematically in Figure 10-4. It consists of two parts: the strip line part and the coaxial cable part. The strip line is used to minimize the transmission line inductance so to maximize the current delivered to a flashboard for UV generation. It also serves as a vacuum feed-through. The strip line is made of a pair of Kapton-insulated brass shims bounded together with epoxy. One end of the strip line connects to a flashboard, the other end join with a bundle of six coaxial cables to connect with a pulser.

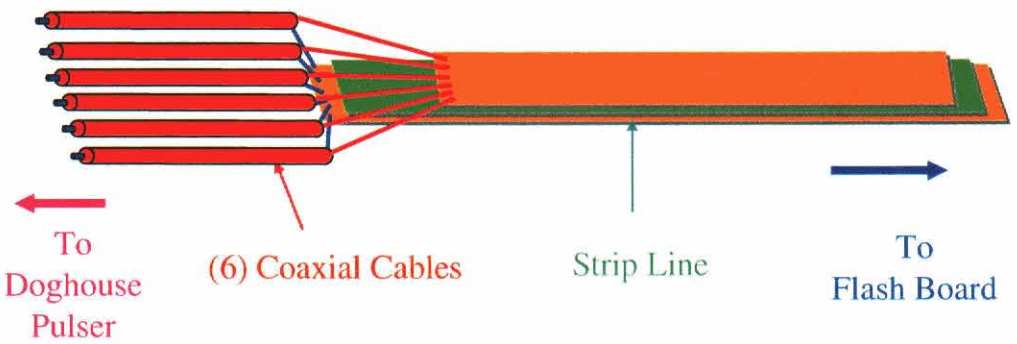

Figure 10-4. Transmission line of the DM2 pre-ionizer.

The pulsers used by the DM2 pre-ionizer are a pair of NRL low-inductance "doghouse" pulsers. Each pulser uses 1.8 μF of total capacitance, with electric energy storage up to 560 J. The electrical parameters of the DM2 pre-ionizer are summarized in Table 10-1.

Table 10-1. Electrical parameters of the DM2 Pre-ionizer*

Pulser Capacitance	1.8 μF
Charging Voltage	20 – 25 kV
Total Inductance	≈190 nH
Total Resistance	≈0.3 Ω
Pulse Half period	2.0 μs
Pulse Peak Current	≈40 kA (at 20 kV)

* Parameters are for one of the two flashboard circuits.

A test of the DM2 pre-ionizer was performed at NRL. The argon gas puff used a 7-cm diameter solid-fill PRS nozzle. A schematic representation of the pre-ionizer in relation to the nozzle is shown in Figure 10-5. Both of the pulsers were charged to 20 kV, providing ≈40 kA peak discharge current on each of the flashboards. High-sensitivity dual wavelength laser interferometry was used to measure the neutral gas distribution and the free electron density produced by pre-ionization. The measurement indicated 1% – 10% ionization at the periphery of the argon gas distribution prior to the arrival of the flashboard plasma. The ionization sheath thickness of several mm is consistent with ≥100 μJ/cm^2/μs of 16-27 eV radiation. The result is illustrated in Figure 10-6 with data taken at z = 2 mm from the nozzle (Reference 42).

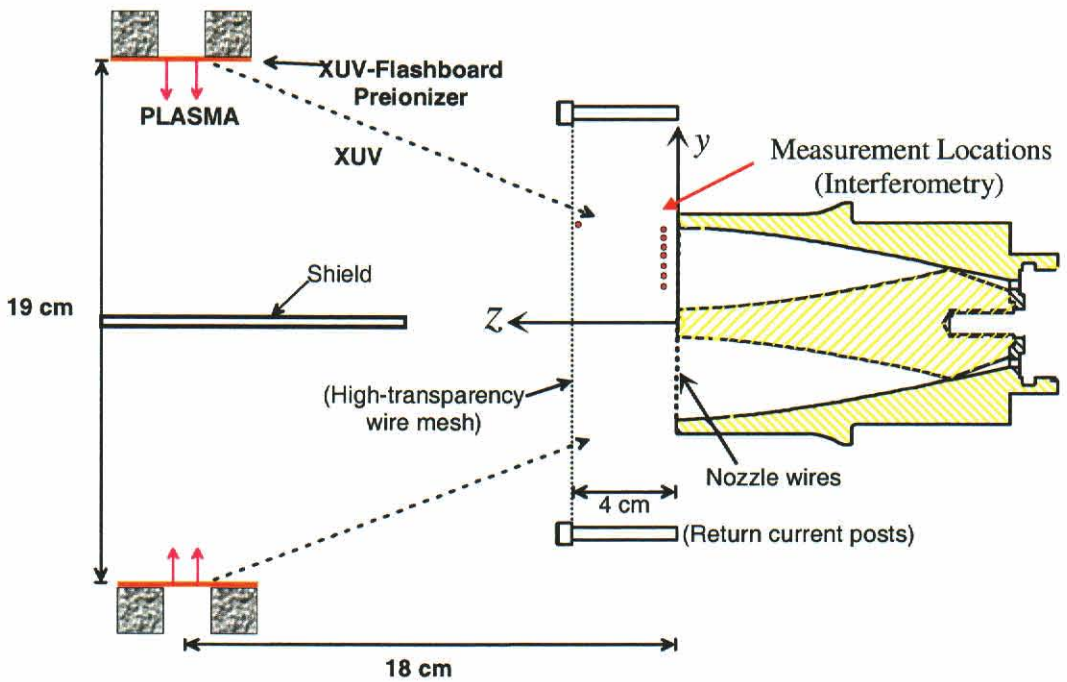

Figure 10-5. Schematic representation of 7-cm nozzle and pre-ionizer; posts and mesh are shown for reference only.

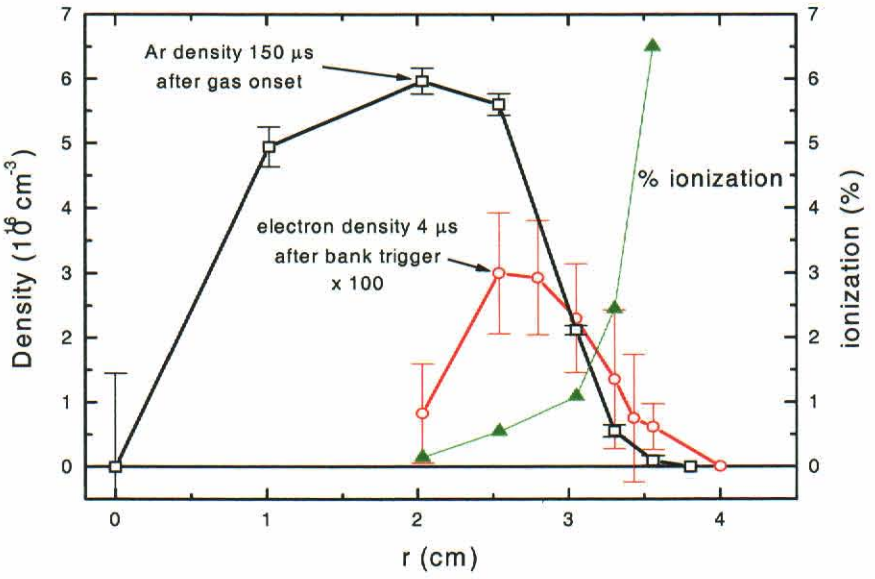

Figure 10-6. Neutral argon and electron radial density profiles at t=150 μs; z = 2mm.

The DM2 pre-ionizer was fielded on DM2 in March 1998 for a limited number of PRS shots. Argon K-shell yields are compared in Figure 10-7 for shots with load currents of 2.25±0.1 MA. The plot on the left compares yields from shots where an array of thin wires were placed over the nozzle exit, while the right side compares yields from shots without wires. Based on these experimental data, one can infer two conclusions. First, without wires across the nozzle face, the yield is on average significantly depressed unless pre-ionization is used. Second, with nozzle wires, the yield is generally higher but the shots with pre-ionization demonstrated reduced scatter and statistically higher yield. (See Section 2.3 for a complete description of the DM2 experiments.)

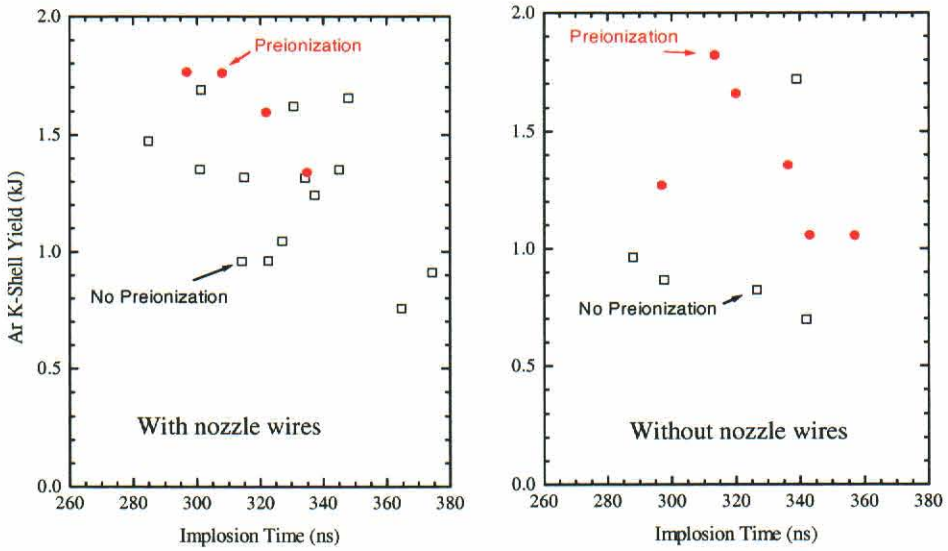

Figure 10-7. DM2 x-ray yield data with and without the pre-ionizer.

The tests on DM2 revealed that a more robust pre-ionizer was required. A frequently encountered problem was the detachment of the copper pads from the flashboards, caused either by debris bombardment or by radiant heating from the PRS. Repairing the pads was required after almost every shot. Another problem is the asymmetric current distribution on the flashboards. As shown in Figure 10-3, each flashboard has two sections, with two rows of copper pads on each section. Photographs of the operating flashboards indicated that the discharge current sometimes ran through only one row of the copper pads in some sections. Another, more serious problem was electrical breakdown, which was observed at the highly field-enhanced edges of the striplines and flashboard junctions. The damage to the strip lines caused by the arcing was difficult to repair because of the way in which the strip lines were fabricated. In fact, the pre-ionizer was out of service during much of the DM2 testing because of arcing damage and difficulty of repair and replacement. Furthermore, the combination of strip lines and the coaxial cables significantly compromised the effort spent in reducing the strip inductance. The inductance at the joints between the cables and the strip line accounts more than half of the system inductance of about 185 nH.

10.3 DOUBLE-EAGLE PRE-IONIZER.

Experience with the DM2 pre-ionizer indicated that UV pre-ionization of the argon gas puffs could help to improve the K-shell yield. However, to field such a pre-ionizer on Double-EAGLE, the issue of survivability or easy replaceability had to be addressed, since the radiation environment on Double-EAGLE is much higher than that on DM2.

The DE pre-ionizer is represented schematically in Figure 10-8. Both its flashboards and its transmission lines are designed differently. The performance of the new pre-ionizer on Double-EAGLE indicates that all problems encountered with the DM2 Pre-ionizer have been successfully addressed. Table 10-2 lists the electrical parameters of the DE pre-ionizer.

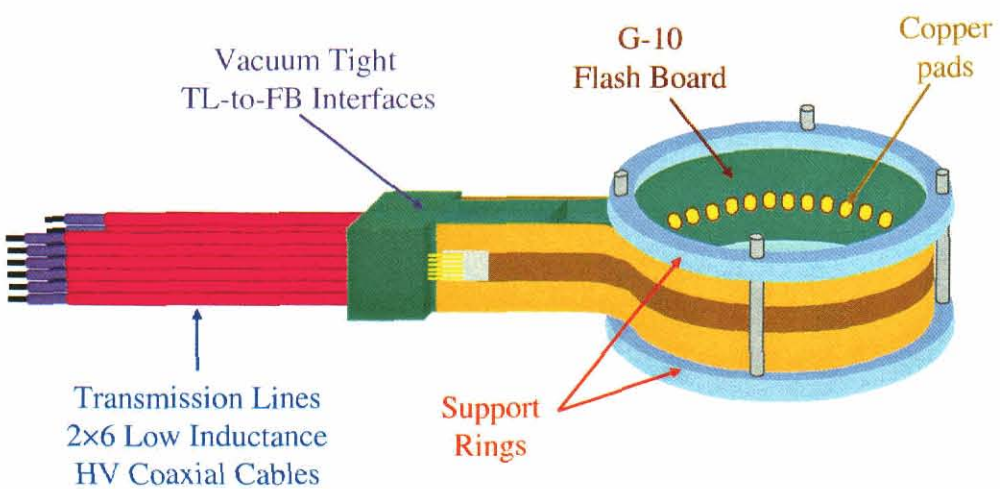

Figure 10-8. Schematic of the DE pre-ionizer

Table 10-2. Electrical parameters of the DE pre-ionizer*

Pulser Capacitance	1.8 μF
Charging Voltage	20–25 kV
Total Inductance	≈90 nH
Total Resistance	≈0.1 Ω
Pulse Half period	1.3 μs
Pulse Peak Current	≈60 kA (at 20 kV)

* Parameters are for one of the two flashboard circuits.

Figure 10-9 shows a flashboard used in the DE pre-ionizer. The new flashboards are made of thin (0.254 mm), imprinted G-10 boards which are robust and long lasting. The bond between the copper pads and the G-10 is very strong. During the PRS experiment on Double-EAGLE, each pair of flashboards of the DE pre-ionizer usually lasted more than ten shots before replacement. Moreover, the new flashboards could be changed without taking the pre-ionizer out of its mounting. Replacing a pair of flashboards normally took less than 20 minutes.

The new flashboards are also more efficient in UV production and less likely to suffer an asymmetric surface discharge. Each new flashboard consists of a single section with one row of copper pads. At a constant total discharge current, the photon yield of the DE pre-ionizer will be twice that of the DM2 pre-ionizer since the photon yield is proportional to the square of the current running through each row of pads. Another advantage of using a single row of copper pads is in preventing the uneven distribution of the surface-discharge current.

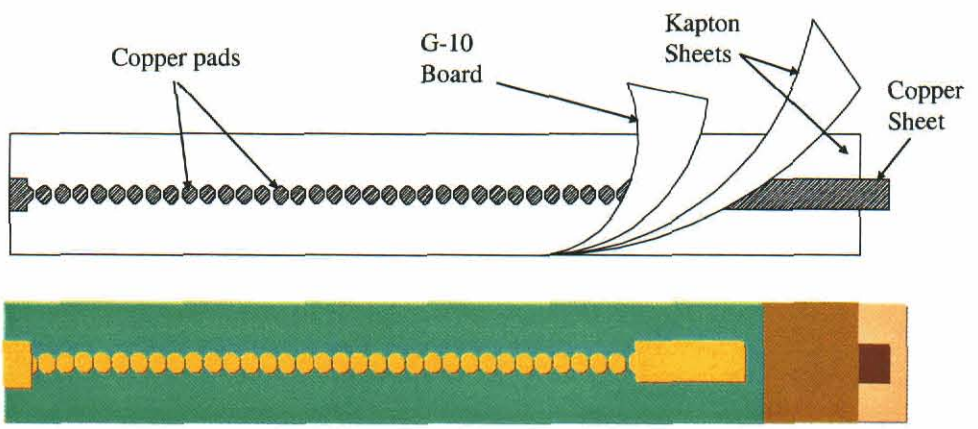

Figure 10-9. Flashboard of the DE pre-ionizer.

A schematic drawing of the transmission lines of the DE pre-ionizer is shown in Figure 10-10. Each transmission line consists of six parallel, coaxial, high voltage cable segments. The cable is commercially available and of low inductance. One end of the transmission line is cast into a vacuum-tight interface, with conductors exposed for easily joining to a flashcard, the other end

directly connects to a pulser. The transmission lines are much easier to make and have only 60 nH inductance for a six-foot long transmission line. This increases the current and the efficiency of the pre-ionizer. Additionally, the new transmission lines are more flexible, which turned out to be a useful feature on Double-EAGLE where the load region is spatially constrained. The transmission lines have proven very robust.

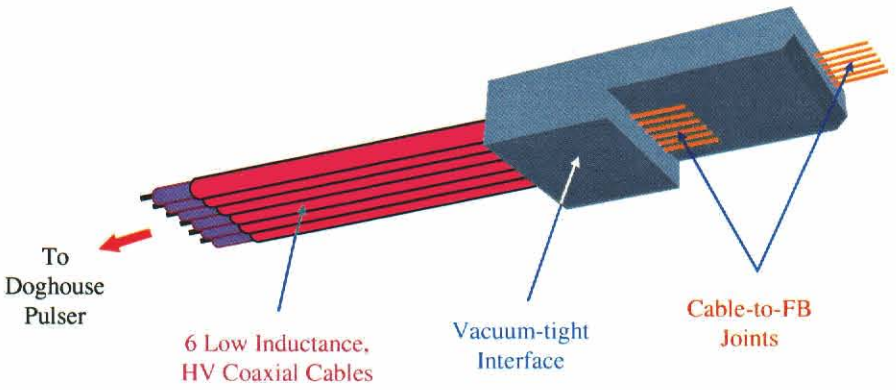

Figure 10-10. Transmission line of the DE pre-ionizer.

Due to time and cost constraints, no systematic comparison shots have been made during the Double-EAGLE tests to demonstrate the effectiveness of the pre-ionization to increase K-shell yield.

10.4 SUMMARY.

A team at NRL designed the DM2 pre-ionizer as an azimuthally symmetric UV source to pre-ionize the argon gas puffs in PRS experiments. Interferometry measurements indicate that such a pre-ionizer can achieve >1% ionization at the outer edge of the flow, with penetration consistent with $\geq 100\ \mu J/cm^2/\mu s$ of 16-27 eV radiation.

The DM2 pre-ionizer was fielded during the DM2 long implosion argon PRS test. The data show that pre-ionization reduced shot-to-shot variations and (statistically) increased the K-shell yield. The DM2 experiment also revealed the need to improve the survivability and replaceability of this type of UV pre-ionizer.

Based on our experience with the DM2 pre-ionizer, the DE pre-ionizer was designed and fabricated at MPI. It has been fielded on Double-EAGLE and Saturn. The DE pre-ionizer has proven to be a robust and reliable UV pre-ionization source.

SECTION 11

ENDNOTES

1. N. R. Pereira and J. Davis, J. Appl. Phys 64, R1, 1988 (Unclassified)
2. C. Deeney et al, J. Appl. Phys. 75, 2781, 1994 (Unclassified)
3. R. B. Spielman et al, AIP Conf. Proc. 195, p. 3, 1989 (Unclassified)
4. K. Whitney et al, Phys. Rev. E 50, 2166, 1994 (Unclassified)
5. J. W. Thornhill et al, J. Appl. Phys. 80, 710, 1996 (Unclassified)
6. C. Deeney et al, Phys.Plasmas 6, 2081, 1999. (Unclassified)
7. J. C. Riordan et al, Maxwell Physics International Report No. PITR-4646-02, 1997 (Unclassified)
8. K. Whitney et al, J Appl. Phys. 67, 1725, 1992 (Unclassified)
9. D. Petersen et al, Phys. Plasmas 3, 368, 1996 (Unclassified)
10. D. Petersen et al, AIP Conf. Proc. 409, p. 201, 1997 (Unclassified)
11. S. M. Golberg and A. L. Velikovich, Phys. Fluids B5, 1164, 1993 (Unclassified)
12. N. Roderick et al, Phys. Plasmas 5, 1477, 1998 (Unclassified)
13. Coleman, P.L., J.Rauch, W.Rix J.Thompson and R.Wilson, Fourth International Conference on Dense Z-Pinches, AIP Proceedings #409, May 1997, p. 119. (Unclassified)
14. D. Mosher, N. Qi, and M. Krishnan, IEEE Trans. Plasma Science 26, 3, 1998 (Unclassified)
15. Nozzles designed by H. Murphy using RZDELTA code reference M. Chapman, S-Cubed Report No. SSS-R-80-4620, 1980 (Unclassified)
16. B. Weber et al, Naval Research Laboratory Pulsed Power Physics Technotes No. 97-08, 1997 (Unclassified)
17. S. J. Stephanakis, B. Mooseman, and B. V. Weber, Naval Research Laboratory Pulsed Power Technote No. 98-05, 1998 (Unclassified)
18. J. Apruzese et al, J. Quant. Speets. Rad-Tranf., 57, 41, 1997 (Unclassified)

19. C. Deeney, M. R. Douglas, R. B. Spielman, T. J. Nash, D. L. Peterson, P. L. Eplattenier, G. A. Chandler, J. F. Seamen and K. W. Struve, Phys.Rev.Lett. **81**,4883 (1998), and references therein. (Unclassified)

20. R.B. Baksht, A. V. Fedunin, A. Yu. Labetsky, A. G. Russkikh, A. V. Shishlov, O. V. Diyankov, I. V. Glazyrin and S. V. Koshelev, IEEE Trans. Plasma Sci., **26** 1259 (1998) (Unclassified)

21. A.L. Velikovich, F. L. Cochran, and J. Davis, Phys. Rev. Lett. **77**, 853 (1996) (Unclassified)

22. J. H. Hammer, J. L. Eddleman, P. T. Springer, M. Tabak, A. Toor, K. L. Wong, G. B. Zimmerman, C. Deeney, R. Humphreys, T. J. Nash, T. W. L. Sanford, R. B. Spielman, and J. S. De Groot, Phys. Plasma **3** 2063 (1996) (Unclassified)

23. D. L. Book, Phys. Plasmas **3** 354 (1996) (Unclassified)

24. B.V. Weber and Y. Song, Technical Note 99-08, Naval Research Laboratory, (1999). (Unclassified)

25. J.C. Riordan, P. L. Coleman, B. H. Failor, J. S. Levine, Y. Song, E. M. Waisman, C. Deeney, J. S. McGurn, J. P. Apruzese, J. Davis, A. Fisher, B. Mooseman, J. W. Thornhill, B. V. Weber, K. G. Whitney, Bulletin of the American Physical Society 43, 1905 (1998). (Unclassified)

26. C. Deeney, P. D. LePell, B. H. Failor, S. L. Wong, J. P. Apruzese, K. G. Whitney, J. W. Thornhill, J. Davis, E. Yadlowsky, R. C. Hazelton, J. J. Moschella, T. Nash, and N. Loter, Phys. Rev. E. 51, 4823 (1995). (Unclassified)

27. J. P. Apruzese, P. E. Pulsifer, J. Davis, R. W. Clark, K. G. Whitney, J. W. Thornhill, T. W. L. Sanford, G. A. Chandler, C. Deeney, D. L. Fehl, T. J. Nash, R. B. Spielman, W. A. Stygar, K. W. Struve, R. C. Mock, T. L. Gilliand, D. O. Jobe, J. S. McGurn, J. F. Seamen, J. A. Torres and M. Vargas, Phys. Plasmas **5**, 4476 (1998). (Unclassified)

28. J. W. Thornhill, K. Whitney, and J. Giuliani in "PRS Scoping Study I: Scaling Law Estimates for K-shell Radiation Yields on Jupiter-class Generators", Naval Research Laboratory Memo Report NRL/672D-94-7466, 1994 (Unclassified)

29. C. Deeney et al, Phys. Plasmas 5, 2431, 1998 (Unclassified)

30. T. W. L. Sanford et al, Physical Rev. Letter 77, 5063, 1996 (Unclassified)

31. P.L. Coleman and E.M.Waisman, Bulletin American Physical Society 44, 309, 1999. (Unclassified)

32. Henke, B. L., et al., Journal of the Optical Society of America B **3**, 1540 (1986). (Unclassified)

33. Glenzer, S. H., et al., Phys. Rev. E **55**, 927 (1997). (Unclassified)

34. Wong, K. L., et al., Physical Review Letters **80**, 2334 (1998). (Unclassified)

35. Sanford,T.W.L., et.al. Paper 4HP14, IEEE International Conference on Plasma Science Abstracts, June 1996, p. 251. (Unclassified)

36. L. Poletto, A. Boscolo, and G. Tondello, Applied Optics **38**, 29 (1999). (Unclassified)

37. See http://www.prinst.com/pdfs/512sf.pdf (Unclassified)

38. N. Qi et al, Alameda Applied Sciences Corporation Report 98 TM-85, 1998 (Unclassified)

39. B. V. Weber and S. F. Fulghum, Rev. Sci Instrum. 68, p. 1227, 1997 (Unclassified)

40. R. E. Peterkin, Jr., et al., *IEEE Trans. Plasma Sci.* **21**, 552 (1993). (Unclassified)

41. DELTA2dRZ code developed at Maxwell Technologies. (Unclassified)

42. B. Mooseman et al, Rev Sci. Instrum. 70, p. 672, 1999 (Unclassified)

43. D. A. Verner et al, Astrophysics Journal 465, p. 487, 1996 (Unclassified)

44. J. R. Woodworth and P. F. McKay, J. Appl. Physics 58, 3364, 1985. (Unclassified)

DEPARTMENT OF DEFENSE

DEFENSE TECHNICAL
INFORMATION CENTER
8725 JOHN J. KINGMAN ROAD,
SUITE 0944
FT. BELVOIR, VA 22060-6201
2 CYS ATTN: DTIC/OCA

DEPARTMENT OF DEFENSE CONTRACTORS

ITT INDUSTRIES
ITT SYSTEMS CORPORATION
1680 TEXAS STREET, SE
KIRTLAND AFB, NM 87117-5669
2 CYS ATTN: DTRIAC
ATTN: DARE